Hydrobiogeophysics:

Linking geo-electrical properties and biogeochemical processes in shallow subsurface environments

by

Adrian Mellage

A thesis

presented to the University of Waterloo

in fulfillment of the

thesis requirement for the degree of

Doctor of Philosophy

in

Earth Sciences (Water)

Waterloo, Ontario, Canada, 2018

Examination committee membership

External Examiner	Dr. Yuxin Wu Research Scientist Climate and Ecosystem Sciences Division Laurence Berkeley National Lab
Supervisor	Dr. Philippe Van Cappellen Professor, Canada Excellence Research Chair Laureate Department of Earth and Environmental Sciences University of Waterloo
Co-supervisor	Dr. Fereidoun Rezanezhad Assistant Professor Department of Earth and Environmental Sciences University of Waterloo
Committee member (adjunct)	Dr. Alex Furman Associate Professor Civil and Environmental Engineering Technion – Israel Institute of Technology
Committee member	Dr. Anthony Endres Associate Professor Department of Earth and Environmental Sciences University of Waterloo
Internal-external member	Dr. Frank Gu Associate Professor, Canada Research Chair Department of Chemical Engineering University of Waterloo

Author’s declaration

This thesis consists of material all of which I authored or co-authored: see Statement of Contributions included in the thesis. This is a true copy of the thesis, including any required final revisions, as accepted by my examiners.

Statement of contributions

The research chapters of this thesis are a compilation of a series of co-authored papers. I am the first-author on each paper, and was primarily responsible for experimental study and model design and execution. The contributions of co-authors for each chapter/paper are outlined below.

Chapter 2

Geertje J. Pronk (GJP), Fereidoun Rezanezhad (FR) and I designed and implemented the soil column experiment. I installed the geophysical measurement array and analyzed all geophysical data. Tatjana Milojevic (TM) installed the oxygen electrodes and analyzed those data. GJP and I performed periodic pore water sampling and analyzed the data. GJP, FR, TM and I performed the sacrificial sampling of soil columns, and GJP and I performed the various analyses. I wrote the paper, with inputs from GJP, FR, Estella A. Atekwana (EAA), Alex Furman (AF) and Philippe Van Cappellen (PVC).

Chapter 3

Christina M. Smeaton (CMS) and I designed and ran the experiment with input from PVC. I developed the model and analyzed the data, with inputs from CMS, PVC and AF. I wrote the paper, with inputs from CMS, AF, EAA, FR and PVC.

Chapter 4

FR and I designed the experimental columns. CMS and I designed and ran the experiment. I analyzed the biogeochemical and geophysical data. I wrote the paper with inputs from CMS, EAA, AF and PVC.

Chapter 5

I developed the model with input from CMS and Stephanie E. Slowinski (SES). CMS designed and conducted the batch experiment. I wrote the paper with input from CMS, SES and PVC.

Chapter 6

Andrew B. Holmes (ABH) and I designed and ran the experiment. Start Linley (SL) synthesized the nanoparticles. I developed the model with input from ABH and Neil Thomson (NT). ABH and I wrote the paper with input from SL, FR, NT, Frank Gu (FG) and PVC.

Abstract

Microbially mediated reactions drive (bio)geochemical cycling of nutrients and contaminants in shallow subsurface environments. Environmental forcings exert a strong control on the timing of reactions and the spatial distribution of processes. Spatial and temporal variations in electron acceptor and donor availability may modulate nutrient/contaminant turnover. Characterizing the preferential spatial-zonation of biologically driven reactions, and quantifying turnover rates is hindered by our inability to access the subsurface at the spatial and temporal resolution required to capture reaction kinetics. Typical subsurface sampling methods generate discrete spatial datasets as a function of the prohibitive cost and operational challenges of borehole installation and core sampling, coupled with sparse temporal datasets due to intermittent sampling campaigns. In order to improve our ability to access biogeochemical information within the subsurface, without the need for destructive and intrusive sampling, non-invasive geophysical techniques (a comparatively inexpensive alternative) have been proposed as a means to characterize subsurface reactive compartments and locate zones of enhanced microbial activity and the timing of their development. The challenge lies in linking electrical responses to specific changes in biogeochemical processes.

In this thesis, I assess the potential and suitability of spectral induced polarization (SIP) and self-potential (SP) / electrodic potential (EP) derived geo-electrical signals to detect, map, monitor and quantify microbially mediated reactions in partially- and fully-saturated heterogeneous porous media (*i.e.*, soil). I build on existing literature delineating the sensitivity of SIP, SP and EP to biogeochemical processes and both qualitatively and quantitatively link geo-electrical signal dynamics to specific microbial processes at the experimental scale. I address the monitoring of complex, coupled processes in a well-characterized near-natural system, and combine reactive transport models (RTMs) with single-process reactive experiments (reduced complexity), to isolate diagnostic signatures of specific reactions and processes of interest.

In Chapter 2, I begin by monitoring biogeochemically modulated geo-electrical signals (SIP and EP), in the variably (and dynamically) saturated reactive zone within the capillary fringe of an artificial soil system. SIP and EP responses show a clear dependence on the depth-distribution of subsurface microbes. Dynamic SIP imaginary conductivity (σ'') responses are only detected in the water table fluctuation zone and, in contrast to real conductivity (σ') data, do not exhibit a direct soil moisture driven dependence. Using multiple lines of evidence, I attribute the observed σ''

dynamics to microbially driven reactions. Chapter 2 highlights that continuous SIP and EP signals, in conjunction with periodic measurements of geochemical indicators, can help determine the location and temporal variability of biogeochemical activity and be used to monitor targeted reaction zones and pathways in complex soil environments.

Building on the findings from Chapter 2, that biomass distribution and activation strongly modulate SIP responses, in Chapter 3 and 4, I focus on isolating the geo-electrical contribution of microbes themselves. In Chapter 3, I couple geochemical data, a biomass-explicit diffusion reaction model and SIP spectra from a saturated sand-packed (with alternating layers of ferrihydrite-coated and pure quartz sand) column experiment, inoculated with *Shewanella oneidensis*, and supplemented with lactate and nitrate. The coupled RTM and geo-electrical data analysis show that imaginary conductivity peaks parallel simulated microbial growth and decay dynamics. I compute effective polarization diameters, from Cole-Cole modeling derived relaxation times, in the range 1 – 3 µm; two orders of magnitude smaller than the smallest quartz grains in the columns, suggesting that polarization of the bacterial cells directly controls the observed chargeability and relaxation dynamics.

In Chapter 4, I address the lack of experimental validation of biomass concentrations in Chapter 3. I present a measurement-derived relationship between *S. oneidensis* abundance and SIP imaginary conductivity, from a microbial growth experiment in fully saturated sand-filled column reactors. Cole-Cole derived relaxation times highlight the changing surface charging properties of cells in response to stress. The addition of concurrent estimates of cell size allow for the first measurement-derived estimation of an apparent Stern layer diffusion coefficient for cells, which validates existing modelled values and helps quantify electrochemical polarization during SIP-based monitoring of microbial dynamics.

The relaxation time results from Chapter 4 suggest that bacterial cell surface charge is modified in response to nitrite toxicity-induced stress. In Chapter 5, I present a biomass-explicit reactive transport model, which integrates nitrite-toxicity, as a key modulator of the energy metabolism of *S. oneidensis*, to predict the rates of nitrate and nitrite reduction. I validate the model with results from two separate experiments (at different experimental scales): (1) a well-mixed batch suspension and (2) the flow-through reactor experiment from Chapter 4. The incorporation of toxicity-induced uncoupling of catabolism and anabolism in the reactive term predicts the observed delay in biomass growth, facilitated by endogenous energy storage when nitrite is

present, and consumption of these reserves after its depletion. The model is further validated by the close agreement between the trends in imaginary conductivity and simulated biomass growth and decay dynamics.

Finally, in Chapter 6, I apply the RTM-SIP integrative framework from Chapters 3 and 5 to develop quantitative relationships between SIP signals and engineered nanoparticle concentrations. Therein, SIP responses measured during injection of a polymer-coated iron-oxide nanoparticle suspension in columns packed with natural aquifer sand are coupled to output from an advective-dispersive transport model. The results highlight the excellent agreement between simulated nanoparticle concentrations within the columns and SIP signals, suggesting that polarization increases proportional to increasing nanoparticle concentration. The results from Chapter 6, introduce the possibility of quantitative SIP monitoring of coated metal-oxide nanoparticle spatial and temporal distributions.

Overall, my results show the applicability of SIP and EP to map and monitor the spatial zonation of biogeochemical hotspots and to detect their temporal activation. By coupling RTMs with geo-electrical datasets, I highlight the direct control that polarization of microbial cells exerts on SIP signals in biotic systems. Furthermore the measurement-derived SIP-biomass quantitative relationship provides a first attempt to directly measure *in situ* biomass density, using geo-electrical signals as a proxy. I show that geo-electrical signal dynamics (Cole-Cole relaxation time) can be used to inform processes within RTMs. Finally, the implementation of the combined modeling and electrical monitoring approach, to the case of engineered nanoparticles, confirms SIP's suitability to monitor colloid transport in the environment and highlights considerations for method optimization.

Acknowledgements

I am grateful to Philippe Van Cappellen, for giving me the chance to work in a vibrant and innovative research team, and for the endless exciting opportunities throughout. Your guidance has helped me haze the disciplinary boundaries of this multi-disciplinary project, moving forward in developing truly integrative approaches in biogeochemistry. Working together has been an inspiring and enriching experience.

To Fereidoun Rezanezhad, my co-advisor, thank you for your unwavering support and guidance throughout this PhD. Your energy and positive feedback helped me "hit the ground running" and develop this project. I was fortunate to have a second co-advisor, Alex Furman, to whom I am grateful for his guidance and support in all facets of this project. I thank you for your continuously exceptional feedback and for hosting me for two research visits in Haifa while also introducing me to Israeli gastronomy. I thank Estella Atekwana, my committee member, for hosting me in her lab, her excellent feedback, insightful discussion and guidance. I would also like to thank my committee member Tony Endres, for his feedback and insightful discussions.

During my PhD I had the opportunity to work with Christina Smeaton and Geertje Pronk. I thank you both for your guidance and support, your critical feedback and your outstanding scientific input. The opportunity to learn from you and collaborate with you both helped me become a better scientific researcher. I also want to thank Andrew Holmes for his initiative and research vision in establishing the collaboration between Ecohydrology and Nanotechnology, working together was a pleasure filled with exciting science.

To Marianne Vandergiendt, thank you for your help and guidance in the lab. The opportunity to supervise and work with Shannon Oliphant and Laureline Vallée was an invaluable experience and I thank you both for your engagement.

I want to thank my graduate student colleagues and friends Taylor Maavara, Jeremy Bennett, Katya Markelova, Igor Markelov, Tatjana Milojevic, James Telford, Branden Walker and Alec Maavara for your friendship and support throughout, and your encouragement. I am fortunate to have shared this experience with you. I want to thank Chris Parsons, Homa Kheyrolla Pour and Mahyar Shafii for your constructive advice and open door policy letting me bounce ideas around.

Finally, I would like to thank my father, Chris Mellage, my sisters Tesla and Jessica Mellage, and Alejandro Guzmán for your unconditional love and support throughout my academic career, I would not have made it here without it.

Le dedico esta tesis a María Adel.

Contents

List of Figures

List of tables

1 Introduction

1.1 Accessing the subsurface

Characterizing and quantifying microbially-driven (bio) geochemical reactions in the shallow subsurface (on the scale of tens of meters below the surface), with relevance to nutrient cycling and contaminant transport, hinges on our ability to access reactive compartments of soils, sediments and aquifers at depths exceeding several meters. The common sampling methods employed rely on borehole drilling (observation well installation) and core-logging. These methods are invasive, destructive, logistically difficult and often prohibitively expensive to deploy, impeding comprehensive spatial coverage of a specific study site. The discontinuous nature of grab- and observation well sampling (bulk soil and pore water), results in "missing information" in between sampling points that does not accurately capture physical and biogeochemical heterogeneity.

Biogeochemical reactions in the subsurface require the simultaneous presence of electron acceptor, electron donor and microbes (Rees et al., 2007). Biogeochemical nutrient and contaminant cycling (*e.g.*, degradation) is enhanced across zones of confluence between the key components of microbially mediated reactions, these are referred to as biogeochemical hotspots (McClain et al., 2003). Environmental interfaces or transition zones (*e.g.*, vadose zone, hyporheic zone and contaminant plume fringe) are hotspots of biogeochemical activity, where mixing is induced by dynamic changes in environmental conditions, such as moisture content (*e.g.*, water table fluctuations). Aquifer sediment heterogeneity (*e.g.*, hydraulic conductivity lenses) can result in preferential flow paths, where mixing occurs, also enhancing reactivity (Cirpka et al., 1999). Locating biogeochemical hotspots is therefore imperative for quantifying biogeochemical cycling, even over large spatial scales.

Higher spatial and temporal resolution monitoring of biogeochemistry, using geophysical techniques, has been proposed as a means to characterize subsurface reactive compartments to locate reactive hotspots and moments of enhanced reactivity (Kemna et al., 2012; Atekwana and Atekwana, 2010; Atekwana and Slater, 2009). The key advantages of geophysical techniques are that they (1) can provide *in situ* information, (2) are minimally invasive and non-destructive, and (3) yield high spatial and temporal resolution output, without the need for intrusive sampling and time consuming (and expensive) *ex situ* analyses. The general principle is to monitor the spatial

and temporal changes in electrical properties of a soil, resulting from microbially mediated and abiotic reaction processes as well as physical drivers. The emerging research initiative relies (primarily) on geophysical techniques such as spectral induced polarization (SIP) and self-potential (SP), both of which have been shown to be sensitive to microbially mediated processes (Slater et al., 2007; Abdel Aal et al., 2004; Naudet et al., 2003) that govern the fate and transport of contaminants and nutrients in fully and variably saturated porous media (soils, unconsolidated sediments and porous rocks). Both SIP and SP signals are induced or arise (respectively), due to the charged properties of soil particles and the modifications to the charge induced by geochemical reactions as well as the presence of electron migration pathways. This thesis primarily covers the application of SIP for monitoring microbially mediated reactions. Therefore, in the following, detailed background information is provided on the generation of the induced polarization or IP effect. A description of the self-potential method can be found in the following chapter, with relevance to redox gradients in subsurface transition zones.

1.1.1 The charged properties of soils and colloids

Mineral particles can develop a structural surface charge (primarily negative) because of imperfections caused by the isomorphous substitution of elements (that is, atoms of a different charge, but similar ionic radius) within the mineral lattice (Stumm, 1992). For example, substitution of Si^{4+} by Al^{3+} generates a negative charge in the tetrahedral sheet(s) of clay minerals. Chemical reactions between dissolved species and functional groups on particle surfaces (mineral and organic) also lead to the development of variably charged sites. The magnitude of charge, and whether these are positive, negative or neutral is a function of the degree of ionization of the functional groups (Stumm, 1992). The charge is modulated by pH, where protonation and deprotonation of functional groups leads to a higher proportion of positive or negative sites, respectively. The charge imbalance is neutralized by counterions in solution, which are attracted to charged surface sites.

Electrostatic attraction of counterions towards surface sites results in an accumulation of charge near the surface, which decreases (exponentially) with increasing distance from the charged surface, until reaching the electroneutral bulk solution (Stumm, 1992). The region at the solid-liquid interface of enriched counterion concentration is known as the electrical double layer (EDL). The Gouy-Chapman theory (Chapman, 1913; Gouy, 1910), and modified models thereof, describe

the EDL as a series of layers including a fixed charge layer at the particle surface, a layer of adsorbed ions (Stern layer, Stern (1924)) and the diffuse layer of decreasing potential (and counterion concentration) approaching the bulk solution (Stumm, 1992). The vast majority of isomorphous substitution leads to a net negative structural surface charge for minerals, counterbalanced by dissolved cations. Variably (pH-dependent) charged sites are often positively charged at high pH values, however, and the net positive charge is counterbalanced by anionic species. A schematic representation of the EDL (Stern layer model) surrounding a negatively charged particle, where charge is counterbalanced by dissolved cations, is shown in Figure 1-1. The degree of isomorphous substitution, the presence of functional groups on particle surfaces and their degree of protonation and deprotonation, concurrently determine the magnitude of the overall surface charge density at the particle surface.

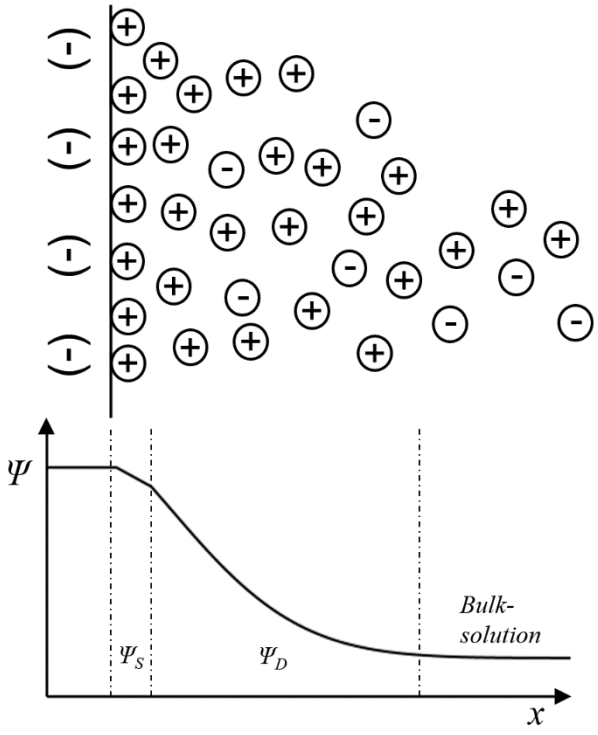

Figure 1-1. Schematic of the electrical double layer (EDL) surrounding a negatively charged particle surface. The charged surface has a fixed potential (Ψ), which begins to decrease in the Stern layer (Ψ_S) (Stern, 1924), and decreases exponentially in the positively charged diffuse layer (Ψ_D) until reaching electrostatic equilibrium in the bulk solution (modified from: Stumm (1992)).

1.1.2 Spectral Induced Polarization (SIP)

Spectral induced polarization (SIP) is an active geophysical technique, where an alternating current is injected between electrodes through a medium, and the resultant voltage gradient is measured across the sample, over a broad frequency range (Wong, 1979; Sumner, 1976). The impedance (Z) between injected current and measured voltage potential is given by:

$$Z = |Z|e^{-i\varphi} \tag{1.1}$$

where $|Z|$ is the measured impedance, $i = \sqrt{-1}$ (the imaginary unit), and φ [rad] is the phase shift at a specific frequency. The measurable or apparent conductivity (σ_a) [S m^{-1}] of a medium, is given by:

$$\sigma_a = \frac{1}{KZ} \tag{1.2}$$

where K [m] is the geometric factor (a function of the geometry of the geophysical measurement array, *i.e.*, electrode emplacement). Substituting equation 1.1 into equation 1.2 yields the following expression for the complex conductivity (σ^*):

$$\sigma^* = \frac{1}{K|Z|}e^{-i\varphi} \tag{1.3}$$

Based on Euler's equation for the complex exponential function, equation 1.3 can be separated into real and imaginary contributions, for $|\sigma| = \frac{1}{K|Z|}$:

$$\begin{aligned} \sigma^* &= |\sigma|\cos\varphi + |\sigma| i \sin\varphi \\ \sigma^* &= \sigma' + i\sigma'' \end{aligned} \tag{1.4}$$

An example of current injection, and resultant voltage potential, for a single frequency is illustrated in Figure 1-2. Energy dissipation and the charged properties of soils lead to a dampening of the amplitude of the measured waveform. The peaks (and troughs) arrive later, with respect to the injected current, leading to a negative φ. The real conductivity (σ') is influenced by conduction in the pore-fluid, and at the grain-fluid interface, while the imaginary conductivity (σ'') is a function of charge storage (Vinegar and Waxman, 1984).

1.1.3 The sources of the geo-electrical signal

At low frequencies (0.01-1000 Hz) current injection induces electrochemical polarization (Olhoeft, 1985). Electrochemical polarization can manifest itself as (1) the migration of ions within the Stern layer of the EDL, known as **Stern layer polarization** (Lesmes and Morgan, 2001;

Chelidze and Gueguen, 1999; Schön, 1996; de Lima and Sharma, 1992; Schwarz, 1962), and (2) the back-diffusion of ions within the diffuse layer at bottlenecks in the pore space, where charge accumulates as a function of pore geometry (strongly modulated by clay content), referred to as **membrane polarization** (Revil and Florsch, 2010; Titov et al., 2002; Vinegar and Waxman, 1984; Marshall and Madden, 1959). The magnitude of electrochemical polarization is a function of the surface charge density of the charged particles (or pores, in the context of consolidated media), their surface area and the effective surface ionic mobility of counterions in the EDL (Lesmes and Frye, 2001). The energy consumed to induce the tangential migration of ions along charged surfaces, results in the signal differences, as illustrated in Figure 1-2. An illustration of the IP effect along the surface of a negatively charged spherical particle (*i.e.*, Stern layer polarization) is shown in Figure 1-3.

At frequencies above 100 Hz, a third polarization mechanism becomes a relevant charge storage source, and dominates above 1000 Hz. **Maxwell-Wagner (MW) polarization** (also known as interfacial polarization) arises from the tangential migration of ions at interfaces of charge build-up (Olhoeft, 1985), due to the discontinuity of the displacement current (Revil and Florsch, 2010). Interfacial charge build-up occurs in the presence of materials or phases of different dielectric and conductive properties (Jougnot et al., 2010; Chen and Or, 2006). Furthermore, In the presence of metallic particles **electrodic polarization** hinders the flow of electric current between the solution and the metallic particles (or ore bodies), requiring the build-up of an overvoltage to overcome ohmic losses (Marshall and Madden, 1959). However, this charge storage mechanism is typically irrelevant for most environmental applications.

The application of SIP as a proxy measurement tool for detecting and monitoring biogeochemical processes in the subsurface, relies on electrochemical polarization phenomena (to a lesser extent MW-polarization), which lead to charge storage. Polarization cannot be induced in the absence of a charge imbalance at the solid-liquid interface. Specific interest is, therefore, given to processes that modify the charged properties of a porous medium, by modulating conduction pathways, thereby influencing σ', and/or resulting in changes to particle surface complexation and surface area, influencing σ''.

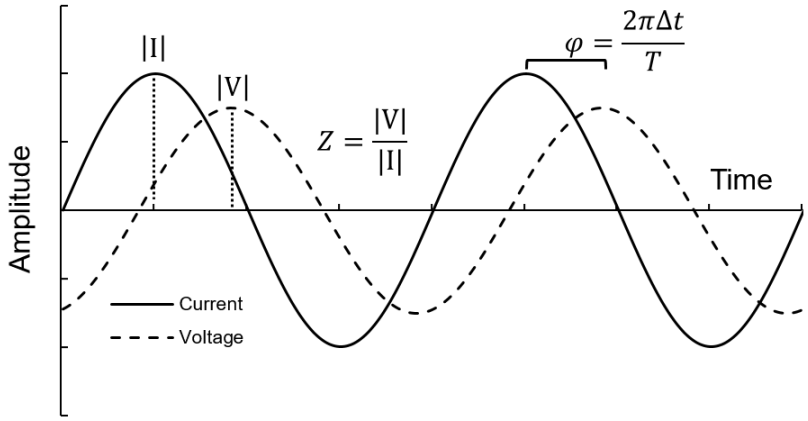

Figure 1-2. Injected current and resultant voltage potential between two current electrodes, during a spectral induced polarization (SIP) measurement, at a single frequency (modified from: Ontash & Ermac Inc. (2014)).

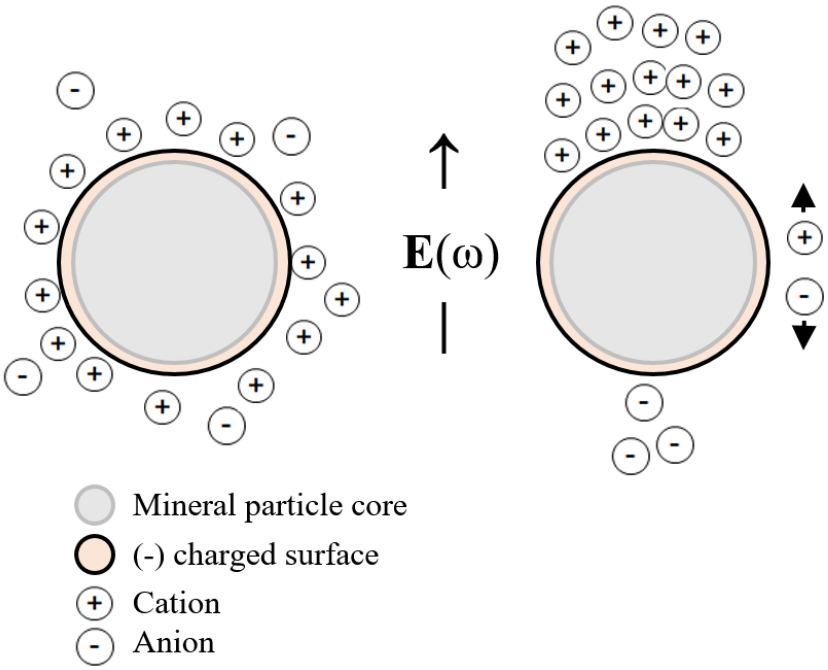

Figure 1-3. Tangential migration of ions along the surface of a negatively charged spherical particle during the application of a frequency-dependent electrical current, **E**(ω). (modified from: Ulrich and Slater (2004)).

1.2 On the importance of capturing the role of microbes in subsurface biogeochemistry

Microbes at the confluence of a substrate (nutrient source and electron donor, ED) and electron acceptor (EA) catalyze the coupled oxidation and reduction of carbon source (*i.e.*, ED) and EA, respectively. The exergonic reduction-oxidation (redox) reaction provides energy for growth and metabolic processes, resulting in sustained microbial turnover. This process can be illustrated in the following idealized equation:

$$CH_2O + O_2 \xrightarrow{\textbf{Bio}} CO_2 + H_2O \qquad 1.5$$

where CH_2O is an idealized formulation for dissolved organic carbon (DOC), which in this case acts as both the ED and carbon source, and O_2 as the EA. Organic carbon is oxidized (from oxidation state 0 to +4) to CO_2 and oxygen is reduced (from an oxidation state of 0 to -2) to water. The energy produced from the reaction fuels microbial metabolic activity (**Bio**).

The simplified formulation in equation 1.5, contains the building blocks for microbially mediated chemical reactions which govern the fate and transport of organic contaminants (typically sources of carbon and electron donors) and nutrients (typically EAs or taken up during biomass synthesis). Thus, equation 1.5 can be modified for aerobic respiration of more complex organic carbon substrates as well as anaerobic respiration relying on the presence of alternative EAs, such as nitrate, manganese, ferric iron and sulphate.

Accurately estimating reaction rates in subsurface environments enables the characterization and quantification of groundwater geochemistry, and the fate and transport of geochemical species of concern (*e.g.*, contaminants and nutrients). *In situ* monitoring of substrate and EA concentration changes are often used to estimate reaction rates, but require extensive sampling (which is often not possible) and analytical capabilities (Williams et al., 2009b). Furthermore, rates of microbial metabolism are reflected in the turnover of substrate pools and not necessarily on their concentrations (Wardman et al., 2014). Therefore, to get a handle on microbial metabolic rates, typically soils and sediments collected in the field are incubated in the lab (Wardman et al., 2014; Williams et al., 2009b).

In the subsurface, microbes partition between the aqueous and solid phases. For groundwater systems, aquifer sediments have been shown to harbor 97.7 to 99% of degrading microbes (Anneser et al., 2010; Griebler et al., 2002), which exhibit 5 to 6 orders of magnitude higher

enzymatic activities than their suspended counterparts (Anneser et al., 2010). Lobete et al. (2015) highlight that microbial behavior is, in large part, modulated by the organisms' environment; in soils, composed of a mixture of solid structures and fluid-filled pore space. Therefore, Lobete et al. (2015) highlight the importance of studying microbial colony behavior in their porous environment.

Traditional microbial quantification techniques are destructive. Sample preparation, separation techniques (*e.g.*, density centrifugation) and treatments to stain cells (Vives-Rego et al., 2000), inherently modify cell properties in order to enhance detection, potentially altering the size, activity and viability of cells (Wardman et al., 2014). Field and bench-scale studies have used invasive sampling methods to quantify biomass in porous media relying on labour intensive techniques such as direct counting using microscopy (*e.g.*, Anneser et al. (2008)), luminescence based techniques to measure adenosine tri-phosphate (*e.g.*, Mellage et al. (2015)), automated counting using flow cytometry (*e.g.*, Anneser et al. (2010)), phospholipid-PO_4 content (*e.g.*, Blume et al. (2002)), carbon analysis (*e.g.*, Joergensen and Mueller (1996)) and optical density measurements (*e.g.*, Zhang et al. (2014)).

Currently, the necessity of sample removal and treatment prior to microbiological characterization, greatly limits our ability to capture temporal variations and spatial changes in microbial abundance, at both the field and lab scales. Our understanding of microbially catalyzed biogeochemical exchange is hindered by the lack of methods to characterize processes in real time and at their location. It is recognized in the current literature that knowledge gaps regarding specific biogeochemical cycles of interest, or the effect of specific environmental forcings, will only be possible by bridging the gap between our theoretical understanding and our measurement capabilities. The dynamic nature of environmental conditions and adaptability of microbial communities necessitates high-resolution *in situ* techniques for quantifying microbial processes that modulate the fate and transport of contaminant and nutrient cycling in subsurface environments (Wardman et al., 2014; Williams et al., 2009b; Kappler et al., 2005). Taking advantage of our ability to measure soil electrical properties at high temporal and spatial resolutions, with high spatial coverage, and the changes on soil charging properties that various biogeochemical processes of interest result in, poise non-invasive geophysical methods as ideal candidates to bridge the highlighted mechanistic knowledge gap.

1.2.1 Microbially driven changes to soil electrical properties

This thesis focuses on the application of geophysical methods to monitor biogeochemical processes that directly result in changes in the charging properties of soil. Redox reactions result in mineralogical changes to particle surfaces, modulating the surface area and surface charge density of oxide minerals, cation exchange on clays, and clay-organo complexation (Olhoeft, 1985). In 2004, Atekwana et al. shifted the attention of the hydrogeophysical scientific community to the role of microbes in modulating subsurface geo-electrical properties at contaminated sites. Atekwana et al. (2004) correlated zones of elevated pore water conductivity with the presence of hydrocarbon degrading microbes, suggesting that microbial hydrocarbon degradation contributed to elevated fluid conductivities. The authors established a connection between microbially-driven contaminant degradation and potential changes to subsurface geo-electrical properties, linking the electrical properties of the subsurface to microbially mediated reactions.

Abdel Aal et al. (2004) built on the findings by Atekwana et al. (2004), and used SIP to monitor microbial degradation processes in contaminated sediments, taking advantage of SIP's unique sensitivity to conduction pathways and energy storage mechanisms (*i.e.*, decoupling of processes in the fluid and solid-fluid interface), separately. Their study showed that microbial processes specifically altered the interfacial electrical properties of unconsolidated sediments rich in organic carbon, by inducing changes in surface chemistry at the solid-fluid interface, modulating low-frequency electrochemical polarization processes. Further studies confirmed the direct effect of the presence of microbes on SIP charge storage responses, (*i.e.*, σ'') (Abdel Aal et al., 2006; Davis et al., 2006). While the contribution of microbes to charge storage was unequivocal, the specific controlling mechanisms remained elusive, and a combination of processes were thought to modulate measured signals. The high surface area of cells coupled to their attachment onto charged surface sites, within a porous medium, was theorized to increase surface roughness and enhance electrochemical polarization, and biofilm formation was suggested to enhance polarization and conduction pathways (Slater et al., 2007; Davis et al., 2006; Abdel Aal et al., 2004). The effect of adsorption of cells onto sand of varying iron-oxide coating density was directly investigated by Abdel Aal et al. (2009). Therein, the authors highlighted the direct dependence of SIP-σ'' on adsorbed cells, attributing it to increased surface roughness, but did not consider the charged properties of cells themselves.

Revil et al. (2012) proposed a model for polarization of microbial cells, suggesting that polarization at the EDL of cells, can drive significant charge storage, due to the charged nature of microbial cell membranes. Zhang et al. (2014) measured the polarization associated with cell suspensions and cell-sand mixtures, providing evidence to support Revil et al. (2012)'s model, as yet another mechanism controlling microbially driven SIP responses. The signals recorded by Zhang et al. (2014) provided exciting evidence to show that SIP signals, specifically σ'', could be used as a quantitative measure on microbial abundance. However, their measurements were close to the instrument's detection limit, even for high cell densities, 10^8 cells mL^{-1} (Griebler et al., 2002), and the signals were measured on freshly cultured cells, not under *in situ* growing conditions (more realistic).

Efforts to establish the realm of SIP's application within biogeochemistry have largely been focused on identifying processes. While the characterisation of controlling processes remains imperative for the development of the field of biogeophysics, and is a key component of this thesis, the work outlined herein attempts not only to determine what biogeochemical processes drive geophysical signals, but also to extract information regarding biogeochemical reaction rates from biogeophysical datasets. Quantitative and qualitative information of *in situ* reaction rates, from geo-electrical signal changes can aid in addressing the recognized knowledge gap between our theoretical understanding of biogeochemical responses to environmental forcings and our ability to capture these by way of measurements.

1.3 Engineered nanoparticles: sensing abiotic catalysts of contaminant degradation

Engineered nanoparticles are employed as remediation agents. They act as catalysts of specific contaminant breakdown reactions, fulfilling a similar role as subsurface microbes, and exhibiting similar geochemical and colloidal transport behavior. Environmental remediation techniques that rely on the deployment of engineered nanoparticles (NPs) are becoming increasingly prevalent (Legg et al., 2014), due to the targeted functionality of NPs as catalysts for specific processes. The high surface area and increased reactivity (Tuček et al., 2017) of nanoscale iron-oxides, zero valent iron (nZVI), bimetallic nanoparticles, and other iron complexes have resulted in their application in the treatment of a variety of heavy metal and organic contaminants (Lin et al., 2018; Gong et al., 2014; Liang et al., 2012; An et al., 2011). A major barrier in the development of nanoparticle-based treatment methods for aquifer treatment is the lack of accurate

in situ monitoring techniques to ensure the targeted delivery of nanoscale reactive materials (Shi et al., 2015).

In their review of the state-of-the-art of nanoparticle characterization and quantification in the environment, Shi et al. (2015) highlighted the necessity to further develop geophysical methods, specifically SIP, to fill this analytical gap. The high surface area of nanoparticles, analogous to bacteria, makes SIP a suitable measurement technique. Despite the method's suitability to measure NPs in porous media, SIP's practical application is hindered, in part due to the complex physical and chemical mechanisms modulating nanoparticle-associated electrical responses.

SIP measurements of micro- and nanoparticles, including microscale zerovalent iron (nZVI), nanoscale cerium and titanium dioxide ($nCeO_2$ and $nTiO_2$), zinc oxide (nZnO) and silver (nAg), have shown the methods applicability at both the field (Flores Orozco et al., 2015) and lab scales (Joyce et al., 2012). Quantitative relationships between metal-based NPs and SIP-σ'' have been shown in fully- and partially-saturated sand columns (Abdel Aal et al., 2017). Nevertheless, the handful of studies that have applied SIP in NP studies have focused on metal-based NPs, and lab-scale studies have applied the method to measure uncoated NPs.

Under more realistic conditions, NPs are coated with a polyelectrolyte to improve their stability in solution, ensuring deliverability, and potentially targeting reactivity (Bhaumik et al., 2011; Hotze et al., 2010; He and Zhao, 2007). The surface coating greatly alters NP surface charging properties, by completely modifying the chemical composition of particle surfaces, drastically changing the SIP response between coated (Shi et al., 2015) and uncoated NPs (Abdel Aal et al., 2017; Joyce et al., 2012).

1.4 Deconvolution of parallel signal contributions

The key challenge in using exploratory methods such as SIP, however, is to establish baselines for the measured geophysical signatures, as they are typically modulated by multiple, and often coupled, hydrological, mineral, geochemical and biotic properties of the subsurface environment. Figure 1-4 illustrates electrochemical polarization within a pore-throat in a complex soil containing mineral matter, organic matter and bacteria. In such a system, baseline responses are determined by petrophysical properties, such as the surface area, grain size, porosity and bulk surface charge density, as modulated by the different soil components. Environmental changes

such as variations in electron acceptor availability, soil moisture and the presence of a hydrocarbon will affect each system component differently resulting in a bulk change to electrical properties often masking individual processes (Shefer et al., 2013; Schwartz et al., 2012).

In the context of colloids, bacteria and nanoparticles, changes in concentration along with colloid-soil interactions (*e.g.*, attachment/detachment) can, in conjunction, result in opposing signal contributions, by modulating the electrical properties of the background medium while also introducing their own unique contributions. Monitoring reactive processes and colloid transport with geophysical techniques is still in its qualitative stage; it is therefore necessary to develop relationships between specific reactive processes of interest and changes in electrical properties. In order to do so, targeted experiments with coupled biogeochemical monitoring (and reactive transport models therefore) and geophysical measurements are necessary to deconvolute parallel signal contributions and move forward the inclusion of SIP and SP as geomicrobiological measurement tools.

1.4.1 The applicability of reactive transport models

Processes based, deterministic reactive transport models (RTMs) provide a quantitative tool for testing the conceptual understanding of a reactive system. The processes built into an RTM, are based on experimental and field observations. RTMs are applied ubiquitously across environmental science disciplines at various spatial and temporal scales (Li et al., 2017). The high resolution computation of transport and reaction rates allows output of predictive concentration profiles and time-series of relevant geochemical species in groundwater. The ability to fit geochemical measurements provides validation of conceptual models as well as the ability to (1) gap-fill missing information between measurement points, and (2) modify forcings to forecast the response of a system to environmental change.

The finely resolved spatial and temporal resolution rate-of-change output from a reactive transport model, can be compared to temporal and spatial signal changes from an SIP monitoring campaign, and used to inform processes governing geophysical signal dynamics. Concurrently, the higher spatial and temporal resolution information of geophysical methods can be used to calibrate reactive processes. Such approaches are already taken into account when building the spatial domains of models, using ground penetrating radar (GPR) and resistivity (ERT) datasets (for example), to map subsurface layering (Bowling et al., 2005). Incorporating dynamic signal

changes into model design and calibration, can help uncover key-insights, improving our overall theoretical understanding of how biogeochemical dynamics modulate the surface charging properties of the subsurface, and subsequently how we can harness this information into sensing applications.

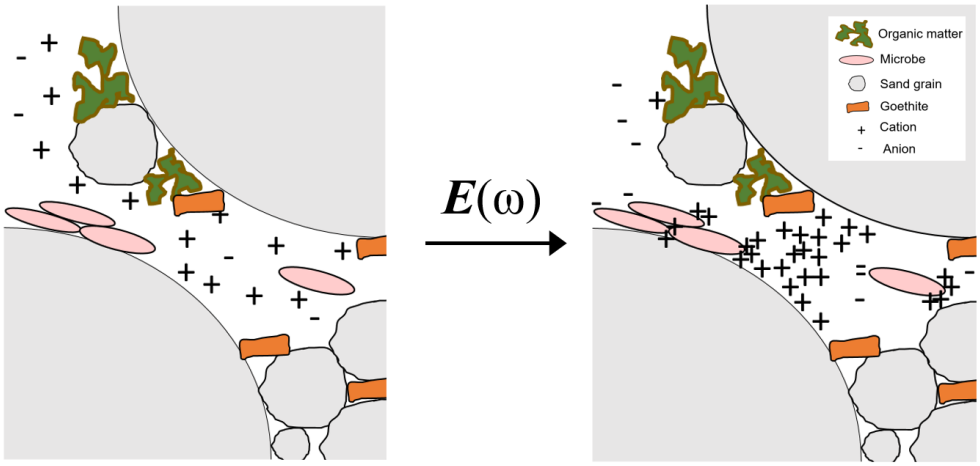

Figure 1-4. Schematic illustration of coupled polarization processes in a biologically active porous medium with a complex organo-mineral soil matrix.

1.5 Thesis structure

1.5.1 Aims

Given the scarcity of quantitative relationships in hydrobiogeophysics, the objective of my research is to elucidate the processes driving SIP and SP signals in complex soil environments and to assess their application as diagnostic monitoring tools for locating zones of enhanced microbial activity above, within and below the capillary fringe, Herein, the specific interest surrounding the capillary fringe is with relevance both to its characteristics as an environmental transition zone, and the enhanced biogeochemical cycling within this zone under dynamic water table fluctuations (Rezanezhad et al., 2014). The specific aims of this thesis are as follows:

(1) Assess the effectiveness of SIP and SP in probing biogeochemical changes across a dynamic soil transition zone
(2) Establish links between changes in physical, chemical and microbial properties and observed geophysical signals
(3) Couple biogeochemical data, reactive transport modeling and SIP in order to elucidate the specific processes and properties that govern the electrical responses of microbially active porous media
(4) Using a coupled experimental and modeling approach, develop quantitative relationships between colloid concentration and chargeability for subsurface microbes and engineered nanoparticles in sandy porous media
(5) Couple measurements of polarization length- (polarizing particle size) and time- (relaxation time) scales to quantify the surface ionic mobility properties of polarizing cells, offering insights into microbial physiological state

1.5.2 Research chapters

The research portion of this thesis is organized into five chapters (Chapters 2-6). I begin by assessing the application of non-invasive geophysical methods, specifically SIP and SP, for monitoring a reactive zone within the capillary fringe of a soil column experiment under periodic variations in moisture regime. In the study of Chapter 2, *Non-invasive monitoring of a reactive soil transition zone during water table fluctuations using spectral induced polarization (SIP) and*

electrodic potential (EP), I highlight the strong contribution of enhanced microbial activity during periods of oxygen influx, to measured SIP-σ'' signals. In Chapter 2, I also highlight the effectiveness of SP in delineating zones of sulfate redox cycling in the unsaturated soil-depth profile.

In an attempt to characterize the individual contribution of microbes themselves on SIP signals, in Chapter 3, *Linking spectral induced polarization (SIP) and subsurface microbial processes: Results from sand column incubation experiments*, I use a well characterized experimental system of sand packed columns with low background chargeability. Therein, I combine geochemical measurements, SIP measurements RTM output and Cole-Cole modeling of SIP spectral responses, to show that the electrochemical polarization of bacterial cells themselves modulates increases in charge storage.

Building on the findings from chapter 3, the controlled experiment in Chapter 4, *Bacterial Stern-layer diffusion: a window into microbial metabolic state derived from spectral induced polarization (SIP) measurements*, introduces a quantitative relationship between SIP-σ'' and measured *in situ* changes in microbial abundance. The results of the experiment in Chapter 4 are modeled in Chapter 5, *Microbial uncoupling and energy storage: a modeling study of nitrite toxicity-induced stress response*, building on Cole-Cole modeling results that show the effect of nitrite toxicity on the surface charging properties of cells. The model formulation in Chapter 5, based on geophysical data, introduces a framework with which to account for microbial metabolic uncoupling, energy storage, and microbial growth following the depletion of electron acceptor. This chapter illustrates an instance where geophysical data aids in RTM calibration.

In Chapter 6, *Sensing iron-oxide nanoparticles with spectral induced polarization (SIP): Experiments in natural sand packed flow-through columns*, I apply a similar approach as in chapter 3, to monitor transport of engineered iron-oxide nanoparticles in flow-through column experiments. Using the high resolution output of an RTM, fitted to nanoparticle breakthrough curves, allows me to establish quantitative relationships between SIP-σ'' and pore water nanoparticle concentrations.

A final concluding chapter (Chapter 7), synthesizes major research findings, highlights the breakthroughs outlined in this thesis, and delineates a way forward in the integration of SIP into geomicrobiology as a non-invasive monitoring tool.

2 Non-invasive monitoring of a reactive soil transition zone during water table fluctuations using spectral induced polarization (SIP) and electrodic potential (EP)

This chapter is modified from:

Mellage, A., Pronk, G.J., Milojevic, T., Endres, A.L., Furman, A., Atekwana, E.A., Rezanezhad, F. and Van Cappellen, P. (in preparation). Non-invasive monitoring of a reactive soil transition zone during water table fluctuations using spectral induced polarization (SIP) and electrodic potential (EP).

2.1 Summary

Transition zones separating the unsaturated and saturated domains in soils are a hotspot of biogeochemical activity. They are challenging to study because they are dynamic, requiring high resolution temporal and spatial data acquisition methods to capture the biogeochemical processes across the water table. Non-invasive geophysical techniques, such as spectral induced polarization (SIP) and electrodic potential (EP), offer comparatively inexpensive monitoring approaches that yield data on changes in soil electrical properties, driven by reactive processes at high spatial and temporal resolutions. We investigated SIP and EP signal variations in artificial soil-filled columns, experiencing periodic water table fluctuations in order to: (1) assess the effectiveness of SIP and EP in monitoring a complex soil transition zone, and (2) couple the measured geophysical signals to changes in physical, chemical and microbial properties. SIP responses showed a clear dependence on the depth-distribution of microbial biomass. Dynamic imaginary conductivity (σ'') responses were only detected in the water table fluctuation zone and, in contrast to real conductivity (σ') data, did not exhibit a direct soil moisture driven dependence. We attribute the observed dynamics in σ'' to microbial activity. An EP anomaly arose concurrent to the production of SO_4^{2-} as a result of oxygenation at depth during drainage of the columns. Our findings show that continuous SIP and EP signals, in conjunction with periodic measurements of geochemical indicators, can help determine the location and temporal variability of biogeochemical activity and be used to monitor targeted reaction zones and pathways in complex soil environments.

2.2 Introduction

Subsurface transition environments, such as the capillary fringe, are characterized by steep physical and chemical gradients (Haberer et al., 2012; Jost et al., 2011; Maier et al., 2007). Spatial and temporal variations in electron acceptor and donor availability have been shown to enhance organic matter degradation relative to environments exposed to static conditions (Stegen et al., 2016; Rezanezhad et al., 2014; Sasaki et al., 2009; Nikolausz et al., 2008; Aller, 1994). Rezanezhad et al. (2014) showed that the redox oscillations accompanying variations in water table elevation result in more complete degradation of soil organic matter and greater emission of CO_2 to the atmosphere. A number of studies have directly linked variations in geochemical and physical properties of the subsurface to changes in microbial community composition, pore-water

geochemistry, contaminant mobility and greenhouse gas emissions (Rühle et al., 2015; Zhou et al., 2015; Rezanezhad et al., 2014; Peralta et al., 2013; Farnsworth et al., 2011; Chow et al., 2006).

The biogeochemical processes underlying elevated biogeochemical activity in transition zones and their feedbacks need to be understood to accurately construct predictive models that characterize the impacts of environmental change and anthropogenic pressures on soil and groundwater resources (Stegen et al., 2016; Rühle et al., 2015; McClain et al., 2003). Monitoring biogeochemical activity at a high spatial and temporal resolution would help fill this mechanistic knowledge gap. However, obtaining direct access to subsurface biogeochemical processes is logistically difficult, invasive and usually expensive. Minimally invasive geophysical techniques offer a comparatively inexpensive alternative and can provide data at high spatial and temporal resolution (Heenan et al., 2017; Lund et al., 2017; Atekwana et al., 2014). Specifically, the methods of spectral induced polarization (SIP) and self-potential (SP) / electrodic potential (EP) have been shown to be sensitive to microbially mediated reactions in subsurface environments (Mellage et al., 2018; Kemna et al., 2012; Atekwana and Atekwana, 2010; Knight et al., 2010; Atekwana and Slater, 2009). These methods provide *in situ* information without the need for intrusive sampling and time consuming and expensive analyses.

SIP measures the impedance (magnitude and phase shift) between an injected current and the resulting voltage gradient across a sample (Wong, 1979; Sumner, 1976), over a broad frequency range (*e.g.*, 0.01 – 1,000 Hz). The measurable decrease in electrical field amplitude away from the current source and the phase shift arise from energy storage and dissipation processes due to the polarized/charged character of soils (see review by Kemna et al. (2012)). The complex conductivity (σ^*) describes the measured energy dissipation and polarization phenomena:

$$\sigma^* = \sigma' + i\sigma'' \quad 2.1$$

where σ' and σ'' are the real and imaginary contributions, respectively, to the complex conductivity response, and $i = \sqrt{-1}$.

$$\sigma' = |\sigma| \cos \varphi \quad 2.2$$

$$\sigma'' = |\sigma| \sin \varphi \quad 2.3$$

The measured conductivity ($|\sigma|$) and phase shift (φ) determine the magnitude of σ' and σ''; σ' is an electromigration term, which is primarily a function of the presence (which relates to the relative saturation of a porous medium) and properties of the electrolyte and the surface conductivity at

the grain fluid interface (relevant mostly for clay-rich soils), while the capacitive properties (charge storage or chargeability) are related to σ'' (Vinegar and Waxman, 1984). In the low frequency range (0.01–1000 Hz), electrochemical polarization phenomena are the dominant mechanisms governing SIP responses below 100 Hz (Olhoeft, 1985). Electrochemical polarization is the result of tangential migration of counter ions (in most soils, predominantly cations) in the Stern layer of the electrical double layer (EDL), after current is applied (Lesmes and Morgan, 2001; Chelidze and Gueguen, 1999; Schön, 1996; de Lima and Sharma, 1992; Schwarz, 1962).

Pore fluid geochemistry and soil physical and chemical properties exert primary controls on both σ' and σ''. Robust comparisons of consolidated and unconsolidated media have highlighted the inverse control of grain size on σ'' (Slater and Glaser, 2003; Slater and Lesmes, 2002) and a positive correlation between surface area and σ'' (Weller et al., 2010; Slater and Glaser, 2003; Börner et al., 1996). Increasing clay content results in higher surface charge density and surface conduction (Okay et al., 2014; Slater et al., 2006). In organic rich soils, organo-mineral complexes can reduce ionic mobility (Schwartz and Furman, 2014). The pH can exert a strong control on σ'', where changes in pH result in protonation or deprotonation of surface sites, effectively changing the surface charge density governing the magnitude of polarization (*i.e.*, a drop in pH decreases σ'' and the opposite occurs with an increase in pH) (Peruzzo et al., 2018; Skold et al., 2011). The temperature dependence of σ'' is mainly governed by the increase in ionic mobility and chargeability with increasing temperature (Zisser et al., 2010a). Pore water (electrolyte) conductivity and ionic composition govern σ'. Slater and Lesmes (2002) highlighted the positive dependence of σ' on pore water conductivity and its lesser effect on σ'', which can induce a reduction in polarization at high conductivities (Peruzzo et al., 2018; Slater and Glaser, 2003), related to ion-ion interactions, which result in an effective compression of the diffuse layer, reducing ion mobility (Lesmes and Frye, 2001).

In partially saturated media, the degree of water saturation (S_w) and saturation history jointly affect both σ'' and σ' (Ghorbani et al., 2009; Ulrich and Slater, 2004). Saturation changes the effective cross-sectional area available for conduction (Ulrich and Slater, 2004), and the conductive geometry and tortuosity affecting membrane polarization (Shefer et al., 2013; Weller et al., 2010). Changes in conduction, as pores drain and fill, exhibit a hysteretic dependence (Ulrich and Slater, 2004), hypothesized to be controlled by polarization at a continuous air-fluid interface (Knight, 1991).

Secondary controls on SIP signals include those exerted by the presence and dynamics of soil microbes, ion adsorption/desorption processes, and mineral precipitation and dissolution. SIP measurements conducted in controlled experiments at the lab scale have focused on determining changes in soil electrical properties induced by physico-chemical changes as a result of (bio)geochemical reactions. Polarization signals (σ'') have been shown to be sensitive to microbial properties and processes in soils: the presence of microbes (Zhang et al., 2014), changes in cell abundance (Mellage et al., 2018; Davis et al., 2006) and cell attachment onto the soil matrix (Abdel Aal et al., 2009). SIP signal variations have further been linked to secondary mineral precipitation stemming from microbially mediated reactions (Wu et al., 2009; Personna et al., 2008; Slater et al., 2007; Ntarlagiannis et al., 2005a; Williams et al., 2005) as well as mineral dissolution of disseminated sulfides (Placencia-Gómez et al., 2013). Adsorption of ions onto soil grains has been shown to dampen electrochemical polarization, due to a reduction in ion mobility dependent on the strength of the complexation bond (Vaudelet et al., 2011b; Vaudelet et al., 2011a). The partitioning of dissolved ions onto the solid phase also alters pore water ionic composition, potentially influencing σ'. In complex soil environments, many or all of the aforementioned processes happen in parallel. Therefore, signal deconvolution of individual drivers is a major challenge to the use of SIP as a diagnostic monitoring tool.

The major primary and secondary controls that affect SIP responses in uncontaminated soils are summarized in Table 2-1. The table highlights the mechanisms by which a certain property or process controls σ^*, along with the directionality of its effect on both real and imaginary components of σ^*. For biogeochemically active systems, where lithological properties and overall soil composition and temperature remain relatively constant, the interplay between changes in saturation, pH, pore water conductivity (and ionic strength), sorption, and microbial and mineral dynamics will govern the SIP response.

Self-potential (SP) is a voltage signal stemming from the subsurface itself, generated by internal electrical current sources (Naudet et al., 2004; Sato and Mooney, 1960). To ensure that only contributions from internal sources are recorded, signals are measured with non-polarizing reference and measurement electrodes, where a gel or aqueous solution separates the metal electrode from direct contact with the porous medium and pore fluid (Zhang et al., 2010; Slater et al., 2008). Signal contributions stem from three major processes. Streaming potentials arise due to fluid-flow through pores, where a streaming current source results from the transport of excess

charge in the EDL in response to viscous drag through the pores (Zhang et al., 2010). Chemical gradients of ionic species can also contribute to SP signals (Revil and Linde, 2006). A third natural source of current flow arises from strong redox potential (E_h) differences in the subsurface, known as a geobattery. Current flow is facilitated by a metallic conductor (*e.g.*, ore body) driven by electrochemical half-cell reactions taking place at the limits of the redox anomaly (Bigalke and Grabner, 1997; Sato and Mooney, 1960). A biogeobattery arises as a result of microbial processes (Naudet et al., 2004), where electronic conduction, across a redox gradient, is facilitated by microbial networks linked via filamentous appendages (*e.g.*, pili) that have been shown to facilitate electron transfer (Revil et al., 2010). Direct contact between electrodes and the pore fluid can lead to interactions between the electrode itself and dissolved chemical species, generating significant voltages from galvanic cell potentials, known as electrodic potential (EP), that are not self-potential signals (Slater et al., 2008). The galvanic cell potential resulting in EP responses, stems from electrode surface interactions with the electrolyte, driven by redox differences between a reference and measurement electrode (Atekwana and Slater, 2009; Slater et al., 2008). The magnitude of EP signals is on the order of the non-standard cell potential of the coupled anodic and cathodic reactions modifying the electrode chemistry (typically hundreds of millivolts) (Williams et al., 2007).

A number of studies have intentionally or unintentionally monitored biogeochemically driven EP signals in bench-scale experiments (Zhang et al., 2010; Personna et al., 2008; Slater et al., 2008; Ntarlagiannis et al., 2007; Williams et al., 2007). All of the studies outlined above used Ag-AgCl non-polarizing electrodes, in a fluid filled casing, separating the metal electrode from direct contact with the porous medium, but allowing it to come into contact with the pore solution. Most notably, Ntarlagiannis et al. (2007) interpreted self-potential anomalies of up to 600 mV as biogeobattery driven, but did not consider the possible added contributions of reactions between the electrolyte and the metal electrode, *i.e.*, the EP contribution (Atekwana and Slater, 2009). Conversely, Williams et al. (2007) measured electrodic potentials of up to -700 mV related to SO_4^{2-} reduction and the production of 1 mM of total dissolved sulfide. They attributed these variations in potential to changes in the cathodic half-cell reaction at the electrodes; from a standard Ag-AgCl electrode, equation 2.4, to an Ag_2S coated electrode, equation 2.5:

$$AgCl_{(s)} + e^- \rightarrow Ag^0_{(s)} + Cl^-_{(aq)} \quad 2.4$$

$$Ag_2S_{(s)} + H^+_{(aq)} + 2e^- \rightarrow 2Ag^0_{(s)} + HS^- \quad 2.5$$

The changes in the cathodic half-cell reactions were directly linked to the solubility products of electrode coating precipitates and attributed to an effective substitution of Cl^- in the AgCl coating, by HS^-:

$$2AgCl_{(s)} + HS^-_{(aq)} \rightarrow Ag_2S_{(s)} + H^+_{(aq)} + 2Cl^-_{(aq)} \quad 2.6$$

The authors provided strong evidence to suggest the applicability of EP as a quantitative tool to determine concentrations of HS^-, but did not consider the possible contribution of a biogeobattery redox-gradient induced current, generating SP signal contributions (Zhang et al., 2010).

The challenge in implementing SIP and SP/EP as non-target (*i.e.*, without prior knowledge of the specific reactive contributions expected to control the response) environmental monitoring tools lies in linking electrical responses to specific biogeochemical processes. The main aim of our study was to establish these links using laboratory experiments in a well characterized model soil system. We monitored SIP and SP signal variations in artificial soil-filled columns experiencing periodic water table fluctuations. The experimental design was analogous to that in Rezanezhad et al. (2014), with added geophysical monitoring capabilities that allowed for in-line SIP and SP measurements in order to: (1) assess the effectiveness of SIP and SP in probing biogeochemical changes across the soil transition zone, and (2) establish links between changes in physical, chemical and microbial properties and the observed geophysical signals.

Table 2-1. Summary of primary and secondary mechanisms controlling SIP-σ^* responses in variably saturated media. The effect of a certain property or process (along with its directionality, *e.g.*, increase ↑ or decrease ↓) are denoted as relative positive (+) or negative (-) effects/correlations.

Primary controls on σ^*: *Property/Process*	*Controlling mechanism*	*Effect on σ'*	*Effect on σ''*	*Reference*
Grain size	Decreasing characteristic diffusion length for electrochemical polarization with decreasing grain size.	No direct effect reported	(-)	(Slater and Glaser, 2003; Slater and Lesmes, 2002)
Surface area	Higher polarizable surface and higher interface for surface conduction.	(+)	(+)	(Weller et al., 2010; Slater and Glaser, 2003; Börner et al., 1996)
Clay content	Clay minerals have higher surface charge density, surface conduction and surface area. Minerology and its effect on surface charge density (and CEC) determines the magnitude of increase in surface conduction (1:1 vs. 2:1 clays), morphology affects pore geometry.	(+)	(+)	(Okay et al., 2014; Slater et al., 2006)
Organic matter content	Organo-mineral complexation results in a reduction of ionic mobility.	No direct effect reported	(-)	(Schwartz and Furman, 2014)
Electrolyte conductivity	Increased fluid conduction due to the presence of charge carriers. Increasing surface charge density and conduction with increasing conductivity / ionic strength. At high ionic strength ion-ion interactions result in compression of the diffuse layer in the EDL decreasing in ionic mobility.	(+)	Weekly (+) Can be (-) at high EC	(Slater and Glaser, 2003; Slater and Lesmes, 2002; Lesmes and Frye, 2001; Börner et al., 1996)
pH	Modification of surface charge density via protonation (as pH decreases) and deprotonation (as pH decreases) of surface exchange sites (*e.g.*, silonol groups).	No direct effect reported	↑ pH (+) ↓ pH (-)	(Peruzzo et al., 2018; Skold et al., 2011)
Temperature	Increase in conduction with temperature, and increased ionic mobility and chargeability.	(+)	(+)	(Zisser et al., 2010a; Revil and Glover, 1998)
Degree of saturation	Drainage and filling of pores results in changes in the cross-sectional area available for conduction. Hysteresis associated with saturation history is suggested to be controlled by polarization at the continuous air-fluid interface.	(+)	(+)	(Ulrich and Slater, 2004)
Secondary (bio)geochemical controls on σ^*: *Property/Process*	*Controlling mechanism*	*Effect on σ'*	*Effect on σ''*	*Reference*
Microbes	Increased charge storage stemming from electrochemical polarization of cells, with increasing abundance.	No direct effect reported	(+)	(Mellage et al., 2018; Zhang et al., 2014; Davis et al., 2006)
Mineral precipitation/dissolution	Mineral conduction, polarizable surface area, pore constriction or expansion. Dissolution results in release of charged species, possible pH changes.	Generally: Precip. (-) Diss. (+)	Generally: Precip. (+) Diss. (-)	(Placencia-Gómez et al., 2013; Personna et al., 2008; Slater et al., 2007; Williams et al., 2005)
Adsorption	Dependent on electrostatic or inner sphere complexation. Reduction in ion mobility in the EDL with increased adsorption.	Sorption (+) Desorption (-)	Sorption (-) Desorption (+)	(Vaudelet et al., 2011b; Vaudelet et al., 2011a)

2.3 Materials and Methods

A total of six experimental columns were prepared and used in two sets of three columns each (Figure 2-1). The triplicate static water table columns were labelled C1, C2, C3, while the fluctuating water table columns were labelled F1, F2 and F3. Along with pore water sampling ports, the triplicate columns (for both static and fluctuating treatments) were outfitted for additional measurements and sampling. Columns C1 and F1 were equipped with soil sampling ports, columns C2 and F2 with E_h and O_2 electrodes and columns C3 and F3 with a geophysical measurement array for SIP and SP. To avoid interferences with SIP and SP signals, no other biogeochemical measurements were carried out on columns C3 and F3.

2.3.1 Soil column system and instrumentation

2.3.1.1 Soil column setup

An artificial, homogenized mixture consisting of minerals and organic matter was used to provide a well-defined and representative starting material (Pronk et al., 2017). The soil mixture was composed of 77.5% quartz sand (3Q-ROK, US Silica, Berkeley, West Virginia), 10% montmorillonite (Ceratosil WG, Süd Chemie AG, Moosburg, Germany), 2.5% goethite (Bayoxide EF 200, Lanxess, Leverkusen, Germany) and 10% humus (collected from a forested riparian zone at the *rare* Charitable Research Reserve field site, Cambridge, Ontario, Canada). A microbial inoculum was extracted from the humus, enriched and inoculated into the soil mixture at a ratio of 6 g of extracted humus per kg of artificial soil. Additionally, dibasic calcium phosphate was added to the mixture as a phosphate supplement (0.81 mg g^{-1}).

The artificial soil was packed into six columns, made of hard acrylic with an inner diameter of 7.5 cm and a length of 60 cm (Soil Measurement Systems, LLC, USA, Model Cl-C021), to a height of 45 cm and a bulk density of ~1 g cm^{-3}. For the packing procedure, the soil was slightly wetted to avoid loss and sorting of clay-sized particles during packing. The water table in the experimental columns was controlled by the water level in the hydrostatic equilibrium reservoir, which was connected to a storage column (Figure 2-1). The automated soil column system used in this experiment allowed for the height of the water level in the equilibrium reservoir to be manipulated through the use of a computer-controlled, multi-channel pump (9-channel Tower II pump, CAT. M. Zipperer, GmbH, Germany). For further technical details on the soil column

system, the reader is referred to Rezanezhad et al. (2014).

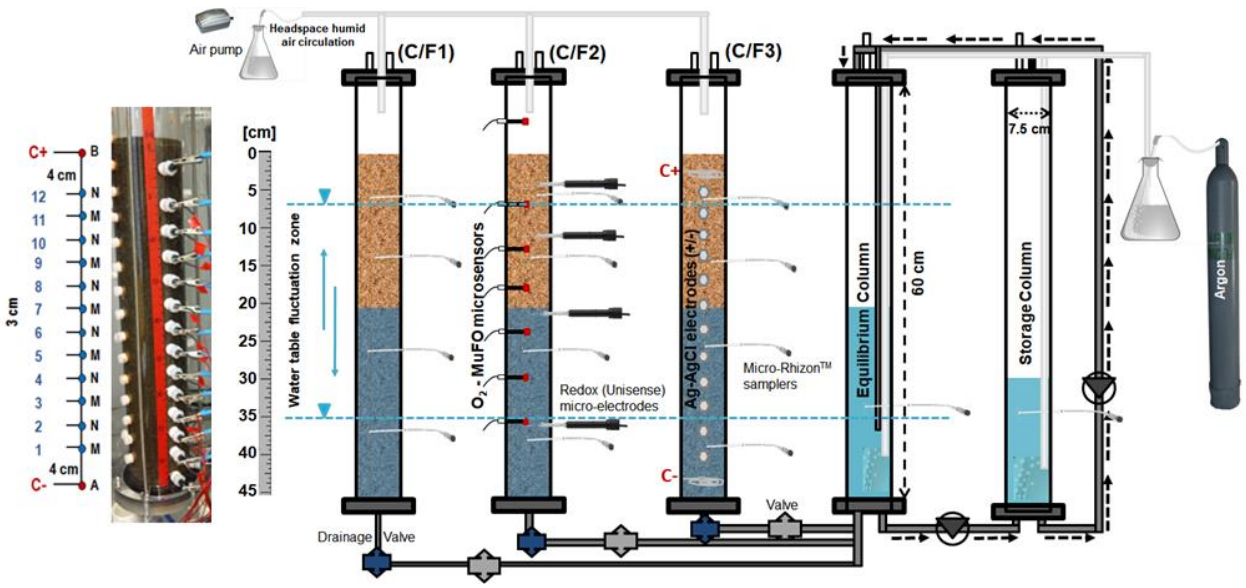

Figure 2-1. Triplicate soil column experimental setup adapted from Rezanezhad et al. (2014): three soil columns are hydraulically connected to the equilibrium column that controls the pressure head at the lower boundary of the soil columns. A picture of the geophysical measurement array is shown on the left hand side.

Three replicate soil columns (C1, C2 and C3) were incubated with the water table in each column being maintained at 20 cm below the soil surface (herein referred to as static treatment). The other three columns (F1, F2 and F3) alternated between drainage and imbibition cycles, resulting in dynamic saturation changes (herein referred to as fluctuating treatment). After packing, all six soil columns were saturated by upward flow of an artificial groundwater (AGW) solution containing 0.5 mM $KHCO_3$, 1 mM $CaCl_2$ and 1 mM $MgCl_2$ in deoxygenated water. Once saturated, the columns were drained, reaching a water level in the equilibrium reservoir of 20 cm below the soil surface (b.s.s). The equilibrium and storage columns were continuously sparged with argon gas to generate anoxic conditions. Humid air was continuously circulated in the headspace of each column in order to minimize evaporation from the soil surface. The experiment was run under constant temperature conditions at 23.6 ($\pm$1.6) °C.

All columns were fitted with sampling ports for the extraction of pore water at 5, 15, 25 and 35 cm depths. Each port was equipped with ceramic samplers that were 5 cm in length and 2.5 mm

in diameter with a filter pore-size of 0.15 µm (CSS5 MicroRhizon™ samplers, Ejikelamp, Netherlands, #19.21.23F). One column of the fluctuating treatment and one of the static treatment (C2 and F2, respectively) were fitted with redox potential micro-electrodes (10µM glass tip micro-electrodes, Unisense, Denmark) as well as multi-fibre optode (MuFO) oxygen sensors, positioned at regular depth intervals.

2.3.1.2 Hydraulic regimes and moisture responses

All soil columns were pre-equilibrated under partially saturated conditions, with the water level in the equilibrium reservoir maintained at 20 cm b.s.s. for 37 days prior to starting the water table fluctuations. Following the pre-equilibration phase (t_0 = 37 days), periodic imbibition and drainage cycles were imposed in the fluctuating treatment, while in the static treatment the water table remained at 20 cm b.s.s. Imbibition was imposed by instantaneously increasing the water level in the equilibrium column to the height of the soil surface (0 cm) and maintaining that level for 28 days. Drainage periods consisted of free drainage of the soil columns into an outflow reservoir. The hydraulic connection between the soil columns and the equilibrium column resulted in a lowering of the water level in the hydrostatic equilibrium reservoir. Drainage was halted once the water level in the equilibrium reservoir was at 40 cm b.s.s. The water level was then kept constant at this level for 28 days. Drainage and imbibition periods, following the pre-equilibration phase, are abbreviated as DRN_n and IMB_n, where the subscript *n* denotes the chronological number following the first saturation period (IMB_1) immediately after the pre-equilibration phase.

A separate flow column experiment was conducted under similar conditions as the F1-F3 soil columns in order to characterize soil moisture dynamics in response to the imposed hydraulic regime. A column packed with the same artificial soil and AGW that were used in all experimental columns was fitted with soil moisture sensors (EC-5 Small Soil Moisture Sensor, Decagon Devices, Inc., USA), which were calibrated for the specific soil mixture and connected to an equilibrium reservoir. Free-drainage and constant head imbibition were imposed on the system and the response of the moisture content to these changes was recorded every 5 minutes (Parsons and Bandaranayake, 2009).

2.3.1.3 SIP and SP instrumentation

Non-polarizing Ag-AgCl potential electrodes and Ag-AgCl current coil-electrodes were used for SIP and SP measurements. The potential Ag-AgCl electrodes were encased in nylon NPT fittings (1/4”). The NPT fittings were filled with an agar gel electrolyte (15 g L^{-1} agar). Due to the

already elevated levels of Cl^- in the AGW, no KCl was added to the gel, as additional increases in salinity (especially from the diffusion of KCl into the columns, due to the long exposure time of the electrodes); (Jougnot and Linde, 2013), could have resulted in potentially negative effects on microbial respiration (Rath et al., 2017). The SIP responses were acquired at each potential electrode pair using a Portable Spectral Induced Polarization (PSIP) Unit (Ontash & Ermac Inc., NJ, USA). Phase shift (φ) (accurate down to 0.1 mrad) and conductivity magnitude ($|\sigma|$) were measured at 51 log frequency intervals between 0.01 and 1000 Hz. SIP measurements were made weekly (based on the expected time-scale of changes driven by the imposed hydraulic regime). To account for the effects of the column dimensions on SIP signals, a geometric factor (k) was determined by measuring the impedance magnitude (Z) response of a solution of known resistivity (ρ_a) ($\rho_a = k \times Z$), for each electrode pair in the columns (Mellage et al., 2018; Zhang et al., 2014). The PSIP unit was turned off and disconnected when it was not taking measurements, to avoid interference with the E_h measurements and allow for weekly SP measurements.

SP was measured using a digital multimeter with a high input impedance (>10 MΩ) (Keithley Model 2700 Multimeter, Keithley Instruments, Inc., Cleveland, OH, U.S.A.). Direct current (DC) voltage was recorded with respect to an Ag-AgCl non-polarizing reference electrode (placed at a soil depth of 43 cm) at each potential electrode (12 depth-measurements per column) once per week. The SP reference electrode was constructed in the same fashion as the potential electrodes described above. At 43 cm, conditions remained anaerobic and stable for the duration of the experiment. Measurements were conducted over a one hour period at 60 s intervals and the average value over the one hour period was then calculated as the potential value for that time point. Agar gel filled electrodes were used for SP signal monitoring in order to avoid direct contact between the electrolyte and metal electrodes (Zhang et al., 2010; Slater et al., 2008). Logistically, this design was also preferable because it allowed for sustained electrode contact during drainage periods when unsaturated conditions prevailed, in the upper (close to the surface) portions of the column.

For each of the replicate soil column sets (fluctuating and static), one column was equipped with non-polarizing potential electrodes and current coil-electrodes. Two current electrodes were inserted at the top and bottom of each soil column and 12 potential electrodes (allowing for 6 SIP measurement pairs) were placed in between, 4 cm from each current electrode, with a 3 cm spacing between each potential electrode (see Figure 2-1). Current was injected through the outer coil

electrodes while the output voltage was recorded at each electrode pair, effectively yielding six different four-electrode arrays.

2.3.1.4 Batch SIP measurements

To establish the saturation dependence of the complex conductivity response for this specific soil mixture, a series of SIP measurements were also performed on batches of the artificial soil at different gravimetric moisture contents (0.15, 0.25, 0.35, 0.40 and 0.45) packed to the same bulk density as the incubation soil column experiment and placed in a smaller acrylic column (14 cm long and 3.4 cm diameter). The small column was fitted with two Ag-AgCl potential electrodes (of the same construction as that outlined above) placed 5.5 cm from each edge of the column, with a 3 cm spacing between them. The column was sealed at both ends with rubber stoppers, which were fitted with an Ag-AgCl coil electrode that pierced the stopper at its center, similar to the setup reported in Abdel Aal and Atekwana (2014).

2.3.2 Analytical Methods

2.3.2.1 Pore-water geochemistry

Before each period in the fluctuating regime (*i.e.*, before the onset of either drainage or imbibition), 5 mL pore-water samples were extracted from the ceramic samplers installed at four depths (5, 15, 25 and 35 cm) and then sub-sampled into separate vials. A 400 µL pore water sample was analyzed for Fe^{2+} using the ferrozine method (Viollier et al., 2000); 500 µL were filtered through a 0.2 µm membrane filter (Thermo Scientific Polysulfone filter) for analysis of SO_4^{2-} by ion chromatography (IC, Dionex ICS-5000; MDL=0.27 µM for SO_4^{2-} analysis); 1 mL was used to measure the dissolved organic carbon (DOC) concentrations using the non-purgeable organic carbon (NPOC) method on a total organic carbon analyzer (Shimadzu TOC-LCPH/CPN, MDL= 0.011 mM). The samples for DOC analysis were acidified with 20 µL of 1 M HCl. In addition, roughly 600 µL were used to measure the pore water electrical conductivity (EC) and pH using handheld Horiba B-213 LAQUATwin pH and EC meters. The volume required for all analyses was not always successfully extracted, due to the unsaturated conditions as well as the clogging of the filter membrane of the ceramic samplers. Therefore, analyses were carried out when possible, depending on the amount of sample volume collected.

2.3.2.2 Oxygen

O_2 concentration measurements were taken along the depth profile of both the static and fluctuating treatments using a luminescence-based optode technique. The latter used optical sensors made of fibre optic cables. Each cable had one sensing tip and one imaging tip. The sensing tips were made using a solution of Pt(II) meso-Tetra(pentafluorophenyl)porphine (PtTFPP) (Badocco et al., 2012). The sensing ends were installed into the soil columns; 6 were in the fluctuating column F2 at depths of 2.5, 8.5, 14.5, 20.5, 26.5 and 32.5 cm b.s.s. with 6 sensors at the same depths in the static column C2. The uncoated ends were placed in front of a DSLR camera and blue LED light (447.5 nm wavelength) (Larsen et al., 2011). The LED provided the excitation light source to trigger the emission of PtTFPP luminescence. This emitted light was photographed and the light intensity was analyzed using ImageJ software (Rasband, 2015). The intensity was related to the O_2 concentration by the Stern-Volmer (SV) equation:

$$\frac{I_0}{I} = 1 + K'_{sv}[O_2] \qquad 2.7$$

where I_0 denotes the emitted light intensity in the absence of O_2; I is the light intensity in the presence of O_2; $[O_2]$ is the concentration of O_2 present; and K'_{sv} is the SV constant (Badocco et al., 2012). Images were taken every 3 hours for the duration of the experiment.

2.3.2.3 Microbial biomass carbon (MBC) and ATP

After sacrificial sampling of the columns (extruded via the top of the column using a lifting jack and sliced every 2 cm) at the end of the experiment (and at 99 days of incubation for columns C1 and F1), samples were homogenized and used to determine microbial biomass carbon (MBC) concentrations with the chloroform fumigation extraction (FE) method (Joergensen and Mueller, 1996; Vance et al., 1987). Each soil sample was sub-sampled for the procedure, and all analyses were carried out in duplicate (approximately 2 g of soil were extracted with 0.5 M KSO_4, either after 24 h exposure to chloroform or without fumigation). The DOC concentration of the extract from treated samples (both fumigated and non-fumigated samples) were analysed and the extractable microbial biomass carbon (MBC) concentrations were calculated from the difference between the DOC concentrations in the fumigated and the non-fumigated samples. ATP was extracted from flash frozen 2 g samples using a method adapted from (Redmile-Gordon et al., 2011) and (Jenkinson and Oades, 1979). ATP concentrations were determined through triplicate luminescence measurements (FlexStation 3 Multi-Mode Microplate Reader, Molecular Devices,

LLC) in multiwell-plate format using a cell viability assay kit (BacTiter-GloTM Microbial Cell Viability Assay).

2.4 Results

O_2 concentration measurements, periodic pore water geochemical measurements and microbial biomass carbon values are presented below in conjunction with SIP and SP measurements, with emphasis on the dynamic geophysical responses measured under fluctuating water table conditions. Both the presentation of results and the subsequent discussion primarily focus on fluctuating columns F2 and F3. Results for the static columns, C2 and C3, serve as the experimental control and are presented for comparison. Columns C1 and F1 were sacrificially sampled after 99 days of incubation. The corresponding solid phase characterization will be presented in a forthcoming paper.

2.4.1 Hydrology and biogeochemistry

The results of the complementary flow characterization experiment for the fluctuating treatment (Figure 2-2) showed that, during free drainage, the water level in the equilibrium reservoir dropped linearly over a period of roughly 4 hours (Figure 2-2). The degree of water saturation (θ_{Sat}) dropped sharply, 1 hour after onset of drainage at a depth of 9 cm, followed by sharp drops at 14, 18 and 27 cm, respectively, staggered in time (Figure 2-2b). The onset of imbibition resulted in a two-step saturation behavior. Initially, the soil exhibited a fast response to imbibition with a sharp increase in saturation in less than 2.4 h across all depths. This response was followed by a slow rise in saturation at 18 cm. The soil at depths of 14 and 9 cm remained unsaturated.

Redox potential (E_h) values at depths 10 and 21 cm in the fluctuating water table column oscillated between oxidizing (600 mV) conditions during drainage and reducing (-500 mV) conditions during imbibition. Near the top of the column at a depth of 3 cm, relatively constant oxidizing conditions prevailed (E_h between 450 and 540 mV). Conversely, at 37 cm below the surface, the conditions were reducing, with E_h remaining between -300 and -500 mV. Relatively constant redox potentials (E_h), on the order of -600 mV, were recorded in the static treatment (measured in C2) at 37 cm. At 3 cm, however, E_h measurements drifted from 300 mV to near zero, within the six-month electrode lifetime. This may have been caused by a slow drying of the electrode during the experiment, or

possibly due to emplacement in a local anaerobic microsite created by limited transport of oxygen into clay- and organic matter-rich soil aggregates. Because of the E_h electrode lifetime of only six months, and our reliance on O_2 concentration dynamics in the interpretation of the results in what follows, we have omitted the E_h time-series (which are predominantly modulated by O_2 delivery into the system).

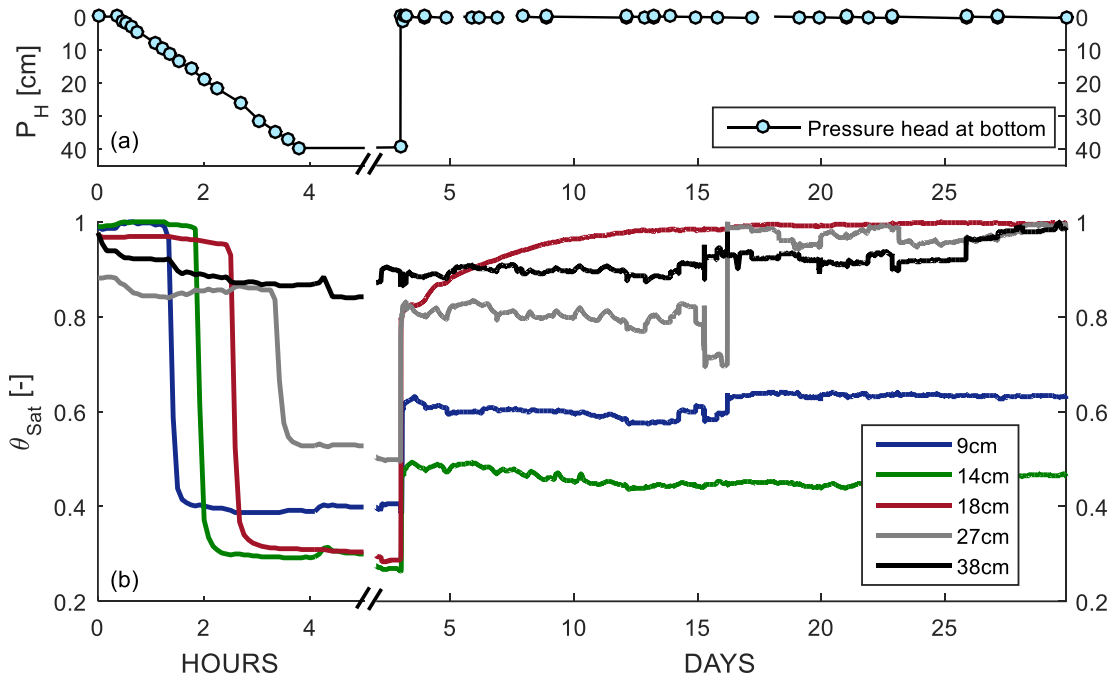

Figure 2-2. Saturation regime (θ_{Sat}) at 9, 14, 18, 27 and 38 cm, shown in (b), in a parallel flow characterization experiment of a column packed with an identical artificial soil composition and to the same bulk density as the experimental treatments, subjected to free-drainage and imbibition induced by variations in the pressure head (P_H) at the lower boundary, shown in (a). The lower boundary pressure head (water level in the equilibrium reservoir) is presented with reference to the soil surface of the experimental columns.

Dynamic changes in time-series O_2 concentrations were observed in the fluctuating treatment measured in column F2 (Figure 2-3a). Drainage periods resulted in sharp increases in O_2 concentrations at depths of 8.5, 14.5, 20.5, and ~3 days later, at 20.5 cm. O_2 levels reached a maximum of about 0.22 mM at 8.5 cm and 14.5 cm depths and then remained constant for the remainder of the drainage periods. (Note: at 338 m a.s.l. and for an average lab temperature of 23.6 ±1.7 °C, O_2 saturation = 0.254 ±0.0075 mM.) At 20.5 cm O_2 slowly increased from 0.12 to 0.20 mM throughout the drainage period. Imbibition periods resulted in a staggered drop in O_2 concentrations as a function of depth. Sharp decreases in O_2 concentration occurred approximately 4 days after the start of the imbibition period at 20.5 cm and up to 19 days at 8.5 cm. No changes in O_2 concentrations were observed below 26.5 cm. O_2 concentrations in the static treatment were below 0.07 mM at all monitored depths prior to day 78 as a result of the slow equilibration of the system to a water table at 20 cm, after initial incubation under fully saturated conditions. Between 78 and 152 days, the O_2 concentration at the depths above the water table (20 cm) increased to ~0.25 mM and remained at that value. At the depths below 20 cm, O_2 concentrations remained unchanged below 0.05 mM for the whole incubation period (Figure 2-3b).

Porewater SO_4^{2-} concentration time-series measured in two of the fluctuating and static water table replicates (F2, F3, C2 and C3), for depths of 15, 25 and 35 cm are presented in Figure 2-4. Dissolved SO_4^{2-} concentrations at 25 and 35 cm remained consistently below 1 and 0.1 mM in all replicates for both fluctuating and static treatments, respectively (Figure 2-4). Despite being replicates, F2 and F3 columns did exhibit differences with respect to SO_4^{2-} concentration peak values. SO_4^{2-} concentrations at 15 cm in column F2 showed an increase during DRN_1 and DRN_2 (Figure 2-4a), where SO_4^{2-} concentrations reached values of 2.57 and 4.50 mM, respectively. In F3, SO_4^{2-} increased to 2.25 mM during DRN_2 and then decreased during the following 28-day imbibition period (IMB_3) (Figure 2-4a). Insufficient sample volume was collected in F3 at 15 cm during DRN_1 for analysis. Between days 78 and 127, SO_4^{2-} concentrations at 15 cm in the static treatment column C3 increased from 0.29 to 2.64 mM and then slowly decreased until day 183 (Figure 2-4c). A similar, but lower magnitude increase was observed in column C2, where SO_4^{2-} increased between days 127 and 155 (delayed with respect to C3) from 0.24 to 1.23 mM and then steadily decreased until day 183.

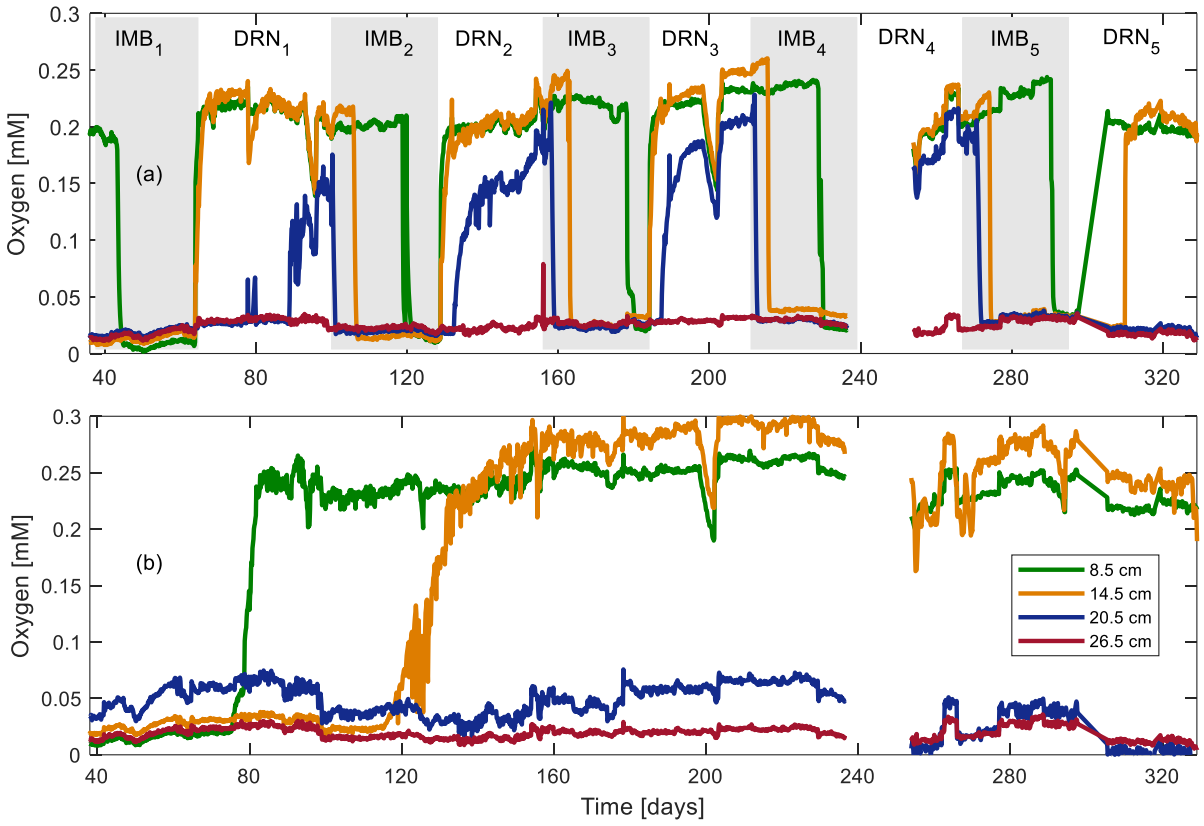

Figure 2-3. Time-series oxygen concentration for the fluctuating (a) and static (b) water table experimental treatments, measured in columns F2 and C2, respectively. Grey rectangles in panel (a) represent the duration of an imbibition (IMB_n) period, when the water level in the equilibrium column was held at the height of the soil surface. Each imbibition period is followed by a drainage (DRN_n) period, denoted by a white background. The subscript *n* refers to the chronological number associated with each period, where the 1st of each period follow the 37 day pre-equilibration time. Data from measurement depths 2.5 and 32.5 cm are omitted, as these do not exhibit dynamic variations and remain constantly aerobic and anaerobic, respectively.

Average dissolved Fe^{2+} and DOC concentrations measured throughout the experiment at each depth are shown in Table 2-2 along with MBC concentrations measured at the end of the experiment. Higher Fe^{2+} concentrations were consistently measured with increasing depth, with the highest concentrations occurring below 20 cm in both the static and fluctuating treatments. Time series Fe^{2+} concentrations are presented in Figure 2-5, for both replicates of the fluctuating (F2 and F3) and static (C2 and C3) treatments. Time series DOC concentrations are presented in Figure 2-6. Measured pH values were relatively constant at each depth ($\pm$0.5), and average pH at each depth along with the standard deviation of the samples within a certain depth are presented in Table 2-3.

DOC concentrations ranged from 15.3 to 18.8 mM in the fluctuating treatment and from 10.3 to 18.1 mM in the static treatment, with no clear depth dependence. Following an initial drop in DOC in the first 100 days of incubation (Figure 2-6), concentrations remained relatively stable at depths 25 and 35 cm in the fluctuating treatment. At 15 cm, DOC concentrations fluctuated in response to drainage and imbibition cycles. Figure 2-6a illustrates the drop in DOC during drainage periods and increase during imbibition measured in column F3 (the most complete time series). The cyclic DOC behavior is likely modulated by a combination of enhanced aerobic decomposition during drainage periods and a loss due to the drainage outflow, and accumulation of DOC during imbibition likely stems from particulate organic matter hydrolysis in the absence of dissolved oxygen (Vavilin et al., 2008), as there is no aqueous source of DOC in the artificial groundwater saturating solution.

Aqueous Fe^{2+} concentrations were consistently below 0.09 mM in the fluctuating columns and below 0.03 mM, with little variation within the static columns (except for the measurement at 183 hours in C3 at 25 cm of 0.31 mM). Treatment replicates exhibited similar temporal trends. Concentration generally dropped at depths below 25 cm in the fluctuating treatment, and exhibited fluctuations associated with drainage and imbibition cycles at a depth of 15 cm.

The average MBC concentrations are presented in Table 2-2 as a function of depth zones. The three different depth zones correspond to the predominant conditions in each: the aerobic zone, transition or water table fluctuation zone and the anaerobic zone, with depth intervals varying between fluctuating and static treatments (see Table 2-2). The water table fluctuation zone in the fluctuating treatment was defined as the depth interval between 8 and 20 cm, based on the

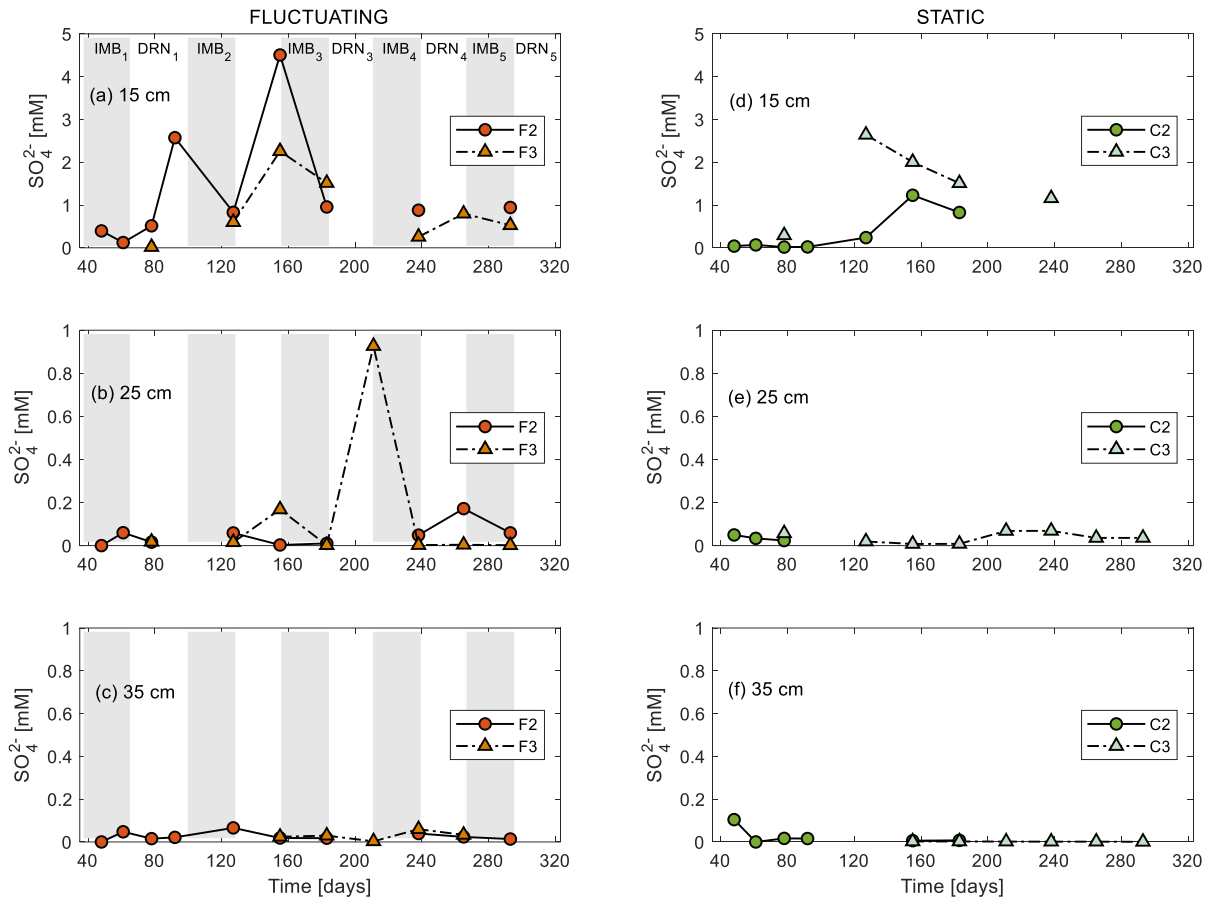

Figure 2-4. Aqueous SO_4^{2-} concentrations at (a) 15, (b) 25, and (c) 35 cm in replicates F2 and F3 of the fluctuating treatment, respectively, and at (d) 15, (e) 25, and (f) 35 cm in replicates C2 and C3 of the static treatment.

Table 2-2. Average dissolved Fe^{2+} for all samples throughout the duration of the experiment at each pore water sampling depth and MBC concentrations for different depth zones measured at the end of the experiment in F2, F3, C2 and C3 columns for fluctuating and static treatments.

	Fe^{2+}				DOC				MBC				
	Fluctuating		*Static*		*Fluctuating*		*Static*			*Fluctuating*		*Static*	
Depth [cm]	**Fe^{2+} [µM]**	**SD**	**Fe^{2+} [µM]**	**SD**	**DOC [mM]**	**SD**	**DOC [mM]**	**SD**	**Depth zone***	**MBC [ug/g]**	**SD**	**MBC [ug/g]**	**SD**
5	3.6	1.4	5.0	5.2	18.5	9.3	10.3	0.3	Aerobic	324.5	45.8	296.9	32.1
15	15.2	6.5	16.8	2.8	15.3	1.8	18.1	2.8	Transition	175.3	68.3	130.7	91.5
25	40.9	11.4	60.9	11.1	18.8	5.0	18.1	3.6	Anaerobic	84.2	76.1	59.5	28.4
35	39.8	22.2	43.4	50.9	15.8	1.4	17.6	5.2					

*Aerobic zone 0-15 and 0-8 cm in static and fluctuating columns, respectively; transition zone 15-20 and 8-20 cm in static and fluctuating columns, respectively; anaerobic <20cm

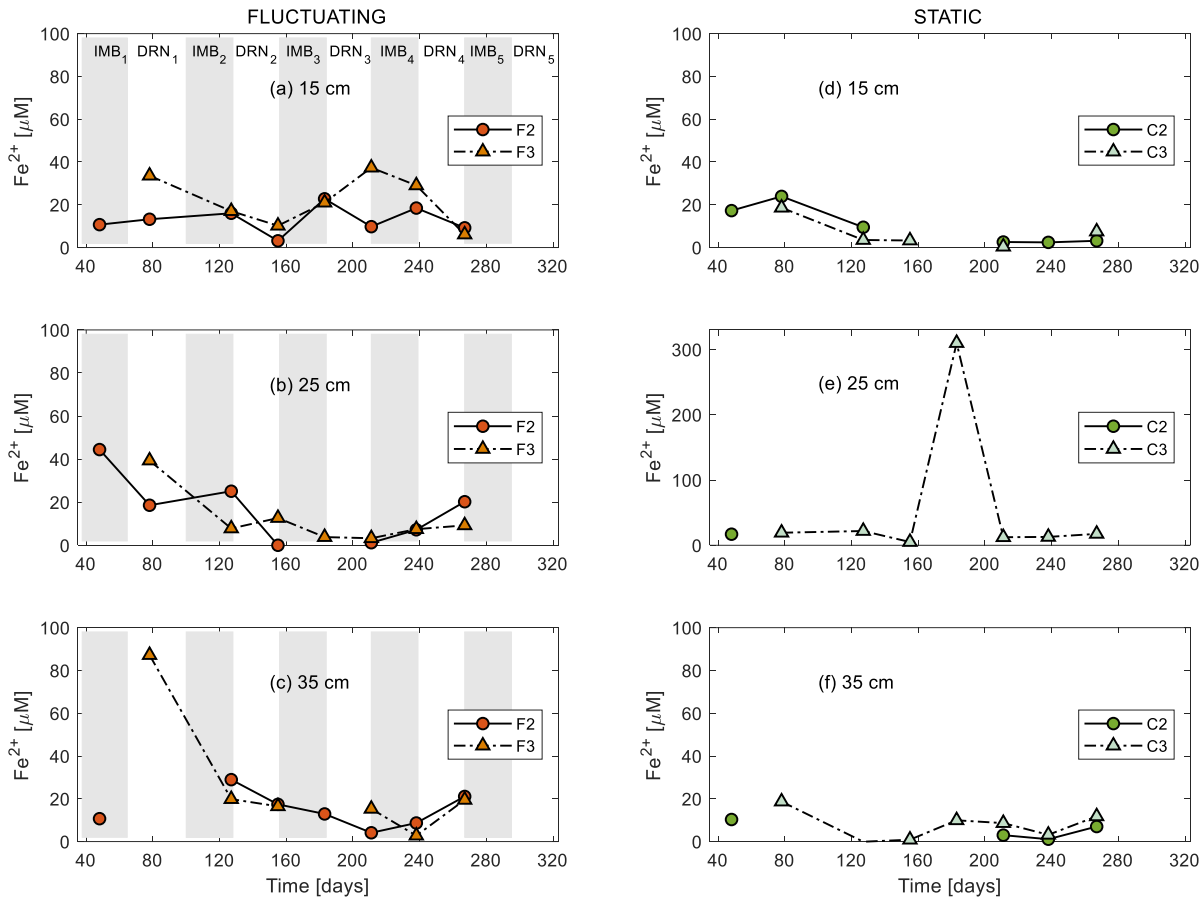

Figure 2-5. Pore water Fe^{2+} concentrations in both fluctuating and static treatments at (a) 15, (b) 25, and (c) 35 cm in replicates F2 and F3 of the fluctuating treatment, respectively, and at (d) 15, (e) 25, and (f) 35 cm in replicates C2 and C3 of the static treatment.

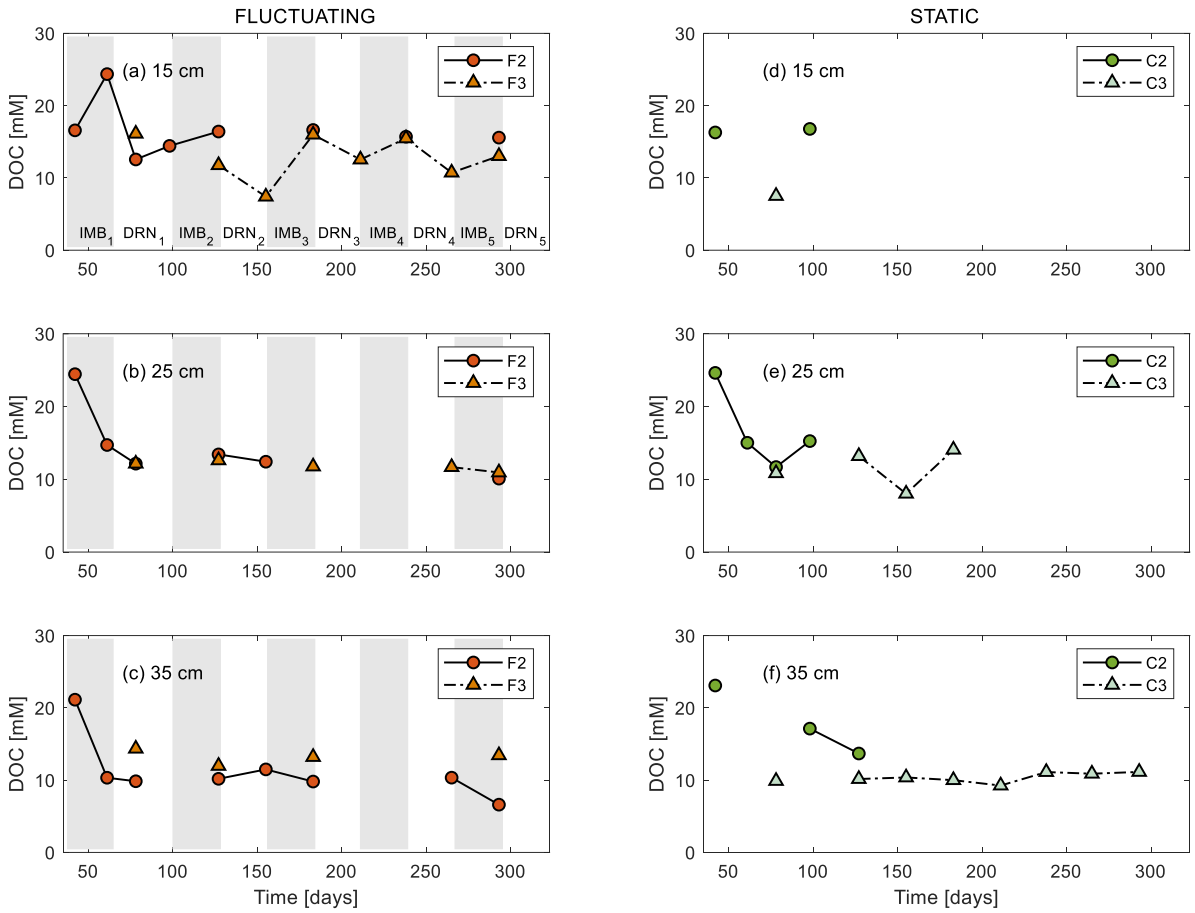

Figure 2-6. Pore water DOC concentrations from samples taken at 15, 25 and 36 cm in both the fluctuating and static columns.

measured O_2 dynamics. No significant variations in O_2 were measured outside this delineated zone (Figure 2-3). The chloroform fumigation extraction revealed higher concentrations of MBC in the aerobic zones of both treatments (static: 297 and fluctuating: 325µg-MBC g^{-1}). MBC decreased with increasing depth, with lower average values in the transition zone (static: 130 and fluctuating: 175 µg-MBC g^{-1}) and the lowest concentrations (static: 60 and fluctuating: 84 µg-MBC g^{-1}) observed below 20 cm, in the predominantly anaerobic zones. ATP concentration results are reported with the SIP data below.

Table 2-3. Average and standard deviation of pore water pH at 15, 25 and 35 cm, measured in both replicates of the fluctuating and static water table treatments.

Column:	**F2**		**F3**		**C2**		**C3**	
Depth [cm]	$\overline{pH}$	*SD(±)*	$\overline{pH}$	*SD(±)*	$\overline{pH}$	*SD (±)*	$\overline{pH}$	*SD(±)*
15	8.33	0.49	8.16	0.33	8.03	0.25	8.03	0.24
25	8.09	0.48	8.03	0.38	8.00	0.26	8.06	0.17
35	8.11	0.30	7.88	0.24	8.19	0.21	8.36	0.37

2.4.2 SIP response

SIP imaginary conductivity (σ'') spectra, measured in column F3, are presented in Figure 2-7. The spectra exhibited no strong peak behavior, but rather increased continuously in magnitude with increasing frequency, which has been shown to be typical for sand-clay mixtures (Okay et al., 2014; Slater et al., 2006). Figure 2-7 shows the temporal evolution of the imaginary conductivity response over one drainage and imbibition cycle (the second drainage, DRN_2 and the subsequent imbibition period, IMB_3) in the fluctuating water table column, F3. The magnitude of σ'', across the measured frequency range, increased with the progression of drainage and decreased during the subsequent imbibition period. The shape of the spectra remained relatively unchanged throughout the cycles. Spectra in the static treatment were of similar shape and have been omitted to avoid redundancy.

Time-series data for σ' at 10 Hz (frequency within typical field instrumentation measurement range) (Kemna et al., 2012), at different depths, for both the static (C3) and fluctuating (F3) treatments are shown in Figure 2-8. Periodic pore water EC measurements at 15, 25 and 35 cm are plotted alongside σ'. Signals recorded in F3 exhibited dynamic variations in response to the shifting moisture regime at 13.5 and 19.5 cm with the most pronounced variations at 13.5 cm (Figure 2-8a). Values of σ' recorded at 25.5, 31.5 and 37.5 cm in the fluctuating column exhibited no clear trend in response to the water table variations and decreased gradually over the course of the experiment, with predominantly higher σ' values at 31.5 cm, for most of the experiment (Figure 2-8b and c). In the static treatment (C3), σ' signals (Figure 2-8d-f) decreased throughout the experiment at depths 25.5, 31.5 and 37.5 cm and increased at depth 19.5 cm after day 86. The magnitudes of the σ' signal were similar at 25.5, 31.5 and 37.5 cm, but were lower at 19.5 cm, prior to 252 days of incubation. Pore water EC trends (specifically in the SIP measurement columns, C3 and F3, circle markers in Figure 2-8) were similar to σ'(10 Hz). (Note: missing EC measurements are due to low or no extraction of volume during sampling, attributed to the unsaturated conditions and fine grains clogging the ceramic samplers). EC at 15 cm was slightly lower than at 25 and 35 cm in both C3 and F3, and generally decreased with time in all columns.

Time-series σ'' at 10 Hz at different depths, for both the static (C3) and fluctuating (F3) treatments are shown in Figure 2-9. The 10 Hz σ'' values exhibited a strong depth dependence in both static and fluctuating treatments (columns F3 and C3). Generally, the highest σ'' signals were

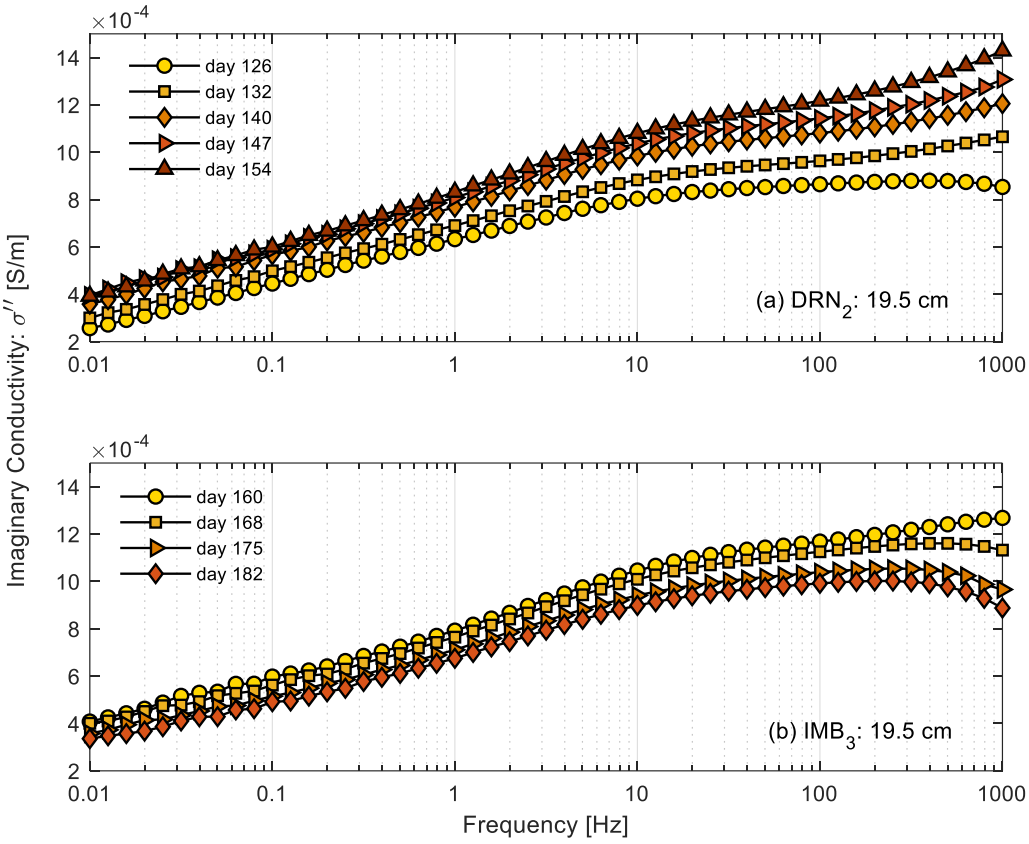

Figure 2-7. Spectral imaginary conductivity response over one drainage and imbibition cycle in the fluctuating water table column measured at 19.5 cm, in column F3, during the second drainage period (DRN_2), in (a), and the subsequent imbibition period (IMB_3), in (b), at the different measurement time-points during each period.

recorded at shallower depths (13.5 and 19.5 cm), and the magnitude of the signal decreased with depth (Figure 2-9a). A general decrease in magnitude through time was also observed across all measurement depths in the fluctuating treatment (column F3). The σ'' magnitude in the static column (C3) remained relatively unchanged for the duration of the experiment (Figure 2-9c). (Note: σ'' results at 13.5 cm in the static column are not presented due to poor electrode contact at that depth, likely because of entrapped air near the electrode-soil interface stemming from packing heterogeneities.)

Depth profiles of ATP concentrations measured at the end of incubation are presented in Figure 2-9, alongside σ'' data, as a qualitative measure of microbial activity (Bastida et al., 2008). ATP concentrations measured at 99 days (in columns F1 and C1) are presented in Appendix A, in Figure AA 1. ATP concentration depth-profiles showed marked differences between fluctuating and static treatments. The static treatment replicates exhibited a gradual decrease in ATP with depth with maximum values near the surface (Figure 2-9d). Conversely, peak ATP concentrations (below the surface 0-2 cm soil sample) were measured between 8 and 18 cm in the fluctuating treatment replicates, columns F2 and F3 (Figure 2-9b). We speculate that the elevated levels of ATP, measured in column F3 for the 0-2 cm sample, were likely a function of modified packing structure in the upper layer of the column, as a result of current coil electrode emplacement at 2 cm b.s.s.

A distinct temporal evolution in the σ'' signals was only recorded in the fluctuating treatment. Specifically, dynamic signal responses associated with the imposed changes in water table occurred at depths of 13.5 and 19.5 cm, with less pronounced variations at 25.5 cm, in contrast to the static treatment and the relatively constant responses at depths of 31.5 and 37.5 cm in the fluctuating column (see Figure 2-9a). Following the drop in σ'' in F3 during the first imbibition period (IMB_1 in Figure 2-9a), σ'' at 13.5 cm increased from 0.79×10^{-3} to 1.19×10^{-3} S m^{-1} during the subsequent drainage period (DRN_1 in Figure 2-9a). A similar increase (from 0.80×10^{-3} to 1.08×10^{-3} S m^{-1}) in σ'' occurred at 19.5 cm during the second drainage period (DRN_2 in Figure 2-9a), while σ'' dropped at 13.5 cm. After 240 days of incubation, σ'' followed a decreasing trend across all measurement depths with a notably sharp drop at 13.5 cm. The resulting magnitudes of σ'' remained relatively constant below 13.5 cm until the end of the experiment, exhibiting little to no response to changes in hydrology.

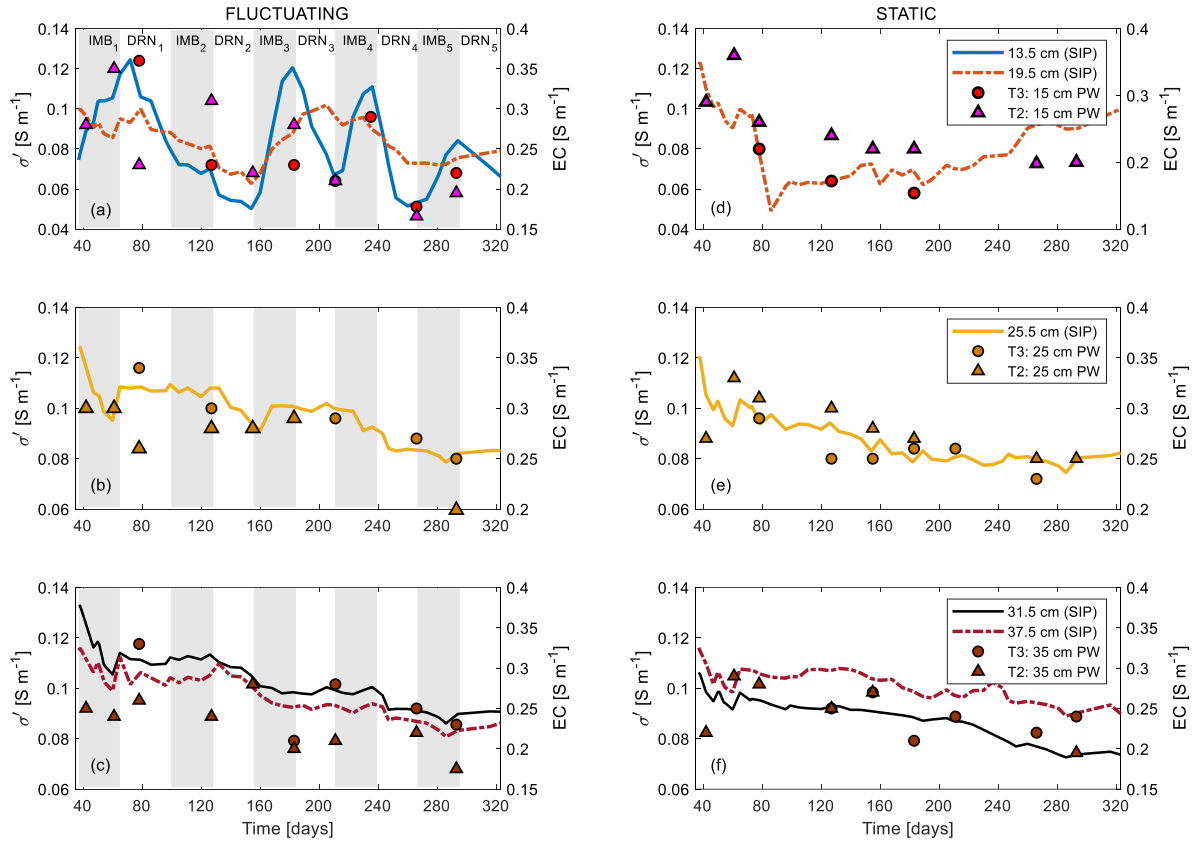

Figure 2-8. Real conductivity (σ') and pore water conductivity (EC) in both the fluctuating (left) and static water (right) table treatments. EC from both F2 and F3 and C2 and C3 columns are compared to SIP- σ' measured in F3 and C3 only (Note: T in T3 and T2 refers to either fluctuating "F" or static "C" treatments). Panels (a) and (d) are for data between 13 and 20 cm, (b) and (e) for data at an approximate depth of 25 cm and (c) and (f) for depths below 30 cm.

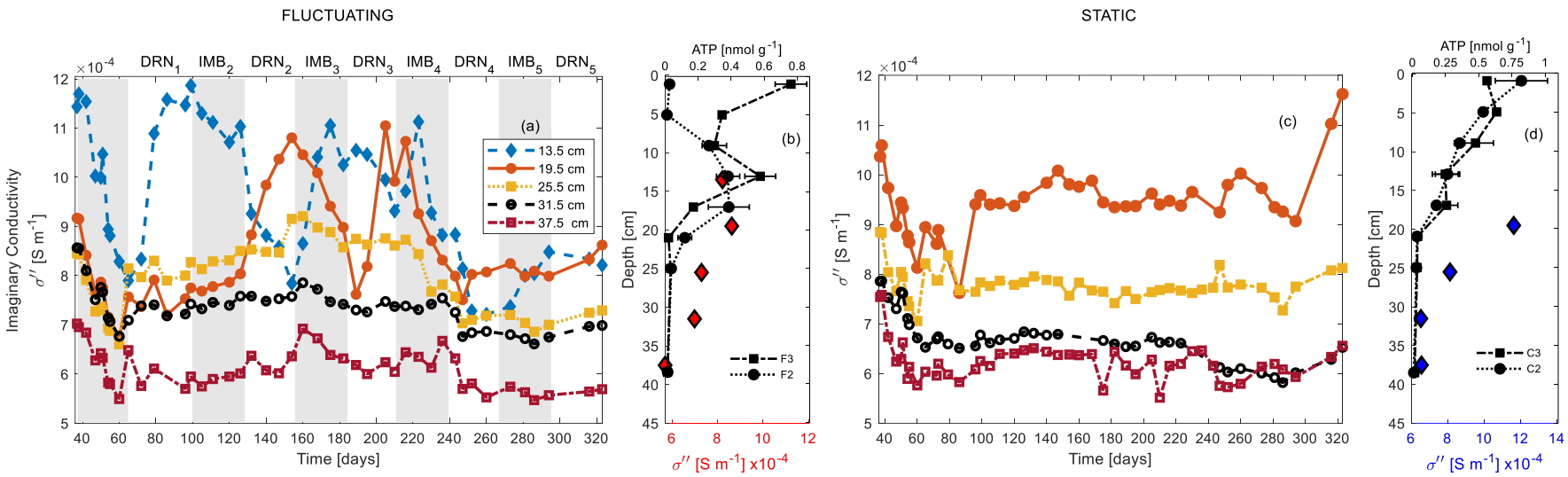

Figure 2-9. Time-series imaginary conductivity (σ'') response (10 Hz), measured in columns F3 and C3, for the (a) fluctuating water table treatment and the (c) static treatment are plotted alongside ATP depth-profiles, measured in F2, F3, C2 and C3, at the end of incubation for the fluctuating (b) and static (d) treatments. The alternating grey and white backgrounds represent imbibition (IMBn) and drainage (DRNn) cycles, respectively. The subscript n refers to the chronological number associated with each period following an initial 37 day pre-equilibration phase.

The SIP responses in the series of soil batches packed with the same artificial soil mixture under variable gravimetric moisture contents are presented in Figure 2-10. Both σ' and σ'' (at 10 Hz) exhibited a linear relationship with increasing moisture content. That is, both polarization and conductance exhibited a strong moisture dependence in the artificial soil mixture.

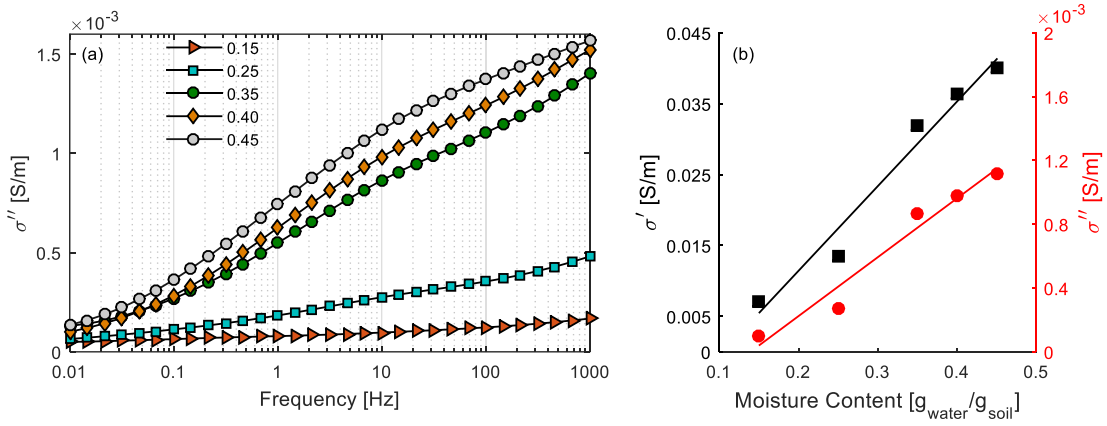

Figure 2-10. Spectral imaginary conductivity (σ'') response of the artificial soil mixture at different gravimetric moisture contents (a), and the relationship between real and imaginary conductivities at 10 Hz and over the range of measured moisture contents (b). Saturation exponents *n* and *p* are 1.54 and 1.23, respectively, for the acritical soil mixture.

2.4.3 Self-potential / electrodic potential measurements

Voltage potential depth profiles for the static and fluctuating treatments are presented in Figure 2-11. The DC voltages recorded by the Ag-AgCl electrodes in the measurement array revealed the appearance of a strong voltage anomaly between 15 and 30 cm depths in column F3, during DRN_2 (Figure 2-11a), relative to the preceding drainage period, DRN_1 (profiles for day 96 and 141 are compared in Figure 2-11a). Following the detection of the EP anomaly, the electrodes were removed from column replicates F3 and C3 for visual inspection, on day 225 (during IMB_4). Electrodes at depths of 18, 21 and 24 cm showed a strong discoloration of the agar gel (the potential electrode filling), revealing the presence of a black precipitate. This agar discoloration was not observed in electrodes at the same depths in column C3. The coating of the electrodes in F3 was further examined using energy dispersive X-ray spectrometry (EDS) (TM300 Table Top Scanning Electron Microscopre, Hitachi Technologies, Canada), which revealed that the coating was primarily composed of Ag and sulfur (S). These results, along with the presence of a black precipitate on the electrode, provided evidence that the electrode coating composition changed from being predominantly AgCl to Ag_2S, as a result of chemical interactions between the pore water and electrode coating (Atekwana and Slater, 2009; Slater et al., 2008; Williams et al., 2007). Despite our efforts to remove possible EP signals due to electrolyte-electrode interactions, our measured signals (presented in the results section) showed substantial evidence of electrodic potential contributions. Therefore, the measurements conducted detected a contribution of both SP and EP and are henceforth interpreted as such. In the discussion section below, we refer to our voltage potential signals as electrodic potentials. The inspection of the electrode gel and coating composition are discussed in detail, with reference to Figure AA 2 and Figure AA 3 in Appendix A, along with evidence to show that the modifications to the electrode coating did not impact SIP measurements in Figure AA 4 and Figure AA 5.

The voltage potential depth profile in the static treatment (Figure 2-11b) showed similar trends at 96 and 141 days, but with an offset of < 200 mV between the two profiles. The static profiles, however, did not exhibit the same depth dependence as those in the fluctuating treatment. In the fluctuating treatment (Figure 2-11a), the highest EP magnitude occurred on day 141 at 21 cm and the measured anomaly exhibited a strong depth dependence, where large-scale variations in EP occurred between 15 and 25 cm only. The most pronounced changes in EP with respect to the preceding drainage period occurred between 18 and 27 cm below the soil surface. Variations

in EP between day 96 and day 141 were on the order of 200 – 500 mV within the fluctuating transition zone. EP at 21 cm dropped during the following imbibition cycle to a similar magnitude as that prior to the development of the anomaly and shifted towards lower values across the 15 to 27 cm depth interval. The voltage anomaly developed after 120 days of incubation, during the onset of drainage, following a ~100 day period of relatively constant values, as shown in Figure 2-14, at depths of 19 and 21 cm.

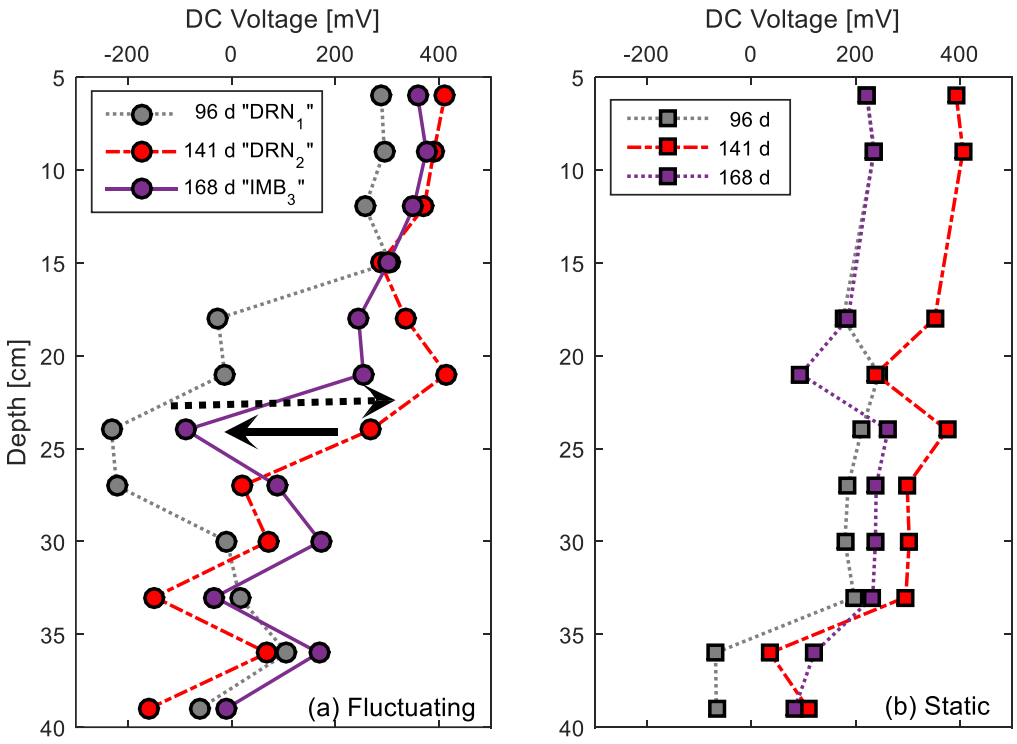

Figure 2-11. Electrodic potential depth profiles in the (a) fluctuating (b) static water table columns (F3 and C3, respectively) during the first drainage (DRN_1) period preceding the EP anomaly (96 d), the second drainage (DRN_2) period (141 d) during the peak of the anomaly and during the third imbibition (IMB_3) period, following the anomaly (168 d). The dashed arrow in panel (a) traces the development of the positive EP anomaly (concurrent with increasing SO_4^{2-}) and the full arrow traces the subsequent recession of the anomaly (concurrent with decreasing SO_4^{2-}, sulfur reduction).

2.5 Conceptual reactive system

The interpretation of results in the discussion section (below) is based on the following conceptual soil biogeochemical reactive system. Organic carbon present in the natural organic matter (10% - wt. % organic matter) undergoes microbially mediated oxidative degradation: aerobic in the presence of O_2 and anaerobic in the absence of O_2. Under aerobic conditions, mineralization of organic sulfur present in the organic matter produces SO_4^{2-}, which can be used as a terminal electron acceptor in the absence of O_2. Structural Fe^{3+} in goethite also acts as an electron acceptor for anaerobic respiration. During anaerobic conditions, organic matter fermentation results in the production of labile fermentation products that can be readily oxidized upon reinstatement of aerobic conditions. Aerobic respiration is more thermodynamically favorable than Fe^{3+} and SO_4^{2-} respiration and, therefore, can sustain higher biomass growth.

2.6 Discussion

Our results highlight that the water table fluctuations greatly affect the biogeochemical functioning of the artificial soil, in particular by modulating O_2 delivery into the soil. Changes in the proportion of air- and water-filled pore space directly and indirectly control the dynamic geophysical responses, (1) by modulating the cross-sectional area available for conduction, largely affecting σ' (and to a lesser extent σ''), (2) by mobilizing charged species, affecting the bulk conductivity and ionic composition, and (3) by stimulating microbial activity and/or growth (via the influx of electron acceptor, O_2). These parallel signal contributions cannot be fully deconvoluted from our dataset. Nevertheless, we highlight the specific control that O_2-stimulated microbial respiratory activity exerts on σ'', during specific cycles, within the water table fluctuation zone (measured at 13.5 and 19.5 cm). In what follows, we discuss the different hydrological and reactive processes underlying the measured geophysical signals.

2.6.1 SIP: spatial distribution

As highlighted in the results section, the σ'' data exhibit a strong depth dependence. The drop in σ'' with depth (Figure 2-9a) contrasts with the expected increase of σ'' with increasing water saturation (Figure 2-10). Surface area per unit pore volume (S_{por}) has also been shown to exert a strong, positive control on both σ'' and σ' (*e.g.*, Börner et al. (1996)). All columns showed signs of

compaction due to packing with increasing S_{por} with depth (calculated from porosity measured during sacrificial sampling, presented in Figure 2-12).

Note that porosity was determined from bulk density measurements on solid phase samples taken at 99 days from columns F1 and C1, and at the end of the experiment, at 329 days, from columns F2, F3, C2 and C3. Despite the homogeneous packing of the experimental setup, measured porosity (n) decreased with depth, with values around 0.68 near the surface, gradually decreasing to around 0.60 at depth. We attribute the decrease in n to compaction of the soil material during packing.

Specific surface area (SSA) was measured, using the N_2-BET method (Gemini VII 2930, Micrometrics, USA), to be 9.34 $m^2\ g^{-1}$, for the soil mixture. The measured SSAs for each of the soil materials are presented in Appendix A, in Table AA 1. The surface area per unit pore volume (S_{por}) was computed for each porosity measured along the depth profile (using the measured SSA for the combined mixture and a matrix density (ρ_s) of 2.51 g cm^{-3}), based on equation 2.8 (Riepe et al., 1979).

$$S_{por} = \rho_s \cdot SSA \cdot \frac{(1-n)}{n} \qquad 2.8$$

Figure 2-12 illustrates the decrease in S_{por} with depth across all experimental columns. Well established petrophysical relationships, (*e.g.*, Weller et al. (2010); Börner et al. (1996)) suggest that both σ' and σ'' increase with increasing S_{por}. However, our SIP measurements, indicate that σ'' decreases with depth, opposite to the dependence on S_{por}, hence, suggesting an alternative control on the depth-dependent SIP signatures. The positive correlation between σ' and saturation and S_{por}, in contrast, is more apparent in both of the treatments (Figure 2-9c and d).The discrepancies between the depth trends in σ'' and σ' indicates that the surface charging properties of the bulk soil (*i.e.*, biomass plus organic and mineral fractions) vary within the soil profile and drive σ'', whereas σ' is controlled predominantly by changes in water saturation and changing pore water chemistry.

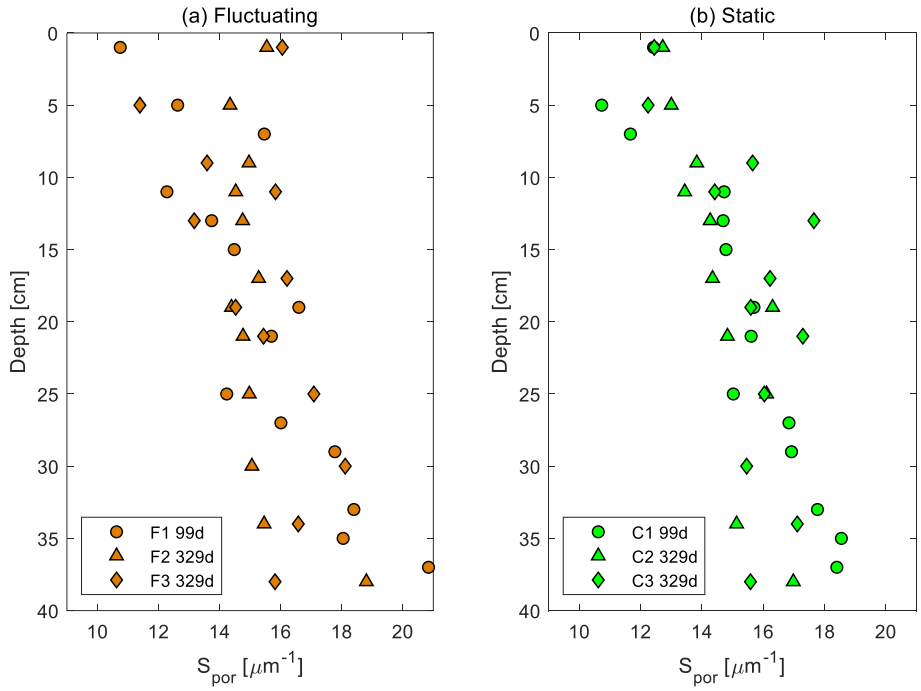

Figure 2-12. Surface area per unit pore-volume (S_{por}), calculated from the porosity measured during solid phase sampling events at 100 days (columns F1 and C1) and 329 days after incubation (columns F2, F3, C2, C3), for both the (a) fluctuating and (b) static treatments.

The general decrease in measured σ'' with increasing depth (Figure 2-9a) correlates with decreasing MBC concentrations with depth (Table 2-2), in both static and fluctuating column treatments. MBC is a direct measure of the total carbon stemming from bacterial cells. Abdel Aal et al. (2004) and Davis et al. (2006) established the dependence of measured σ'' on the presence of bacteria and changes in microbial abundance from SIP measurements in flow-through reactor experiments packed with hydrocarbon-contaminated sand and mixed microbial cultures. Furthermore, in controlled experiments isolating the SIP signal contributions associated with microbial cells, distinct SIP signals and signals changes have been reported for microbial suspensions (Zhang et al., 2014), and sands mixed with microbes (Mellage et al., 2018; Zhang et al., 2014), providing direct evidence for enhanced charge-storage, and hence polarization, associated with cell biomass.

SIP measurements in natural or "near-natural" environments (such as the artificial soil columns) result from a combination of concurrent processes that contribute to measured spectra. The reductive dissolution of goethite, making up 2.5 % (per mass) of the artificial soil mixture:

$$FeOOH_{(s)} + 3H^+ + e^- \rightarrow Fe^{2+} + 2H_2O \quad (1)$$

potentially results in the loss of polarizable mineral surface (Placencia-Gómez et al., 2013). With continuous reducing conditions below 20 cm, reductive dissolution of goethite cannot be ruled out as a factor contributing to the observed depth distribution of σ'', as evidenced by the consistently higher Fe^{2+} concentrations measured below 20 cm in both treatments (Table 2-2).

Measured σ' signals are in agreement with the expected soil moisture-σ' relationship for this artificial soil (see Figure 2-10) and the increase in S_{por} with depth due to compaction (in all columns, Figure 2-12). In the static treatment, measured σ' is highest at 37.5 cm and decreases towards the soil surface, with the most pronounced difference between 19.5 cm (within the capillary fringe) and 25.5 cm (saturated conditions), from 80 and 247 days. The shift in the zonation of σ' measured after day 247 in the static treatment, is likely a function of a localized increase in ionic strength, driven by evaporation near the measurement electrodes. After day 247, σ' at 19.5 cm increases above values measured at saturated depths (promoted by the constantly dry conditions in the upper section of the column, despite the cycling of humid air in the headspace). Additionally, σ' in the fluctuating treatment exhibits the expected depth zonation driven by soil

moisture conditions. This is best illustrated during periods of drainage (*e.g.*, DRN_2 and DRN_4, refer to Figure 2-9e) where the σ' is lowest at 13.5 cm and increases with depth to 31.5 cm.

A clear water saturation and petrophysical (*i.e.*, S_{por}) dependence for the SIP response is only detected in the real contribution to the complex conductivity. The imaginary component of the response behaves inversely in space, with respect to σ', and correlates strongly with the microbial biomass distribution in the column. These controls become apparent over time, driving signal variations in the water table fluctuation depth interval.

2.6.2 Temporal changes in σ′ and EC

The dynamic σ' responses measured at 13.5 cm in the fluctuating treatment column (F3) generally follow the trend in measured pore water EC, at 15 cm, within that column (circle markers in Figure 2-8a). The lack of a clear response in σ' to the second imbibition (IMB_2) period is likely due to incomplete wetting (specifically in column F3) and the soil's varied response to drainage and imbibition during the different cycles. (Note: there is some difference in response to imbibition between columns F2 and F3). During IMB_2, the period when σ' showed no response to imbibition, EC decreased in column F3, with respect to the preceding drainage period (DRN_1), but increased in column F2 (Figure 2-8a). This disparate behavior between replicates provides evidence to suggest that F3's response to DRN_1 and IMB_2 was different than F2's response. Measured O_2 concentrations in F2 show evidence of drying and rewetting during these periods, but these measurements were not made in F3. Oxygenation during DRN_1 in columns F2 also resulted in an increase in SO_4^{2-}, at 15 cm. Unfortunately, insufficient sample was collected from F3, and SO_4^{2-} concentration is therefore missing for the same period. Nevertheless, no EP anomaly was detected during DRN_1 in F3, but was detected during DRN_2, in relation to SO_4^{2-} concentration changes. The voltage potential anomaly is discussed in detail in relation to sulfur dynamics, below.

The relative contributions of saturation and EC cannot be fully decoupled from the entire dataset because EC measurements were only made periodically (and were often not possible due to insufficient sample collection). In Appendix A, an attempt is made to normalize σ' at 13.5 cm by interpolated EC measurements, between 183 and 293 days (the period for which no sampling points are missing in the EC time-series). The normalization of σ' with EC, highlights the direct control of moisture dynamics on the observed variations (see Figure AA 6 in Appendix A).

Measured σ' at 19.5 cm did no correlate well with EC at 15 cm. Nevertheless, changes in σ' at 19.5 cm, showed evidence of a pore water geochemical control, most apparent between 160 and 240 days. The increase in σ' during IMB_3 and DRN_3 (Figure 2-8a) corresponds to an increase in Fe^{2+} (at 15 cm) from 10.2 to 37.2 mM (Figure 2-5a). Furthermore, the subsequent decrease in σ', spanning across IMB_4 and DRN_4, matches the gradual drop in Fe^{2+} to 9.2 mM. We speculate that at 19.5 cm, EC variations were less pronounced, but that Fe^{2+} dynamics would have been more similar to those at 15 cm, than at fully saturated depths (*i.e.*, below 25 cm). At depths below 25 cm, σ' time series for both fluctuating and static treatments match the measured decreasing trend in EC across all depths.

2.6.3 Temporal σ″ response and oxygen availability

Time-series σ'' data exhibit dynamic temporal responses across the water table fluctuation depth interval (between 8 and 20 cm, based on O_2 dynamics). Within the transition zone of the fluctuating water table column (F3), a sharp increase in σ'' was recorded at 13.5 cm (Figure 2-9a) during DRN_1 (with a slight increase at 19.5 and 25.5 cm). The decrease in σ'' (at 13.5 cm) in the following imbibition period (IMB_2) continued into DRN_2. During DRN_2, σ'' increased sharply at 19.5 cm with a delayed slight increase at 25.5 cm (Figure 2-9a). Concurrently, O_2 concentrations at 20.5 cm (measured in replicate F2) reached values above 0.15 mM early into DRN_2 (Figure 2-3), in contrast to the delayed increase in O_2 levels at 20.5 cm in DRN_1 (reaching a maximum of 0.15 mM, shortly before the onset of IMB_2). This suggests that oxygenation occurred earlier and reached deeper into the soil profile from DRN_2 onwards. A similar sharp increase in σ'' was measured at 19.5 cm during DRN_3. The increase in σ'' values during drainage and the decrease during subsequent imbibition (initially at 13.5 cm, then at 19.5 cm after DRN_2, for two consecutive cycles) is contrary to the measured σ''-saturation relationship for this artificial soil (Figure 2-10) and the reported SIP-saturation relationship of Ulrich and Slater (2004). This apparent anti-correlation suggests that a control other than changes in soil moisture is driving measured temporal variations in σ'' measured during DRN_1/IMB_2, DRN_2/IMB_3 and DRN_3/IMB_4. In contrast σ' exhibited variations that agree both with pore-water geochemistry changes and the expected saturation dependence.

The onset of drainage and subsequent lowering of the water table in the equilibrium column to 40 cm b.s.s. drains macropores in the upper portion of the soil column, enabling air infiltration

into the system and resulting in an influx of O_2. The influx of a high energy yielding electron acceptor stimulates aerobic respiration of organic carbon (present as 10% per mass of soil and persistently high concentrations of DOC in the pore water, 15.3-18.8 mM, see Table 2-2). An increase in aerobic respiration (with sustained O_2 supply) provides suitable conditions for sustained microbial activity (Hibbing et al., 2010).

We conclude that the increases in σ'' (shown in Figure 2-9a) at depths of (1) 13.5 cm during DRN_1, (2) 19.5 cm during DRN_2 and DRN_3 (and into the onset of imbibition, IMB_4, from days 204 to 223), are controlled by increases in microbial growth and activity driven by the influx of O_2. The shift from 13.5 to 19.5 cm, in DRN_2 is a function of increased drainage in the columns, as evidenced by elevated O_2 concentrations at depth (Figure 2-3). The lack of a clear microbially mediated signal after DRN_1, at 13.5 cm, results from the interplay between saturation and stimulated microbial activity masking each other's contribution. Despite the onset of imbibition at 211 days following the end of the third drainage cycle, O_2 concentrations remain steady at 0.22 mM until day 229 when they begin to drop (Figure 2-3). O_2 remains in the soil allowing for continued aerobic respiration, resulting in enhanced microbial activity (and likely growth), in agreement with the slight increase in σ'' at 19.5 cm until day 216 and at 13.5 cm until day 223. Our conclusion is further supported by elevated levels of ATP (plotted alongside σ'' profiles in Figure 2-9b and d) measured between 8 and 18 cm in the fluctuating treatment, providing evidence of elevated microbial activity in the range of depths where dynamic SIP signal variations were recorded. After 99 days of incubation, ATP, also showed elevated concentrations closer to the surface, but showed no evidence of a development of a peak concentration in the transition zone (data are presented Appendix A, Figure AA 1).

Throughout the periods of pronounced variations in σ'', pH measurements were relatively constant at the different measurement depths. Periodic measurements of the pH of extracted pore water samples at depths of 15, 25 and 35 cm are compared to measured σ'' in both the fluctuating and static treatments in Figure 2-13. The magnitude of pH exhibited only slight variations with depth. There are no clear trends between pH and σ''. The surface charge of soil particles is modulated by pH. Protonation and deprotonation of surface exchange sites (*e.g.*, surface hydroxyl groups) results in a modification of surface charge density, which controls polarization of the electrical double layer (EDL) (Peruzzo et al., 2018). An increase in pH is expected to increase the proportion of positively charged pH dependent sites. The most pronounced increase in pH within

the fluctuating column (F3) at 15 cm occurred during IMB_4 (Figure 2-13a), while σ'' at 13.5 and 19.5 cm during that period decreased, yet the increase in pH should have resulted in a concurrent increase in σ''. Based on the lack of strong trends between pH and σ'' and the low magnitude of measured pH variations we deemed pH variations as having a negligible influence on the dynamic SIP signals recorded in this study.

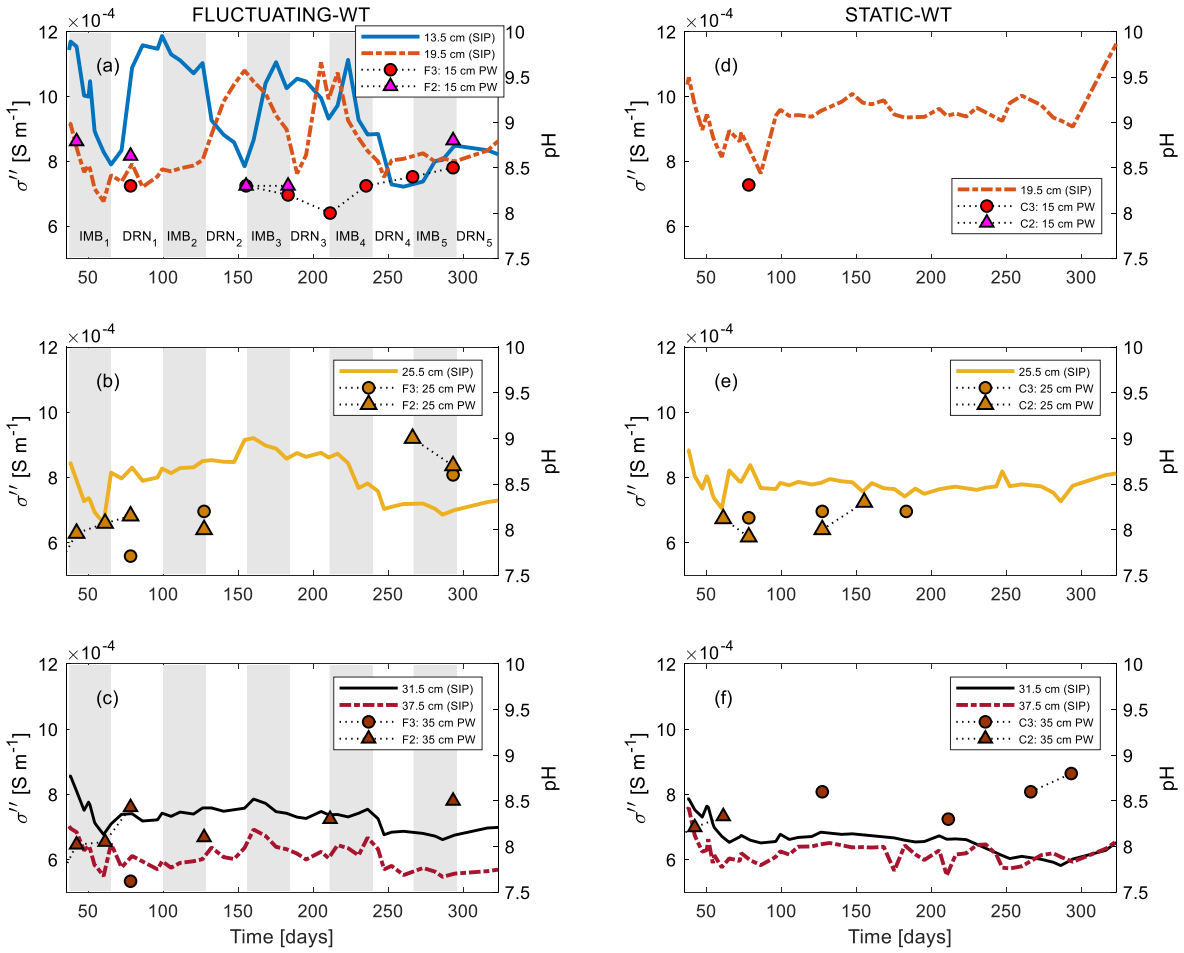

Figure 2-13. Imaginary conductivity (σ'') measured in fluctuating (left) and static (right) columns F3 and C3 compared to periodic pore water pH measurements from samples extracted at 15, 25 and 35 cm depths. (Note: pH measured in columns F2, F3, C2 and C3 are presented for completion, but SIP measurements were only conducted on F3 and C3). Panels (a) and (d) compare σ'' at 13.5 and 19.5 cm to pH from samples extracted at 15 cm, panels (b) and (e) compare σ'' at 25.5 cm with pH at 25 cm, and σ'' at 31.5 and 37.5 cm is compared to pH measurements at 35 cm in (c) and (f).

Furthermore, significant variations in Fe^{2+} across different DRN/IMB cycles were only measured in the fluctuating treatment, at 15 cm. These variations do not appear to have a strong control on σ''. For example, an increase in Fe^{2+} could increase sorption onto negatively charged sites, reducing ion mobility in the EDL of polarizing particles (Vaudelet et al., 2011b), but during the increase in Fe^{2+}, in IMB_3 (at 15 cm), σ'' at 13.5 cm increases. The opposite effect would be induced by a decrease in Fe^{2+} concentration, but σ'' decreases during the sharp drop in Fe^{2+} during DRN_4.

The persistence of O_2 into the imbibition period is related to hysteresis in the moisture response of the artificial soil, as driven by drainage versus imbibition, modulating the saturation conditions above 20 cm. The separate flow characterization experiment (simulating one shift from drainage to imbibition, Figure 2-2) shows that conditions above 14 cm remain unsaturated, following a sharp increase in moisture content after imbibition onset (Figure 2-2). At 18 cm, soil moisture exhibited a two-tiered response to saturation with a sharp increase, followed by a gradual increase to values near saturation 6 days after imbibition. This response is in agreement with the two-step wetting of swelling clay minerals, such as montmorillonite (Xie et al., 2004; Saiyouri et al., 2000), present in the soil at 10% per mass. The hysteretic response in saturation, shown in Figure 2-2, is observed throughout the incubation in the O_2 concentration profiles (Figure 2-3). The onset of drainage periods results in concurrent sharp increases in O_2 at 8.5 and 14.5 cm. Conversely, during imbibition, O_2 at 14.5 cm only begins to drop 6 days after imbibition onset, and 19 days after at 8.5 cm (this occurs consistently across all imbibition periods). The drop in O_2 measured above 14.5 cm, despite evidence of persistently unsaturated conditions could be related to the diffusion controlled delivery of O_2 into the columns, where aerobic respiration kinetics outpace oxygen resupply.

After 240 days of incubation, the σ'' response at 13.5 cm falls below the magnitude of the response at 19.5 cm, to the same range of values as measured at 25.5 cm. A small drop in σ'' is also measured at lower depths. Following this drop, measured signals exhibit less pronounced variations despite shifts in hydrology. The artificial soil is a system with no substrate inputs, that is, with a finite initial supply of organic carbon. Over time, substrate availability decreases with continuous consumption of the more labile components (Pronk et al., 2017). Therefore, despite the

influx of electron acceptor, microbial biomass density is unable to respond due to the lack of labile carbon needed for respiration, resulting in the constant σ'' signals measured at 13.5 and 19.5 cm. This phenomenon was reported in Rezanezhad et al. (2014), where CO_2 fluxes in a similar experiment progressively decreased during the experiment due to the depletion in electron donor availability.

The correlation between persistent oxygenation and increases in σ'', despite decreasing moisture content, highlights SIP's applicability as a non-invasive characterization and monitoring tool for soils. Previous laboratory experiments in controlled environments have largely focused on simple reactive systems (Schwartz and Furman, 2014; Placencia-Gómez et al., 2013; Abdel Aal et al., 2009; Slater et al., 2007). Our results highlight the feasibility of implementing SIP in a complex reactive environment as a monitoring tool to allow direct access to biogeochemical information. The role and importance of microbes in subsurface environments is well understood (Blagodatskaya and Kuzyakov, 2013; Atekwana and Atekwana, 2010). In a review focusing on active microorganisms in soils, Blagodatskaya and Kuzyakov (2013) highlight the central importance of microbial biomass as drivers of biogeochemical cycles and suggest that the current microbial characterization techniques are invasive and often fail to effectively distinguish between bulk and active populations.

During dynamic environmental conditions, it is well understood that a combination of physical (Stegen et al., 2016; Rezanezhad et al., 2014; Totsche et al., 2010; Dunn et al., 2005) and biological (Pett-Ridge and Firestone, 2005) drivers result in the development of biogeochemical hotspots and hot moments. Nevertheless, the true driver(s) behind the development of biogeochemical hotpots in dynamic transition zones remain(s) yet to be understood. SIP measurements have the potential to provide a relative measure of microbial activity at the spatial and temporal scales needed to monitor systems experiencing dynamic environmental changes.

Overall, both σ' and σ'' signals exhibit strong responses to the imposed variations in soil moisture, where saturation directly controls variations in σ' and indirectly controls variations in σ'' through biogeochemical reactions that are modulated by the influx of O_2. Variations in σ' in time and with depth were in agreement with the saturation regime, whereas σ'' variations were predominantly inversely related to soil moisture and varied specifically in response to O_2 availability in the water table fluctuation zone. Our results highlight the sensitivity of σ'' to bulk

soil charge characteristics as controlled by biogeochemical reactions and the sensitivity of σ' to changes in saturation.

2.6.4 Ag-AgCl electrodes as sensors of sulfur cycling

Voltage potentials recorded between measurement and reference electrodes stem from both self- and electrodic potential contributions in the absence of uncoupled monitoring of SP and EP in parallel, as done in Zhang et al. (2010). The necessity to maintain electrode contact under unsaturated conditions (*i.e.*, preventing electrode filling solution from draining out) required that the non-polarizing electrodes used in this experiment be filled with a gel. Despite the separation between the pore water and the metal electrodes our measurement electrodes did undergo considerable interactions with the electrolyte. The long exposure time of the electrodes to the pore water coupled with pressure induced flow (the electrodes effectively sealed the experimental system at their insertion ports and were therefore under constant pressure) resulted in migration of dissolved pore water species into the agar gel (a contribution from $H_2S_{(g)}$ diffusion into the gel cannot be ruled out), which then interacted with the metal electrodes. The potentials measured here are attributed largely to galvanic cell potentials generated by chemical reactions at the electrodes themselves (based on the ~400 mV magnitude) and are hence interpreted as an EP anomaly. The strong redox gradients, coupled with the presence of bacteria and 2.5% goethite, also likely contributed to the bulk response by way of SP signals from a (bio)geobattery. The SP contributions, however, are expected to be small, on the order of tens of millivolts.

The development of the EP anomaly within the 15 to 27 cm depth interval of the fluctuating treatment (column F3, Figure 2-11) coincides with the measured increase in O_2 at 21 cm. A superposition of O_2 (measured in F2) and EP at 19 and 21 cm (measured in F3) is presented in Figure 2-14. The artificial groundwater used in the experiment is devoid of any sulfur, leaving the organic matter as the only significant source of sulfur in the system (Mitchell and Fuller, 1988; David and Mitchell, 1987). The production of sulfate therefore suggests that sulfur mineralization was taking place (Blodau et al., 2007), resulting in the release of SO_4^{2-} via the oxidation of reduced solid organic sulfur (Houle et al., 2001). The correlation between the EP anomaly and the increase in SO_4^{2-} (Figure 2-14), and subsequent reduction provides evidence for direct interaction between the originally Ag-AgCl electrodes and sulfur in the pore water (which migrated into the electrode gel).

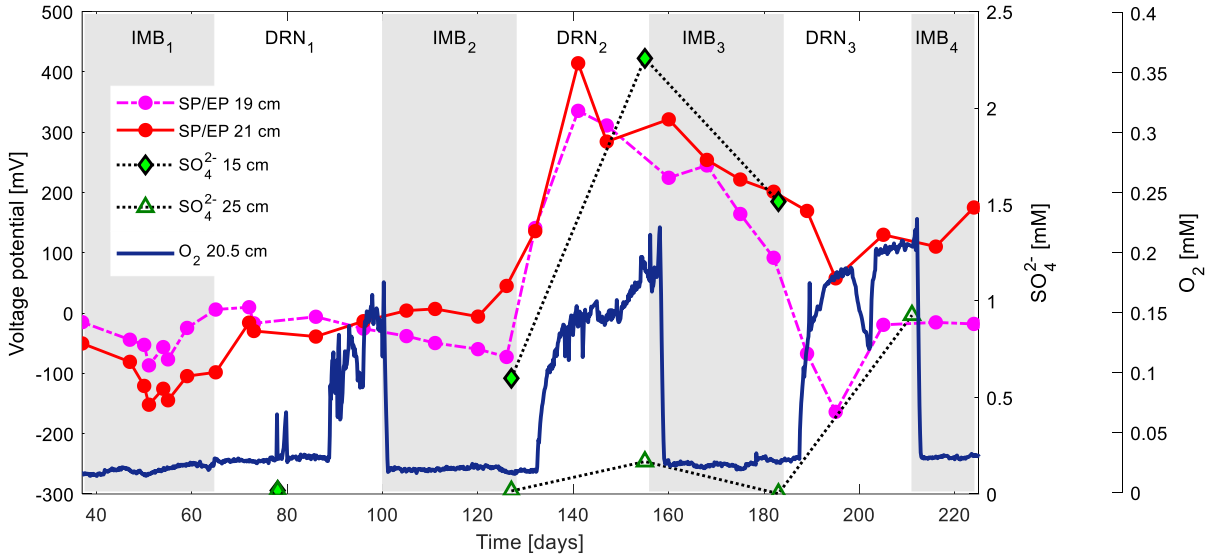

Figure 2-14. Time-series electrodic potential (EP) measured at 19 and 21 cm, compared to pore water SO_4^{2-} samples taken at 15 and 25 cm measured in the same column as the EP measurements (F3) and O_2 concentrations at 20.5 cm in column F2 (note: EP measurements were collected in replicate F3 and O_2 concentrations were measured in F2).

Despite other studies showing a direct sensitivity of Ag-AgCl electrodes to sulfide concentrations (Personna et al., 2008; Slater et al., 2008; Williams et al., 2007), our measurements suggest a direct interaction between SO_4^{2-} as well as HS^-. AgCl has a much lower solubility product (K_{sp}) than Ag_2SO_4: 10^{-10} and 10^{-5}, respectively (Chen et al., 2015; Xiu et al., 2011). It is therefore unlikely that Ag_2SO_4 formation would be more favorable, but the semi-porous nature of the AgCl coating (Williams et al., 2007), along with increasing SO_4^{2-} concentrations in solution likely resulted in formation of Ag_2SO_4 due to direct contact of exposed Ag^0 with SO_4^{2-} as well as some reactivity with the AgCl coating due to an increasing ion activity product (IAP) driven by rising SO_4^{2-} levels. The interactions between SO_4^{2-}, exposed Ag^0 and AgCl would have contributed to the measured potentials at the respective electrode.

The sensitivity of Ag-AgCl electrodes to changes in sulfur pore water geochemistry has been previously documented (Slater et al., 2008; Williams et al., 2007). Our results suggest a strong interaction between dissolved sulfur species and the Ag-AgCl electrodes, and also further confirm the effectiveness of EP (and Ag-AgCl electrodes) at detecting changes in sulfur geochemistry in porous media. The recorded EP anomaly presented here successfully detected the development of organic soil S mineralization, a microbial functionality (Houle et al., 2014; Houle et al., 2001) that had not been present before that period. EP, in conjunction with periodic geochemical markers, can serve as an indicator for determining the location and temporal variability of microbially mediated organic sulfur mineralization and sulfate reduction in complex soil environments.

Zhang et al. (2010) addressed the joint contribution of SP and EP measured with fluid filled electrodes, by also monitoring SP with longer, gel filled reference electrodes with high concentrations of Cl^- in order to homogenize the conditions surrounding the metal electrode. The longer casing helped minimize diffusive contamination into the electrode. Their coupled electrode design enabled them to separate the self-potential contribution from the electrodic potential contribution, enabling a more accurate estimation of HS^- concentrations. Monitoring microbially driven processes with SP/EP, therefore, necessitates careful data interpretation and electrode design as well as the consideration of possible electrode contamination due to extended exposure times (Slater et al., 2008).

2.7 Conclusions

In this chapter, the SIP responses in a near-field bench-scale setup showed a clear dependence of the polarization response on redox zonation driven predominantly by microbial biomass distribution. Dynamic imaginary conductivity (σ'') responses were only detected in the water table fluctuation zone and, in contrast to real conductivity data, did not exhibit a direct petrophysical dependence, highlighting that the observed dynamics in σ'' were a result of microbial activity. EP measurements detected the onset of SO_4^{2-} release from soil organic matter after the second drainage period, which correlated with oxygenation at depth. The sensitivity of Ag-AgCl electrodes to sulfur allowed us to detect the development of oxidative sulfur mineralization within the artificial soil columns, which did not occur during the initial 110 days of incubation. The findings reported in this chapter show that non-invasive biogeophysical techniques (specifically SIP and EP), in conjunction with periodic geochemical measurements, can yield indicators of the location and temporal variability of microbial distribution and activity in soils. Furthermore, our findings highlight that biogeophyscal techniques can be used to monitor processes such as organic sulfur mineralization and sulfate reduction in complex soil environments (*i.e.*, "near-natural" soils containing organic matter, clay and goethite). At the field scale, where the direct observation of subsurface biogeochemical properties and processes are difficult to implement, SIP and EP can be used to remotely detect temporal variations and depth zonation of redox sensitive processes, allowing for more cost-effective and timely site characterization and locating of reactive zones.

2.8 Future work

Building on the findings from this work, key biogeochemical parameters of interest can be defined as a means to reduce the instrumentation load in future column experiments. Such considerations would allow for the inclusion of soil moisture probes and enable continuous measurements of *in situ* soil moisture dynamics. Monitoring of soil moisture *in situ* would address the quantitative deconvolution of parallel primary and secondary signal controls on measured complex conductivity (and self-potential) responses. Normalizing geophysical signals to soil moisture would aid in directly resolving the dynamic biogeochemical contributions.

Furthermore, hysteresis in the soil moisture retention curve, between drainage and imbibition, largely controls the availability of O_2 in the system. While this was not directly assessed here, it is clearly observed in both the soil moisture response to the fluctuating regime (Figure 2-2) and the O_2 concentrations (Figure 2-3). Therefore, the duration of drainage and imbibition periods has potentially important implications in modulating the biogeochemical activation of the system. For example, shorter duration, may not allow for complete drainage and O_2 penetration down to 20 cm, significantly altering the depth at which aerobic respiration processes occur. Exploring the effects of fluctuation frequency, on biogeochemically-controlled SIP responses will shed further light on the "hot-moments" of microbial activity and the physical constraints on reactive species delineating vadose zone biogeochemical hotspots.

3 Linking spectral induced polarization (SIP) and subsurface microbial processes: Results from sand column incubation experiments

This chapter is modified from:

Mellage, A., C. M. Smeaton, A. Furman, E. A. Atekwana, F. Rezanezhad, and P. Van Cappellen (2018). Linking Spectral Induced Polarization (SIP) and Subsurface Microbial Processes: Results from Sand Column Incubation Experiments. *Environmental Science & Technology*. 52(4), 2081-2090.

3.1 Summary

Geophysical techniques, such as Spectral Induced Polarization (SIP), offer potentially powerful approaches for in-situ monitoring of subsurface biogeochemistry. The successful implementation of these techniques as monitoring tools for reactive transport phenomena, however, requires the de-convolution of multiple contributions to measured signals. Here, we present SIP spectra and complementary biogeochemical data obtained in saturated columns packed with alternating layers of ferrihydrite-coated and pure quartz sand, and inoculated with *Shewanella oneidensis* supplemented with lactate and nitrate. A biomass-explicit diffusion-reaction model is fitted to the experimental biogeochemical data. Overall, the results highlight that (1) the temporal response of the measured imaginary conductivity peaks parallels the microbial growth and decay dynamics in the columns, and (2) SIP is sensitive to changes in microbial abundance and cell surface charging properties, even at relatively low cell densities ($<10^8$ cells mL^{-1}). Relaxation times (τ) derived using the Cole-Cole model vary with the dominant electron accepting process, nitrate or ferric iron reduction. The observed range of τ values, 0.012 – 0.107 s, yields effective polarization diameters in the range 1 – 3 μm, that is, two orders of magnitude smaller than the smallest quartz grains in the columns, suggesting that polarization of the bacterial cells controls the observed chargeability and relaxation dynamics in the experiments.

3.2 Introduction

Direct access to subsurface biogeochemical processes is logistically difficult and usually expensive. The deployment of non-invasive geophysical techniques is comparatively inexpensive and can provide data with high spatial and temporal resolution. Spectral induced polarization (SIP), in particular, is an attractive alternative for monitoring subsurface biogeochemistry (Hao et al., 2015); it has been shown to be sensitive to microbially driven subsurface biogeochemical processes, including microbial growth (Zhang et al., 2014; Personna et al., 2008; Davis et al., 2006), (bio)mineral transformations (Personna et al., 2008; Slater et al., 2007), and mineral dissolution (Placencia-Gómez et al., 2015; Placencia-Gómez et al., 2013; Ntarlagiannis et al., 2005a). In SIP, the impedance magnitudes ($|\sigma|$) and phase-shifts (φ) between injected currents and resulting voltage potentials are measured over a broad frequency range (Abdel Aal and Atekwana, 2014; Schwartz and Furman, 2014; Schwartz et al., 2012; Williams et al., 2009a; Personna et al.,

2008). The technique is based on energy dissipation processes and the charging properties of the porous medium of interest (Schwartz and Furman, 2014; Schwartz et al., 2012).

The response of a porous medium to an injected current is expressed in terms of the complex conductivity, σ^*:

$$\sigma^* = \sigma' + i\sigma'' \qquad 3.1$$

where σ' and σ'' [S m^{-1}] are the frequency-dependent real and imaginary conductivities and i is the imaginary unit (Abdel Aal and Atekwana, 2014): σ' is a conduction term largely determined by the electrolyte or pore-water conductivity, and σ'' represents an energy storage term which stems mainly from polarization phenomena. The latter are usually attributed to the migration of counter-ions (cations) within electrical double layers (EDL) at the grain (Revil and Florsch, 2010) and pore-interface (Marshall and Madden, 1959) scales. However, our knowledge of the role of microorganisms in the polarization dynamics of porous media remains limited. As emphasized in two review papers on the emerging topic of biogeophysics (Atekwana and Atekwana, 2010; Atekwana and Slater, 2009), there is a need for a better understanding of the microbiological drivers of the electrical responses of subsurface environments.

Electrical techniques have been shown to detect the presence and differences in abundance of cells: Prodan et al. (2004) measured variations in dielectric permittivity of *E. coli* suspensions proportional to differences in abundance. A dependence of the complex conductivity σ^* on the presence of microorganisms was first shown in flow-through reactor experiments performed with mixed cultures and sands from hydrocarbon contaminated sites (Davis et al., 2006; Abdel Aal et al., 2004), while experiments on microbially induced iron sulfide transformations (Personna et al., 2008; Slater et al., 2007) demonstrated the sensitivity of SIP signals to microbe-mineral interactions. These studies also highlighted the composite nature of σ^*, with contributions from multiple, often coupled, processes. The detection of polarization of pure culture bacterial suspensions (Zhang et al., 2014) further implies that SIP signals may, at least in part, reflect the electrical properties of the subsurface microorganisms themselves (Abdel Aal et al., 2009; Davis et al., 2006; Ntarlagiannis et al., 2005b; Abdel Aal et al., 2004). The successful implementation of SIP as a monitoring tool for microbially driven reactive processes in the subsurface therefore requires the deconvolution of parallel signal contributions to spectra measured in the frequency range 0.01–1000 Hz. Available evidence clearly shows that SIP signals are sensitive to biotic and abiotic geochemical processes (Placencia-Gómez and Slater, 2014; Revil et al., 2012; Abdel Aal

et al., 2009; Slater et al., 2007); SIP measurements have also been linked to membrane (Ntarlagiannis et al., 2005b) and grain (Stern-layer) polarization mechanisms (Revil et al., 2012; Vaudelet et al., 2011b; Revil and Florsch, 2010; Leroy and Revil, 2009).

Phenomenological models like the Cole-Cole model (Pelton et al., 1978; Cole and Cole, 1941) are used to describe the frequency dependence of the impedance and phase shift during SIP experiments (Nordsiek and Weller, 2008). The generalized form of the Cole-Cole model can be expressed in terms of σ^* [S m^{-1}]:

$$\sigma^*(\omega) = \sigma_0 \left[1 + m\left(\frac{(i\omega\tau)^c}{1 + (i\omega\tau)^c(1-m)}\right)\right] \quad 3.2$$

where σ_0 [S m^{-1}] is the direct current (DC) conductivity, m [-] is the chargeability, τ [s] is the relaxation time, ω [rad s^{-1}] is the angular frequency and c [-] is a constant describing the shape of the observed phase dispersion (Ustra et al., 2012; Zisser et al., 2010b). The normalized chargeability provides a measure of the total polarization of the porous medium and is thus related to the interfacial charge storage, analogous to σ'' over the measured frequency range (Ustra et al., 2012; Chen et al., 2008; Slater, 2007). The relaxation time is related to the characteristic grain size, d [m], that is, the apparent length-scale over which polarization takes place, and is generally assumed to describe the length scale over which ion migration takes place in the EDL (Zhang et al., 2012; Slater, 2007; Slater et al., 2007), according to:

$$\tau = \frac{d^2}{8D_s} = \frac{d^2\left|q_{(+)}\right|}{8k_bT\beta_{(+)}} \quad 3.3$$

where D_s [m^2 s^{-1}] is the surface diffusion coefficient. Equation 3.3 implies that the relaxation time for EDL polarization is inversely proportional to D_s. The latter can be estimated as $k_bT\beta_{(+)}/\left|q_{(+)}\right|$, where k_b is the Boltzmann constant (1.3807×10^{-23} J K^{-1}), T [K] is the absolute temperature, $\beta_{(+)}$ [m^2 s^{-1} V^{-1}] is the effective counter-ion mobility in the Stern layer, and $\left|q_{(+)}\right|$ [C] is the absolute value of the charge of the counter-ions.

In this study, we couple biogeochemical data, reactive transport modeling, and electrical measurements (similar to the coupled geophysical monitoring and modeling approach of Slater et al. (2009)), in order to relate SIP data to microbial biomass changes and respiratory activity in saturated columns filled with alternating layers of ferrihydrite-coated (FS) and pure quartz sand (QS), and inoculated with the metabolically diverse heterotrophic bacterium *Shewanella oneidensis* in the presence of nitrate and lactate. By recording SIP spectra under well-characterized

conditions, we aim to shed new light on specific processes and properties that govern the electrical responses of a spatially heterogeneous and microbially active porous medium.

3.3 Materials and methods

3.3.1 Column reactors

Six identical column reactors made of acrylic tubing, with an inner diameter of 3.2 cm, length of 24 cm and wall thickness of 3 mm, were used (Figure 3-1). The six reactors had identical sets of ports allowing for electrode placement in the SIP column (and kept sealed with NPT stoppers in the five non-SIP columns), as well as for pore-water and soil sampling. The reactors were closed at both ends by rubber stoppers. All parts required to assemble the columns were sterilized separately, either using an autoclave or a cold sterilant (Spor-Klenz®).

The columns were wet-packed in an anaerobic chamber (Coy®, < 1ppmv O_2 in N_2 with 3% H_2) with sterilized quartz and iron(III)-coated (Abdel Aal et al., 2009; Müller et al., 2008) quartz sands (U.S. Silica®, F-45, grain size range: 0.15 – 0.42 mm). The packing of the columns alternated 4.5 cm thick layers of pure quartz sand (QS) and ferrihydrite-coated sand (FS), resulting in the layered packing arrangement shown in Figure 3-1. This layered packing arrangement was designed to test whether the iron oxide coating would preferentially focus microbial activity in the FS layers, because of the cells' attachment affinity to ferric iron oxyhydroxides (Abdel Aal et al., 2009). A microbial growth medium (modified M1-media (Myers and Nealson, 1988); see Appendix B for medium composition details) inoculated with 3.5×10^7 cells mL^{-1} plus 20 mM lactate and 1 mM nitrate was used as the saturating pore solution. The uniform porosity, ϕ, derived from the volume of water required to saturate the sand was 0.36 ($\pm$0.04).

Note that SIP data from a parallel non-growth (NG) control column experiment and an abiotic reference medium are also presented herein. Concurrent to the biotic experiment a NG column-batch reactor was packed with the same porous media layering and packing procedure as outlined above. The media used for the NG treatment contained the same concentrations of all constituents as in the biotic growth experiment without the addition of NO_3^- and lactate. The NG treatment was inoculated with the same *S. oneidensis* community to the same target cell density, to serve as a control devoid of an external carbon source (except for the bacteria themselves), electron donor and electron acceptor. SIP signals were periodically monitored in the NG column and the column was sacrificially sampled at the end of the experiment (237 hours). Furthermore,

an additional layered sand column (*i.e.*, containing FS, QS and FS layers) was packed with the microbial growth medium, but without the presence of *S. oneidensis* cells, to serve as an abiotic reference.

A 1M HCl extraction was used to measure the amount of ferric iron associated with the iron-coated sand following the procedure of Müller et al. (2008). The Fe^{3+} concentration in the extractant solution was determined using the ferrozine method after Viollier et al. (2000). X-ray diffractograms (PANanalytical Empyrean II, New Orleans, LA, USA) of FS samples did not reveal the presence of specific iron mineral phases, likely due to the thinness and amorphous nature of the coating. The ferric-oxide coating was inferred to be ferrihydrite (FH) based on the speed of complete reduction of the coating by ascorbic acid (< 30 min) (Schwertmann, 1991). (Note: model fitting to the geochemical data also agrees with the stoichiometry of FH reduction, see Results and Discussion.) The average coating concentration obtained from the HCl extraction was 0.9 mmol Fe g^{-1}.

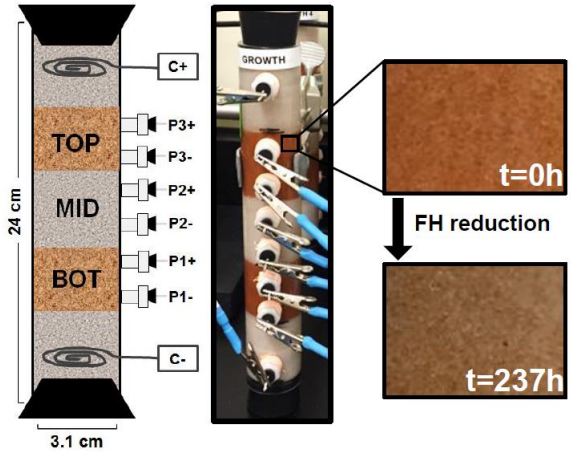

Figure 3-1. Schematic diagram and photograph of the packed column reactor equipped with nonpolarizable Ag-AgCl electrodes. The TOP and BOT layers consist of ferrihydrite (FH) coated quartz sand and the MID layer of pure quartz sand. C and P followed by a number correspond to (+) or (−) current and potential electrodes, respectively. The magnification on the right shows the color of theFH coating at the start of the experiment and after 237 h.

3.3.2 Biogeochemical analyses

The six column reactors were kept in the anaerobic chamber and simultaneously inoculated with bacteria, nitrate and lactate (t = 0). The entire duration of the experiment was 237 hours, during which the column reactors were sequentially sacrificed at pre-specified time points and sampled under fully anaerobic conditions. Small, 1 mL volumes of pore water were extracted with syringes through the ports (after removal of the NPT stoppers) using ceramic MicroRhizon™ samplers (model CSS5, pore size 0.15 µm). A mini-auger (length = 5 cm and inner diameter = 3.5 mm) was inserted into the ports adjacent to those used for pore water sampling in order to retrieve bulk sand samples (approximately 2 g), which were stored in 15 mL centrifuge tubes.

Pore water samples were analyzed for lactate, acetate, NO_3^-, NO_2^- and Fe^{2+} in order to monitor the progress of nitrate respiration and reductive FH dissolution: *S. oneidensis* carries out dissimilatory nitrate reduction to ammonium (DNRA) (Zhang et al., 2013; Gao et al., 2009a) and is able to grow on Fe(III) as a sole electron acceptor (Heidelberg et al., 2002). Ammonium was not measured, as the concentration in the growth media was 18 mM, far more than could be produced from DNRA. Lactate, acetate and NO_3^- were analyzed by ion chromatography (Dionex ICS-5000 equipped with a capillary IonPac® AS18 column; LOD = 0.92, 3.23 and 0.54 µM for lactate, acetate and NO_3^-, respectively); NO_2^- was measured using a microplate reader-based colorimetric method (LOD = 0.08 µM) (Ringuet et al., 2011b); Fe^{2+} concentrations were determined by the ferrozine method (Viollier et al., 2000). Note that NO_3^- concentrations in excess of the 1 mM concentration of the saturating solution were measured during the early stages of the experiment because of NO_3^- contamination of the FH-coating due to the coating procedure (Müller et al., 2008).

The relatively low inoculated cell densities and the presence of iron mineral phases interfered with direct cell counting by fluorescence microscopy (Hobbie et al., 1977). Although cells were detected, their abundance was difficult to estimate reliably, with less than 200 cells per slide. We therefore used the adenosine triphosphate (ATP) contents of the bulk sand samples as a semi-quantitative proxy for the abundance of active *S. oneidensis* cells (see Appendix B, Table AB 2 for ATP contents). Approximately 1.5 g of sand, collected with the mini-auger samples, were added to 10 mL of PBS buffer (137 mM NaCl, 10 mM PO43- and 2.7 mM KCl adjusted to pH 7.5) and sonicated for 10 minutes. The supernatant was then immediately sampled and concentrations determined through triplicate luminescence measurements (FlexStation 3 Multi-

Mode Microplate Reader, Molecular Devices, LLC) in multiwell-plate format using a cell viability assay kit (BacTiter-GloTM Microbial Cell Viability Assay).

3.3.3 SIP measurements

One of the six columns was instrumented with non-polarizing Ag-AgCl potential electrodes and Ag-AgCl current coil-electrodes (Figure 3-1). This column was the last one to be sacrificially sampled at the end of the experiment (t = 237 hours). The potential Ag-AgCl electrodes were encased in nylon 1/2" NPT compression fittings that were filled with sterile 15 g L^{-1} agar gel electrolyte containing 1M KCl. Two current electrodes were inserted, one at the top of the column, the other at the bottom. Six potential electrodes were placed in between the current electrodes, hence allowing for three SIP measurement pairs – bottom, middle and top. The top- and bottom-most potential electrodes were 4 cm away from the current electrodes; the distance separating the potential electrodes was 2 cm. Note that, in order to minimize interference of the current electrodes in the potential measurements, different distances between current and potential electrodes were tested during preliminary trials. Also, once installed, the electrodes were not removed or replaced from the columns for the entire duration of the experiment.

For the geophysical measurements, the SIP column was temporarily moved out of the anaerobic chamber to a laboratory bench. Current was injected through the outer coil electrodes, while the output voltage was recorded at each electrode pair, following the approach of Abdel Aal and Atekwana (2014). The geometric factor, *k*, of the electrode array was determined by measuring the impedance magnitude (Z) response of a series of solutions of known resistivity (ρ_a) ($\rho_a = kZ$) (Zhang et al., 2014). The SIP responses were recorded at each potential electrode pair using a Portable Spectral Induced Polarization (PSIP) Unit (Ontash & Ermac Inc., NJ, USA). Phase shift ($-\varphi$) and conductivity magnitude ($|\sigma|$) were measured at 51 log frequency intervals between 0.01 and 1000 Hz. A Cole-Cole relaxation curve was fitted to the spectral phase and impedance responses (Weigand and Kemna, 2016c).

3.3.4 Diffusion-reaction model (DRM)

A one-dimensional DRM was developed to help interpret the observed spatial and temporal geochemical distributions. The model assumes that the main drivers of the observed changes are DNRA and dissimilatory iron(III) reduction coupled to the oxidation of lactate to acetate (Zhang

et al., 2013; Gao et al., 2009a; Bretschger et al., 2007). The products of dissimilatory iron reduction include aqueous and adsorbed Fe^{2+} as well as various reduced iron mineral phases, in particular magnetite (Coker et al., 2006). The reaction stoichiometry with magnetite and Fe^{2+} as end products was chosen here, as it yielded the best fits of the DRM to the data (see Results and Discussion) and agreed with visual evidence for the formation of a reduced mineral coating during the iron respiration phase (Figure 3-1).

The reactions included in the DRM are listed in Table 3-1, together with the corresponding Gibbs energies of reaction (ΔG_r) and growth yields (Y) estimated for the initial chemical conditions in the columns. In order to explicitly account for the concentration changes of the reaction intermediate NO_2^-, DNRA is represented by two consecutive steps, from NO_3^- to NO_2^- (step 1), and from NO_2^- to NH_4^+ (step 2). In the calculations, pH is kept constant at 7.5, that is, the pH of the saturating aqueous medium. The microbial biomass is modeled as an immobile, solid-bound constituent. Reactive transport of dissolved chemical species within the columns is described by:

$$\frac{\partial C}{\partial t} = D_e \frac{\partial^2 C}{\partial x^2} + R \qquad 3.4$$

where C [mol L^{-1}] is the aqueous concentration of the mobile species, D_e [m^2 h^{-1}] is the effective diffusion coefficient, and R [mol L^{-1} h^{-1}] is the sum of all the reactions producing the chemical species minus the reactions that consume it.

Microbially mediated reaction rates were simulated with dual-Monod kinetics. The microbial growth rates, r_{DNRAx} [cells L_{PM}^{-1} h^{-1}] (where L_{PM} refers to the bulk volume of the porous medium, that is, solid phase plus pore water), for the two successive DNRA steps are then given by:

$$r_{DNRAx} = \mu_{max}^{DNx} \cdot \frac{C_{Lac}}{C_{Lac} + K_{Lac}^{DN}} \cdot \frac{C_{NO_x}}{C_{NO_x} + K_{NO_x}} \cdot X \qquad 3.5$$

where μ_{max}^{DNx} [h^{-1}] is the corresponding maximum specific growth rate of the bacteria, C_{Lac} [mol L^{-1}] is the lactate concentration, C_{NO_x}[mol L^{-1}] the concentration of nitrate (x = 1) or nitrite (x = 2), K_{Lac}^{DN} [mol L^{-1}] is the half-saturation constant for lactate uptake (assumed the same for both DNRA steps), K_{NO_x} [mol L^{-1}] is the half-saturation constant for nitrate (x = 1) or nitrite (x = 2), and X [cells L_{PM}^{-1}] is the cell abundance or biomass.

Microbial growth using ferrihydrite (FH) as the terminal electron acceptor is energetically less favorable than DNRA. Dissimilatory FH reduction is therefore assumed to be kinetically inhibited by the presence of the higher energy yielding electron acceptors nitrate and nitrite:

$$r_{FHRED} = \mu_{max}^{F3} \cdot \frac{C_{Lac}}{C_{Lac} + K_{Lac}^{F3}} \cdot \frac{S_{Fe(III)} \cdot f}{S_{Fe(III)} \cdot f + K_{Fe(III)}} \cdot \frac{K_{NO_x}^{inh}}{C_{NO_x} + K_{NO_x}^{inh}} \cdot X \quad 3.6$$

where μ_{max}^{F3} [h^{-1}] is the maximum specific growth rate supported by dissimilatory FH reduction, $S_{Fe(III)}$ [mol g^{-1}] is the concentration of FH (multiplied by a conversion factor, $f = \rho_b \cdot \left(\frac{1}{\phi}\right)$, where ρ_b is the bulk density), and K_{Lac}^{F3} and $K_{Fe(III)}$ [mol L^{-1}] are the half-saturation constants for the electron donor and acceptor, respectively. The fourth term on the RHS is a generalized inhibition term,[47] where $K_{NO_x}^{inh}$ [mol L^{-1}] is the inhibition constant due to the presence of NO_3^- or NO_2^-. When both nitrogen species are present, the expression for r_{FHRED} [cells L_{PM}^{-1} h^{-1}] contains two inhibition terms.

With the above reaction rate expressions, the DRM yields the following system of equations governing the changes in aqueous and solid-bound chemical concentrations, plus the biomass:

$$\frac{\partial C_{Lac}}{\partial t} = D_e \frac{\partial^2 C_{Lac}}{\partial x^2} + \left(-r_{DNRA1} \cdot \frac{1}{Y_1} - r_{DNRA2} \cdot \frac{1}{Y_2} - r_{FHRED} \cdot \frac{1}{Y_3}\right) \cdot \left(\frac{1}{\phi}\right) \quad 3.7$$

$$\frac{\partial C_{Ac}}{\partial t} = D_e \frac{\partial^2 C_{Ac}}{\partial x^2} + \left(r_{DNRA1} \cdot \frac{1}{Y_1} + r_{DNRA2} \cdot \frac{1}{Y_2} + r_{FHRED} \cdot \frac{1}{Y_3}\right) \cdot \left(\frac{1}{\phi}\right) \quad 3.8$$

$$\frac{\partial C_{NO3}}{\partial t} = D_e \frac{\partial^2 C_{NO3}}{\partial x^2} - 2r_{DNRA1} \cdot \frac{1}{Y_1} \cdot \left(\frac{1}{\phi}\right) \quad 3.9$$

$$\frac{\partial C_{NO2}}{\partial t} = D_e \frac{\partial^2 C_{NO2}}{\partial x^2} + \left(2r_{DNRA1} \cdot \frac{1}{Y_1} - 0.67 r_{DNRA2} \cdot \frac{1}{Y_2}\right) \cdot \left(\frac{1}{\phi}\right) \quad 3.10$$

$$\frac{\partial C_{NH4}}{\partial t} = D_e \frac{\partial^2 C_{NH4}}{\partial x^2} + 0.67 r_{DNRA2} \cdot \frac{1}{Y_2} \cdot \left(\frac{1}{\phi}\right) \quad 3.11$$

$$\frac{\partial C_{Fe}}{\partial t} = D_e \frac{\partial^2 C_{Fe}}{\partial x^2} \cdot \left[1 + \frac{1-\phi}{\phi} \rho_s K_d\right]^{-1} - 0.8 r_{FHRED} \cdot \frac{1}{Y_3} \cdot \left(\frac{1}{\phi}\right) \quad 3.12$$

$$\frac{dC_{FH}}{dt} = -10.4 r_{FHRED} \cdot \frac{1}{Y_3} \quad 3.13$$

$$\frac{dC_{MAG}}{dt} = -3.2 r_{FHRED} \cdot \frac{1}{Y_3} \quad 3.14$$

$$\frac{dX}{dt} = r_{DNRA1} + r_{DNRA2} + r_{FHRED} - r_{DECAY} \quad 3.15$$

In equations 3.7 to 3.15, rates describing concentration changes of aqueous species (in units of mol L^{-1} h^{-1}) are obtained by dividing the microbial growth rates by their corresponding growth yields, Y_i [cells mol_{Lac}^{-1}]. The Y_i values are continuously updated during a simulation based on the temporally changing Gibbs energies of the catabolic reactions (Heijnen and Van Dijken, 1992), using the Gibbs free energy dissipation method:

$$\Delta G_r^{cat} = \Delta G_{cat}^{\circ} + RT \cdot ln(Q_{cat}) \quad 3.16$$

$$\Delta G_r^{an} = \Delta G_{an}^{\circ} + RT \cdot ln(Q_{an}) \quad 3.17$$

$$Q_i = \frac{\prod\{products\}^n}{\prod\{reactants\}^n} \quad 3.18$$

where ΔG_r^{cat} is the Gibbs free energy of the catabolic reaction [kJ $mol_{Lactate}^{-1}$], ΔG_r^{an} is the Gibbs free energy of the anabolic reaction [kJ $mol_{Lactate}^{-1}$], ΔG_{cat}° [kJ $mol_{Lactate}^{-1}$] is the standard Gibbs free energy of the catabolic reaction per one mole of lactate, and ΔG_{an}° [kJ $mol_{Lactate}^{-1}$] is the standard Gibbs free energy of the anabolic reaction per one mole of lactate. ΔG_{cat}° is calculated from the Gibbs free energies of formation of products and reactants of the relevant catabolic reaction. R is the ideal gas constant ($8.314 \cdot 10^{-3}$ kJ mol^{-1} K^{-1}) and T is the temperature, in this case 298.15 K. Q_i is the reaction ratio (i = cat/an), it is determined from the ratio of the activity of products and reactants as well as the stoichiometry of the catabolic and anabolic reactions (Heijnen and Van Dijken, 1992).

The dynamic Y [mol_{bioC}/mol_{Lac}] is then calculated from the Gibbs free energy of the reaction at each time step, in the model, using the following expression:

$$Y = -\frac{\Delta G_r^{cat}}{\Delta G_r^{an} + \Delta G_{diss} - \Delta G_r \cdot Y_{an}} \quad 3.19$$

ΔG_{diss}, 348.3 [kJ $mol_{Lactate}^{-1}$] (Heijnen and Van Dijken, 1992), the Gibbs free energy of dissipation and the anabolic growth yield, Y_{an}, 0.383 [mol_{bioC}/mol_{Lac}], were held constant. Figure 3-2, illustrates the dynamic evolution of the yield coefficient from all three reactions considered (Figure 3-2a), as well as the ΔG_r^{cat} as it changes throughout the simulation (Figure 3-2b).

The rate of change of the biomass concentration, equation 3.15, is expressed in units of cells L_{PM}^{-1} h^{-1}, while changes of FH and magnetite concentrations over time are given in mol L_{PM}^{-1} h^{-1}. Sorption of Fe^{2+} produced by the reductive dissolution of FH is included assuming a linear isotherm, which yields the retardation term in squared brackets on the RHS of equation 3.12. Transport and reaction were solved iteratively at each time step (Δt = 60 s) in MATLAB®. The Crank-Nicolson method was implemented to solve the diffusive transport of dissolved species (Δx = 1 mm), with zero-flux boundary conditions at the top and bottom of the domain. The solutions for the ordinary differential equations describing the reactive terms were approximated using the fifth-order Runge-Kutta (Butcher, 2016) method.

Table 3-1. Microbially mediated reactions; stoichiometries are normalized to 1 mol of lactate.

	Dissimilatory nitrate reduction to ammonium (DNRA)	ΔG_r [kJ mol_{Lac}^{-1}] [a]	Y [cells mol^{-1}] [a,b]
1	$C_3H_5O_3^- + 2NO_3^- \rightarrow C_2H_3O_2^- + 2NO_2^- + HCO_3^- + H^+$	-320	5.72×10^{13}
2	$C_3H_5O_3^- + 0.67NO_2^- + 0.67H_2O + 0.33H^+ \rightarrow C_2H_3O_2^- + 0.67NH_4^+ + HCO_3^-$ $C_3H_5O_3^- + 0.5NO_3^- + 0.5H_2O \rightarrow C_2H_3O_2^- + 0.5NH_4^+ + 2HCO_3^-$	-301	5.44×10^{13}
	Ferrihydrite reduction to magnetite (FHRED)	ΔG_r [kJ mol_{Lac}^{-1}] [a]	Y [cells mol^{-1}] [a]
3	$C_3H_5O_3^- + 10.4Fe(OH)_{3(s)} + 0.6H^+ \rightarrow$ $C_2H_3O_2^- + 3.2Fe_3O_{4(s)} + 0.8Fe^{2+} + 16.4H_2O + HCO_3^-$	-252	4.76×10^{13}

[a]Gibbs free energies and microbial growth yields [cells mol_{Lac}^{-1}], under the initial experimental conditions (Heijnen and Van Dijken, 1992).

[b]Yield coefficients converted from [C-$mol_{biomass}$ mol_{Lac}^{-1}] using an average cell mass of $3.5\cdot10^{12}$ [cells g^{-1}] for *Shewanella* sp. (Yoon et al., 2013; Bonneville et al., 2006; Saltikov et al., 2003) assuming an idealized biomass chemical composition of $C_5H_9O_{2.5}N$.

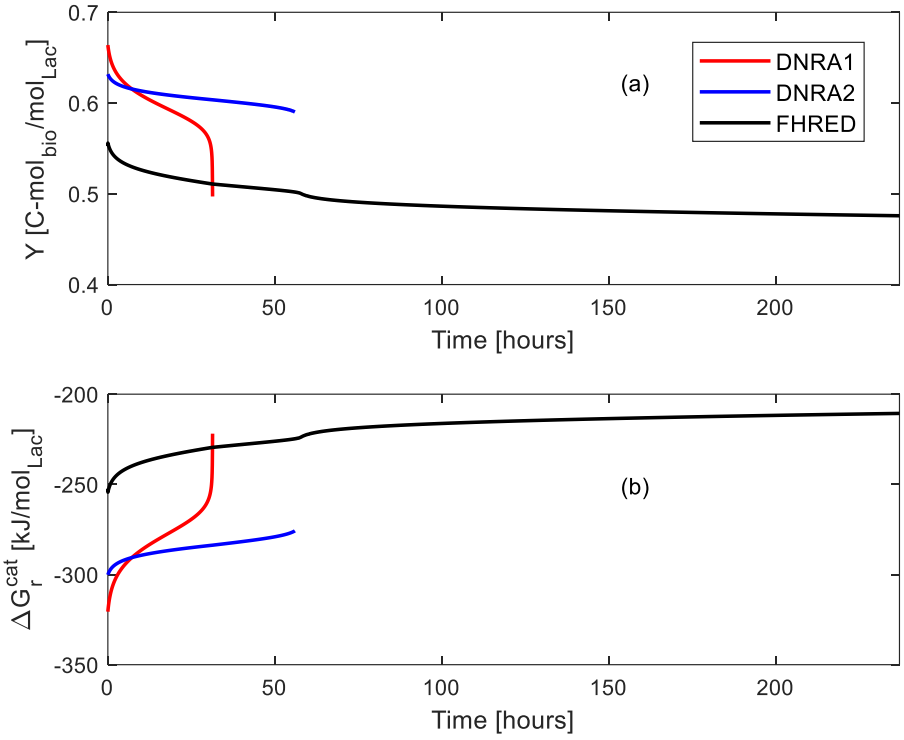

Figure 3-2. Mean dynamic growth yield (a) and Gibbs free energy of the catabolic reaction (b) for both DNRA steps and the reduction of ferrihydrite, FHRED, computed within the top ferrihydrite layer throughout the simulation run.

3.4 Results and discussion

3.4.1 Geochemistry and DRM

The aqueous geochemical data along with fitted DRM trends for the three layers in the column reactors (*i.e.*, the top and bottom FS layers and the middle QS layer) are presented in Figure 3-3. The overall agreement between the model simulations and the experimental results support our conceptual understanding of the reactive system. During the initial 56 hours of the experiment, DNRA dominates: NO_3^- concentrations decrease rapidly within the first 32 hours of the experiment, resulting in the production of NO_2^- which is concurrently consumed as the electron acceptor in the second DNRA step (Figure 3-3d-f). The simulated peak concentration of NO_2^- in all three layers coincides with the complete depletion of NO_3^-, beyond which, according to the DRM simulations, NO_2^- is no longer produced. Continued utilization of NO_2^- then causes its disappearance by t = 56 hours.

Upon the complete consumption of NO_2^-, the detection of aqueous Fe^{2+} followed by its generally increasing concentration provides evidence for iron reduction in both FS layers for the remaining 181 h of the experiment (Figure 3-3g-i). In the two FS layers, FH reduction is accompanied by the further decrease in the lactate concentration and increase in the acetate concentration. By contrast, the concentrations of lactate and acetate in the FH-free QS layer remain nearly constant after cessation of DNRA. The slight increase in aqueous Fe^{2+} in the QS layer is due to diffusion from the FS layers.

Given that the geochemical data were obtained from six successive sacrificial columns, the consistency of the temporal trends in Figure 3-3 imply that the experimental design yielded reproducible reactive geomicrobial systems. Notwithstanding the differences in the measured aqueous concentrations of NO_3^-, NO_2^- and Fe^{2+} between the top and bottom FS layers, lactate consumption was not significantly different between the two layers (regression p-value = 0.017), thus suggesting comparable microbial growth kinetics. The slower conversion of lactate to acetate after t = 56 hours, indicates, as expected, that *S. oneidensis* grows faster when using DNRA as its energy-yielding reaction, relative to dissimilatory FH reduction. The model fit to the data yields maximum specific growth rates with NO_3^- and NO_2^- as terminal electron donors that are 5-6 times higher than with FH. A complete list of the values of the reaction parameters applied in the simulations shown in Figure 3-3 is given in Table 3-2 (see Appendix B for the transport parameter values, Table AB 1).

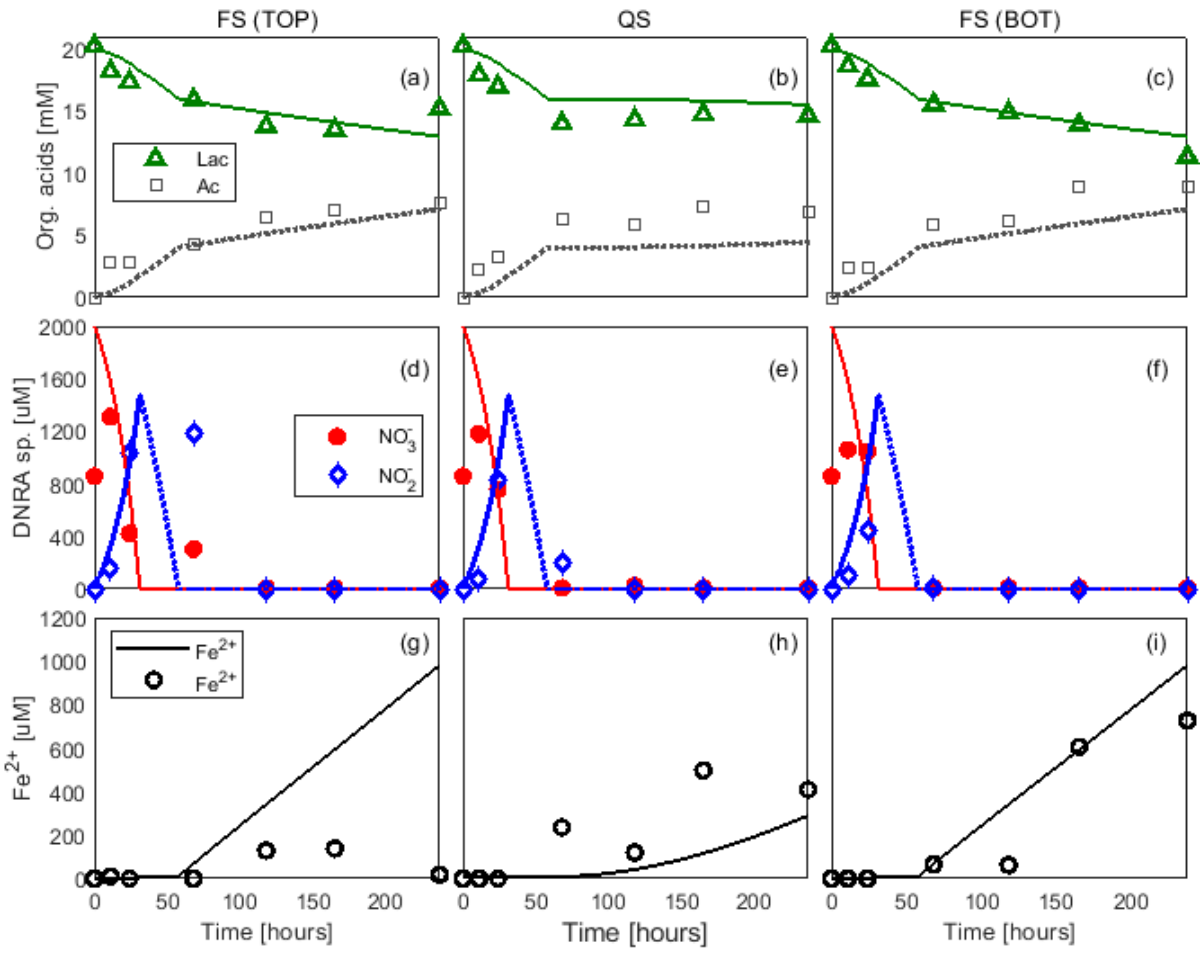

Figure 3-3. Measured pore-water geochemistry from the sacrificially sampled column reactors and corresponding diffusion-reaction model (DRM) fits (equations 3.7 to 3.15). Data points are represented by individual markers and model fits are plotted as solid (lactate, nitrate and ferrous iron) and dashed lines (acetate and nitrite).

Table 3-2. Reaction parameters of the diffusive reactive transport model (DRM) where ED and EA are the electron donor and electron acceptor, respectively.

Parameter	Units	Value		Parameter	Units	Value	
Maximum specific growth rates				*EA Monod and inhibition constants*			
μ_{max}^{D1}	[h^{-1}]	2.5×10^{-2}	[a]	K_{NO_3}	[mol L^{-1}]	2.0×10^{-6}	[c]
μ_{max}^{D2}	[h^{-1}]	2.0×10^{-2}	[a]	K_{NO_2}	[mol L^{-1}]	4.1×10^{-6}	[c]
μ_{max}^{F3}	[h^{-1}]	4.0×10^{-3}	[a]	$K_{Fe(III)}$	[mol L^{-1}]	2.0×10^{-3}	[d]
				$K_{NO_x}^{inh}$	[mol L^{-1}]	1.6×10^{-5}	[b]
ED Monod constants				*Decay and sorption*			
K_{Lac}^{DN}	[mol L^{-1}]	1.0×10^{-3}	[c, d]	k_{DECAY}	[h^{-1}]	2.2×10^{-3}	[a]
K_{Lac}^{F3}	[mol L^{-1}]	5.2×10^{-4}	[e]	K_d	[L kg^{-1}]	0.4	[a]

[a]fitted parameter
estimated from literature ranges:
[b](Watson et al., 2003); [c](Yan et al., 2016); [d](Roden, 2008); [e](Liu et al., 2001)

3.4.2 Biomass growth

The DRM predicts the changes in microbial biomass under the experimental conditions (see equation 3.15). The calculations assume a uniform initial cell density equal to that of the saturating pore solution (1.26×10^7 cells mL_{PM}^{-1}). During the DNRA phase, relatively rapid growth occurs in both the FS and QS layers reaching a maximum cell density of 6.6×10^7 cells mL_{PM}^{-1}. The best fit to the geochemical results was obtained by using a slightly lower maximum specific growth rate (μmax) for the second step in the overall DNRA reaction (see Table 3-2), possibly reflecting a toxic effect of NO_2^- on *S. oneidensis* (Zhang et al., 2013).

Upon complete consumption of NO_2^-, the predicted microbial growth rate slows down in the FS layers, with the biomass increasing up to 8.1×10^7 cells mL_{PM}^{-1} by the end of the experiment. In the absence of an electron acceptor, cellular decay dominates in the QS layer, with the biomass decreasing to a final concentration of 3.9×10^7 cells mL_{PM}^{-1}. The DRM predicted cell densities fall within the ranges estimated from the ATP concentrations measured in the FS and QS layers over the course of the experiment, $1.26 - 8.1\times10^7$ and $0.3 - 7.1\times10^7$ cells mL_{PM}^{-1}, respectively (based on an empirical relationship between ATP and cell density, see Appendix B, Figure AB 1).

3.4.3 SIP responses

SIP phase shift ($-\varphi$) spectra obtained on a saturated layered sand column (*i.e.*, containing FS, QS and FS layers) packed with the microbial growth medium, but without the presence of *S. oneidensis* cells, are presented in Figure 3-4. The measured $-\varphi$ responses for each of the layers are compared to those measured in the biotic (*i.e.*, inoculated with *S. oneidensis*) experimental column. From these abiotic control measurements it is evident that the polarization of both the FH coated and quartz sand layers is negligible in comparison to the measured signals in the biotic experimental column.

The time-dependent (spectral) imaginary conductivities (σ'') measured in the top FS and middle QS layers at selected time-points during the experiment are shown in Figure 3-5. A frequency peak for σ'' appeared approximately 12 hours after starting the experiment. Presumably, this is the time required for equilibration of electrochemical exchange processes affecting the chemistry of the EDL of the cells and sand grains in the freshly packed columns. In the top FS layer, σ'' showed a distinct peak developing between 5 and 10 Hz and increasing in magnitude from 2.3×10^{-4} to a maximum of 5.2×10^{-4} S m^{-1} (Figure 3a). The peak in the FS layer first shifted

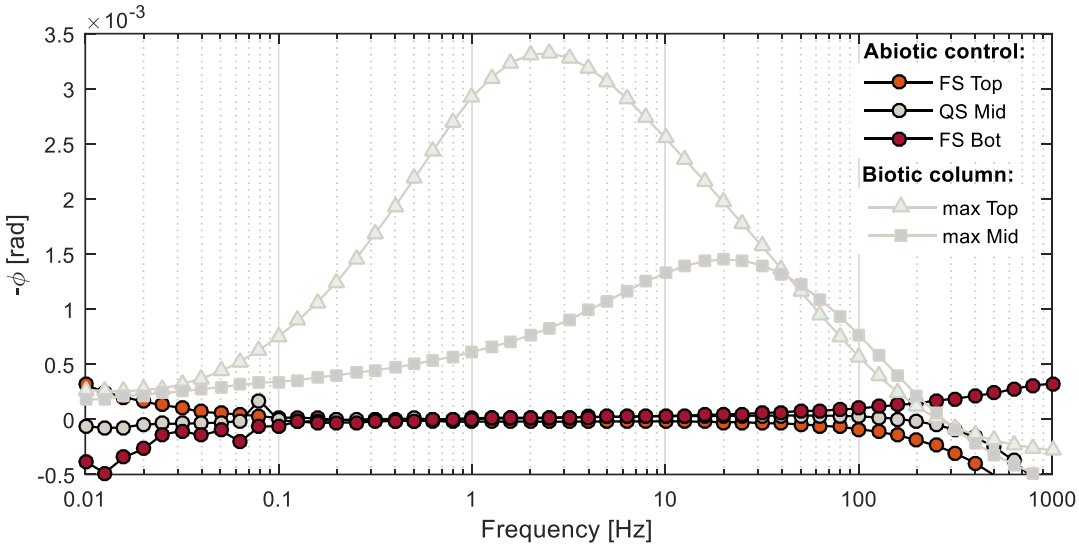

Figure 3-4. Phase shift (-φ) measured in an abiotic (not inoculated with *S. oneidensis*) control column packed with the same layered FS/QS packing arrangement as the biotic experiment using the same microbial growth medium and packed under sterile, anaerobic conditions. The abiotic phase values are compared to the phase shifts measured during the biotic experiment at 162 h.

to lower frequencies with increasing time, followed by a shift to higher frequencies between 124 and 237 hours. A similar peak developed in the QS layer (Figure 3-5b), but at a slightly higher frequency, between 10 and 40 Hz, and only reached a maximum value of 2.7×10^{-4} S m^{-1}. The measured maximum phase shifts in the top FS and QS layers were 3.6 and 1.4 mrad, respectively. The σ'' spectra prior to 72 h in the QS layer did not exhibit a peak and measurable polarization was only detected between 0.01 and 0.1 Hz (Figure 3-5b). We ascribe this to poor contact at the electrode-sand interface, likely due to air entrapment during the packing procedure. Shortly before the 72 h measurement, the potential electrodes in the QS layer were tightened, which improved contact and yielded the σ'' spectra shown Figure 3-5b. The absence of a frequency peak before 72 h in the QS layer is thus believed to reflect a technical issue rather than variations in the EDL.

In the NG control column, the limited carbon source (the cells themselves) would have led to little growth and allocation of all available energy primarily for cell maintenance. This is evidenced in the lower magnitude SIP responses recorded throughout the NG incubation period, summarized in Figure 3-6.

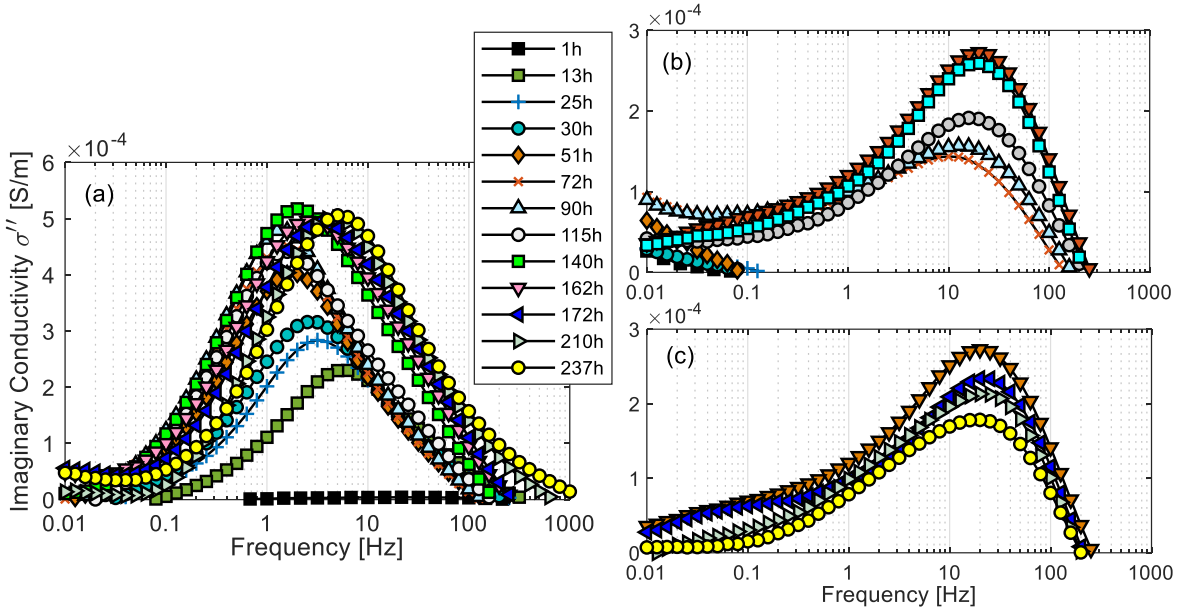

Figure 3-5. Imaginary conductivity (σ'') response between 0.01 and 1000 Hz at selected time points: (a) increase in σ'' and stabilization within the upper iron coated sand (FS) layer; (b) increase in σ'' in the quartz sand (QS) layer during the first 162 hours, and (c) decrease in σ'' in the QS layer beyond 162 hours.

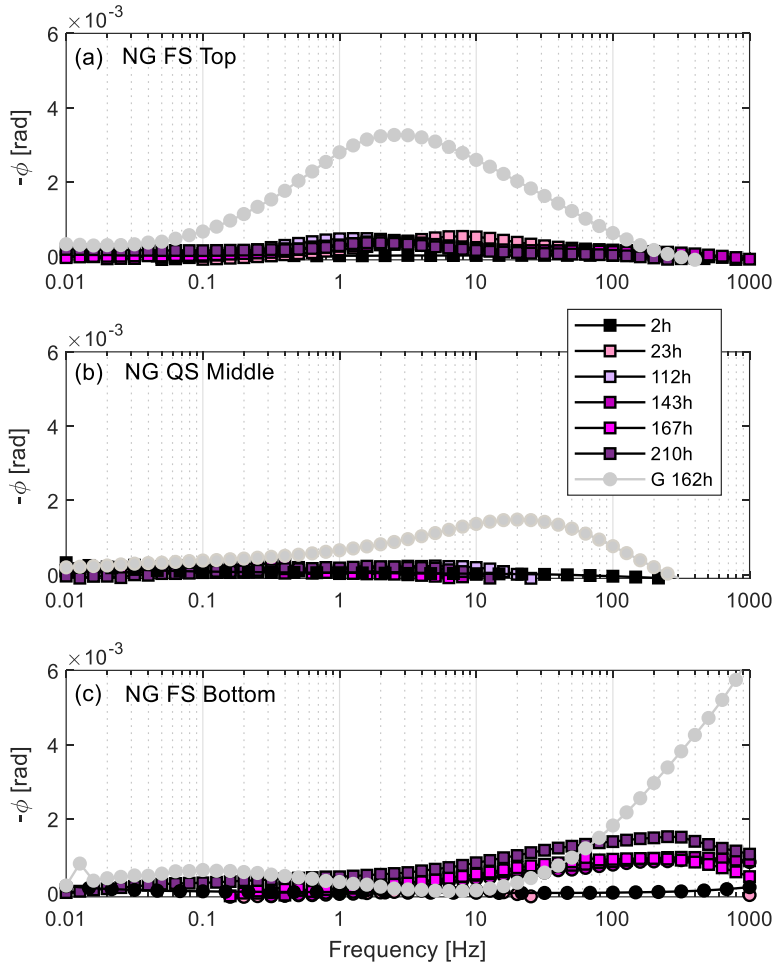

Figure 3-6. Phase shift (-φ) recorded during the 237 h incubation period of the non-growth (NG) treatment, inoculated with *S. oneidensis* without the addition of lactate and NO_3^-. The phase shifts recorded at 162 h in the growth columns are plotted alongside, the measured spectra in the bottom channel of the growth treatment (FS bottom) is also included, these were the data omitted from the coupled analysis of the SIP data and reactive transport model.

Measured maximum phase shift ($-\varphi$) and impedance magnitude (Z) data for all SIP channels in both the growth and non-growth (NG) treatments (NG treatment is discussed below) are presented in Figure 3-7. No distinct spectral $-\varphi$ peak was measured in the bottom layer of the growth treatment (Figure 3-7a), and therefore, σ'' spectral response in the bottom FS layer did not exhibit a distinct peak. The measured impedance is different between layers (Figure 3-7b), with the lowest Z recorded in the bottom channel and sequentially increasing from the middle QS layer to the top FS layer. The impedance in the NG control treatment also exhibits variations between the layers, with the same trend as the growth column, highest impedance at the top FS layer and lowest at the bottom FS layer (Figure 3-7d). These measured variations in impedance recorded in both growth and NG columns were also measured in columns packed with the same porous media layering, but using de-ionized (DI) water (EC = 0.8×10^{-3} S m^{-1}) and tap water (EC = 0.07 S m^{-1}) as the saturating pore water (Figure 3-8a and b, respectively).

The variations in measured impedance appear to be systematic across analogously packed columns. We attribute these variations to the column packing procedure and the FH-coating itself (Müller et al., 2008). The ferrihydrite coating is composed of mineral particles with a heterogeneous size distribution. Small iron oxide particles may be released from the FH-coated sand during packing and settle at the bottom of the column. Together with the higher solubility of very small iron oxide particles, this could result in an increase in pore water conductivity (σ_w) and, consequently, explain the lower impedance measured in the bottom channel (Atekwana et al., 2004). Elevated σ_w can also affect the phase response resulting in a drop in σ'' (Slater and Glaser, 2003). We speculate that elevated σ_w, stemming from iron oxide nanoparticle sedimentation, coupled with possible nanoparticle attachment onto negatively charged cells (Sokolov et al., 2001), both contributed to the absence of a frequency peak in $-\varphi$ for the bottom FS channel. Hence, the SIP data from the bottom FS layer are omitted from the biogeochemical discussion herein.

The production of dissolved ionic species from both DNRA and reductive dissolution of the FH coating could potentially affect the EDL polarization of both the sand grains and bacteria. The production of about 2 mM NH_4^+ by DNRA likely had little impact on the electrochemical polarization of the Stern layer because of the already high porewater concentration of NH_4^+ (18 mM), and the fact that monovalent cations remain hydrated and tend to form mobile outer sphere complexes at solid surfaces (Vaudelet et al., 2011b). In contrast, Fe^{2+} more strongly adsorbs, forming inner sphere complexes at the cell membrane and sand grain surfaces, resulting in a

reduction of ion mobility in the EDL and a potential dampening of polarization (Vaudelet et al., 2011b; Vaudelet et al., 2011a). Nonetheless, the effect of Fe^{2+} production on the measured temporal dynamics of σ'' is not considered to be very strong, as evidenced by the relaxation time dynamics discussed in the next section.

The different spectral locations of the σ'' peaks in the FS and QS layers likely reflect the presence or absence of the FH coating, due to the possible contribution of membrane polarization to the measured spectra. Additionally, the shift in peak frequency observed in the FS layer (but not observed in the QS layer, Figure 3-5b and c) may be due to changes in EDL properties of the iron coating, for example, as a result of cell attachment and, following the end of DNRA, sorption of Fe^{2+} and the formation of a reduced precipitate, tentatively identified as magnetite. Because these effects are absent from the QS layer, the corresponding changes in the σ'' spectra should be more uniquely related to biomass changes (Placencia-Gómez et al., 2015). The spectra recorded in the QS layer fall in the same spectral range as those previously reported for cell suspensions and cell-sand mixtures of *Zymomonas mobilis*, whose SIP responses were attributed to the polarization of the bacterial cells (Zhang et al., 2014). Thus, overall, the measured SIP responses appear to be sensitive to the abundance and surface electrical properties of the cells, even at the relative low cell densities used in the experiment (Griebler et al., 2002).

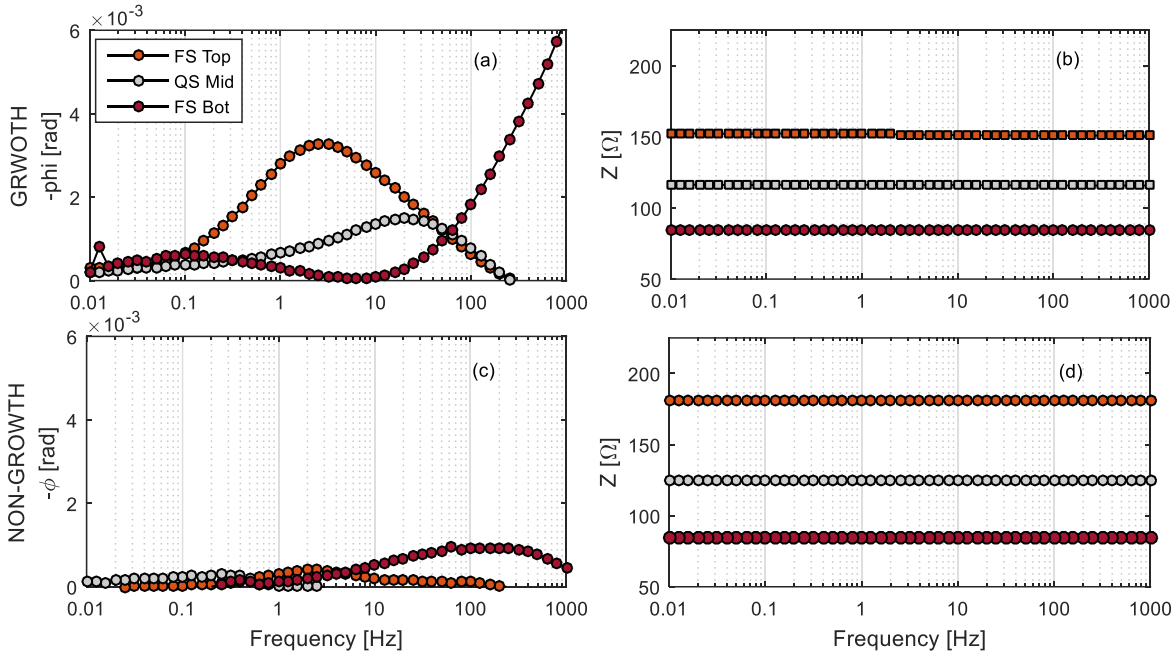

Figure 3-7. Comparison of SIP response (*i.e.*, measured phase shift and impedance magnitude) in growth and non-growth (NG) treatments, upper and lower plots respectively. The data shown are for 162 and 167 hours for the growth and NG treatments, respectively.

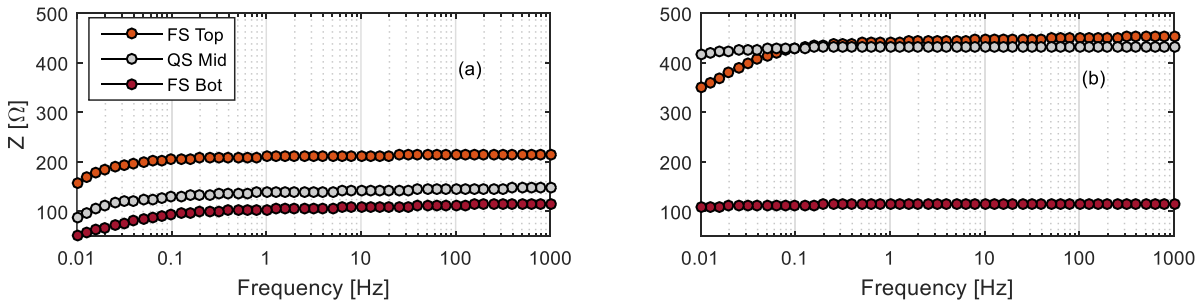

Figure 3-8. Measured impedance magnitude in layered columns saturated with tap water (a), σ_w = 0.07 S m^{-1} and deionized water (b), $\sigma_w = 0.8\times10^{-3}$ S m^{-1}.

3.4.4 Linking SIP and biogeochemistry

The dependence of the SIP signals on changes in the microbial biomass are supported by comparing the temporal trends in the peak values of σ'' and the cell densities predicted by the DRM (Figure 3-9). For the FS layer, the σ'' peak values capture the sharp decrease in net biomass growth that accompanies the transition from DNRA to dissimilatory iron reduction. In the QS layer, however, the trend of the σ'' peak value lags behind the predicted cell density curve. We attribute the initial lag in electrode response before 72 h to poor contact as discussed in the previous section. The lag between 72 and 118 h, possibly stems from low point of zero charge of pure quartz (pH_{pzc} = 3.0) (Sverjensky, 1994) creating a less favorable environment for attachment of the negatively charged cells, than the FH coated sand (pH_{pzc} = 8.0 for pure FH) (Schwertmann and Fechter, 1982), thus hindering the build-up of stationary chargeable surfaces. This hypothesis is consistent with Abdel Aal et al. (2009) who measured higher levels of bacterial adsorption and increasing σ'' as a function of the increasing fraction of iron-oxide coated sand. Nonetheless, in contrast to the FS layer, the peak σ'' value in the QS layer decreases during the second half of the experiment, consistent with the predicted biomass decay following the exhaustion of all external terminal electron acceptors.

The maximum σ'' peak value reached in the QS layer is about half that in the FS layer (Figure 3-9). A higher chargeability in the FS layer is expected because of the additional polarization associated with the presence of the FH coating (Slater et al., 2007). Higher pore water conductivity in the middle QS layer likely also contributed to reduce σ'' in the QS layer (Slater and Glaser, 2003). The results therefore highlight that the relationship between SIP and microbial abundance is non-unique and depends on the nature of the matrix. This obviously complicates the interpretation of SIP signals in natural porous media.

The fitted relaxation times (τ) extracted from the Cole-Cole model fits (Weigand and Kemna, 2016c) (refer to Appendix B, Figure AB 2, for an example of goodness-of-fit) show systematic changes over time (Figure 3-10c and d). Normalized chargeability (m_n) values were also extracted and are presented in Appendix B, for the top FS layer. Trends in m_n are analogous to those measured for peak σ'' and are therefore not further discussed. In both the FS and QS layers, the highest τ values occurred towards the end of the DNRA phase. Subsequently, τ values in the QS layer dropped abruptly, while they decreased more slowly in the FS layer. Given that τ is related to the length-scale over which ionic back-diffusion takes place after current is applied (equations

3.3), several processes could explain the observed τ trends. If the observed SIP spectra mainly result from the polarization of the microbial cells (Zhang et al., 2014), then the temporal changes of τ could be due to changes in cell size, where cells become smaller during periods of energetic stress (Mellage et al., 2015) as they consume internal energy reserves (Lever et al., 2015; Lennon and Jones, 2011). In other words, the τ trends could reflect the variable energetic conditions in the FS and QS layers. The most favorable catabolic reaction (i.e., DNRA) would result in cells growing larger, while the cells would shrink slowly under the less favorable iron reducing conditions and more rapidly in the absence of external electron acceptors (Riedel et al., 2013).

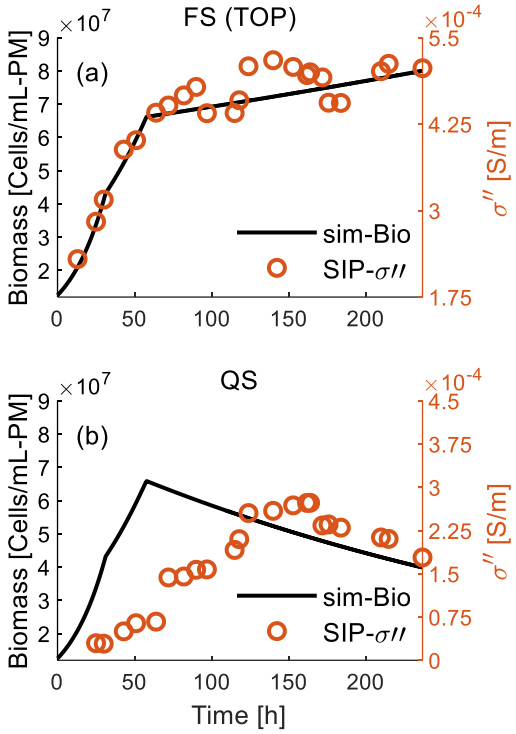

Figure 3-9. Comparison of the temporal trends of the diffusion-reaction model (DRM) simulated abundance of *Shewanella oneidensis* and the measured peak SIP-imaginary conductivity in the upper iron coated sand (FS) layer (a) and quartz sand (QS) layer (b). The right-hand axis scale varies between the plots due the difference in the magnitude of the peak σ'' values between the layers. The scale was adjusted to highlight the similarities between the cell density and σ'' trends.

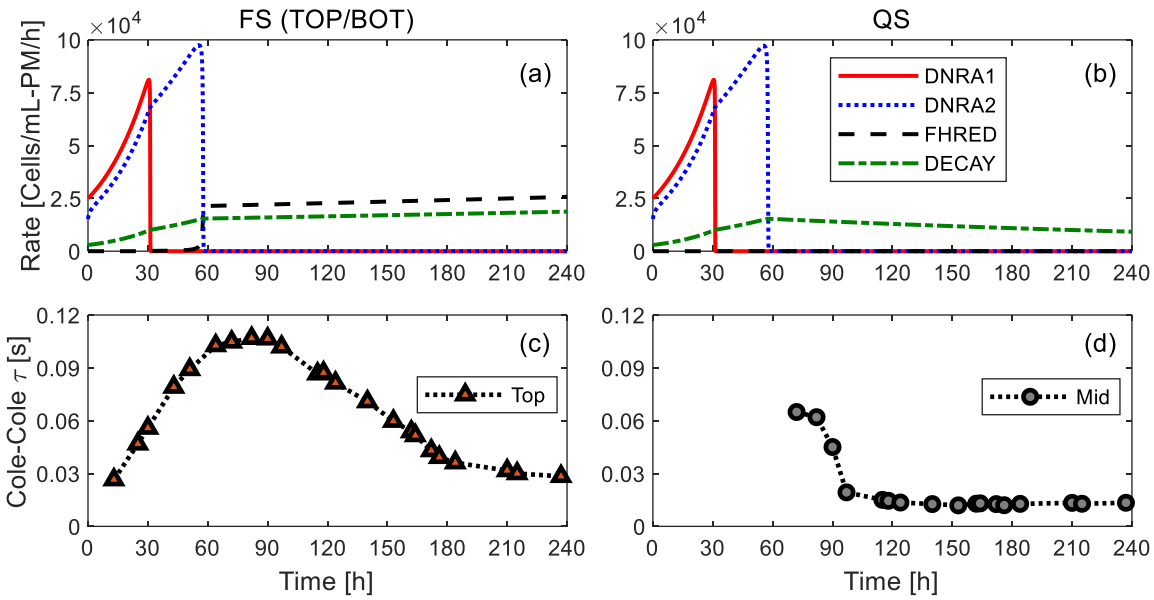

Figure 3-10. Temporal changes in diffusion-reaction model (DRM) predicted reaction rates (a and b) and SIP-derived relaxation times (c and d); DNRA1 and 2 are the two consecutive steps in dissimilatory nitrate reduction to ammonium; FHRED is the rate of ferrihydrite (FH) reduction and DECAY is the first-order cellular decay rate. The plots on the left are for the upper iron coated sand (FS) layer, those on the right for the QS layer. The omission of relaxation time data before 70 hours in the quartz sand (QS) layer is due to the late appearance of a spectral peak in the SIP responses, related to electrode contact issues discussed in the text, which yields Cole-Cole fits that are dependent on the initial conditions.

Without any direct experimental evidence to confirm changes in cell size we acknowledge that other factors may contribute to variations in Cole-Cole parameters including, for example, surface complexation of divalent cations (in particular Fe^{2+}, which would have resulted in an increase in τ, the opposite of what is observed and therefore not likely a major driver of the temporal trends of τ) (Vaudelet et al., 2011b; Vaudelet et al., 2011a), mineral transformations (Personna et al., 2008; Slater et al., 2007), plus changes in the morphology (Lever et al., 2015; Lennon and Jones, 2011), chargeability (Revil et al., 2012) and other EDL properties of the cells (Soni et al., 2008).

The range in relaxation times obtained here (0.012 – 0.1068 s) corresponds to effective polarization diameters between 1.04 and 3.1 µm, using equation 3.3 together with the model of Revil et al. (2012) for the polarization of a typical bacterial cell (which yields D_s = 11.2 $\mu m^2\ s^{-1}$). Estimates of diffusion coefficients of ion mobility in the Stern layer remain uncertain (Weller et al., 2016). Weller et al. (2016) highlight the large variations in surface diffusion coefficients among different sandstones and postulate that d, the length scale defined by τ in equation 3.3, is not only a function of particle size, but also particle surface characteristics and the mineral composition of a given sample. For bacterial cells, cell surface chemistry along with cell size controls D_s. Both of these properties are temporally dynamic and we acknowledge that the value for D_s is likely quite variable. Nevertheless, the available D_s estimate for bacterial cells yields dimensions that fall within the range of typical cell diameters or lengths in the case of rod-shaped bacteria such as *S. oneidensis* (Lee et al., 2016), but are orders of magnitude smaller than the smallest sand grains (150 µm), ruling out a major control associated with electrochemical polarization at the sand-grain scale. The magnitude of the relaxation time, together with the evidence discussed earlier, thus strongly suggest that polarization of the cells largely controls the observed SIP responses, even in the presence of the iron coating in the FS layer.

In their study of microbially mediated iron sulfide mineral transformations, Slater et al. (2007) derived τ values between 0.2 and 0.4 s, that is, values at the upper end of our range. They further calculated effective polarization diameters that were much larger than the FeS encrusted cells observed in their study. Their calculation, however, was based on a surface ionic diffusion coefficient for sands (D_s = 3000 $\mu m^2\ s^{-1}$) (Tarasov and Titov, 2007). If, instead, the D_s value for bacterial cells proposed by Revil et al. (2012) is used (D_s = 11.2 $\mu m^2\ s^{-1}$), then the effective polarization diameter is on the order of 4 – 6 µm, which agrees well with the size of the FeS

encrusted cells. Thus, we speculate that in the study of Slater et al. (2007) SIP signals were also controlled by polarization processes acting at the cellular scale, rather than at the grain or pore space scales.

In summary, the SIP signatures obtained in the sand columns record changes in the density, size and surface charging properties of the bacterial cells, even at relative low cell densities ($\leq 10^8$ cells mL^{-1}), such as those found in subsurface environments, and in the presence of polarizable mineral surfaces. While our results are encouraging, the acquisition of SIP data that can reliably detect variations in phase shifts in the range reported here is not yet feasible at the field scale. However, our results provide new insights into the mechanisms controlling measured polarization responses. Hence, they help posit SIP as a non-invasive method for monitoring microbial activity in bench-scale reactive transport studies, and they highlight the need to improve the sensitivity of SIP measurements as a necessary condition for its use in field applications.

4 Bacterial Stern-layer diffusion: Experimental determination with spectral induced polarization (SIP) and sensitivity to nitrite toxicity

This chapter is modified from:

Mellage, A., Smeaton, C.M., Furman, A., Atekwana, E.A., Rezanezhad, F. and Van Cappellen, P. (submitted). Bacterial Stern-layer diffusion: Experimental determination with spectral induced polarization (SIP) and sensitivity to nitrite toxicity. *Geophysical Journal International*. GJI-S-18-1031L.

4.1 Summary

Spectral induced polarization (SIP) signatures have been used as proxies for microbial abundance in subsurface environments, by taking advantage of the charged properties of microbial cell membranes. However, SIP's adoption as a geo-microbiological tool requires robust biomass density-SIP relationships, and a detailed understanding of the nature of the cell membrane surface charge dynamics. We present results from a fully saturated sand-filled column reactor experiment where *Shewanella oneidensis* growth on nitrate reduction to ammonium (DNRA) was monitored using SIP. While our results further confirm the direct dependence of imaginary conductivity on changing cell density, Cole-Cole derived relaxation times also record the changing surface charging properties of the cells, ascribed to toxic stress due to nitrite accumulation. Concurrent estimates of cell size yield the first measurement-derived estimation of the apparent surface ion diffusion coefficient for cells (D_s = 5.4 ±1.3 μm^2 s^{-1}), strengthening the link between SIP and electrochemical cell polarization.

4.2 Introduction

Functional groups on bacterial cell membranes (Claessens et al., 2004; Sokolov et al., 2001; Cox et al., 1999), result in the development of a net negative surface charge at near-neutral pH, for both gram-positive and gram-negative bacteria (Revil et al., 2012). Because of this surface charge, bacteria in contact with water are surrounded by an electrical double layer (EDL) (Zhang et al., 2014). Spectral induced polarization (SIP) is an active geophysical method that measures electric conduction and charge storage, based on the difference in properties between injected and detected waveforms (see Kemna et al. (2012) for method details). Below 100 Hz, electrochemical polarization (*i.e.*, the tangential migration of counterions when current is applied) within the EDL of particles is responsible for the bulk of charge storage (Vaudelet et al., 2011b; Revil and Florsch, 2010).

Imaginary conductivity (σ''), the charge storage component of SIP, has been shown to exhibit a dependence on microbial abundance (Davis et al., 2006). Using suspensions of *Z. mobilis*, Zhang et al. (2014) showed the dependence of σ'' on variable cell concentrations. These authors proposed a linear-relationship between cell density and σ'', based on measurements performed at three cell concentrations. Mellage et al. (2018) showed that time series σ'' peak values parallel the microbial growth and decay dynamics in an *S. oneidensis* inoculated column experiment. These authors

introduced a conceptual model in which charge storage is governed by the cell EDL, and where the time scale for ion back-diffusion, as measured by Cole-Cole relaxation time, τ, is a function of cell size and surface charging properties of the cells. However, the potential for monitoring microbial dynamics in bench-scale laboratory experiments with SIP, without the need for destructive sampling, necessitates the development of quantitative relationships to derive cell densities from electrical signals in porous media.

This chapter builds on the work of Mellage et al. (2018) and proposes a quantitative relationship between cell density and σ'' for *Shewanella oneidensis* in microbial growth quartz sand column incubations. Our analysis further sheds light on the mechanisms driving the observed relaxation time dynamics as a result of changes in microbial abundance and activity. Moreover, cell size measurements coupled to a model of charge relaxation of the EDL (Schwarz, 1962) are used to estimate the surface ion diffusion rates of polarizing cells. Our analysis further shows that relaxation time anomalies are linked to changes in microbial physiological state, here likely induced by nitrite (NO_2^-) toxicity.

4.3 Materials and Methods

4.3.1 Flow-through reactors

The experiment was run in ten identical high density polyethylene (HDPE) column reactors with an inner diameter of 4.1 cm, length of 15.8 cm (Figure 4-1), fitted with four lateral ports, allowing pore water and bulk sand sampling and, in the two columns fitted for SIP measurements (herein referred to as G1 and G2), electrode emplacement. In the eight (out of ten) replicates not fitted with SIP electrodes, ports were sealed with NPT compression fittings. Prior to column assembly, all experimental components, including the sand, were sterilized as described in Mellage et al. (2018).

Columns were wet-packed to a porosity of 40% (determined from a tracer breakthrough curve, see Appendix C, Figure AC 1) in an anaerobic chamber (Coy®, < 1ppmv O_2 in N_2 with 3% H_2) with sterile quartz sand (U.S. Silica®, F-45, grain size range: 0.15 – 0.42 mm). A microbial growth medium containing 10 mM lactate, 1.5 mM nitrate (NO_3^-) and 0.4 mM ammonium (NH_4^+) was used as the saturating pore solution and the inflow solution during injections (see Mellage et al. (2018)). An overnight aerobic culture of *Shewanella oneidensis* MR1 was grown in Luria Bertani (LB) medium, harvested via centrifugation, and inoculated into the growth medium. The

growth medium was then used as the saturating pore solution to wet pack the columns yielding a starting cell density of 8.3×10^4 cells mL_{PM}^{-1}. The columns were incubated for a total of 315 hours, following the first substrate injection (see details below).

Reactors were sealed with HDPE screw end-caps at either end, fitted with inflow and outflow channels at the bottom and top, respectively. Two filter membranes were placed at each end (0.2 µm polypropylene and 5 µm glass), to promote laminar flow conditions, and minimize the loss of bacteria from the flow-through reactor system. Viton tubing (1/16″ i.d.; 1/8″ o.d.; 1/32″ wall, Cole-Parmer Instrument Company, Vernon Hills, IL, USA) was used to connect the columns to a peristaltic pump (Minipuls 3; Gilson, Middleton, WI, USA) for flow injection (Figure 4-1).

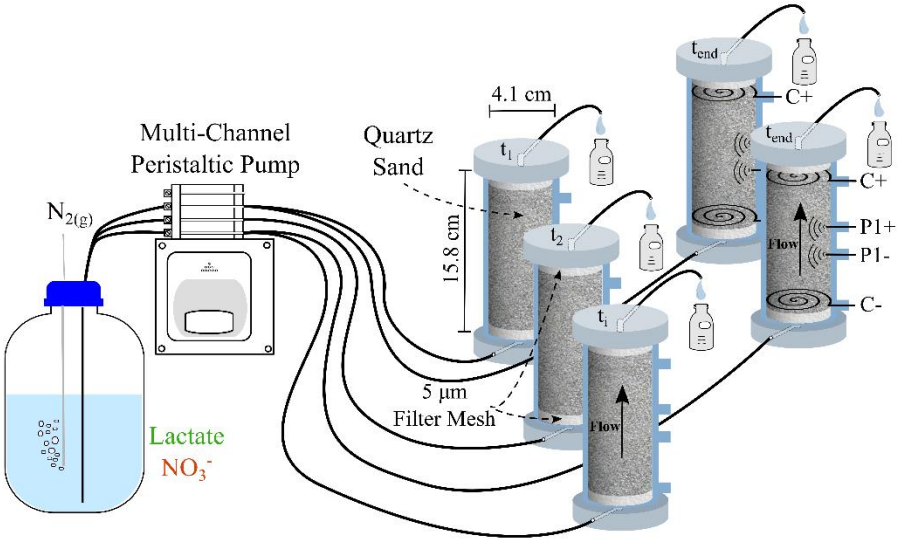

Figure 4-1. Schematic of the flow-through reactor setup. The experiment consisted of 10 columns, 2 of which were fitted with the electrode array for SIP measurements. The other 8 columns were sacrificially sampled at specific times during the experiment. The two SIP columns were sampled at the end of the experiment.

4.3.2 Microbial activity

Injections of lactate and NO_3^- were aimed to mimic the experimental conditions in Mellage et al. (2018) and stimulate growth of *S. oneidensis*. During dissimilatory nitrate reduction to ammonium (DNRA), *S. oneidensis* oxidizes lactate to produce acetate, and NO_3^- is reduced to NH_4^+ via NO_2^- (Zhang et al., 2013; Gao et al., 2009b):

$$C_3H_5O_3^- + 2NO_3^- \rightarrow C_2H_3O_2^- + 2NO_2^- + HCO_3^- + H^+ \quad 4.1$$

$$C_3H_5O_3^- + 0.67NO_2^- + 0.67H_2O + 0.33H^+ \rightarrow C_2H_3O_2^- + 0.67NH_4^+ + HCO_3^- \quad 4.2$$

NO_2^-, the intermediate product, is toxic to *S. oneidensis* at concentrations higher than 1 mM (Zhang et al., 2013), and can inhibit both DNRA and biomass growth (Sijbesma et al., 1996). Conceptually, NO_3^- and lactate replenishment via two 12-hour injections supplies both energy and a carbon source and should result in growth, thereby resulting in higher σ'' magnitudes. However, the potential accumulation of NO_2^-, in excess of 1 mM, potentially inhibits microbial growth.

Following an initial no-flow pre-equilibration phase, inflow solution containing both lactate and NO_3^- was injected (t_0) for 12 hours at an average flow rate of 8.9 ($\pm$1.0) mL h^{-1}, herein referred to as phase I. Inflow solution injection replaced the pore water in the columns and replenished the electron acceptor (NO_3^-) and electron donor/carbon source (lactate). Flow injection lasted for the minimum time-interval required to completely replace the pore volume of the columns (*i.e.*, 12 hours), as confirmed by the chloride breakthrough tracer curve, see Appendix C, Figure AC 1. After 12 hours, flow was stopped, the columns were sealed and incubated under no-flow conditions for 155 hours, hereafter referred to as phase II. A second 12 hour injection (*i.e.*, phase III) occurred at 167 hours at an average flow rate of 9.3 ($\pm$0.5) mL h^{-1}. Following the second injection, the columns were incubated for 136 hours under no-flow conditions (phase IV).

4.3.3 Pore water and bulk sand sampling and analysis

The first replicate column was sacrificially sampled prior to phase I, at t_0, followed by sequential sampling of the other columns at selected time points. Pore water samples (1 mL) were collected using ceramic samplers, 5 cm in length and 2.5 mm in diameter with a filter pore-size of 0.15 µm (CSS5 MicroRhizon™ samplers, Ejikelamp, Netherlands, #19.21.23F). Samples were analyzed for lactate, acetate and NO_3^- using ion chromatography (Dionex ICS-5000, IonPac® AS18 column), and NO_2^- and NH_4^+ were analyzed using microplate-based colorimetric methods (FlexStation 3, Molecular Devices, San Jose, CA, USA) (Ringuet et al., 2011a).

To remove biomass from the sand for cell counting with flow cytometry, bulk sand samples (approximately 2 g) were collected from the ports at the center of the columns (see Figure 4-1) with a mini-auger, weighed, treated with 10 mL of a 10 mM Tris-HCl, 1 mM EDTA buffer solution (Tris-EDTA pH = 7.4; Sigma-Aldrich, MilliporeSigma Canada Co., Oakville, ON, Canada) containing 0.1% IGEPAL (IGEPAL CA-630, Sigma-Aldrich), and sonicated for 10 minutes (Neal et al., 2003). Adenosine triphosphate (ATP) content was determined through luminescence measurements using a cell viability assay kit (BacTiter-GloTM Microbial Cell Viability Assay). Enumeration and size estimation (Flow cytometry size calibration kit, F-13838, Thermofisher; see flow cytometry size calibration in Appendix C, Figure AC 2) of total, unfixed cells was performed on a FACSaria^{TM} Fusion flow cytometer (BD Biosciences).

4.3.4 Spectral Induced Polarization (SIP) measurements

Two of the ten columns were fitted with non-polarizing, electrolyte-filled (1M KCl, 15 g L^{-1} agar gel), Ag-AgCl potential electrodes encased in nylon 1/2" NPT compression fittings, and Ag-AgCl current coil-electrodes (Figure 4-1). Potential electrodes were placed in the center of the columns (2.5 cm apart), current electrodes were placed 4 cm from each potential electrode at either end of the column. A Portable Spectral Induced Polarization (PSIP) unit (Ontash & Ermac Inc., NJ, USA) was used to measure phase shift ($-\varphi$) and conductivity magnitude ($|\sigma|$) over 51 log frequency steps between 0.01 and 1000 Hz.

The Cole-Cole relaxation model (Pelton et al., 1978) was fitted to measured SIP spectra (Weigand and Kemna, 2016b; a), to extract relaxation times, τ [s]:

$$\sigma^*(\omega) = \sigma_0 \left[1 + m\left(\frac{(i\omega\tau)^c}{1 + (i\omega\tau)^c(1-m)}\right)\right] \quad 4.3$$

where the σ_0 [S m^{-1}] is the direct current conductivity, m [-] is the chargeability, τ [s] is the relaxation time, ω [rad s^{-1}] is the angular frequency and c [-] is a constant describing the shape of the observed phase dispersion. As postulated by Mellage et al. (2018), for signals dominated by electrochemical polarization of bacteria τ is a relative measure of the time for polarization and ion back-diffusion as calculated by (Schwarz, 1962):

$$\tau = \frac{d^2}{8D_s} \quad 4.4$$

Equation 4.4 implies that both the size of the polarizing bacteria (*i.e.*, the effective diameter, d) and their surface charging properties (*i.e.*, the surface diffusion coefficient, D_s), control the magnitude of τ.

4.4 Results and Discussion

4.4.1 SIP: spectral response

Spectral σ'' responses for selected time points following the first and second injections are presented in Figure 4-2. In the interest of conciseness, only the spectral results from SIP column G2 are presented (temporal trends in peak-σ'' for G1 are presented in Appendix C along with a baseline comparison for spectra prior to, and shortly after, injection for both SIP columns, see Figure AC 3 and Figure AC 4). Trends in the second SIP column were similar during the first injection, but diverged during the second injection. This divergence between the columns was also observed in the measured cell density, suggesting that the microbial community underwent faster decay, in column G1. The inter-column discrepancies are discussed in Appendix C, in the "SIP-columns" section.

Following injections, σ'' decreased due to a flow-induced loss of cells, despite the presence of a filter membrane (pore size: 0.2 μm) at the outflow. This was substantiated by measurements of cell counts in outflow samples on the order of $1(\pm 0.27)\times 10^4$ cells mL^{-1}, 2 hours after injection started, during both injection periods. Following the initial drop, σ'' increased and the spectra developed a distinct frequency peak between 4 and 8 Hz (Figure 4-2a). Maximum σ'' (2.23×10^{-5} S m^{-1}) was reached following the second injection at 191 hours (Figure 4-2b). The response decreased in magnitude by a factor of 2 during a 4 hour period, with an abrupt change in the location of the frequency peak from 4 to 0.2 Hz (195 hours in Figure 4-2b). After the drop in response, σ'' began to recover and the peak shifted back to higher frequencies.

4.4.2 Temporal trends: geochemistry

Time-series measurements of aqueous DNRA reactants and products, normalized peak-σ'' (for both SIP columns), τ for each SIP measurement (G2), and cell counts and size are presented in Figure 4-3. Lactate and acetate concentrations are presented in Appendix C (Figure AC 5).

The different starting conditions, as a result of the preceding period (*i.e.*, pre-equilibration phase vs. following injection), resulted in slight variations in reaction kinetics between phases II

and IV. Most notably, DNRA kinetics were slower after phase III than after phase I (Figure 4-3a and b). At the end of phase I, the measured NO_3^- concentration was 0.24 mM implying that 84% of NO_3^- was reduced during phase I, while NO_2^- accumulated up to a value of 1.32 mM (Figure 4-3b). Conversely, at the end of phase III, NO_3^- accumulated to 1.34 mM (Figure 4-3a), which translates to only 10% consumption, and NO_2^- rose to 0.25 mM (Figure 4-3b). At 195 hours, 28 hours after the onset of phase III, NO_2^- had increased further to 0.65 mM, and NO_3^- had dropped to 0.22 mM, suggesting that DNRA was still taking place. Depletion of both NO_3^- and NO_2^- was measured at 221 hours. During both phases I and III, NH_4^+ decreased to values close to the inflow concentration (0.4 mM), and increased during phases II and IV with the progression of DNRA to reach a maximum value of 1.54 and 1.6 mM, respectively.

Differences in DNRA kinetics can, in part, be a function of the activity of the bacteria, where despite the higher cell density and σ'', the number of active cells may have been lower during phase III. This is supported by the lower ATP concentrations (presented in Appendix C, Figure AC 6), a proxy for microbial activity (Bastida et al., 2008), measured during phases III and IV.

The observed maximum NH_4^+ concentrations did not reach the expected value after complete DNRA, which would have been 1.9 mM (sum of NH_4^+ present in the media and produced by DNRA). About 0.05 mM of NH_4^+ would have been used by the bacteria as a nitrogen source to build microbial biomass (Russell and Cook, 1995), estimated from the amount of biomass growth measured here, assuming an idealized biomass chemical composition of $C_5H_9O_{2.5}N$. The missing ~0.25 mM of NH_4^+ were likely bound in outer-sphere complexes at negatively charged sites on both the sand and cell membranes (Revil et al., 2012; Ceazan et al., 1989).

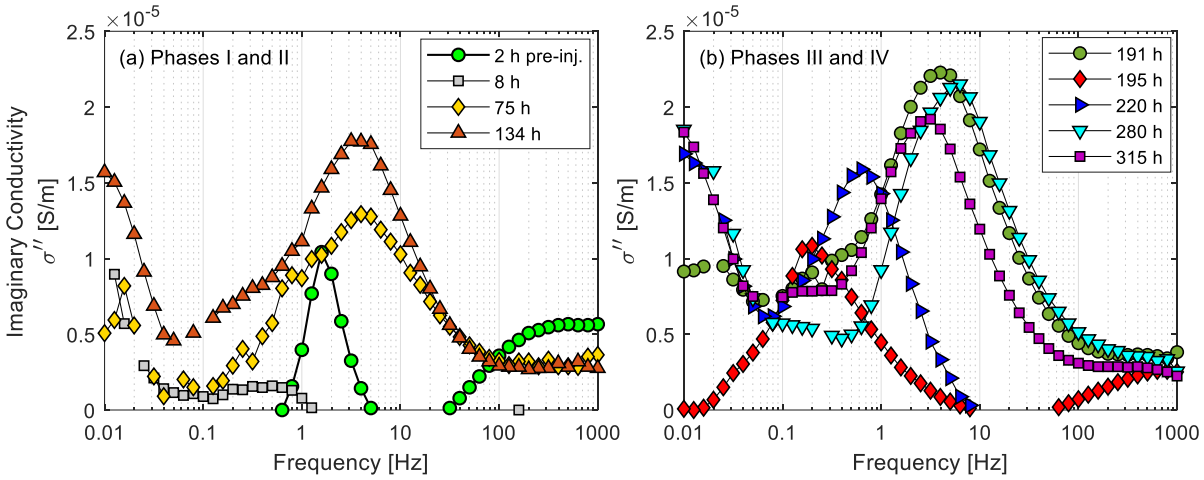

Figure 4-2. Spectral imaginary conductivity (σ'') results for selected time points before lactate and NO_3^- injection and following the first (a) and second injections (b), in SIP-column G2.

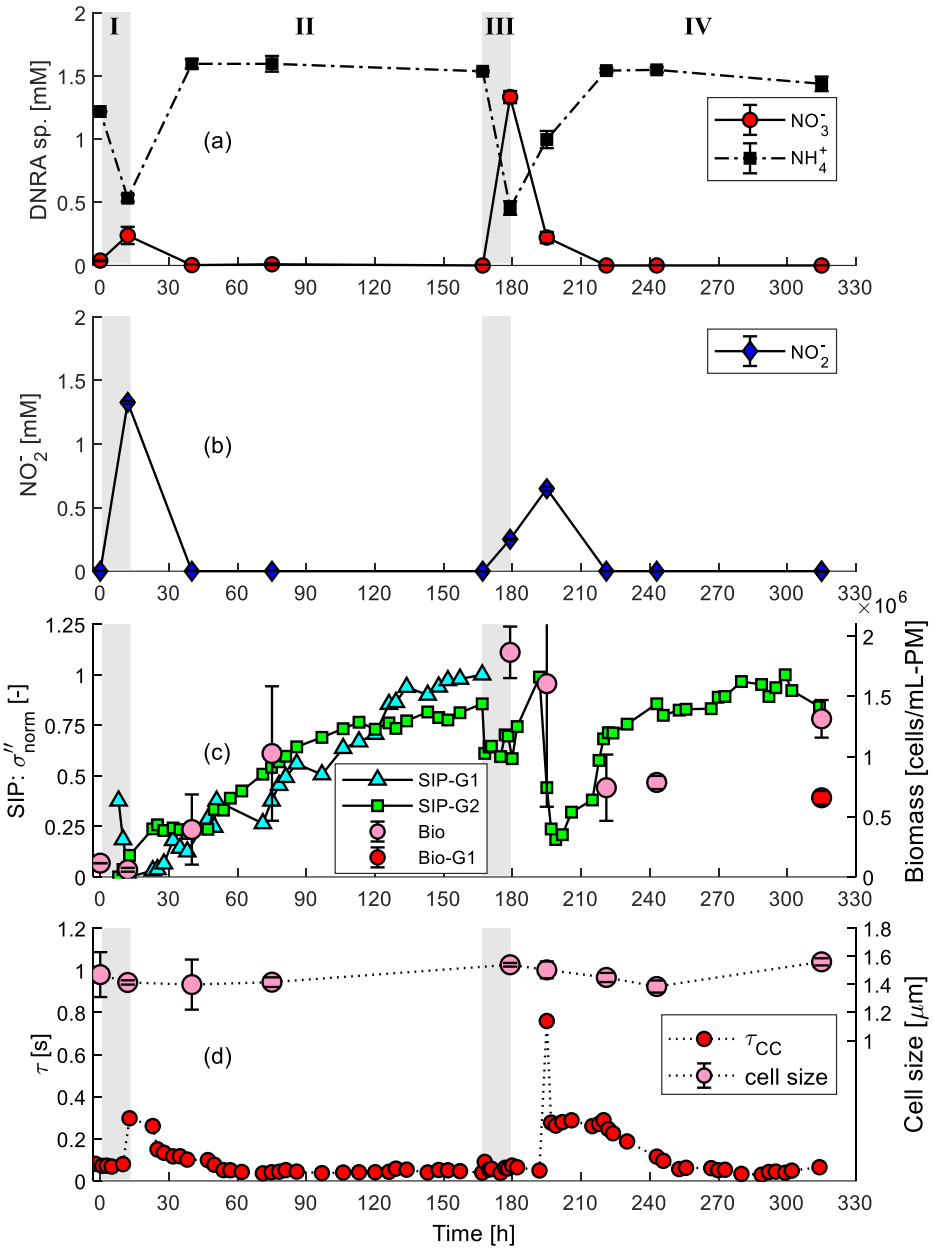

Figure 4-3. DNRA species (NO_3^- and NH_4^+ (a), NO_2^- (b)) in each of the sacrificially sampled columns from the onset of lactate and NO_3^- injection. Biomass cell counts are compared to normalized imaginary conductivity (σ'') measured in duplicate (c) and cell-size is compared to relaxation time (τ) dynamics (d). Grey bars represent injection periods.

4.4.3 Temporal trends: SIP and biomass

Growth of *S. oneidensis* was stimulated following the injection of phase I, with increasing cell counts measured until the end of phase III (Figure 4-3c). The biomass increase was matched by increasing σ'' signals in both SIP-columns (see Appendix C, Figure AC 7, for a comparison with a non-growth control). Cell counts for the column sacrificially sampled immediately before phase II are omitted, because propionate was detected, suggesting that the bacteria fermented lactate (Seeliger et al., 2002), and that that column did not behave as a replicate.

Biomass density decreased following phase III (Figure 4-3c), and increased only after 221 hours from 0.74×10^6 to 1.31×10^6 cells mL_{PM}^{-1}, at the end of incubation (315 hours). Peak-σ'' values dropped during phase III, but increased once injection had ceased reaching a maximum at 191 hours after which σ'' precipitously declined to a minimum by 199 hours. The decline in both cell density and peak-σ'' matched the timing of NO_2^- accumulation (Figure 4-3b). Following the drop, σ'' recovered gradually and increased until the end of the experiment, matching the increase in biomass.

Measured σ'' in column G1 decreased over time and did not recover, which did not match the general trend in biomass and σ'' in G2. The cell densities in the two SIP columns were different (1.31×10^6 and 0.66×10^6 cells mL_{PM}^{-1}, for columns G2 and G1, respectively) at the end of incubation, therefore, σ'' measured in G1 was omitted during phases III and IV (for further details see Appendix C). Estimated cell size remained relatively stable, between 1.4 and 1.6 µm, throughout the experiment (Figure 4-3d).

The matching trends of cell density and σ'' (Figure 4-3c) provide direct experimental evidence for a correlation between SIP-σ'' and the electrochemical polarization of cells. The maximum magnitude of phase shift measured here was 0.6 mrad, for a maximum measured cell density of 1.87×10^6 cells mL_{PM}^{-1}, and a minimum of 0.09 mrad for a density of 5.97×10^4 cells mL_{PM}^{-1} (at the PSIP instrument detection limit of 0.1 mrad). A linear relationship for estimating cell counts from peak-σ'' in quartz sand is presented in Figure 4-4, giving the equation:

$$Bio = 1.46\times10^{11}(\sigma'') - 4.22\times10^5 \qquad 4.5$$

where *Bio* [cells mL_{PM}^{-1}] is the density of cells. The linear relationship in equation 4.5 is derived directly from cell counts measured using flow cytometry and peak-σ'' values in G2, prior to the

precipitous drop in σ'' measured after 195 hours ($R^2 = 0.83$). The regression was performed only on the time points prior to 195 hours, because of evidence suggesting strong changes in the cells' surface charging properties thereafter, based on the measured τ dynamics (Mellage et al., 2018).

Equation 4.5 predicts cell concentrations consistent with those simulated in a previous study (Mellage et al., 2018) for the same cell strain and porous medium (Figure 4-4). The data from Mellage et al. (2018) fall close to, but not directly on the line predicted by equation 4.5. The presence of elevated Fe^{2+} concentrations, stemming from the iron-coated sand in that experiment could have, in part, contributed to the discrepancy. Furthermore, slight variations in reaction kinetics across the replicate columns could have resulted in an offset between the timing of changes in σ'', measured in the SIP columns, and concentration changes, measured in the sampled column.

The slope of equation 4.5 is two orders of magnitude lower than that between SIP measurements and cell densities reported in Zhang et al. (2014). The discrepancy between the relationship derived for *S. oneidensis* in non-polarizing quartz sand (see Mellage et al. (2018)), and *Z. mobilis* suspensions in Zhang et al. (2014) is likely a function of several factors in their experiments, including the different potential electrode construction (*i.e.*, encased in electrolyte vs. in direct contact with sample), different cell strains, the metabolic/physiological state of the cells (*i.e.*, recently prepared suspension vs. cells under growth conditions), and the similar magnitude of the three cell densities in the regression in Zhang et al. (2014). Future research must address these key factors with the goal of developing unified relationships for estimation of cell density from σ'' measurements. Nevertheless, the agreement between the dataset presented here and that reported in Mellage et al. (2018) (see Figure 4-4), provides confidence in the validity of the empirical relationship (equation 4.5) and is promising for the development of SIP as an in-line monitoring technique for microbial growth dynamics.

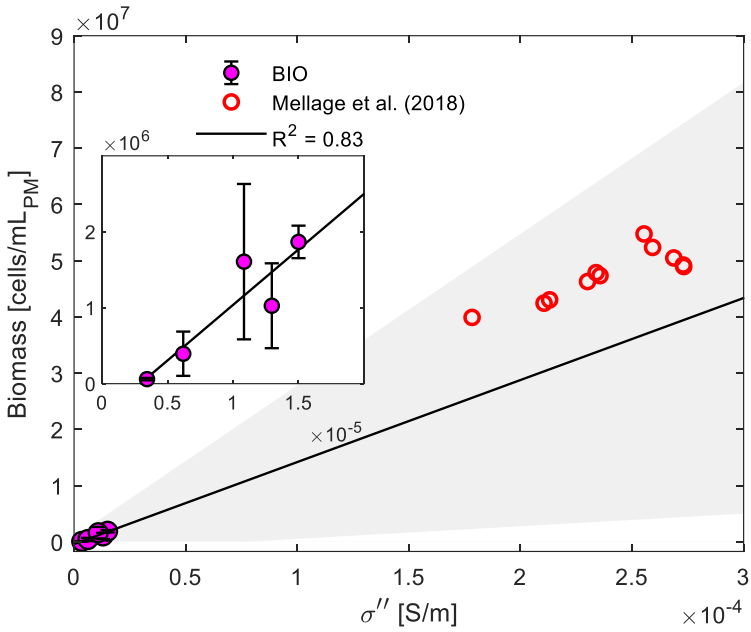

Figure 4-4. Linear relationship (equation 4.5) between measured cell counts (FACS) and imaginary conductivity (σ'') (R^2 = 0.83), prior to the precipitous decline in σ'' at 195 hours (95% CI, grey shaded area). Mellage et al. (2018) σ'' values, following 124 h of incubation in quartz sand, fall close to the measurement-derived line.

4.4.4 NO_2^- induced relaxation time anomalies

Despite the relatively constant cell size, the relaxation times (extracted from the fit a Cole-Cole relaxation) exhibited two distinct anomalies (Figure 4-3d). An example of the goodness of fit for a single Cole-Cole model (Weigand and Kemna, 2016b; a), to measured impedance magnitude $|Z|$ [Ω] and phase shift $-\varphi$ [mrad] data, is presented in Figure 4-5. At 178 hours, τ increased to 0.3 s from a stable 0.08 s during phase I. During phase II, it gradually decreased over 40 hours and levelled off at 0.05 s after 53 hours, and remained relatively constant until phase IV. A second anomaly was measured in phase IV. At the same time as the peak-σ'' dropped (Figure 4-3c), τ increased from 0.06 to 0.3 s. Concurrent to the σ'' rebound, τ gradually decreased at 220 h to level off at around 0.05 s at 253 hours.

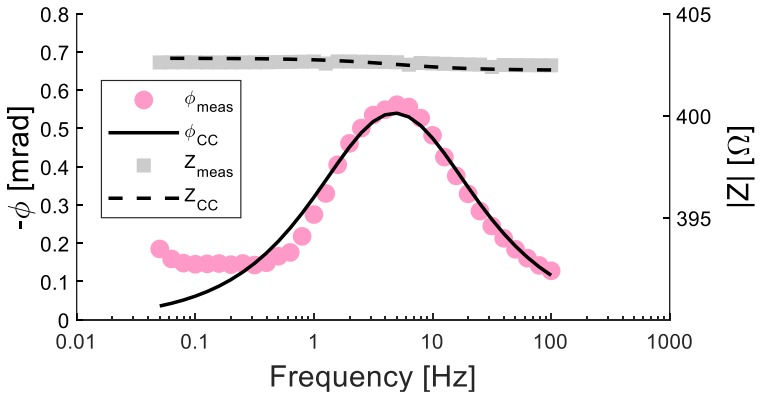

Figure 4-5. Fit of single Cole-Cole relaxation to phase and impedance data in column G2 at 280 hours.

Both anomalies in τ matched the timing of NO_2^- accumulation in excess of 0.5 mM. Nitrite is known to have toxic effects on *S. oneidensis* (Zhang et al., 2013). It has also been shown that NO_2^- can act as a protonophore (Sijbesma et al., 1996), a compound that decouples microbial catabolism from anabolism (hence, inhibiting cell growth) by inducing drastic changes in the chemistry (*e.g.*, pH changes) at or in direct proximity of the cell membrane (Saini, 2014).

The presence of cells throughout the incubation and their relatively constant cell size, suggests that the anomalies in τ are not a function of changes in cell size, but of changes in the surface charging properties of the cells in response to NO_2^- induced stress (Soni et al., 2008). We speculate that the increase in τ could be related to the localized build-up of protons at the outer cell membrane during uncoupling, decreasing pH, resulting in a localized reduction in negatively charges sites (Saini, 2014). As an added line of evidence, we compare σ' trends with τ dynamics in Appendix C (Figure AC 8). The comparison highlights that τ anomalies are coincident with sharp increases in σ' (followed by a small gradual increase until the end of each no-flow phase), suggesting a change in the surface charge density of the cells which alters aqueous and sorbed concentrations of cations. These findings support those in Mellage et al. (2018), where τ dynamics were linked to changes in the metabolic state of *S. oneidensis* cells.

4.4.5 Cell surface diffusion coefficient

Relying on the relatively constant trend in cell size, the average cell size for the period after the anomaly in τ and before the second injection (phase III) of 1.45 μm (within the range of widths and lengths reported for *S. oneidensis*, 1 – 5 μm (Lee et al., 2016)), was used to compute an apparent surface diffusion coefficient (Kruschwitz et al., 2010), for *S. oneidensis*, by rearranging equation (3). During the period between 35 and 167 hours, the calculated D_s for the polarizing bacteria is 5.4 (±1.3) $\mu m^2\ s^{-1}$. It is noteworthy that the cell size estimation is only an indirect measure of cell size as a function of light scatter, which can also be affected by changing cell physiology, highlighting the inherent uncertainty in the estimation of effective cell diameters (Vives-Rego et al., 2000). Nevertheless, the value D_s reported here, is within the range of values for D_s computed from Revil et al. (2012): 0.44 to 14 $\mu m^2\ s^{-1}$, using ion mobility coefficients reported therein (1.7 - 5.5×10^{-10} $m^2\ s^{-1}\ V^{-1}$), for various cell strains, and similar to D_s proposed for clay minerals (3.8 $\mu m^2\ s^{-1}$, Revil (2013)), which have ionic mobility coefficients similar to bacterial cells (Zhang et al., 2014; Revil et al., 2012). To our knowledge, this is the first reported estimate

of a Stern-layer ionic diffusion coefficient computed directly from measurements of the effective diameter of polarizing bacterial cells. The estimated D_s reported here, for *S. oneidensis* cells, may also be used to extract qualitative information of cell size from the peak relaxation of SIP datasets.

4.5 Conclusion

The strong dependence of σ'' on biomass density in porous media, highlighted herein, supports its applicability as a tool for estimating bacterial concentrations in natural porous media. Measured anomalies in τ corresponding to peak NO_2^- accumulation are evidence for the changing surface diffusion characteristics of cell membranes in response to NO_2^- induced stress (toxic effects and uncoupling) and, additionally, highlight that SIP can be used as a qualitative tool to infer changes in microbial activity. The potential for development of a cell size calibration with SIP would greatly benefit from targeted experiments to monitor mixed microbial communities (*e.g.*, two or more strains of distinct sizes), as opposed to pure cultures. Nonetheless, our analysis of the response of σ'' to microbial growth provides a theoretical framework from which to build upon using bench-scale experiments of increasing complexity, leading to the eventual field scale SIP deployment.

5 Microbial uncoupling and energy storage: a modeling study of nitrite toxicity-induced stress response

This chapter is modified from:

Mellage, A., Smeaton, C.M., Slowinski, S.E. and Van Cappellen, P. (in preparation). Microbial uncoupling and energy storage: a modeling study of nitrite toxicity-induced stress response. For submission to *Applied and Environmental Microbiology*.

5.1 Summary

Nitrite is a reactive intermediate in dissimilatory nitrate reducing reactions that can accumulate in the environment due to its wide-ranging toxic effects. The role of NO_2^- in modulating nitrogen-cycling as a combined function of its reactivity, electron accepting power and toxicity remains largely unaddressed. Herein, we present a biomass-explicit reactive transport model, which integrates NO_2^--toxicity, as a key modulator of the energy metabolism of *Shewanella oneidensis*, to predict the rates of dissimilatory nitrate reduction to ammonium (DNRA), coupled to lactate oxidation, validated with results from two separate experiments. Biogeochemical data from (1) a well-mixed batch suspension and (2) a flow-through reactor experiment, show that biomass growth is delayed in the presence NO_2^-. Our results suggest that nitrite toxicity for *S. oneidensis* occurs at concentrations well below 1 mM, the previously reported toxicity threshold. The incorporation of toxicity-induced uncoupling, of catabolism and anabolism, in the reactive term predicts the observed delay in biomass growth, facilitated by endogenous energy storage when NO_2^- is present, and consumption of these reserves after its depletion. The model presented herein is, to our knowledge, the first attempt to simulate biogeochemical kinetics under uncoupling of oxidative phosphorylation and delayed microbial growth.

5.2 Introduction

Nitrogen cycling in sediments and soils is modulated by microbes that catalyze a series of nitrate (NO_3^-) dissimilatory reduction reactions (Song et al., 2014; Rütting et al., 2011; Rütting et al., 2008). Denitrification and dissimilatory nitrate reduction to ammonium (DNRA) both occur under similar low-oxygen conditions and thus compete for available NO_3^- (Tiedje et al., 1983). Recently, isotopically labeled nitrogen approaches have shown that DNRA can outcompete denitrification in both aquatic sediments and soil environments, and significantly modulate NO_3^- reduction (Song et al., 2014; Rütting et al., 2011; Schmidt et al., 2011; Rütting et al., 2008; Pett-Ridge et al., 2006; Yin et al., 2002). In contrast to denitrification, which results in a loss of N, DNRA conserves nitrogen within a system, eliminating gaseous losses.

$$C_3H_5O_3^- + 2NO_3^- \rightarrow C_2H_3O_2^- + 2\mathbf{NO_2^-} + HCO_3^- + H^+ \quad 5.1$$

$$C_3H_5O_3^- + \mathbf{0.67NO_2^-} + 0.67\ H_2O + 0.33H^+ \rightarrow C_2H_3O_2^- + 0.67NH_4^+ + HCO_3^- \quad 5.2$$

During the two-step DNRA process (and during denitrification), outlined in equations 5.1 and 5.2, with lactate ($C_3H_5O_3^-$) as a model carbon source, nitrite (NO_2^-) the reactive intermediate

(Philippot and Hojberg, 1999), has the potential to accumulate. Nitrite is toxic to a range of microorganisms (Korte et al., 2015; Zhang et al., 2013; Gao et al., 2009a; Sijbesma et al., 1996; Beccari et al., 1983), and despite being an electron acceptor, its accumulation has inhibitory implications on N-cycling as modulated by its antimicrobial properties (Akbarzadeh et al., 2018; Kelso et al., 1997; Klebanoff, 1993; Beccari et al., 1983). Despite being considered an important reactive nitrogen intermediate, the role of NO_2^- in modulating N-cycling as a combined function of its reactivity, electron accepting power and toxicity remains poorly characterized.

A simplistic representation of a microbial metabolism is as an energy coupled reaction network driven by the consumption of energy generating substrates (catabolism), which is subsequently invested in biomass formation (anabolism) (Kleerebezem and Van Loosdrecht, 2010), as depicted in Figure 5-1. Catabolism and anabolism are coupled by an energy carrier (adenosine tri-phosphate, ATP), while uncoupled, ATP is either consumed for non-growth-related maintenance processes (Kleerebezem and Van Loosdrecht, 2010), or wasted/spilled (Russell, 2007; Liu, 1998; Russell and Cook, 1995). Using a well-known denitrifier, *Pseudomonas fluorescens*, Sijbesma et al. (1996) showed that at elevated concentrations (> 1 mM), NO_2^- acts as a protonophore, an uncoupler of oxidative phosphorylation, effectively decoupling energy-yielding processes (*e.g.*, catabolic reaction) from energy consuming processes (*e.g.*, biomass synthesis) (Hotchkiss, 1944). Nitrite thereby stimulates electron transport while disrupting ATP synthesis, stimulating ATP hydrolysis, and inhibiting ATPase-catalyzed exchange reactions (Rottenberg, 1990). Protonophores increase the cell membrane proton permeability, maintaining (and sometimes increasing) the substrate utilization rate while ATP synthesis slows down (Wang et al., 2015; Saini, 2014; Saini and Wood, 2008). During protonophore uncoupling, microbial catabolism is either enhanced or remains undisturbed, but anabolism slows down, reducing microbial growth yield (*i.e.*, lower biomass synthesis).

Accordingly, the results outlined in Chapter 4 of this thesis, showed delayed *Shewanella oneidensis* growth in a flow-through reactor experiment, with periodic NO_3^- additions, similar to that reported in Gao et al. (2009a). Elevated levels (~1 to 2 mM) of NO_2^- are reportedly toxic to *S. oneidensis*, inhibiting and delaying growth (Zhang et al., 2013; Gao et al., 2009a). Increasing cell counts were only measured in the experiment after complete NO_2^- consumption (see results therein). Spectral induced polarization (SIP) measurements were made throughout the experiment, as a useful proxy for microbial abundance (Mellage et al., 2018). Cole-Cole relaxation time (τ)

was extracted from the SIP dataset and compared to concurrent cell size estimates. The time-scale over which polarization of bacterial cells occurs is related to τ, which is a function of the size and surface charge of the cells (Mellage et al., 2018). Time-series τ results, showed the development of two distinct τ-anomalies coincident with NO_2^- accumulation, without any significant changes in cell size. Furthermore, the SIP signal directly related to the quantity of biomass, imaginary conductivity (σ''), did not increase during the periods of the τ-anomaly (and NO_2^- accumulation). In Chapter 4, Mellage et al. (in prep.) suggest that (1) the inhibitory effects of NO_2^- are present at lower concentrations (> 0.2 mM) than those previously reported, and that (2) NO_2^- toxicity suppresses microbial growth until complete NO_2^- consumption thereby necessitating a secondary energy synthesis/storage pathway to fuel the delayed growth phase.

Based on the observations that NO_2^- inhibitory effects are present at lower than expected NO_2^- concentrations, and that biomass growth occurs only after complete consumption of NO_2^-, during DNRA, we propose the following metabolic/reactive conceptual framework. During the first step of DNRA, NO_2^- accumulates, which inhibits *S. oneidensis* growth, effectively reducing microbial growth yields and enhancing biomass decay, due to its known toxic effects. Under these conditions, the rates of electron donor and carbon source (lactate) and electron acceptor (NO_3^- and NO_2^-) consumption, in viable cells, increase, but do not directly translate into growth, because of the increased cell membrane proton permeability in the presence of NO_2^-. As a response to toxicity induced stress, in this case induced by NO_2^-, *S. oneidensis* cells conserve energy within their structure (for example, in the form of poly-phosphates, Poly-P) (Kulakovskaya et al., 2016), storing some of the "excess" catabolic energy and biomass building nutrients. Upon depletion of NO_2^-, anabolic consumption of reserve compounds, from which ATP can be synthesized (Tocheva et al., 2013), translates into biomass synthesis and growth, mediated by the amount of reserves that accumulate during uncoupling.

Building upon our conceptual model, herein we present and validate a biomass-explicit reactive transport model for DNRA which integrates nitrite toxicity to predict the rates of substrate consumption (*e.g.*, lactate and nitrate), product formation (*e.g.*, acetate and ammonium), energy storage and microbial growth. Using results from two separate DNRA experiments: (1) a batch suspension and (2) a flow-through reactor experiment, we show that to capture biomass growth dynamics, NO_2^- induced yield reductions and energy storage (and later consumption of these reserves) are required. Our analysis provides new insights for microbial survival during metabolic

uncoupling and, to our knowledge, a first attempt at an approach to model delayed-growth in the absence of an electron acceptor.

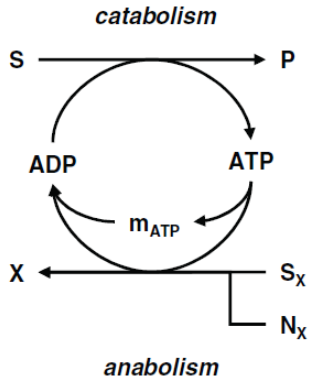

Figure 5-1. Simplified schematic representation, from Kleerebezem and Van Loosdrecht (2010), of microbial metabolism as a joint network of catabolism and anabolism, coupled by an energy carrier. In the catabolic reaction, substrate (S) is converted to a product (P), and metabolic energy is generated and conserved in the form of ATP. In the anabolic reaction, biomass (X) is constructed from substrate carbon (Sx) and nitrogen (Nx) sources and energy, in the form of ATP, is consumed.

5.3 Experimental setups

Two separate experimental datasets are considered in this analysis: (1) a well-mixed cell-slurry (batch) experiment monitoring the growth-kinetics of *S. oneidensis* and NO_2^- concentrations during DNRA; and (2) the flow-through experiment in sand-packed reactors inoculated with *S. oneidensis* experiencing periodic injections of NO_3^- and lactate, presented in Chapter 4 of this thesis. The experiments are briefly described below.

5.3.1 DNRA batch experiment

Shewanella oneidensis MR-1 was incubated for 124 hours, in the presence of 1 mM NO_3^- and 2.2 mM lactate, under anaerobic conditions in M1 microbial growth medium (Myers and Nealson, 1988), following the modifications in Mellage et al. (2018), with amended phosphate and ammonium concentrations of 50 and 150 µM, respectively. Well-mixed cell slurries (30 mL), containing approximately 5.7×10^6 cells mL^{-1} (OD_{600} = 0.003 Mellage et al. (2018)), were dispersed into three 150 mm long anaerobic culture tubes, with an 18 mm outer diameter and crimp-sealed under a 95%-N_2/5%-H_2 atmosphere, with blue butyl rubber stoppers (Bellco Glass, Inc., Vineland, N.J.). The tubes were placed on a rotating mixer (Glass-Col®), in an anaerobic chamber (Coy, <1 ppmv O_2 in N_2 with 3% H_2), and rotated end over end for the duration of the incubation. Slurries were sampled inside the anaerobic chamber at varying intervals, ranging from 5 to 22 hours, using 19" sterile needles connected to sterile 5 mL syringes (Normject). The extracted volume (2 mL) was subsampled for NO_2^- and optical density. Nitrite was measured using a microplate reader based colorimetric method (Ringuet et al., 2011b). Optical density at 600 nm (OD_{600}) was measured on a UV-vis spectrophotometer (Evolution™ 260, ThermoFisher Scientific).

5.3.2 Flow-through reactor (FTR) periodic injection experiment

For a detailed description of the experimental setup refer to section 4.3.1 Flow-through reactor, in Chapter 4. Briefly, ten identical column reactors (see Figure 4-1) wet-packed, using a microbial growth medium as the saturating pore water, in an anaerobic chamber with quartz sand (porosity of 40%) were inoculated with *S. oneidensis* (starting cell density of 8.3×10^4). The reactors were incubated for a total of 480 hours, and growth was stimulated by 12 hour periodic injections of an anaerobic growth medium containing 10 mM lactate and 1.5 mM NO_3^-, following

an initial 165 hour establishment phase. Each injection was followed by a no flow incubation period, for simplicity the phases in the experiment will be referred to as phases I, II, III and IV, referring to the first injection, the following no-flow incubation, the second injection and the final no-flow incubation, respectively.

Reactors were sacrificially sampled under anaerobic conditions at pre-specified time points for time series pore water geochemistry (lactate, acetate, NO_3^-, NO_2^- and NH_4^+) and microbial (flow cytometry derived biomass density, cell size and adenosine tri-phosphate (ATP) content) analyses. During both injection periods, outflow samples were collected from all reactors for pore water analysis, at 2 and 8 hours after the start of injection. Pore water and bulk porous media samples (for geochemical and microbial analysis, respectively) were extracted from the center of the columns at the location of sampling ports using a soil mini auger (and electrode emplacement ports for the two columns fitted with the geophysical array). Along with biogeochemical measurements the two columns that were sampled in duplicate at the end of the incubation were fitted with a geophysical measurement array for spectral induced polarization (SIP) measurements. Refer to the previous thesis chapter, Chapter 4, (section *4.3.4 Spectral Induced Polarization (SIP) measurements*), for SIP measurement details.

5.4 Reactive transport model

Building on the conceptual framework for lactate oxidation during DNRA, in the presence of an uncoupler, outlined in the introduction, microbial kinetics were simulated by taking an energy rerouting approach, in this case by partitioning the microbial growth rates into consumption and storage. Microbial consumption rates were assumed to remain unhindered by the presence of NO_2^-, but the translation of the forward reaction rates into immediate growth, spilled as wasted energy or stored in reserve compounds for later use, was mediated by the degree of NO_2^- accumulation. Both a transient flow advection-dispersion-reaction model (ADRM) and a well-mixed batch model were setup to simulate the biogeochemical dynamics in the two experiments described above, according to the rate expressions outlined below.

DNRA was simulated using dual-Monod kinetics. The microbial growth rate, r_{DNRA1} [cells L_{PM}^{-1} h^{-1}] (where L_{PM} refers to the bulk volume of the porous medium, that is, solid phase plus pore water), describes the reduction of NO_3^- in the presence of lactate:

$$r_{DNRA1} = \mu_{max}^{DN1} \cdot \frac{C_{Lac}}{C_{Lac} + K_{Lac}^{DN}} \cdot \frac{C_{NO_3^-}}{C_{NO_3^-} + K_{NO_3^-}} \cdot f_{FITC} \cdot X \quad 5.3$$

where μ_{max}^{DN1} [h^{-1}] is the corresponding maximum specific growth rate of the bacteria, C_{Lac} [mol L^{-1}] is the lactate concentration, $C_{NO_3^-}$[mol L^{-1}] is the concentration of nitrate, K_{Lac}^{DN} [mol L^{-1}] is the half-saturation constant for lactate uptake (assumed the same for both DNRA steps), $K_{NO_3^-}$ [mol L^{-1}] is the half-saturation constant for nitrate, and X [cells L_{PM}^{-1}] is the cell abundance or biomass density. Biomass density is scaled here by the fraction of total cells that exhibited green autofluorescence in the fluorescein isothiocyanate (FITC) flow cytometry measurement channel (in the green region of the visible spectrum, 500-560 nm), f_{FITC} [-].

Autofluorescence is used as a proxy for active cells (Mihalcescu et al., 2015; Yang et al., 2012). In prokaryotic cells, autofluorescence has been attributed to the presence of intracellular flavins (Mihalcescu et al., 2015; Billinton and Knight, 2001). Flavins are coenzymes, found in and excreted by cells, crucial in the metabolism of most organisms (Yang et al., 2012). Von Canstein et al. (2008) quantified the proportion of intracellular and extracellular flavins in *S. oneidensis* MR-1 cells, confirming the presence of internal flavins in viable *S. oneidensis* cells. Yang et al. (2012) showed, through dithionate (a strong reducing agent) reduction and air re-exposure experiments, that green autofluorescence, in excess of 80 FITC equivalents, for a variety of cell strains, stems primarily from endogenous flavins. Based on the existing evidence outlined above active biomass was assumed to be equal to the proportion of cells exhibiting FITC-autofluorescence.

The inhibition of NO_2^- reduction in the presence of NO_3^- is incorporated into the microbial growth rate, r_{DNRA2} [cells L_{PM}^{-1} h^{-1}], for the second step of DNRA, to account for the preferential consumption of NO_3^-:

$$r_{DNRA2} = \mu_{max}^{DN2} \cdot \frac{C_{Lac}}{C_{Lac} + K_{Lac}^{DN}} \cdot \frac{C_{NO_2^-}}{C_{NO_2^-} + K_{NO_2^-}} \cdot \left(\frac{K_{NO_3^-}^{inh}}{C_{NO_3^-} + K_{NO_3^-}^{inh}} \right) \cdot f_{FITC} \cdot X \quad 5.4$$

where μ_{max}^{DN2} [h^{-1}] is the corresponding maximum specific growth rate of the bacteria for the second DNRA step, $K_{NO_2^-}$ [mol L^{-1}] is the half-saturation constant for nitrite, and $K_{NO_3}^{inh}$ [mol L^{-1}] is the inhibition constant for nitrite, in the inhibition term in brackets on the RHS.

To account for continued electron donor and acceptor consumption, but uncoupled anabolism and catabolism in the presence of NO_2^-, rates r_{DNRA1} and r_{DNRA2} are partitioned into a consumption

($r_{consume}$) and a storage rate (r_{store}) in order to capture the observed delayed growth in the presence of NO_2^-.

$$r_{consume} = (r_{DNRA1} + r_{DNRA2}) \cdot (1 - \alpha) \quad 5.5$$

$$r_{store} = (r_{DNRA1} + r_{DNRA2}) \cdot \alpha \quad 5.6$$

Partitioning into catabolic consumption and storage is modulated by α, a fitting parameter that represents the fraction of total energy that is immediately consumed during uncoupling, energy that is wasted and does not translate into anabolic biomass production (Russell, 2007; Low and Chase, 1999; Liu, 1998), and energy that is stored in energy storage compounds such as Poly-P. The use of stored energy for growth (anabolism in the absence of an electron acceptor) is modeled as the first-order reserves rate ($r_{reserves}$):

$$r_{reserves} = k_{res} \cdot S \quad 5.7$$

where k_{res} [h^{-1}] is the first-order rate constant for the consumption of built up reserves, S [cells L_{PM}^{-1}]. Biomass decay is simulated as a combination of decay induced by a loss of cells during periods of flow injection, substantiated by measurements of cells at the outflow during injection periods, and toxicity induced decay in the presence of NO_2^-.

$$r_{decay} = \left[k_{tox} \cdot (1 - F_{tox}) + k_{flow}\right] \cdot X \quad 5.8$$

In equation 5.8, k_{tox} [h^{-1}] and k_{flow} [h^{-1}] are first-order decay rates for toxicity and flow-induced (*i.e.*, during flow injection) decay, respectively. The toxicity function, F_{tox} [-] ($1 \geq F_{tox} \leq 0$), a modified toxicity function for uranyl ions (UO_2^{2+}), applied here for NO_2^- induced toxicity on *S. oneidensis* (Belli et al., 2015) is described by the following equation:

$$F_{tox} = \frac{1}{1 + \left(\frac{C_{NO2}}{IC_{50}}\right)^p} \quad 5.9$$

where the aqueous concentration of NO_2^-, C_{NO2} [mol L^{-1}], modulates the toxicity response of the bacteria, IC_{50} [mol L^{-1}], is the concentration of NO_2^- at 50% inhibition and p, is an exponent characterizing the slope of the curve at the IC_{50} inflection point. Both IC_{50} and p are fitting parameters. The shape of F_{tox} as a function of NO_2^- concentration is plotted in Figure 5-2.

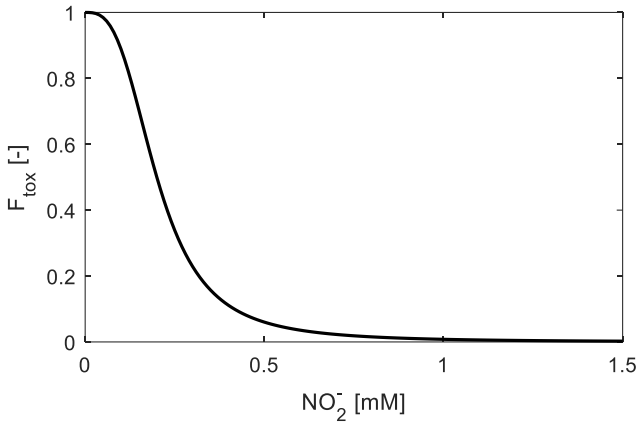

Figure 5-2. Modified (from: Belli et al. (2015)) toxicity function, F_{tox}, plotted as a function of aqueous NO_2^- concentration.

Combining the reaction rate expressions summarized above, the coupled transport and reaction governing equations for aqueous chemical species, biomass concentrations and energy reserves, simulated by the ADRM, are given below, during injection (*i.e.*, flow) periods:

$$\frac{\partial C_{Lac}}{\partial t} = D_l \frac{\partial^2 C_{Lac}}{\partial x^2} - v\frac{\partial C_{Lac}}{\partial x} + \left(-r_{DNRA1}\cdot\frac{1}{Y_1} - r_{DNRA2}\cdot\frac{1}{Y_2}\right)\cdot\left(\frac{1}{\phi}\right) \quad 5.10$$

$$\frac{\partial C_{Ac}}{\partial t} = D_l \frac{\partial^2 C_{Ac}}{\partial x^2} - v\frac{\partial C_{Ac}}{\partial x} + \left(r_{DNRA1}\cdot\frac{1}{Y_1} + r_{DNRA2}\cdot\frac{1}{Y_2}\right)\cdot\left(\frac{1}{\phi}\right) \quad 5.11$$

$$\frac{\partial C_{NO3}}{\partial t} = D_l \frac{\partial^2 C_{NO3}}{\partial x^2} - v\frac{\partial C_{NO3}}{\partial x} - 2r_{DNRA1}\cdot\frac{1}{Y_1}\cdot\left(\frac{1}{\phi}\right) \quad 5.12$$

$$\frac{\partial C_{NO2}}{\partial t} = D_l \frac{\partial^2 C_{NO2}}{\partial x^2} - v\frac{\partial C_{NO2}}{\partial x} + \left(2r_{DNRA1}\cdot\frac{1}{Y_1} - 0.67r_{DNRA2}\cdot\frac{1}{Y_2}\right)\cdot\left(\frac{1}{\phi}\right) \quad 5.13$$

$$\frac{\partial C_{NH4}}{\partial t} = D_l \frac{\partial^2 C_{NH4}}{\partial x^2} - v\frac{\partial C_{NH4}}{\partial x} + 0.67r_{DNRA2}\cdot\frac{1}{Y_2}\cdot\left(\frac{1}{\phi}\right) \quad 5.14$$

$$\frac{dX}{dt} = r_{consume}\cdot F_{tox} + r_{reserves}\cdot F_{tox} - r_{DECAY} \quad 5.15$$

$$\frac{dS}{dt} = r_{store} - r_{reserves}\cdot F_{tox} \quad 5.16$$

In equations 5.10-5.16, rates describing concentration changes of aqueous species (in units of mol L^{-1} h^{-1}) are obtained by dividing the microbial growth rates by their corresponding growth yields, Y_i [cells mol_{Lac}^{-1}]. The rate of change of the biomass concentration and the rate of change of energy stored, equations 5.15 and 5.16, respectively, are expressed in units of cells L_{PM}^{-1} h^{-1}, where anabolic processes (*i.e.*, biomass production) are all modulated by F_{tox}. During no-flow periods, following each 12-hour injection of NO_3^- and lactate in the experiment, the advective transport term in equations 5.10 to 5.14 drops out, and diffusive transport becomes dominant:

$$\frac{\partial C_{Lac}}{\partial t} = D_e \frac{\partial^2 C_{Lac}}{\partial x^2} + \left(-r_{DNRA1}\cdot\frac{1}{Y_1} - r_{DNRA2}\cdot\frac{1}{Y_2}\right)\cdot\left(\frac{1}{\phi}\right) \quad 5.17$$

equation 5.17 illustrates the no-flow formulation for the rate of change of lactate concentration, where D_e is the effective diffusion coefficient (Mellage et al., 2018). For the well-mixed batch case, the system of governing equations is modified by the removal of transport terms.

Transport and reactions were solved iteratively at each time step (Δt = 60 s), in MATLAB. Using an operator-split approach, the Crank-Nicolson method was applied to numerically solve advective-dispersive (during flow) and diffusive (during no-flow) transport of dissolved species (Δx = 1 mm). During flow periods, a constant-flux and prescribed advective-flux boundary

condition were set at the inlet and outlet, respectively. During no-flow periods, a zero-flux boundary condition was imposed at the top and bottom of the domain. As a benchmark for the ADRM code, a non-reactive tracer breakthrough profile, numerically solved by the ADRM, is compared to that solved in Hydrus 1D, in Figure 5-3 – both fitted to Cl^- breakthrough in the quartz sand-packed columns. The solutions of the ordinary differential equations, describing the reactive terms, were approximated using the Runge−Kutta method.

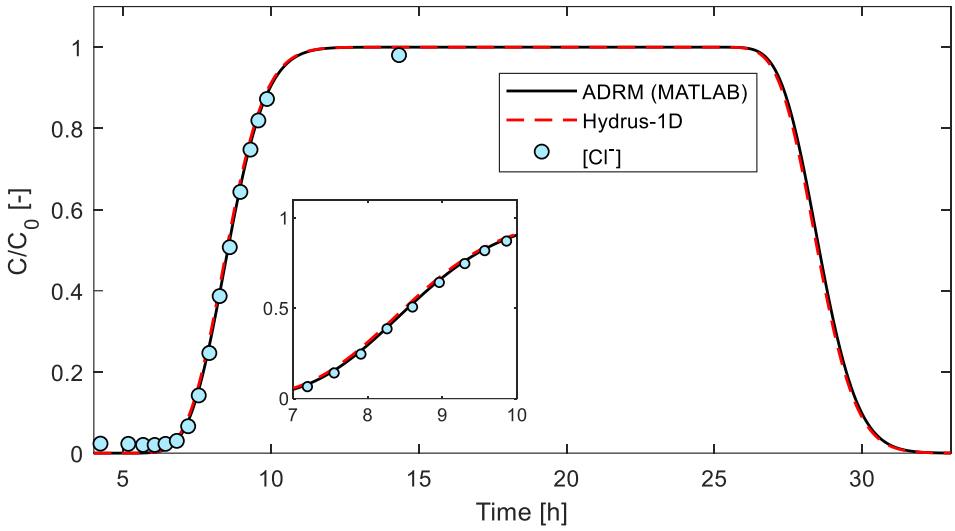

Figure 5-3. Chloride (Cl^-) tracer breakthrough, with fitted advection-dispersion-reaction model (ADRM) outflow curve, compared to the fitted breakthrough curve solved in Hydrus 1D.

5.5 Results and discussion

Herein, modelling and experimental results for each experiment are presented individually, and then discussed together with a focus on energy re-routing (uncoupling). The geochemical kinetics in from the experiment in Chapter 4 are discussed in detail therein, and will not be the focus of this section.

5.5.1 Well-mixed batch system

Simulation results are compared to measured NO_2^- and biomass concentrations in Figure 5-4. Parameters for the fitted batch model are presented in Table 5-1. The timing of simulated NO_2^- accumulation and consumption closely match measured concentrations. Nitrite accumulates to a maximum of 1 mM during the first 12 hours of DNRA (Figure 5-4a), and is consumed following complete NO_3^- depletion (NO_3^- inhibition), resulting in production, and accumulation of NH_4^+ in the system. Simulated lactate and acetate concentrations are summarized in the appendix (Figure AD 1).

The growth-lag observed in the measured microbial growth curve (Figure 5-4b) during the first 20 hours of the batch experiment was successfully captured by the energy re-routing approach in the uncoupling reactive model. Buildup of biomass only occurred once NO_2^- was well below 0.25 mM, and continued in the absence of any electron acceptor, to plateau after 40 hours of incubation. The uncoupling model (solid line in Figure 5-4b) closely matches the growth of *S. oneidensis*, whereas a classic Monod version of the model (no uncoupling or energy storage, dashed line in Figure 5-4b) generates effectively identical DNRA species (NO_3^-, NO_2^- and NH_4^+) time series concentrations, but over predicts cell density during the early stages of the experiment. The accumulation of energy reserves while NO_2^- is present, and the exponential consumption thereof, after 20 hours, is shown in Figure 5-4c. The timing of peak-reserve-energy accumulation, matches the timing of NO_2^- production, and the consumption rate of reserves is the inverse of the biomass growth rate after 20 hours.

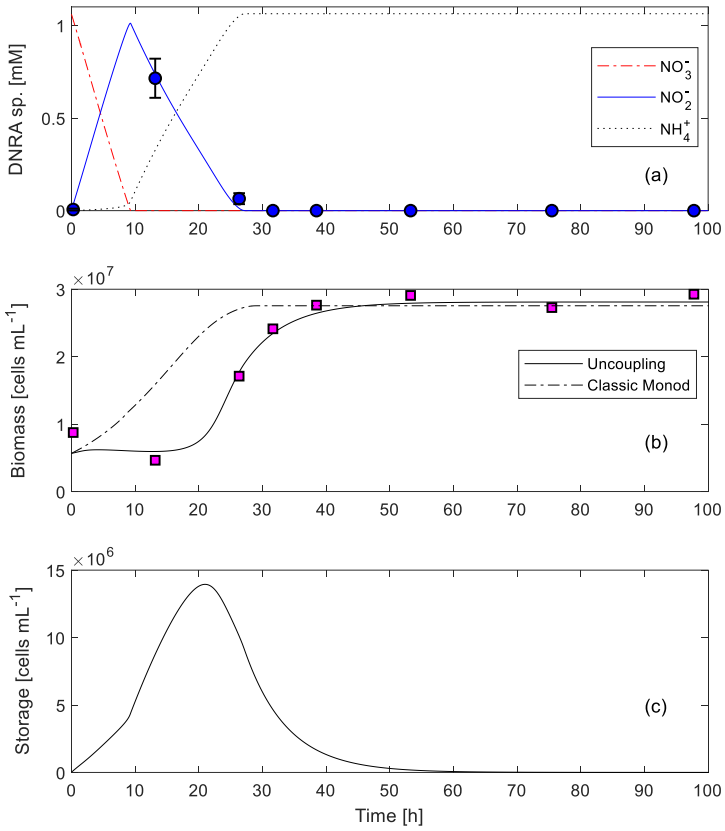

Figure 5-4. Simulation results and concentration measurements for the well-mixed cell slurry experiment (Smeaton, unpublished). Simulated DNRA species profiles are plotted along with measured NO_2^- concentrations in (a), classic Monod and "energy re-routing" biomass concentrations are compared to measured cell densities in (b), and the accumulation of energy reserves is depicted in (c).

Table 5-1. Kinetic and transport parameters for the fitted batch reactor and advection-dispersion reactive transport models.

Batch Reactor Model			**ADR Model** (Mellage et al., in prep, *GRL*)		
μ_{max}^{DN1}	0.15	[h^{-1}]	μ_{max}^{DN1}	0.5	[h^{-1}]
μ_{max}^{DN2}	0.48	[h^{-1}]	μ_{max}^{DN2}	1.4	[h^{-1}]
K_{NO_3}	2.00×10^{-6}	[mol L^{-1}]	K_{NO_3}	2.00×10^{-6}	[mol L^{-1}]
K_{NO_2}	4.10×10^{-6}	[mol L^{-1}]	K_{NO_2}	4.10×10^{-6}	[mol L^{-1}]
K_{Lac}	1.00×10^{-3}	[mol L^{-1}]	K_{Lac}	1.00×10^{-3}	[mol L^{-1}]
$K_{NO_3}^{inh}$	1.60×10^{-5}	[mol L^{-1}]	$K_{NO_3}^{inh}$	1.60×10^{-5}	[mol L^{-1}]
Y_1	1.03×10^{13}	[cells mol_{Lac}^{-1}]	Y_1	0.86×10^{12}	[cells mol_{Lac}^{-1}]
Y_2	1.55×10^{13}	[cells mol_{Lac}^{-1}]	Y_2	0.86×10^{12}	[cells mol_{Lac}^{-1}]
α	0.7	[-]	α	0.7	[-]
k_{res}	0.15	[h^{-1}]	k_{res}	0.025	[h^{-1}]
k_{decay}	0.01	[h^{-1}]	k_{decay}	0.025	[h^{-1}]
p	3	[-]	p	3	[-]
IC_{50}	2.50×10^{-4}	[mol L^{-1}]	IC_{50}	2.00×10^{-4}	[mol L^{-1}]
			k_{flow}	0.025	[h^{-1}]
			f_{FITC}	0 to 1	[-]
			ϕ	0.40	[-]
			v	1.84×10^{-2}	[m h^{-1}]
			D	1.80×10^{-5}	[m^2 h^{-1}]

Half-saturation constants are estimated from literature ranges (Yan et al., 2016; Roden, 2008; Watson et al., 2003) and the parameter f_{FITC} is based on measured autofluorescence.

5.5.2 ADRM fit to FTR dataset

Simulated concentration time series are compared to measured values during the periodic flow-through injection experiment in Figure 5-5. Measurements represent average concentrations between sampling ports at 6.5 and 9 cm, in the center of the columns, and are compared to average computed concentrations within that interval of the simulated domain. Parameters for the fitted ADRM are summarized in Table 5-1. The first 12 hour injection (phase I) replenished the flow-through reactors with lactate and NO_3^- rich growth medium. Both lactate and NO_3^- concentrations increased, but not to inflow concentrations values (10 and 1.5 mM, respectively), suggesting considerable lactate degradation and NO_3^- reduction (Figure 5-5a and d). The ADRM-generated DNRA species concentration profiles agree well with pore water measurements extracted from the center of the sacrificially sampled columns, taken before and after phase I, and during no-flow in phase II. The implementation of uncoupling and energy re-routing in the model, successfully captured the accumulation of NO_2^- (Figure 5-5b) during phase I, which resulted in delayed biomass growth. Increasing cell density was predicted by the model, only following depletion of NO_2^-, in agreement with the flow-cytometry measured *S. oneidensis* concentrations during phase II (Figure 5-5c). The sample immediately prior to phase III, the second 12 hour injection, was omitted from analysis because propionate was detected in the sampled reactor, suggesting a fermentative degradation pathway for lactate (Seeliger et al., 2002).

The timing of accumulation of NO_3^- and NO_2^- during phases III and IV was successfully captured by the model. The system exhibited slower DNRA kinetics, evident by the persistence of NO_3^- and NO_2^- well into phase III. Scaling of the reaction rates to account for the active proportion of biomass, based on the proportion of green autofluorescent cells, f_{FITC}, allowed for the discrepancy to be captured by a single kinetic-parameter set (Table 5-1) for both injections. Despite higher biomass density at the start of phase III (with respect to phase I), f_{FITC} was less than 5% of the total counts, whereas it was 98% during phases I and II (see Appendix D, Figure AD 2). Thus, during phases I and II, the majority of biomass present in the system was active, and less than 5% of biomass was active in phases III and IV. This is also substantiated by lower ATP concentrations in phases III and IV (see Appendix C, Figure AC 6). The relative changes in biomass concentrations and the timing of growth and decay were closely emulated by simulated cell concentrations. However, the model over predicted biomass decay during NO_2^- accumulation in phase IV, resulting in an under estimation of cell density, with respect to measured values. Despite

the misfit between simulated and measured biomass concentrations between 344 and 386 hours the model was able to capture the recovery of biomass (*i.e.*, growth on reserves) after 386 hours (Figure 5-5c).

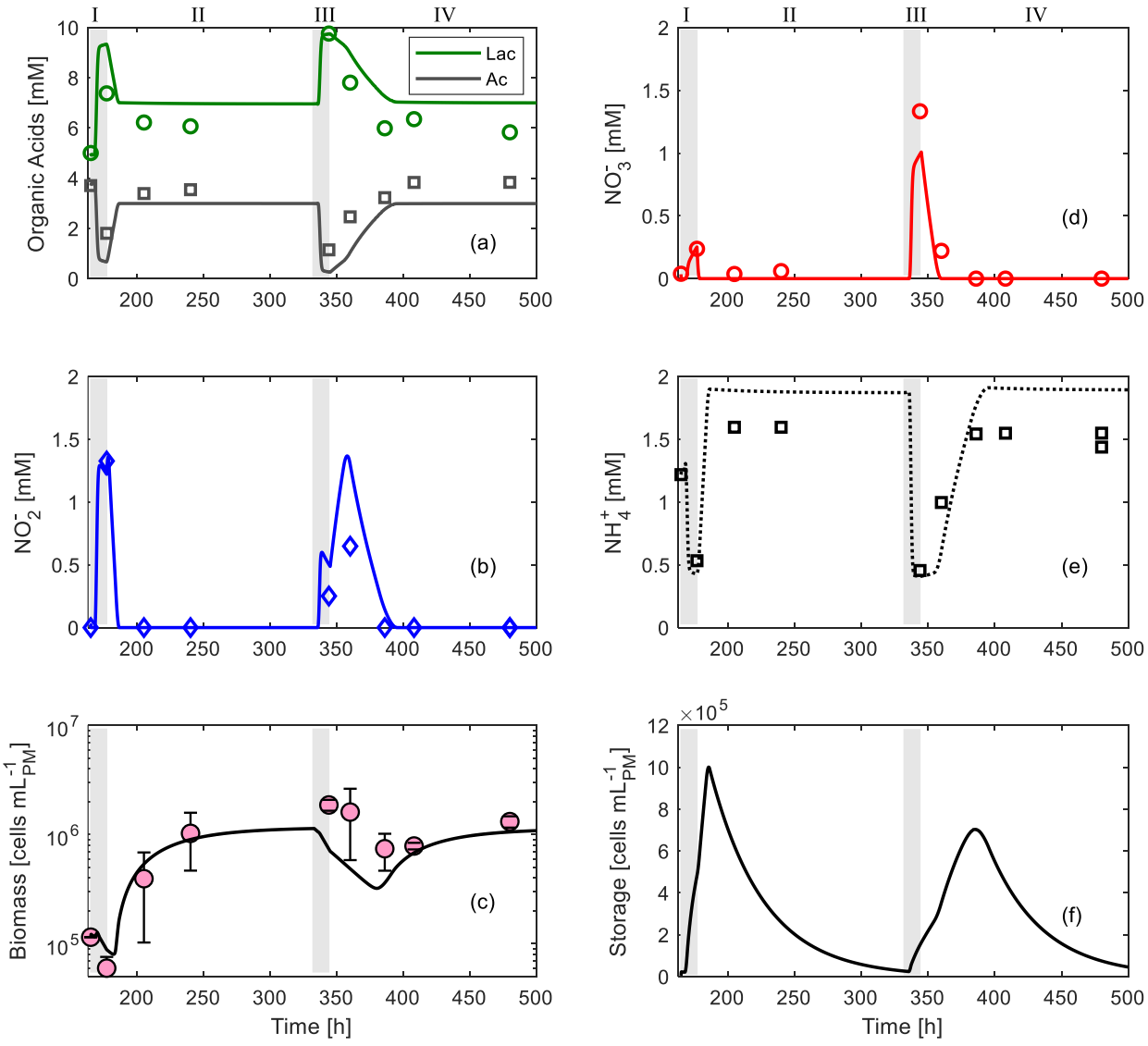

Figure 5-5. Simulation results and measured concentrations of (a) organic acids (*i.e.*, lactate and acetate), (b) NO_2^-, (c) biomass (d) NO_3^-, and (e) NH_4^+ during the periodic lactate and NO_3^- flow-through injection experiment. The accumulation of energy reserves throughout the experiment is depicted in (f).

The model over predicts the accumulation of NH_4^+ in the experiment, despite taking into account NH_4^+ uptake during biomass buildup (assuming an idealized chemical composition for *S. oneidensis* of $C_5H_9O_{2.5}N$). As alluded to in Chapter 4, the discrepancy is likely related to weekly-bound NH_4^+ in outer-sphere complexes at charged surface sites on both the sand and cells themselves. Sorption was not accounted for in the model.

Breakthrough curves for all chemical species are compared to average outflow concentrations measured 2 and 8 hours after the onset of injection during injection phases I and III in Appendix D (Figure AD 3). Cell count samples measured 2 hours after the start of each injection showed a non-negligible flux of cells during flow-injection, despite the presence of an outflow filter membrane. Outflow samples are an average of all replicates, 9 during phase I and 5 during phase III, the decreasing sample size is due to the sequential sacrificial sampling of reactors with progression of the experiment. Cell outflow flux is compared to the simulated rate of flow-induced decay in Appendix D (Figure AD 4). The close agreement between simulated injection-phase breakthrough curves and outflow sample measurements, along with the comparable magnitude of the measured cell outflow flux and the simulated flow-induced loss of cells, provides a robust validation of the model fit and the good agreement between replicate columns.

The accumulation of energy reserves and their consumption following NO_2^- depletion in phases II and IV is shown in Figure 5-5f. Similar to the simulation results for the batch experiment, the timing of each peak in reserve energy accumulation, matches the timing of NO_2^- production, following each of the NO_3^- injections.

As added evidence for validation of the ADRM-predicted biomass trends, simulated biomass concentrations are compared to spectral induced polarization (SIP) imaginary conductivity (σ'') in Figure 5-6. Mellage et al. (2018) and Zhang et al. (2014) showed that SIP-σ'' can be a quantitative measure of biomass density in porous media. The electrochemical polarization of cells, induced by an alternating, low frequency (0.01 to 1000 Hz) current, results in tangential cation (surrounding the negatively charge cells) migration along the cell membrane of negatively charged bacterial cells (Mellage et al., 2018). The work required to induce the ionic migration in the Stern layer is quantified as charge storage, described by σ'' (Vinegar and Waxman, 1984). The magnitude of σ'' is proportional to the abundance of cells, as modulated by their surface charge, and can be used as a proxy for bacterial abundance in porous media with a negligible structural charge, as is the case for quartz sand (Mellage et al., 2018; Zhang et al., 2014).

The agreement between the trend in σ'' and simulated biomass in Figure 5-6 is encouraging evidence to support (1) the validity of the simulated trends in biomass concentration and the implementation of microbial uncoupling, and concurrently, (2) the mechanisms of bacterial-cell electrochemical polarization driving σ'' dynamics. The SIP trends are discussed in detail in Chapter 4, in relation to the measured biomass concentrations in Figure 5-5c. Therein, the author's allude to changes in the surface charging properties of cells during NO_2^- accumulation. Briefly, accumulation of NO_2^- resulted in two distinct increases in the Cole-Cole derived τ, which did not arise from variations in cell size, but rather are likely a function of nitrite-induced changes to the cell membrane chemistry of the bacteria, resulting in changes to their surface charge. These changes in surface charging properties, can in part, be responsible for the slight discrepancies between the rates of change of simulated biomass and σ''.

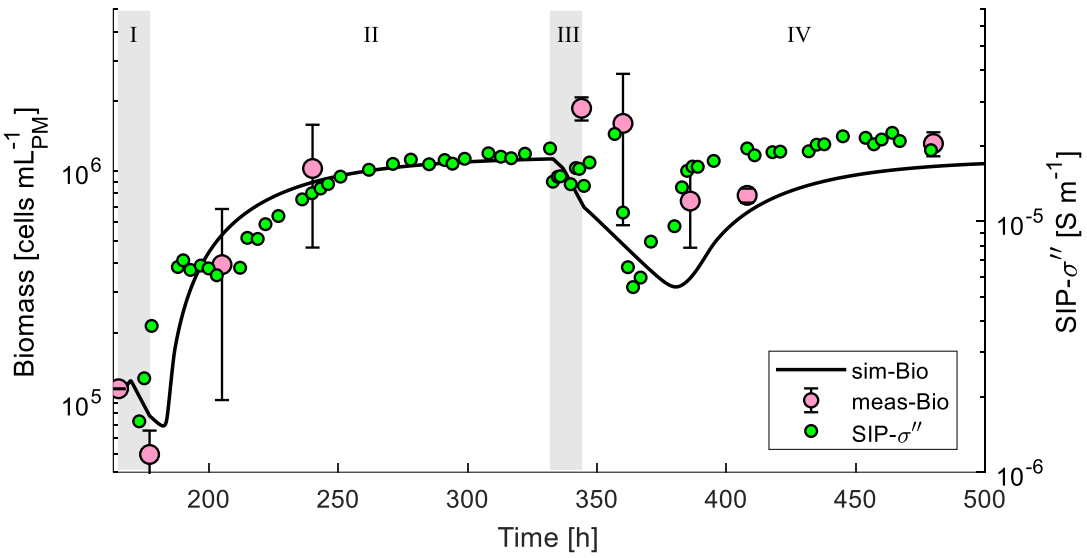

Figure 5-6. ADRM simulated biomass concentration in the flow-through reactor experiment compared to measured spectral induced polarization (SIP) imaginary conductivity (σ'') measured in one of the replicate reactors for the duration of the incubation. SIP results are adapted from Chapter 4.

5.5.3 Model parameters

In agreement with the effects of protonophore induced uncoupling, as is the case for NO_2^-, in both batch and ADRM models, fitted maximum specific growth rates (μ_{max}) for NO_3^- and NO_2^- are between 1 and 2 orders of magnitude higher than expected for DNRA (Mellage et al., 2018; Yan et al., 2016; Pan et al., 2012; Almeida et al., 1997), with significantly lower fitted growth yields (*Y*) (Mellage et al., 2018). A single model is able to capture the dynamics in both batch and flow-through experiments, but fitted kinetic parameters (except for the Monod half-saturation constants) were different between both cases. Biokinetic parameters derived from well-mixed batch and chemostat systems are reported to exhibit significant variation than those from natural and flow-through systems (Grösbacher et al., 2018). Grösbacher et al. (2018) explored these differences and compared growth rates and growth yields between well-mixed batch and flow-through experimental datasets of aerobic toluene degradation experiments. The authors highlighted order-of-magnitude reductions in growth yields in flow-through experiments (compared to batch cultures) as well as differences in mean growth rates between the two systems. The reader is referred to Grösbacher et al. (2018) for a detailed discussion on the flow-velocity and porous media related mechanisms postulated as controls governing parameter discrepancies between experimental setups. Nevertheless, despite the differences in biokinetic parameter values for DNRA kinetics in the batch and flow-through experiments reported here, a unified process model considering energy storage during NO_2^- induced uncoupling and consumption of energy reserves, in both cases, captures delayed growth in the absence of any electron acceptor (here NO_3^- and NO_2^-).

5.5.4 Toxicity as a regulator of reaction rates

The concentrations of toxic intermediates, reaction products and by-products, and the speciation of these, as modulated by redox conditions, regulate the biological attenuation rates of uranium, arsenic, selenium and nitrite (among others) by microbes in the environment (Belli and Taillefert, 2018; Thorgersen et al., 2017; Belli et al., 2015; Zhang et al., 2013; Stolz and Oremland, 1999). The adaptation mechanisms for microbes that use toxic compounds of concern as terminal electron acceptors have been well characterized as well as their inhibitory effects at concentration thresholds (Qambrani et al., 2016; Nancharaiah and Lens, 2015). The incorporation of such mechanisms to inform reactive processes in models, to simulate toxic inhibition can improve our

understanding of the mobility and persistence of toxic compounds in the environment. The incorporation of NO_2^- toxic inhibition and a framework for energy storage scaled by the presence of dissolved NO_2^-, in this study, is an example of such a case. The model presented herein has implications for the inclusion of toxicity into reactive transport models, and the integrating of specific stress responses (Sijbesma et al., 1996) or toxicity-coping mechanisms (Thorgersen et al., 2017; Stolz and Oremland, 1999) to better predict the role of toxicity in modulating reaction rates and biomass metabolic processes.

Furthermore, under certain conditions, excess biomass may be detrimental to in situ bioremediation techniques (Saini, 2014). Disposal of excess sludge can account for 25 to 65% of operating costs for conventional sludge processing plants (Chen et al., 2008). Protonophores have been extensively proposed as compounds that can increase remediation efficiency by accelerating substrate (*e.g.*, organic contaminant or nutrient) uptake and suppressing biomass build up (Podella and Hauptmann, 2009). The model proposed here, introduces the possibility of being able to simulate the response of a biomass population to an uncoupler, in the context of wastewater treatment, and predict the efficiency of the process.

5.5.5 Summarizing remarks

The conceptual bioenergetic framework of coupled catabolism and anabolism to describe microbial growth "is based on the fundamental idea" that the energy required for biomass production should be generated by an energetically favorable catabolic reaction (Kleerebezem and Van Loosdrecht, 2010). Experimental and modeling results presented here from two DNRA experiments provide evidence for anabolic processes that occur after, but in the absence of a favorable catabolic reaction. The model outlined highlights the requirement of some form of energy storage during the forward catabolic reaction, as a means to drive anabolic biomass production in the absence of an electron acceptor. Effectively, the favorable catabolic reaction (*i.e.*, the oxidation of lactate to acetate coupled to the reduction of NO_3^- via NO_2^- to NH_4^+), remains the ultimate energy source, but the timing of energy consumption is delayed, facilitated by re-routing of energy during uncoupling via energy storage mechanisms.

Poly-Ps can serve as energy and phosphorus (P) reservoirs in many microorganisms (Smeaton et al., 2009). In yeast cells specifically, Poly-P accumulates when cell growth is suppressed by nutrient limitation or heavy metal toxicity induced stress (Kulakovskaya et al.,

2016). Nutrients (*e.g.*, N and P) and energy, in the form of high-energy chemical bonds, are stored in Poly-P structures, from which ATP can later be synthesized (Tocheva et al., 2013). Glasauer et al. (2007) provided evidence to support the potential formation of Poly-P in *Shewanella* sp., which has yet to be experimentally confirmed. Furthermore, polyhydroxyalkanoates (PHAs) and polyhydroxbutyrate (PHB), are natural polyesters synthesized by a wide range of bacteria (including *Shewanella* spp. (Numata et al., 2013)), that accumulate as granules within the cytoplasm (Escapa et al., 2012; Budde et al., 2010), and are used as carbon and energy reserves (Johnson et al., 2009). Excess carbon storage in PHAs and PHB, provides a crucial competitive advantage for bacteria exposed to fluctuating carbon availability or limited nutrient availability (Tveit et al., 2015; Budde et al., 2010). Uncoupling induces conditions similar to nutrient limitation, suppressing the ability of cells to synthesize biomass, potentially stimulating the formation of Poly-P, PHAs or PHB as strategic survival mechanisms in *Shewanella oneidensis.* Experimental characterization of the energy storage mechanism enabling growth post electron acceptor depletion, will help refine a more process based mathematical formulation of the proposed energy-rerouting, and can potentially explain the observed delay in growth (after complete EA consumption) during NO_2^- reduction (Chapter 4, and Gao et al. (2009a)).

The model presented herein is, to our knowledge, the first attempt to simulate biogeochemical kinetics under uncoupling of oxidative phosphorylation and delayed microbial growth. Typically a delay in microbial growth is associated with metabolic lag (Nilsen et al., 2012; Wood et al., 1995), where degrading cells require a certain amount of exposure time to synthesize the required enzymes to breakdown a new substrate or consume a new electron acceptor. During a metabolic lag period, however, there is no growth and no substrate and electron acceptor consumption, unlike uncoupling which delays growth while enhancing or maintaining catabolic consumption. Liu (1998) postulated a model to account for uncoupling of microbial growth under substrate-sufficient conditions in order to describe lower observed growth yields under excess substrate availability. The author's proposed model is the only existing quantitative representation of energy uncoupling, but its applicability is limited to substrate sufficient continuous cultures (Liu, 1998) and does not account for the effects of a protonophore.

6 Sensing coated iron-oxide nanoparticles with spectral induced polarization (SIP): Experiments in natural sand packed flow-through columns

This chapter is modified from:

Mellage, A., Holmes, A.B., Linley, S., Vallée, L., Rezanezhad, F., Thomson, N., Gu, F. and Van Cappellen, P. (2018). Sensing coated iron-oxide nanoparticles with spectral induced polarization (SIP): Experiments in natural sand packed flow-through columns. *Environmental Science & Technology*. DOI: 10.1021/acs.est.8b03686.

6.1 Summary

The development of nanoparticle-based soil remediation techniques is hindered by the lack of accurate *in situ* nanoparticle (NP) monitoring and characterization methods. Spectral induced polarization (SIP), a non-invasive geophysical technique, offers a promising approach to detect and quantify NPs in porous media. However, its successful implementation as a monitoring tool requires an understanding of the polarization mechanisms, the governing NP-associated SIP responses and their dependence on the stabilizing coatings that are typically used for NPs deployed in environmental applications. Herein, we present SIP responses (0.1-10,000 Hz) measured during injection of a poloxamer-coated super-paramagnetic iron-oxide nanoparticle (SPION) suspension in flow-through columns packed with natural sand from the Borden Aquifer. An advective-dispersive transport model is fitted to outflow SPION concentration measurements to compute average concentrations at the SIP spatial response domain (within the columns), for direct comparison with real and imaginary components of the complex conductivity. The results highlight the excellent agreement between simulated SPION concentrations within the columns and imaginary conductivity values, suggesting that NP-mediated polarization (charge storage) increases proportional to increasing SPION concentration. Our results introduce the possibility of SIP monitoring of coated metal-oxide spatial and temporal NP distributions, immediately deployable in bench-scale studies with potential real-world applications in monitoring and remediation reliant on delivering NPs to target areas.

6.2 Introduction

The larger surface area and resultant higher reactivity of nanomaterials has led to their increased deployment to remediate groundwater and soils (Dong et al., 2018; Tuček et al., 2017; Su et al., 2016). Nanoscale iron-oxides, zero-valent iron (nZVI), FeS, Fe-Mn oxides and bimetallic nanoparticles (NPs) (among many others) have been used to treat a variety of contaminants including heavy metals and organic compounds (Lin et al., 2018; Gong et al., 2014; Liang et al., 2012; An et al., 2011). A major barrier in the development of nanoparticle-based treatment methods in subsurface systems lies in our inability to accurately monitor the fate and transport of nanoscale reactive materials to ensure the efficacy of targeted in situ treatments (Shi et al., 2015).

Spectral induced polarization (SIP) offers a non-invasive approach to detect (Flores Orozco et al., 2015; Shi et al., 2015; Joyce et al., 2012) and quantify (Abdel Aal et al., 2017) nanoparticles

in soils. By measuring the impedance magnitude ($|\sigma|$) and phase shift (φ) of a voltage potential, relative to an injected current over a broad frequency range (Abdel Aal and Atekwana, 2014; Schwartz and Furman, 2014; Personna et al., 2008; Slater et al., 2007), SIP provides frequency-dependent information on conduction and energy storage in porous media. The measured response is expressed as the complex conductivity (σ^*):

$$\sigma^* = \sigma' + i\sigma'' \tag{6.1}$$

where $i = \sqrt{-1}$. The real conductivity (σ') is an electrolytic conduction term and is controlled primarily by pore water conductivity (σ_w), with a contribution from surface conduction (σ_{surf}) in the electrical double layer (EDL) at the grain-fluid interface (Abdel Aal et al., 2017; Slater et al., 2007; Revil and Glover, 1998). The imaginary conductivity (σ'') represents reversible energy storage, dominated by electrochemical polarization of counter-ions in EDLs at the grain (Revil et al., 2017; Revil and Florsch, 2010) and pore-interface (Marshall and Madden, 1959) scales below 100 Hz, and interfacial (Maxwell-Wagner) (Olhoeft, 1985) polarization at frequencies above 100 Hz.

Typically, SIP is measured between 0.01 to 10,000 Hz in laboratory and field environmental applications (Kemna et al., 2012; Atekwana and Slater, 2009). The Cole-Cole relaxation model (Pelton et al., 1978; Cole and Cole, 1941) is used to describe the frequency dependence of $|\sigma|$ and φ of datasets with well-defined spectral peaks (Mellage et al., 2018), as a means to extract characteristic parameters from frequency dependent spectral responses. Equation 6.2 is the Cole-Cole relaxation for multiple terms, *N*, based on the Pelton et al. (1978) formulation:

$$\sigma^*(\omega) = \sigma_0 \left[1 + \sum_{k=1}^{N} m_k \left(\frac{(i\omega\tau_k)^{c_k}}{1 + (i\omega\tau_k)^{c_k}(1 - m_k)} \right) \right] \tag{6.2}$$

where the σ_0 [S m^{-1}] is the direct current conductivity, m [-] is the chargeability, τ [s] is the relaxation time, ω [rad s^{-1}] is the angular frequency and c [-] is a constant describing the shape of the observed phase dispersion (Ustra et al., 2012; Zisser et al., 2010b). The chargeability, analogous to σ'', is a function of charge storage, while τ is a relative measure of the time for polarization and ion back-diffusion (de Lima and Sharma, 1992; Wong, 1979; Schwarz, 1962). The time-scale captured in the parameter τ, is a function of the length-scale of the dominant polarization mechanism. The ability to extract length-scale information from SIP datasets provides a unique opportunity to measure the relative size contribution at the peak frequency while σ' and σ'' provide information about pore-water conductivity and charge/energy storage, separately.

Complex conductivity signatures have been shown to depend directly on the fate of nano-scale particles in soils and hence, they can provide information on properties and processes such as microorganism abundance and dynamics (Mellage et al., 2018), biotic (Flores Orozco et al., 2013; Flores Orozco et al., 2011; Personna et al., 2008) and abiotic (Placencia-Gómez et al., 2013) mineralization and dissolution, and presence of metallic micro- and nanoparticles (NPs) (Abdel Aal et al., 2017; Flores Orozco et al., 2015; Shi et al., 2015; Joyce et al., 2012). Joyce et al. (2012) were the first to report σ^* responses associated with uncoated NP-sand mixtures of metallic NPs. Furthermore, Abdel Aal et al. (2017) showed a strong relationship between uncoated silver NP (nAg) concentrations and σ'' in nAg-sand mixtures. Werkema et al. (2010) reported increasing σ'' during NP injection of nAg stabilized with human serum albumin (HSA), but observed decreasing sensitivity with increasing nAg suspension concentration due to aggregation.

Typically, NPs engineered for environmental applications are coated with surfactants or polyelectrolytes to improve their stability and mobility in suspension (Shi et al., 2015; Bhaumik et al., 2011; Hotze et al., 2010; He and Zhao, 2007). The excellent transport properties of coated NPs enable direct delivery into contaminated soil and groundwater to facilitate in situ removal of target contaminants (Xiong et al., 2009). In an attempt to sense NPs under more realistic conditions, Shi et al. (2015) investigated the σ^* response of nZVI coated with insulative mineral oil in a sand packed water saturated column. They found that an increasing oxidation of the surface mineral oil coating increases the phase shift, indicating a strong dependence on the coating surface chemistry. In their critical review on methods to characterize the fate of nZVI in groundwater, Shi et al. (2015) highlighted the necessity to further develop geophysical methods as tools to track the fate and transport of NPs in both laboratory and field settings. Flores Orozco et al. (2015) successfully monitored the injection of guar-gum (GG) coated microscale ZVI, and remains to-date the single field-scale application, and only one of two studies that have monitored NPs under realistic conditions, surrounded by a coating. While existing studies have highlighted the method's potential and demonstrated its suitability, the extent to which SIP can serve as a quantitative metric for precise delivery applications, and the effects of stabilizing coatings on NP-mediated polarization mechanisms remain under-characterized.

In this study, we monitored the transport of a poloxamer-coated super-paramagnetic iron-oxide nanoparticle (SPION) suspension through natural aquifer sand using SIP. We computed SPION concentration, within the columns, based on velocity and dispersion coefficients extracted

from a breakthrough-curve analysis of SPION concentrations, and compared these to measured SIP signatures. Using a simple modeling approach, similar to that in Slater et al. (2009) and Mellage et al. (2018), we established quantitative relationships between σ'' and SPION concentrations in the sand material. Through the analysis of parameters extracted from the fit of a double Cole-Cole relaxation to measured spectral responses, we further assessed the application of SIP as a tool for monitoring NP concentration changes in porous media, as well as shed light on the possible mechanisms controlling the SIP response associated with coated NPs in soils.

6.3 Methods

6.3.1 Nanoparticle characterization

SPIONs coated with oleic acid and Pluronic P104 were synthesized through a hydrothermal treatment followed by a Pluronic coating phase-transfer for stabilization in water. The size and morphology of the NPs were characterized by Dynamic Light Scattering (DLS, Brookhaven 90Plus Particle Size Analyzer) and Transmission Electron Microscopy (TEM, Philips CM10, 60 keV) to have an average diameter of 9.54 ± 2.70 nm, (see Figure AE 1 in Appendix E). The lognormal peak diameter measured by DLS was determined to be 44 nm with a polydispersity index of 0.142 (see Figure AE 2 in Appendix E). The larger hydrodynamic radius, measured by DLS, reflects the water-swelled Pluronic P104 polymer shell around the iron oxide NP. A schematic of the coated NP structure is presented in Figure 6-1. Concentration of NPs in aqueous suspension was determined through quantitative Fe analysis by inductively coupled plasma optical emission spectroscopy (ICP-OES, Teledyne Leeman Prodigy, method detection limit (MDL) of 4 µg L^{-1}) after digestion with 6 mol L^{-1} HCl acid. Detailed information regarding the synthesis of the SPIONs can be found in Appendix E.

6.3.2 Flow-through columns

SPION flow-through experiments, with in-line SIP monitoring, were performed in three identical high-density polyethylene (HDPE) columns (wall thickness: 0.5 cm, length: 15.8 cm, inner diameter: 4.1 cm) (Figure 6-2). The columns were all fitted with lateral ports for SIP electrode emplacement (see below). The columns were threaded at either end and sealed with HDPE screw caps. The bottom cap of the columns had an inflow channel to supply input solution, and the top cap had an outflow channel to recover the effluent. A polypropylene membrane filter

(0.2 µm pore size, 50 mm diameter, Pall Life Sciences, Port Washington, NY, USA) and a fibreglass filter (5 µm pore size, 47 mm diameter, Pall Life Sciences) were placed on each side before the endcaps were attached to the columns. The columns were connected to a peristaltic pump (Minipuls 3; Gilson, Middleton, WI, USA) with equal lengths of viton tubing (1/16" i.d.; 1/8" o.d.; 1/32" wall, Cole-Parmer Instrument Company, Vernon Hills, IL, USA). Aquifer material (herein referred to as Borden sand) was collected from the University of Waterloo Groundwater Research Facility at the Canadian Forces Base (CFB) Borden located near Alliston, ON, Canada. The hydrogeological properties of Borden sand have been extensively studied and a grain size distribution analysis is presented in Appendix E, in Figure AE 3 (Mackay et al., 1986; MacFarlane et al., 1983). The Borden sand was sifted with a 3.36 mm mesh (mesh No. 6), dried at 90 °C for 12 hours and wet packed in the columns using a 1 mM NaCl solution as the saturating pore water. The experiments were performed at room temperature (22 ±2 °C).

Following packing, all columns were flushed for at least 38 hours (~2 pore volumes (PVs)) with 1 mM NaCl solution at an average flow rate of 3.7 (±0.12) $cm^3\ h^{-1}$. Two of the columns (Col-1 and Col-2) were further pre-flushed with a solution containing 0.2 g L^{-1} P104 Pluronic surfactant and 1 mM NaCl for 52 hours. The amphiphilic P104 polymer was used to coat the SPION surface to stabilize the NPs in aqueous suspension. P104 polymer is in equilibrium with the surface of the SPIONs and the surrounding solution, resulting in freely mobilized P104 in addition to that attached to the SPION surface. A 0.2 g L^{-1} P104 pre-flush was used to minimize sorption-related interactions between freely mobilized P104 and the Borden sand during SPION transport (by effectively pre-saturating sorption sites), which might affect the SIP response, hence, masking the signal of the SPIONs themselves. The concentration of 0.2 g L^{-1} was chosen on the basis of preliminary SIP measurements on Borden sand batch-columns (no-flow) wet packed with P104 containing solution, where no significant difference was observed on the σ'' response when packed with pore solution containing higher concentrations. This approach was based on findings that NP retention in soils decreases upon successive injections of nanoparticles (*i.e.*, the attachment sites become increasingly saturated) (Zhang et al., 2015). The remaining column (Col-3) was only pre-flushed with 1 mM NaCl, to serve as a baseline to highlight these background interaction effects (for details regarding the preliminary injection phases see Appendiz E, Figure AE 6). Following the P104 pre-flush, a SPION suspension (2.8 ±0.078 $g_{Fe}\ L^{-1}$, equivalent to 3.87 $g_{SPION}\ L^{-1}$) was continuously injected into all columns for 40 hours.

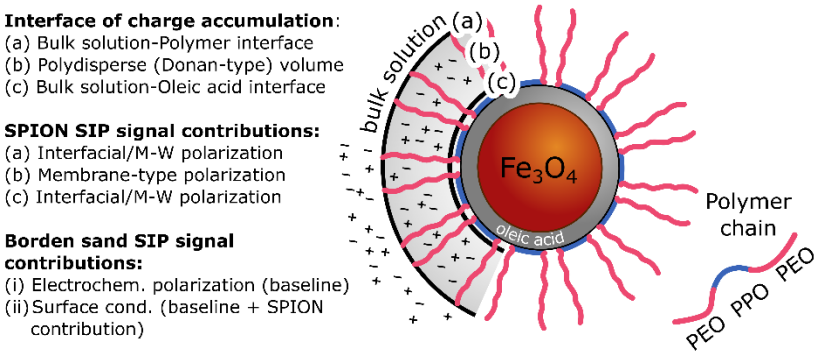

Figure 6-1. Schematic of the coated SPION particles, modified from Linley et al. (2019). Oleic acid covers the SPION iron-oxide core (Fe_3O_4, d = 10 nm), and binds the hydrophobic polyethelene oxide (PEO) blocks of the P104 polymer-chain, effectively binding the coating to the nanoparticles. The hydrophilic polyethylene oxide (PPO) blocks extend away from the core, into the aqueous phase (total hydrodynamic diameter = 44 nm). Interfaces of charge accumulation (a), (b) and (c) include the bulk solution-P104 interface, the polydisperse volume, defined as a Donnan-type volume (Benedetti et al., 1996; Kinniburgh et al., 1996; Plette et al., 1996; Marinsky et al., 1983), within the attached polymer cloud, and the exposed oleic acid-bulk solution interface. Polarization and conduction mechanisms contributing to SIP signals are summarized in the text on the left hand side for each interface and the background Borden sand porous medium.

Effluent samples (see Figure 6-2) were taken at the onset of injection, and every 1 to 2 hours starting at 10 hours after injection, by collecting effluent over a 15 min interval. Samples were acid digested using 0.2 mL of 12.1 M HCl (37%, Fisher Scientific) and diluted by a factor of 71.5. The iron concentration of the digested, diluted sample was measured using Inductively Coupled Plasma – Atomic Emission Spectroscopy (ICP-AES; Teledyne Leeman Labs, NH, USA, MDL of 4 µg L^{-1}). The flow rate of each column was monitored individually by determining the volume collected in each outflow sample.

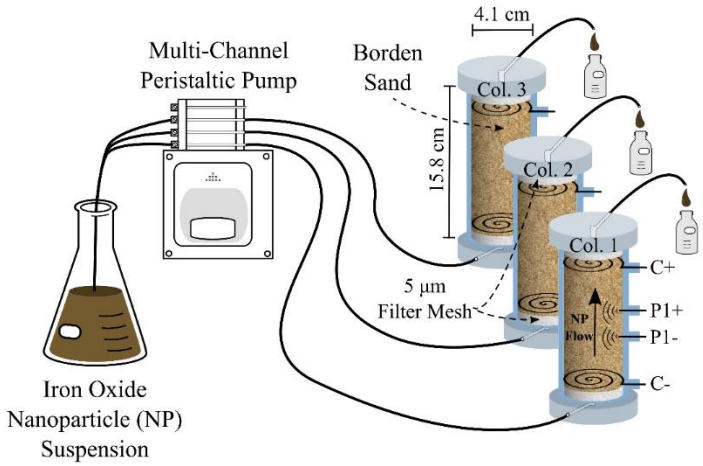

Figure 6-2. Schematic of the column experimental setup, where iron oxide NP suspension was injected via a peristaltic pump into three columns packed with Borden aquifer sand; C and P indicate the current and potential electrodes (+ and -) in the electrode array.

6.3.3 SIP measurements

The three columns were instrumented with non-polarizing Ag-AgCl potential electrodes and Ag-AgCl current coil-electrodes (Figure 6-2), to monitor the response of the moving NP front during SPION injection from the bottom of the columns. Ag-AgCl potential electrodes were filled with 1M KCl, 15 g L^{-1} agar gel, encased in nylon 1/2" NPT compression fittings and placed in the center of the columns, 2.5 cm apart. Two Ag-AgCl coil-current electrodes were placed 4 cm from each potential electrode at the top and bottom of each column. Current was injected through the outer coil electrodes and output voltage was measured at the potential electrode pair, across a spatial response domain (roughly, the distance between the outer edges of the electrodes) (Mellage et al., 2018). Impedance (Z) measurements on a series of solutions of known resistivity (ρ_a) were used to determine the geometric factor, k, of the electrode array ($\rho_a = kZ$) (Mellage et al., 2018; Zhang et al., 2014). SIP responses were recorded at each potential electrode pair using a Portable Spectral Induced Polarization (PSIP) Unit (Ontash & Ermac Inc., NJ, USA). Phase shift ($-\varphi$) and conductivity magnitude ($|\sigma|$) were measured at 51 log frequency intervals between 0.1 and 10,000 Hz. Relaxation times (τ) and chargeabilities (m) were extracted from the spectral response by fitting a double Cole-Cole relaxation model (equation 6.2), using a non-linear least squares fitting algorithm implemented in the SciPy package (Weigand and Kemna, 2016c; a).

6.3.4 SPION transport characterization

Due to the presence of Ag metal electrodes (and Ag's affinity to several anions, *e.g.,* Cl^- and Br^-) within the columns, fluorescein (D_{aq} = 0.0173 cm^2 h^{-1}) was used as a conservative tracer (Haberer et al., 2011; Chiogna et al., 2009) to characterize transport in the SIP-measurement columns. A solution containing 15 mg L^{-1} fluorescein was injected after the NP injection in one of the Borden sand packed columns (Col-2). Samples were collected at the outflow every 30 or 60 min starting at 9 hours after injection. Fluorescence was measured using a FlexStation 3 mutli-mode microplate reader (Molecular Devices, San Jose, CA, USA).

6.3.5 Transport simulation

Transport of SPIONs through the sand columns can be described by the one-dimensional (1D) advection-dispersion equation:

$$\frac{\partial C}{\partial t} = D\frac{\partial^2 C}{\partial x^2} - v\frac{\partial C}{\partial x} - \rho_b \frac{\partial S}{\partial t} \quad 6.3$$

where C [g cm^{-3}] is the aqueous concentration of NPs, D [cm^2 h^{-1}] is the dispersion coefficient, v [cm h^{-1}] is the flow velocity, ρ_b [g cm^{-3}] is the bulk density of the porous medium, S [g g^{-1}] is the solid phase (attached) NP concentration. Attachment and detachment of NPs governs particle mass transfer between the aqueous and solid phases (Zhang et al., 2015). A single-site kinetic colloid attachment and detachment model, assuming Langmuirian dynamics (Adamczyk et al., 1994), was applied to simulate nanoparticle retardation in the Borden sand:

$$\rho_b \frac{\partial S}{\partial t} = k_a C\left(1 - \frac{S}{S_{max}}\right) - k_d \rho_b S \quad 6.4$$

where k_a [h^{-1}] and k_d [h^{-1}] are first-order attachment and detachment coefficients, respectively, and S_{max} [g g^{-1}] is the maximum solid phase concentration of attached NPs. Hydrus 1D (H1D) was used to numerically solve equation 6.3 and simulate solute and nanoparticle (*i.e.*, colloid) transport in the column experiment (Simunek et al., 2005).

6.4 Results and discussion

6.4.1 Dye tracer injection

The fit of the numerical solution of the advection-dispersion equation (H1D) for a continuous tracer injection to the fluorescein breakthrough data (Figure 6-3a) yields transport parameters for the Borden sand in the experimental columns (see Table 6-1). Figure 6-3b illustrates the predicted conservative solute concentration in the middle of the columns, and the average concentration integrated over the spatial response domain of the potential electrodes. The latter was determined to be between 4.5 to 11.5 cm, based on the best fit to the results presented below.

Spatial averaging across the electrode response domain allows us to capture the non-uniform concentration distribution of NPs within the measurement range of the SIP potential electrode pair (Figure 6-3c). Because the SIP measurement is not a point measurement, but integrates signals generated across a region, at early times, the bottom electrode detects slight concentration changes even when the moving front has not yet reached the middle of the column (0.3 PVs in Figure 6-3c). That is, NP breakthrough is detected by SIP before NP concentrations are measurable at the column midpoint. Similarly, up to 0.6 PVs, the upper electrode detects minimal NP signal contribution, effectively "diluting" the apparent concentration being "seen" by the electrodes (Figure 6-3c). The

spatial averaging approach illustrated in Figure 6-3 takes into account the spread of the NP concentrations and relates them to the measured SIP σ' and σ'' responses.

Table 6-1. Transport parameters: v is the flow velocity, n_e is the calculated effective porosity, α_l is the longitudinal dispersivity, D_m^j is the aqueous diffusion coefficient (where j is fluorescein or SPION), t_{PV} is the time for one pore volume, k_a and k_d are the kinetic attachment-detachment model rate constants, and S_{max} is the maximum attachment capacity. The latter parameter values were used to fit the delayed breakthrough in Col-3. Relationships between simulated SPION concentrations (averaged over the 4.5 to 11.5 cm domain) and measured imaginary conductivity (σ'') for all columns (Col-1 and 2 were pre-flushed with P104 co-polymer and Col-3 was not).

Transport Parameters			**SPION-σ'' relationship**[c]		
					R^2
v	[cm h^{-1}]	0.76	Col-1	$\sigma'' = 3.3e\text{-}6 \times C_{NP} + 3.5e\text{-}5$	0.98
n_e	[-]	0.34 ($\pm$0.01)	Col-2	$\sigma'' = 3.9e\text{-}6 \times C_{NP} + 3.9e\text{-}5$	0.99
α_l	[cm]	0.028	Col-3	$\sigma'' = 1.08e\text{-}6 \times C_{NP}^2 - 1.05e\text{-}6 + 4.2e\text{-}5$	0.96
D_m^{Fluo}	[cm^2 h^{-1}]	1.73×10^{-2}			
D_m^{SPION}	[cm^2 h^{-1}]	3.55×10^{-4}			
t_{PV}	[h]	19.5			
k_a	[h^{-1}]	1			
k_d	[h^{-1}]	0.5			
S_{max}	[g g^{-1}]	0.083			

[c]Relationship between simulated aqueous SPION concentrations (C_{NP} [g L^{-1}]) and measured imaginary conductivity (σ'' [S m^{-1}])

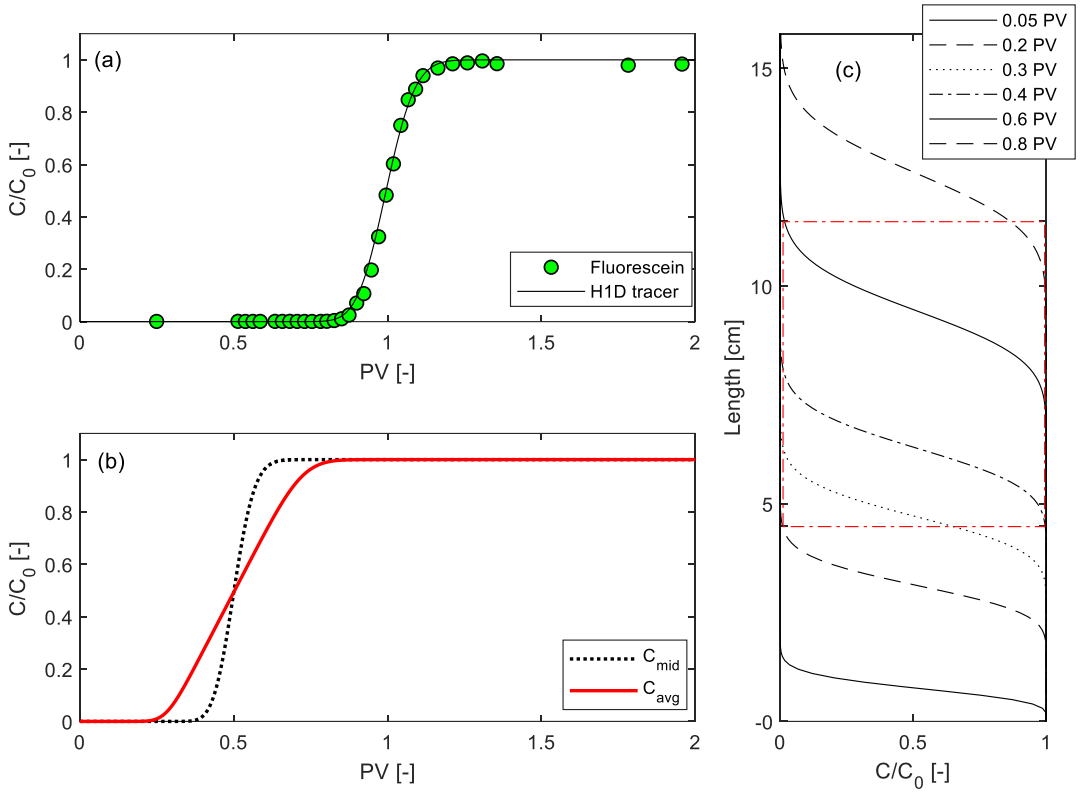

Figure 6-3. Normalized fluorescein breakthrough curve and simulated conservative solute concentration for a continuous injection (a), simulated solute concentration at both the center (l = 7.9 cm) of the column (C_{mid}) and averaged, in space (C_{avg}), over a 4.5 to 11.5 cm length interval (b), and (c) simulated spatial concentration distribution of conservative solute in the 15.8 cm column with increasing pore volume (PV), the red rectangle illustrates the spatial extent of the SIP electrode response domain, where the spatial average of the solute concentration is computed.

6.4.2 SIP responses

The time-variant spectral σ'' responses measured in Col-1 and Col-3 (P104 and NaCl pre-flushed, respectively) during continuous SPION injection are shown in Figure 6-4. The spectral response from Col-2 is presented in the Figure AE 5, in Appendix E. Both pre-treatments, NaCl pre-flushed (Figure 6-4a) and P104 pre-flushed (Figure 6-4b), show the background response of the flushed Borden sand at PV = 0 (onset of injection) with a frequency peak at 600 Hz. We attribute this background σ'' to electrochemical polarization of the unconsolidated sandy medium, and its small clay and silt fractions (2%). Electromagnetic coupling effects are evident in the data above 5,000 Hz, but remain at frequencies well above the background peak frequency. These effects are more pronounced in Col-2 and appear above 2,000 Hz (Appendix E, Figure AE 5). For both pre-treatments, increasing time from injection resulted in an increase in σ'' above 80 Hz and a decrease in σ'' below 80 Hz. The peak σ'' above 80 Hz shifted to higher frequencies with injection progress (discussed with Cole-Cole relaxation results, see below). The changes in σ'' reported in Figure 6-4, correspond to phase changes on the order of 2 mrad. Measured impedance (Z) and phase ($-\varphi$) spectra for Col-1 are presented in Figure 6-5. Increasing time from SPION injection (PV = 0) results in a decrease in Z and an overall decrease in $-\varphi$ with a shift in peak $-\varphi$ to higher frequencies as injection progresses (*i.e.*, increasing SPION concentration). Overall, these signal changes translate to increases in electrolyte conductivity and charge storage as shown in the real and imaginary conductivity datasets presented herein. Spectral phase shift and impedance data for Col-1 are presented in Figure 6-5, and time series are shown in the Appendix E, in Figure AE 4.

In the context of the oleic acid, polymer-coated SPIONs, the polydisperse cloud coating the iron-oxide core (illustrated in Figure 6-1) forms a permeable gel-like phase, similar to that of humic substances and bacterial cell walls. The gel-like, polydisperse interface between polymeric substances (*i.e.*, the P104 co-polymer) and the aqueous phase negates the applicability of the standard EDL model, due to the lack of sharp, non-permeable potentiometric interfaces (Louie et al., 2012; Ohshima, 1995). The NICA-Donnan model (Kinniburgh et al., 1996; Koopal et al., 1994; Marinsky et al., 1983), for metal ion binding, accounts for the three-dimensional (3D) structure and permeable nature of "soft" polymeric substances, and has been shown to robustly capture complexation onto humic acids (Benedetti et al., 1996; Kinniburgh et al., 1996), bacterial cells walls (Plette et al., 1996; Plette et al., 1995), and extracellular polymeric substances (EPS) (Lamelas et al., 2006), by explicitly accounting for a polydisperse so-called Donnan volume.

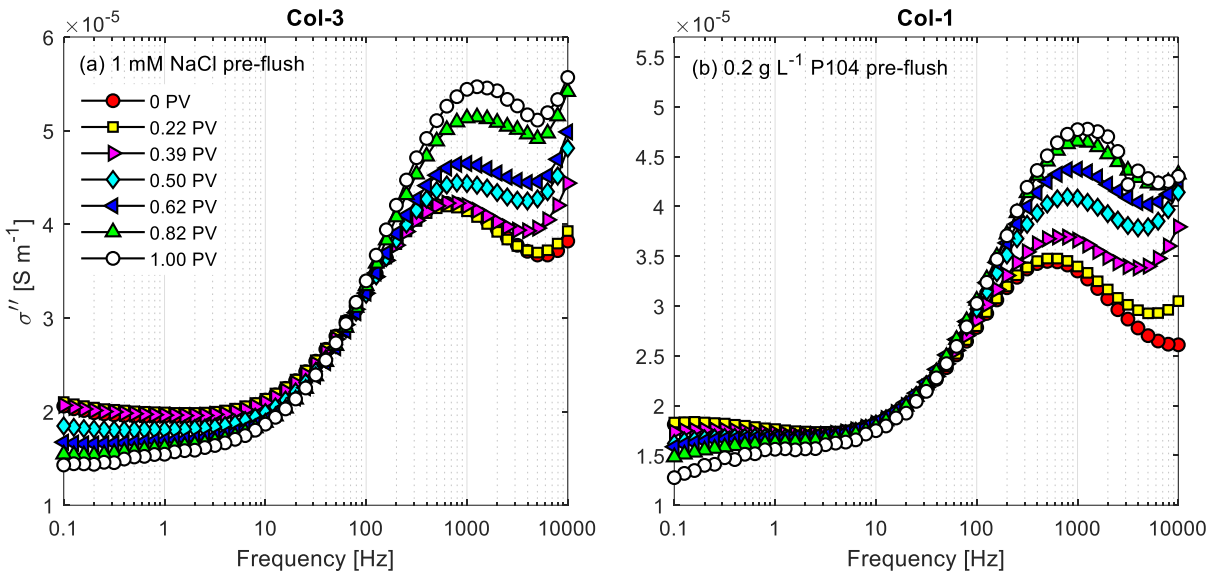

Figure 6-4. Spectral (0.1 to 10,000 Hz) SIP imaginary conductivity response during injection of SPIONs into (a) the column pre-flushed with monoionic 1 mM NaCl solution (Col-3) and (b) one of the columns pre-flushed with P104 Pluronic surfactant (Col-1). Each spectra represents a specific time, normalized as a pore-volume (PV) since SPION injection, here increasing PV, is proxy for increasing concentration.

Ultimately, the mechanisms governing polarization of coated nanoparticles remain largely unknown and have not been investigated in detail. In the following we speculate that the changes in σ'' above 80 Hz are likely a result of increasing NP concentrations, and integrate aspects of the Donnan volume theory to account for charge accumulation within the Donnan-type polydisperse volume of the coating, while also considering processes at the SPION coating-pore water interface. In Figure 6-1, we have delineated three interfaces of charge accumulation, which contribute to the bulk polarization in parallel.

We postulate that entrapped charge within the Donnan-type volume of the polydisperse coating (interface (b) in Figure 1), results in charge accumulation within the polymer cloud, which leads to back-diffusion when current is applied. The latter mechanism is similar to membrane polarization within pore throats (*i.e.*, bottlenecks) (Shefer et al., 2013; Olhoeft, 1985; Marshall and Madden, 1959), and has been labelled as "membrane-type polarization" in Figure 1. The small effective diameter (44 nm) of the SPIONs would result in polarization above 100 Hz (Joyce et al., 2012), where the contribution of Maxwell-Wagner (interfacial) polarization becomes an increasingly important mechanism governing charge storage (*i.e.*, imaginary conductivity, σ'', and chargeability, m) (Leroy and Revil, 2009; Leroy et al., 2008). Interfacial polarization is a result of "field induced free charge distributions near the interface between" phases in a single medium (Leroy and Revil, 2009), and occurs in mixtures of materials or phases with different dielectric permittivities and electrical conductivities (Chen and Or, 2006). The coated nanoparticle-electrolyte interface likely results in the formation of free charge distributions, magnified by the presence of an insulative coating (Pluronic P104 co-polymer) on the SPION surface (interface (a) in Figure 6-1) (Jougnot et al., 2010), resulting in a larger contrast in the dielectric properties of SPIONs and the bulk solution (Chen and Or, 2006). Additionally, the higher electrical conductivity (EC) of the SPION suspension, relative to both the 1 mM NaCl and 0.2 g L^{-1} P104 solutions (EC for all input solutions are presented in Table 6-2), is an added factor contributing to enhance interfacial polarization during SPION injection. A second, but likely less important contribution to Maxwell-Wagner polarization arises at the exposed oleic acid interface (see interface (c) in Figure 1). Schwartz et al. (2012) observed less pronounced differences in σ'' between NAPL contaminated samples and clean samples with increasing frequency, attributed to an increasing contribution of Maxwell-Wagner polarization approaching and above 100 Hz.

Considering the insulative properties of oil phases and their documented reduction of electrochemical polarization (Schwartz et al., 2012), we suggest that the iron-oxide particle core is sufficiently shielded from the external potential field, and does not contribute to polarization. Furthermore, Shi et al. (2015) measured gradually increasing phase shift with H_2O_2 injection into sand packed columns containing mineral oil-coated nZVI, from the gradual exposure of the nZVI particle core with progressive coating oxidation. The measurable increasing in phase shift provided experimental evidence to suggest that an oil coating onto a metal-based particle shields the inner particle core from the external potential field.

We hypothesize that the decreasing response at lower frequencies is a function of electrochemical interactions between the bound P104 surfactant coating of the SPIONs (and in equilibrium with the suspension) and the Borden sand, dampening the background response associated with electrochemical (EDL) polarization of larger diameter soil particles.

Table 6-2. Electrical conductivity (EC) of input solutions for the flow-through column experiments.

	Solution	**Electrical conductivity [μS cm^{-1}], at 24.2°C**
1	1 mM NaCl	127.3
2	0.2 g L^{-1} P104	124.0
3	SPION suspension	194.3

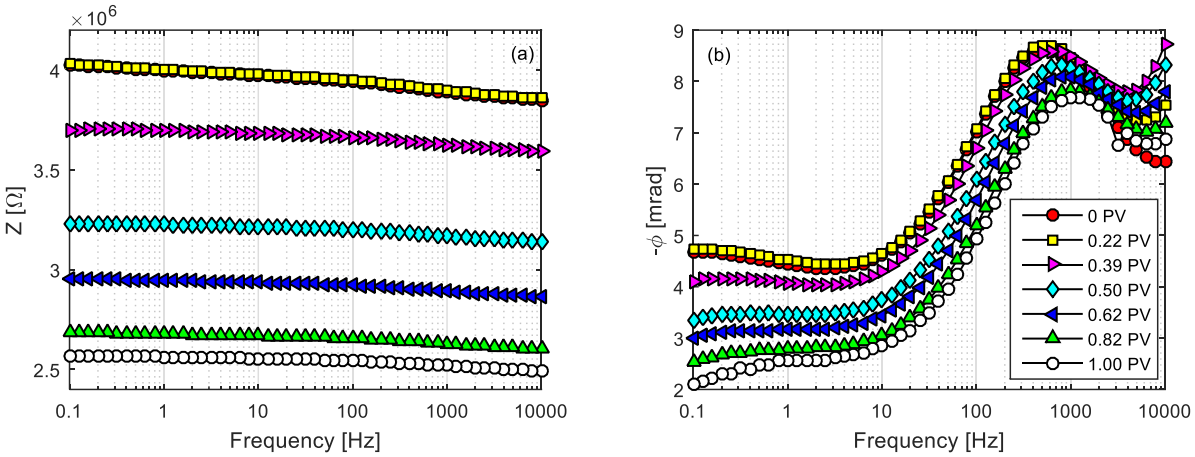

Figure 6-5. Spectral impedance (Z) and phase shift (-φ) responses (a and b, respectively) during SPION injection in column 1.

6.4.3 SPION concentration-SIP relationships

Outflow SPION concentrations along with simulated breakthrough curves are plotted for all three columns in Figure 6-6. The moving SPION front exhibits a sharp breakthrough in all three columns (Figure 6-6d-f). The NP outflow concentrations in both P104 pre-flushed columns (Col-1 and 2) closely match the simulated conservative breakthrough profile (using the v and α_l values from the fluorescein tracer breakthrough and an estimate for a molecular diffusion coefficient for SPIONs, from the Stokes-Einstein equation, see Table 6-1). The delayed breakthrough in Col-3 (not pre-flushed with P104), with respect to the expected conservative tracer breakthrough is fitted (Figure 6-6f) by introducing reversible adsorption (attachment/detachment) of NPs onto the Borden sand and a fitted maximum sorption capacity, S_{max}. Parameters for the Langmuirian attachment-detachment model are presented in Table 6-1, and fall within the ranges of values reported for an array of nanoparticles, coatings and porous media (Zhang et al., 2015).

The simulated spatially averaged concentrations across the potential electrode measurement domain (4.5 to 11.5 cm) are compared to the normalized peak (below 1000 Hz, to reduce electromagnetic coupling biases) σ' and σ'' values in Figure 6-6a-c. In both P104 pre-flushed columns (Figure 6-6a and b), the peak σ'' during SPION injection closely traces the simulated average concentration front. Conversely, there is a lag in the σ' response during injection, increasing after σ'' and lagging behind the simulated concentration changes. In both Col-1 and 2, σ'' exhibited a strong linear dependence on the average SPION concentration (R^2 of 0.98 and 0.99, respectively – see Table 6-1). This relationship, suggests that the coated SPIONs themselves influence the chargeability of the bulk medium. NP-mediated polarization (Leroy et al., 2008; Olhoeft, 1985) phenomena likely increase with increasing SPION concentration resulting in a proportional increase in σ''. (Note: we attribute the slight difference in regression parameters in Table 6-1 to packing heterogeneities between duplicate Col-1 and 2, which explain the slightly different SIP baselines.)

In contrast, σ' did not exhibit a proportional dependence on SPION concentration. In previous SIP-nanoparticle monitoring studies (Abdel Aal et al., 2017; Joyce et al., 2012) the absence of signal changes in the real contribution to σ^* has been reported. Our results suggest that resistivity and electrolyte conductivity (ERT and σ') can be sensitive to coated NP suspensions (for σ_w of all solutions see Table 6-2). Nevertheless, changes in σ' are not proportional to SPION concentration

and are likely governed by increasing σ_w and mixing at the interface between the incoming NP suspension and the pore-water devoid of NPs.

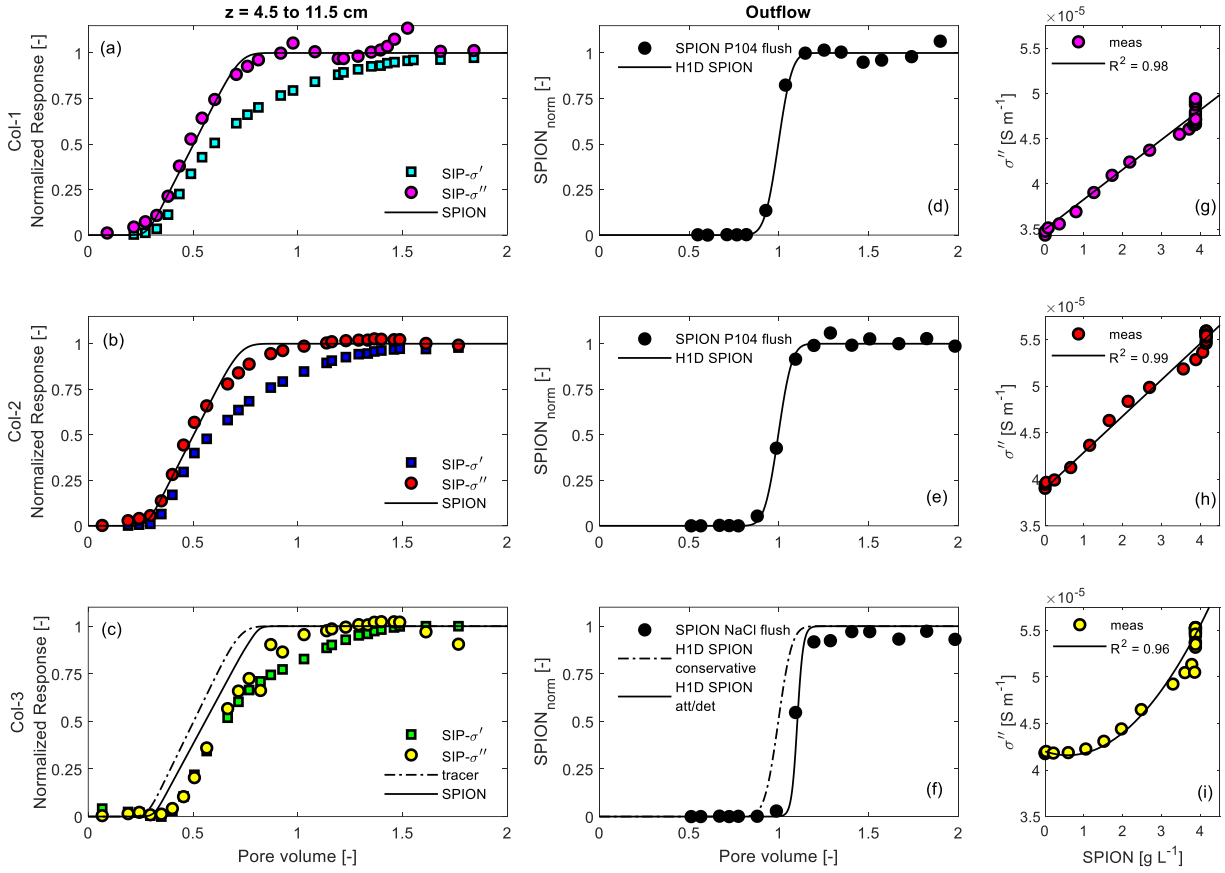

Figure 6-6. Normalized SIP real (σ') and imaginary (σ'') conductivities during injection of SPION suspension compared to numerically simulated average SPION concentrations between 4.5 and 11.5 cm in three Borden sand packed fully-saturated columns (a-c). Simulated (H1D tracer and H1D att/det) normalized breakthrough curves compared to outflow SPION concentrations (d-f). Relationships between σ'' and calculated average SPION concentrations in the effective range of the potential electrodes, for each column (panels g-i).

Despite the incorporation of attachment-detachment to fit the delayed breakthrough of SPIONs in Col-3 (not P104 pre-flushed), measured σ'' during SPION injection exhibited a lag with respect to the simulated concentration front (Figure 6-6c), that could not be captured by transport retardation. The offset between the SPION concentration and σ'' is apparent in the non-linear relationship (second-order polynomial, $R^2 = 0.96$, Table 6-1) between σ'' and the simulated SPION concentrations (Figure 6-6i). We speculate that the lag arises from electrochemical interactions between the Borden sand and the Pluronic P104 co-polymer, which coats the SPIONs and is present in solution in the SPION suspension (in equilibrium with the adsorbed co-polymer, as an artifact of the coating procedure, for NP coating details see Appendix E).

The P104 pre-flush was intended to minimize sorption interactions between the P104 surfactant and the Borden sand. During injection of 0.2 g L^{-1} P104 (see Appendix E, Figure AE 4) σ'' decreased, suggesting sorption of P104 onto Borden sand, which in turn reduces polarization of the sand (Schwartz et al., 2012; Vaudelet et al., 2011b). The P104 pre-flush would have saturated sorption sites and reduced further changes to the baseline SIP response after SPION injection (Zhang et al., 2015), resulting in the linear dependence between SPIONs and σ'' in the pre-flushed columns (Figure 6-6g and h). In the non pre-flushed column (Col-3), however, P104 in the incoming suspension would have attached onto the sand, reducing bulk polarization (Vaudelet et al., 2011b; Vaudelet et al., 2011a) and initially masking the increase of electrochemical and interfacial polarization of incoming SPIONs. These opposing signal contributions could explain the measured lag between σ'' and simulated SPION concentrations in Col-3. These findings suggest that monitoring with SIP of coated NPs in soil, is sensitive to the surface chemistry of the NPs as well as the coating molecules themselves.

6.4.4 Relaxation-time dynamics

Relaxation times (τ) for the high frequency peak (above 80 Hz), extracted from the fit of a double Cole-Cole relaxation (Weigand and Kemna, 2016c) to the measured phase and impedance spectra from Col-1 and 3 (P104 pre-flushed and 1 mM NaCl preflushed, respectively), are presented in Figure 6-7. The goodness of fit of the dual Cole-Cole is illustrated in Figure 6-7c and d. The Cole-Cole equation was not fitted to the spectral data from Col-2 because of strong electromagnetic coupling effects above 2,000 Hz masking the distinct frequency peak (see Figure AE 5, in Appendix E).

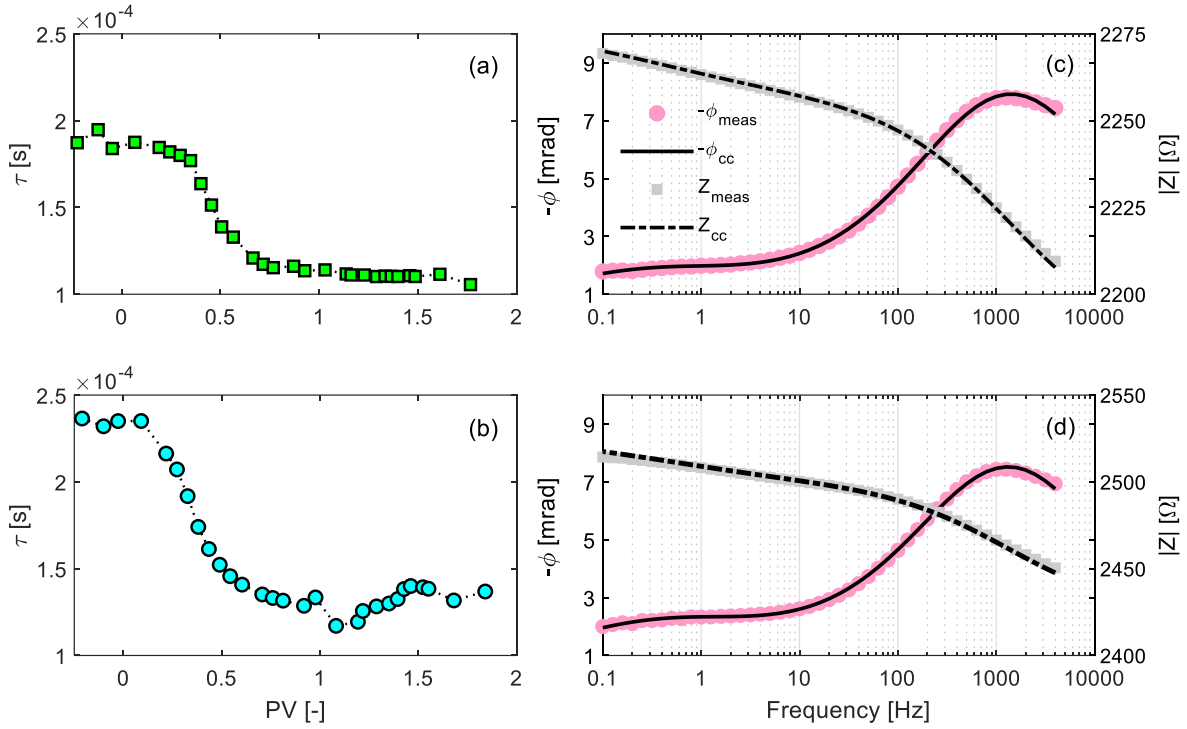

Figure 6-7. Cole-Cole relaxation time (τ) (high frequency peak) during SPION transport in (a) 1 mM NaCl pre-flushed Col-3 and (b) 0.2 g L^{-1} P104 Pluronic pre-flushed Col-1. Panels (c) and (d) are examples of the double Cole-Cole at 1.4 pore volumes for Col-3 and Col-1, respectively.

During continuous SPION injection, τ gradually decreased in both pre-treatments from roughly 2×10^{-4} to level off at 1×10^{-4} s, shortly before and after 0.5 PVs for columns 1 and 3, respectively. We can assert that the two-fold reduction in τ measured here, reflects the increasing contribution of SPIONs to the bulk electrochemical and interfacial polarization of the medium, and that their significantly smaller size (relative to Borden sand grains) reduces the effective polarization length-scale. At 0.5 PVs, the SPION concentration front was about half way through the electrode response domain (Figure 6-3c). The gradual drop in τ and stabilization before reaching maximum concentrations at the electrode spatial response domain suggests that the decrease is controlled by the presence of SPIONs within the electrode response domain and is not a function of increasing concentration. Conversely, Abdel Aal et al. (2017) reported increasing τ with increasing uncoated nAg concentrations. Presumably, the P104 coating used in our study reduced NP aggregation (Shi et al., 2015), while uncoated nAg particles probably aggregated in the soil mixture. The increases in τ, reported for increasing nAg concentrations (Abdel Aal et al., 2017), are, therefore, possibly a function of increased aggregation of nAg and an increase in the effective diameter of the polarizing particles.

In summary, spectral induced polarization (SIP) was successfully implemented to monitor the transport of SPIONs through natural aquifer sand and imaginary conductivity was found to be directly correlated with suspended SPION concentrations. Relaxation time dynamics provided evidence for the increasing contribution of smaller diameter particles to overall charge storage.

6.4.5 Environmental implications

Understanding and predicting NP mobility in heterogeneous porous media has been identified as a critical knowledge gap in NP-based targeted remediation techniques (Joo and Zhao, 2017; Lyon-Marion et al., 2017). Our results highlight the efficacy of SIP as a non-invasive technique for quantitatively detecting nanoparticles in natural porous media. We envision that the dependence of electrical signals on NP surface chemistry has exciting implications for SIP-based monitoring of remediation processes at contaminated sites. For example, oxidation of deployed nanoremediation agents such as nZVI results in reduced polarizability (Joyce et al., 2012; Wu et al., 2008), monitoring this decrease over time may serve as an indicator for the operational time of such agents. Previous literature has shown the possibility of designing nanoparticle coatings which

facilitate preferential attachment to contaminants in soil (Wang and Acosta, 2013; Saleh et al., 2007; Saleh et al., 2005).

As highlighted by Mellage et al. (2018), the magnitude of signals reported here (variations on the order of 2 mrad) would be challenging to resolve at the field scale. Nevertheless, the possibility exists for re-evaluating nanoparticle design to enhance surface charge storage and improve detection (Shi et al., 2015). We recommend that future research focus on integrating techniques such as SIP in NP design considerations, focusing on enhancing surface charge storage to improve detection. Furthermore, our results help advance the understanding of controls governing polarization dynamics of NP suspensions and poise SIP as a method for real-time monitoring of nanoparticle transport in microcosm and mesocosm studies.

7 Conclusions and Perspectives

7.1 Synthesis of major findings

Using a non-target approach (without a priori knowledge of major reactive controls) to geophysical monitoring of biogeochemical processes in Chapter 2, I showed that spectral induced polarization (SIP) and electrodic potential (EP) - in conjunction with periodic geochemical measurements - are powerful tools for determining the location and temporal variability of microbial distribution and activity, and resultant geochemical changes, in complex (near-natural organo-mineral matrix) soil environments. The SIP and EP signals recorded during the soil column incubation experiment, subjected to periodic variations in water saturation, showed a clear dependence on the depth-distribution of subsurface microbes and microbially mediated reactions.

The controlled experiments on growth of subsurface microbes in layered, no-flow and flow-through experiments, presented in Chapters 3 and 4, highlighted the direct dependence of imaginary conductivity (σ'') on microbial growth and decay dynamics (simulated and measured, Chapters 3 and 4, respectively). Integrating Cole-Cole relaxation results into the combined analysis of reactive transport model (RTM)-simulated reaction rates and SIP spectral responses, allowed for determination of polarization time-scales (Cole-Cole relaxation time, τ). Using existing models describing the tangential migration of ions along charged surfaces (Revil et al., 2012; Schwarz, 1962), I determined that the time-scales of polarization in Chapter 3, corresponded to effective polarization diameters between 1 and 3 μm. In Chapter 4, the concurrent measurements of cell size, allowed for the calculation of an apparent surface ionic diffusion coefficient (D_a) from Cole-Cole relaxation times. The match between the calculated D_a and surface-complexation-model predicted values, provided direct evidence to support that polarization of bacterial cells themselves controls chargeability dynamics. This is conceptualized in Figure 7-1.

Furthermore, relaxation time dynamics in Chapter 3 and 4 were shown to vary depending on the energetic conditions (available electron accepting pathway) and the accumulation of elevated concentrations of toxic nitrite (NO_2^-). For spectra with well-defined spectral-peaks, quantifying relaxation time can provide qualitative information of cell size, microbial activity and changes in the bacterial cell surface charging properties in response to metabolic toxicity-induced stress. In cases with less well-defined peaks, relaxation times may represent the combined signal of multiple processes, and would require additional experimental analyses to unravel individual contributions.

The RTM in Chapter 5, of the experimental results presented in Chapter 4, provided key insights into the metabolic stress response of *Shewanella oneidensis* to accumulation of excess NO_2^-. The attempt to inform the processes behind the relaxation time anomalies and SIP-σ'' changes, presented in Chapter 4, highlighted the necessity to account for the toxic effects of NO_2^- even at concentrations below 1 mM (previously reported toxicity threshold). The energy-rerouting framework adopted in the RTM, to fit microbial growth in the absence of electron acceptor, presents clear evidence of an energy storage mechanism by *S. oneidensis* during protonophore uncoupling. The simulated microbial growth curves match the trend in SIP-σ'', further validating the model output.

The coupling of an RTM with outflow sampling and SIP measurements in the flow-through experiments monitoring nanoparticle (NP) breakthrough in natural aquifer sand in Chapter 6, allowed for the development of quantitative relationships between engineered nanoparticle concentrations and SIP-σ''. The excellent agreement between simulated NP concentrations and imaginary conductivity, introduced the possibility of non-invasive monitoring of polymer-coated metal-oxide NPs in natural aquifer sediment, with immediate and potential applications at the lab and field scales, respectively.

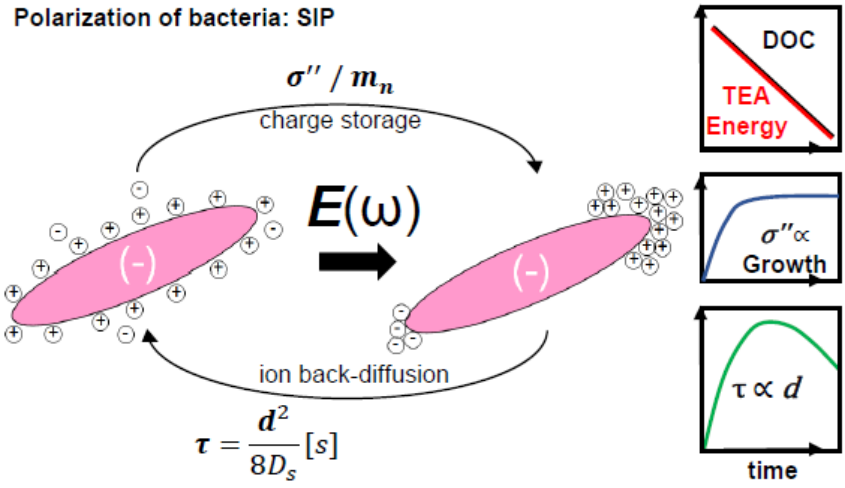

Figure 7-1. Conceptual diagram depicting the electrochemical polarization of negatively-charged microbial cells when a frequency-dependent electrical current, *E(ω)*, is injected. Polarization of cells induce charge storage, quantified as imaginary conductivity (σ'') or normalized chargeability (m_n). The time-scale for ion back-diffusion (*i.e.*, the relaxation time, τ) is governed by the effective length-scale or diameter (d) of the polarizing particles.

7.2 Research perspectives

There has been a substantial body of work that has been successful at determining biogeochemical controls that drive changes in SIP (and other geophysical methods) signals. Despite the overall acceptance of SIP's applicability to monitor subsurface biogeochemistry within the geophysical community, the earth and environment communities (*e.g.*, soil biogeochemistry, contaminant hydrogeology, and geomicrobiology) that can directly benefit from the application of non-invasive techniques have largely ignored the method. I believe this is, in large part, because of the inherent ambiguity of SIP measurement interpretation. A single reaction can result in multiple changes to the overall surface charge of a sample, and at the same time, multiple reactions can affect surface charge, it is therefore challenging to unequivocally couple SIP to a reactive transport process of interest. Future work must focus on outlining SIP's realm of applicability. For example, by delineating cases when it can be used as a qualitative metric to inform site characterization and remediation, and when it has the potential to provide quantitative information of colloidal transport processes and mineral precipitation and dissolution. Furthermore, I believe that the combination of geophysical datasets with microbiological, and geochemical datasets introduces the opportunity to apply innovative data-driven, pattern recognition approaches to take advantage of the large volume of information generated.

7.2.1 Integrating geophysical methods as soil biogeochemistry monitoring tools

The relevance of geophysical methods within soil biogeochemistry lies in applications where traditional techniques are unable to capture the information required to validate or inform the interpretation of processes. Essentially, this was done in chapter 2, where a direct increase in imaginary conductivity was measured during periods of aeration into deeper sections of the soil. In systems undergoing drastic changes in environmental conditions that lead to pulses of stimulated microbial activity, SIP can provide information on the timing and spatial location and extent of microbes driving these responses. An example of such a system, is a humid, temperate soil environment that undergoes a winter freeze and spring thaw. During the spring thaw, field monitoring stations routinely measure large fluxes of soil-derived greenhouse gases (CO_2, N_2O and CH_4), byproducts of aerobic and anaerobic microbial respiration reactions (Raz-Yaseef et al., 2017; Merbold et al., 2013). Production of nitrous oxide (N_2O), for example, has been linked to *de novo* microbial production (Wagner-Riddle et al., 2008), that can lead to significant worldwide

emissions (Wagner-Riddle et al., 2017). However, the depth at which the microbial community activates with warmer temperatures remains unclear. The lack of understanding of mechanisms that drive the spatial and temporally variable response of soil greenhouse gas emissions severely limits our ability to predict a system's response to environmental change (Imer et al., 2013), and relate the dynamics to the controlling environmental factors. Furthermore, increased delivery of dissolved organic and inorganic carbon into groundwater and surface water, during the spring, has been linked to stimulated microbial activity below the snow-covered soil surface (Carey, 2003). The lack of sampling campaigns throughout winter months at northern latitudes make these peak fluxes difficult to capture, let alone the processes that generate them. Applying SIP at both the lab (analogous to the experiment in Chapter 2) and field scales would introduce the possibility of measuring changes in electrical signals directly related to microbial activation, brought on by changes in moisture content, temperature and dissolved organic carbon accumulation. In this case, qualitative geo-electrical information could be used to better inform the timing and depth-zonation of biogeochemical activity. In turn, this would aid in constraining conceptual models characterizing reactive processes and aid in delineating a targeted measurement campaign.

7.2.2 Integrating geophysical datasets with reactive transport at the field scale

Geophysical datasets at the field-scale can aid in informing and validating field-scale RTMs. The approach taken in Chapter 3 can be adapted to larger scale datasets, where time-lapse geophysical signals are used to validate reaction rates as well as the spatial zonation of processes. Additionally, reactive transport signals can be applied to help inform processes within predictive models. The challenge lies in the integration of geophysical methods with existing modeling frameworks. Hydrogeophysical data do not relate directly to RTM-generated outputs (*e.g.*, geochemical speciation data, reaction rates and solute concentrations), therefore, their integration requires the establishment of relationships between model parameters and method-specific outputs (*i.e.*, conductivity) (Li et al., 2017). The development of an integration framework would require bench-scale experiments to develop the relationships between the techniques applied and the targeted information we are trying to gather. For example, high resolution hydrogeophysical signal changes can be related to specific process via computed reaction rates. This would allow for the development of system-specific semi-quantitative relationships that can be applied to inform and setup a catchment- or field-scale model at an analog site.

The increasing volume of data generated from experimental and modeling approaches, across a variety of scientific disciplines, has introduced a new paradigm (in addition to: experimental science, theoretical science, and computer simulations) to scientific research: data-intensive or data-driven science (Bell et al., 2009). The incorporation of geophysical measurements as a tool to aid in characterizing biogeochemical cycling and contaminant transport inherently increases the volume of data from a specific experimental or field application. The necessity to benchmark geophysical measurements with specific geochemical markers, and the need to establish relationships between reactions and geo-electrical signal changes (as demonstrated in this thesis), further increase the general data-load. The integration of different types of data in multidisciplinary measurement campaigns, would benefit from data-driven approaches to recognize patterns across datasets and inform biogeochemical processes. Such approaches are applied when aggregating data types in microbiological applications at the genome scale (Wang et al., 2014; Troyanskaya et al., 2003). Neural network classification is also applied in geophysics for feature recognition in ground penetrating radar (GPR) datasets (Al-Nuaimy et al., 2000). Automated Bayesian and statistical frameworks for pattern recognition across multidisciplinary datasets, collected at different spatial and temporal resolutions, and spatial dimensions would help extract embedded information that would otherwise remain hidden to the observer. The combination of data mining techniques with coupled geophysical-biogeochemical monitoring has the potential to inform reactive processes, improving processes-based model formulations.

7.2.3 Improving SIP's sensitivity to coated-engineered nanoparticles

Flores Orozco et al. (2015), demonstrated the applicability of complex conductivity (σ^*) monitoring of coated micro-scale ZVI delivery in a contaminated aquifer, with implications for nano-scale remediation agents. Both Flores Orozco et al. (2015) and Shi et al. (2015) highlight the importance of surface coating properties of micro and nanoparticles on modulating their surface charge, as well as the importance of changes to those properties with prolonged reactivity. In line with the aforementioned studies, in Chapter 6, I showed that the properties of NP-stabilizing coatings greatly alter the surface chemistry of engineered NPs, modulating their surface charge characteristics. Surface coatings, ensure NP deliverability and are often designed for compound-specific reactivity (Shi et al., 2015; Phenrat et al., 2010; Saleh et al., 2007). Quantitative sensing applications of geophysics for NP monitoring rely on an in-depth understanding of the

modification of polymer coatings to NP surface charge, the possible interactions between coating compounds, and the background porous medium and the durability of coating structural longevity on the NPs themselves (Chapter 6, Mellage and Holmes et al., in review).

The work outlined in Chapter 6, is to my knowledge, the first to explore SIP's quantitative potential for sensing coated metal-oxide NPs. The engineered NPs applied in Chapter 6 are designed to transport conservatively. Nevertheless, the co-polymer pre-flush that was necessary to reduce polymer-soil interactions, highlighted the potential of interactions of the polymer-coatings themselves with the background porous medium and their effect on the bulk chargeability of a sample. Different types of NPs can react differently with aquifer sediments, and the travel path of a particle can modify the integrity of the polymer coating, changing the surface composition of the injected NPs (Saleh et al., 2007). Increasing coating-layer thickness decreases NP agglomeration and deposition, but results in a higher degree of excess (unadsorbed) polymer that can promote flocculation and interact with the soil medium (Phenrat et al., 2010). These processes need to be taken account when developing geophysically-based sensing approaches for deployed nano-remediation agents.

The complex physical and chemical mechanisms modulating NP-associated electrical responses are part of the reason for the lack geophysical sensing applications to characterize targeted delivery of NPs. There is a need for systematic, increasing complexity experiments to explore the relationships between induced polarization of NPs traveling through natural aquifer sediments and (1) different stabilizing coating types, (2) various coating densities or thicknesses, and (3) the effects of unadsorbed (excess) polymer-soil interactions on background chargeability. Effectively, characterizing the effects of these masked processes within complex conductivity responses, will ensure an in-depth understanding of the processes modulating geophysical signal changes during NP delivery and reactivity. The increasing complexity experiments will also help inform ways to not only modify particle coatings to increase deliverability and reactivity (*e.g.*, Phenrat et al. (2010)), but also chargeability – unraveling ways to enhance detection.

References

Abdel Aal, G., Atekwana, E., Radzikowski, S., and Rossbach, S. (2009). Effect of bacterial adsorption on low frequency electrical properties of clean quartz sands and iron-oxide coated sands. *Geophysical Research Letters*. *36*(4), L04403.

Abdel Aal, G., Atekwana, E. A., and Werkema Jr, D. D. (2017). Complex conductivity response to silver nanoparticles in partially saturated sand columns. *Journal of Applied Geophysics*. *137*, 73-81.

Abdel Aal, G. Z., and Atekwana, E. A. (2014). Spectral induced polarization (SIP) response of biodegraded oil in porous media. *Geophysical Journal International*. *196*(2), 804-817.

Abdel Aal, G. Z., Atekwana, E. A., Slater, L. D., and Atekwana, E. A. (2004). Effects of microbial processes on electrolytic and interfacial electrical properties of unconsolidated sediments. *Geophysical Research Letters*. *31*(12), L12505.

Abdel Aal, G. Z., Slater, L. D., and Atekwana, E. A. (2006). Induced-polarization measurements on unconsolidated sediments from a site of active hydrocarbon biodegradation. *Geophysics*. *71*(2), H13-H24.

Adamczyk, Z., Siwek, B., Zembala, M., and Belouschek, P. (1994). Kinetics of localized adsorption of colloid particles. *Advances in Colloid and Interface Science*. *48*, 151-280.

Akbarzadeh, Z., Laverman, A. M., Rezanezhad, F., Raimonet, M., Viollier, E., Shafei, B., and Van Cappellen, P. (2018). Benthic nitrite exchanges in the Seine River (France): An early diagenetic modeling analysis. *Science of the Total Environment*. *628*, 580-593.

Al-Nuaimy, W., Huang, Y., Nakhkash, M., Fang, M., Nguyen, V., and Eriksen, A. (2000). Automatic detection of buried utilities and solid objects with GPR using neural networks and pattern recognition. *Journal of Applied Geophysics*. *43*(2-4), 157-165.

Aller, R. C. (1994). Bioturbation and remineralization of sedimentary organic matter: effects of redox oscillation. *Chemical Geology*. *114*(3), 331-345.

Almeida, J., Reis, M., and Carrondo, M. (1997). A unifying kinetic model of denitrification. *Journal of Theoretical Biology*. *186*(2), 241-249.

An, B., Liang, Q., and Zhao, D. (2011). Removal of arsenic (V) from spent ion exchange brine using a new class of starch-bridged magnetite nanoparticles. *Water Research*. *45*(5), 1961-1972.

Anneser, B., Einsiedl, F., Meckenstock, R. U., Richters, L., Wisotzky, F., and Griebler, C. (2008). High-resolution monitoring of biogeochemical gradients in a tar oil-contaminated aquifer. *Applied Geochemistry*. *23*(6), 1715-1730.

Anneser, B., Pilloni, G., Bayer, A., Lueders, T., Griebler, C., Einsiedl, F., and Richters, L. (2010). High resolution analysis of contaminated aquifer sediments and groundwater—what can be learned in terms of natural attenuation? *Geomicrobiology Journal*. *27*(2), 130-142.

Archie, G. E. (1942). The electrical resistivity log as an aid in determining some reservoir characteristics. *Transactions of the Metallurgical Society of AIME*. *146*(1), 54-62.

Atekwana, E. A., and Atekwana, E. A. (2010). Geophysical signatures of microbial activity at hydrocarbon contaminated sites: A review. *Surveys in Geophysics*. *31*(2), 247-283.

Atekwana, E. A., Atekwana, E. A., Rowe, R. S., Werkema, D. D., and Legall, F. D. (2004). The relationship of total dissolved solids measurements to bulk electrical conductivity in an aquifer contaminated with hydrocarbon. *Journal of Applied Geophysics*. *56*(4), 281-294.

Atekwana, E. A., Mewafy, F. M., Abdel Aal, G., Werkema, D. D., Revil, A., and Slater, L. D. (2014). High-resolution magnetic susceptibility measurements for investigating magnetic mineral formation during microbial mediated iron reduction. *Journal of Geophysical Research: Biogeosciences*. *119*(1), 80-94.

Atekwana, E. A., and Slater, L. D. (2009). Biogeophysics: A new frontier in earth science research. *Reviews of Geophysics*. *47*(4), RG4004.

Badocco, D., Mondin, A., and Pastore, P. (2012). Determination of thermodynamic parameters from light intensity signals obtained from oxygen optical sensors. *Sensors and Actuators B: Chemical*. *163*(1), 165-170.

Bastida, F., Kandeler, E., Moreno, J., Ros, M., García, C., and Hernández, T. (2008). Application of fresh and composted organic wastes modifies structure, size and activity of soil microbial community under semiarid climate. *Applied Soil Ecology*. *40*(2), 318-329.

Beccari, M., Passino, R., Ramadori, R., and Tandoi, V. (1983). Kinetics of dissimilatory nitrate and nitrite reduction in suspended growth culture. *Water Pollution Control Federation*, 58-64.

Bell, G., Hey, T., and Szalay, A. (2009). Beyond the data deluge. *Science*. *323*(5919), 1297-1298.

Belli, K. M., DiChristina, T. J., Van Cappellen, P., and Taillefert, M. (2015). Effects of aqueous uranyl speciation on the kinetics of microbial uranium reduction. *Geochimica et Cosmochimica Acta*. *157*, 109-124.

Belli, K. M., and Taillefert, M. (2018). Geochemical controls of the microbially mediated redox cycling of uranium and iron. *Geochimica et Cosmochimica Acta*. *235*, 431-449.

Benedetti, M., Van Riemsdijk, W., and Koopal, L. (1996). Humic substances considered as a heterogeneous Donnan gel phase. *Environmental Science & Technology*. *30*(6), 1805-1813.

Bhaumik, M., Maity, A., Srinivasu, V., and Onyango, M. S. (2011). Enhanced removal of Cr (VI) from aqueous solution using polypyrrole/Fe3O4 magnetic nanocomposite. *Journal of Hazardous Materials*. *190*(1-3), 381-390.

Bigalke, J., and Grabner, E. W. (1997). The geobattery model: a contribution to large scale electrochemistry. *Electrochimica Acta*. *42*(23-24), 3443-3452.

Billinton, N., and Knight, A. W. (2001). Seeing the wood through the trees: a review of techniques for distinguishing green fluorescent protein from endogenous autofluorescence. *Analytical Biochemistry*. *291*(2), 175-197.

Blagodatskaya, E., and Kuzyakov, Y. (2013). Active microorganisms in soil: critical review of estimation criteria and approaches. *Soil Biology and Biochemistry*. *67*, 192-211.

Blodau, C., Mayer, B., Peiffer, S., and Moore, T. R. (2007). Support for an anaerobic sulfur cycle in two Canadian peatland soils. *Journal of Geophysical Research: Biogeosciences*. *112*(G2).

Blume, E., Bischoff, M., Reichert, J., Moorman, T., Konopka, A., and Turco, R. (2002). Surface and subsurface microbial biomass, community structure and metabolic activity as a function of soil depth and season. *Applied Soil Ecology*. *20*(3), 171-181.

Bonneville, S., Behrends, T., Van Cappellen, P., Hyacinthe, C., and Röling, W. F. (2006). Reduction of Fe(III) colloids by *Shewanella putrefaciens*: a kinetic model. *Geochimica et Cosmochimica Acta*. *70*(23), 5842-5854.

Börner, F., Schopper, J., and Weller, A. (1996). Evaluation of transport and storage properties in the soil and groundwater zone from induced polarization measurements. *Geophysical Prospecting*. *44*(4), 583-601.

Bowling, J. C., Rodriguez, A. B., Harry, D. L., and Zheng, C. (2005). Delineating alluvial aquifer heterogeneity using resistivity and GPR data. *Groundwater*. *43*(6), 890-903.

Bretschger, O., Obraztsova, A., Sturm, C. A., Chang, I. S., Gorby, Y. A., Reed, S. B., et al. (2007). Current production and metal oxide reduction by *Shewanella oneidensis* MR-1 wild type and mutants. *Applied and Environmental Microbiology*. *73*(21), 7003-7012.

Budde, C. F., Mahan, A. E., Lu, J., Rha, C., and Sinskey, A. J. (2010). Roles of multiple acetoacetyl coenzyme A reductases in polyhydroxybutyrate biosynthesis in Ralstonia eutropha H16. *Journal of Bacteriology*. *192*(20), 5319-5328.

Butcher, J. C. (2016), *Numerical methods for ordinary differential equations*, John Wiley & Sons.

Carey, S. K. (2003). Dissolved organic carbon fluxes in a discontinuous permafrost subarctic alpine catchment. *Permafrost and Periglacial Processes*. *14*(2), 161-171.

Ceazan, M. L., Thurman, E. M., and Smith, R. L. (1989). Retardation of ammonium and potassium transport through a contaminated sand and gravel aquifer: the role of cation exchange. *Environmental Science & Technology*. *23*(11), 1402-1408.

Chan, T., and Gu, F. (2013). Development of a colorimetric, superparamagnetic biosensor for the capture and detection of biomolecules. *Biosensors and Bioelectronics*. *42*, 12-16.

Chapman, D. L. (1913). LI. A contribution to the theory of electrocapillarity. *The London, Edinburgh, and Dublin Philosophical Magazine and Journal of Science*. *25*(148), 475-481.

Chelidze, T., and Gueguen, Y. (1999). Electrical spectroscopy of porous rocks: a review—I. Theoretical models. *Geophysical Journal International*. *137*(1), 1-15.

Chen, J., Kemna, A., and Hubbard, S. S. (2008). A comparison between Gauss-Newton and Markov-chain Monte Carlo–based methods for inverting spectral induced-polarization data for Cole-Cole parameters. *Geophysics*. *73*(6), F247-F259.

Chen, L.-T., Ruoh-Huey, U., Song, T.-T., Zhi-Long, C., Chiang, C.-c., and Lin, Y.-H. (2015), Method for preparing silver nanowire, edited, Google Patents.

Chen, Y., and Or, D. (2006). Effects of Maxwell-Wagner polarization on soil complex dielectric permittivity under variable temperature and electrical conductivity. *Water Resources Research*. *42*(6).

Chiogna, G., Eberhardt, C., Grathwohl, P., Cirpka, O. A., and Rolle, M. (2009). Evidence of compound-dependent hydrodynamic and mechanical transverse dispersion by multitracer laboratory experiments. *Environmental Science & Technology*. *44*(2), 688-693.

Chow, A. T., Tanji, K. K., Gao, S., and Dahlgren, R. A. (2006). Temperature, water content and wet–dry cycle effects on DOC production and carbon mineralization in agricultural peat soils. *Soil Biology and Biochemistry*. *38*(3), 477-488.

Christensen, B. T. (1992), Physical fractionation of soil and organic matter in primary particle size and density separates, in *Advances in Soil Science*, edited, pp. 1-90, Springer.

Cirpka, O. A., Frind, E. O., and Helmig, R. (1999). Numerical simulation of biodegradation controlled by transverse mixing. *Journal of Contaminant Hydrology*. *40*(2), 159-182.

Claessens, J., Behrends, T., and Van Cappellen, P. (2004). What do acid-base titrations of live bacteria tell us? A preliminary assessment. *Aquatic Sciences*. *66*(1), 19-26.

Coker, V., Gault, A., Pearce, C., Van der Laan, G., Telling, N., Charnock, J., et al. (2006). XAS and XMCD evidence for species-dependent partitioning of arsenic during microbial reduction of ferrihydrite to magnetite. *Environmental Science & Technology*. *40*(24), 7745-7750.

Cole, K. S., and Cole, R. H. (1941). Dispersion and absorption in dielectrics I. Alternating current characteristics. *The Journal of Chemical Physics*. *9*(4), 341-351.

Cook, R. B. (1984). Distributions of ferrous iron and sulfide in an anoxic hypolimnion. *The Canadian Journal of Fisheries and Aquatic Sciences*. *41*(2), 286-293.

Cox, J. S., Smith, D. S., Warren, L. A., and Ferris, F. G. (1999). Characterizing heterogeneous bacterial surface functional groups using discrete affinity spectra for proton binding. *Environmental Science & Technology*. *33*(24), 4514-4521.

David, M. B., and Mitchell, M. J. (1987). Transformations of organic and inorganic sulfur: Importance to sulfate flux in an Adirondack forest soil. *Journal of the Air & Waste Management Association*. *37*(1), 39-44.

Davis, C. A., Atekwana, E., Atekwana, E., Slater, L. D., Rossbach, S., and Mormile, M. R. (2006). Microbial growth and biofilm formation in geologic media is detected with complex conductivity measurements. *Geophysical Research Letters*. *33*(18), L18403.

de Lima, O. A., and Sharma, M. M. (1992). A generalized Maxwell-Wagner theory for membrane polarization in shaly sands. *Geophysics*. *57*(3), 431-440.

Dong, L., Lin, L., Li, Q., Huang, Z., Tang, X., Wu, M., et al. (2018). Enhanced nitrate-nitrogen removal by modified attapulgite-supported nanoscale zero-valent iron treating simulated groundwater. *Journal of Environmental Management*. *213*, 151-158.

Dunn, A. M., Silliman, S. E., Dhamwichukorn, S., and Kulpa, C. F. (2005). Demonstration of microbial transport into the capillary fringe via advection from below the water table. *Journal of Hydrology*. *306*(1), 50-58.

Escapa, I. F., García, J. L., Bühler, B., Blank, L., and Prieto, M. A. (2012). The polyhydroxyalkanoate metabolism controls carbon and energy spillage in Pseudomonas putida. *Environmental Microbiology*. *14*(4), 1049-1063.

Eydal, H., and Pedersen, K. (2007). Use of an ATP assay to determine viable microbial biomass in Fennoscandian Shield groundwater from depths of 3–1000 m. *Journal of Microbiological Methods*. *70*(2), 363-373.

Farnsworth, C. E., Voegelin, A., and Hering, J. G. (2011). Manganese oxidation induced by water table fluctuations in a sand column. *Environmental Science & Technology*. *46*(1), 277-284.

Fischer, J., and Weiss, A. (1986). Transport properties of liquids VII. Viscosity, ecess volumes, and self-diffusion of binary mixtures of donor-acceptor and of CCl4-carboxylic acid systems. *Berichte der Bunsengesellschaft für physikalische Chemie*. *90*(12), 1141-1153.

Flores Orozco, A., Williams, K. H., and Kemna, A. (2013). Time-lapse spectral induced polarization imaging of stimulated uranium bioremediation. *Near Surface Geophysics*. *11*(5), 531-544.

Flores Orozco, A., Williams, K. H., Long, P. E., Hubbard, S. S., and Kemna, A. (2011). Using complex resistivity imaging to infer biogeochemical processes associated with bioremediation of an uranium-contaminated aquifer. *Journal of Geophysical Research: Biogeosciences*. *116*, G03001.

Flores Orozco, A. n., Velimirovic, M., Tosco, T., Kemna, A., Sapion, H., Klaas, N., et al. (2015). Monitoring the injection of microscale zerovalent iron particles for groundwater remediation by means of complex electrical conductivity imaging. *Environmental Science & Technology*. *49*(9), 5593-5600.

Gao, H., Yang, Z. K., Barua, S., Reed, S. B., Romine, M. F., Nealson, K. H., et al. (2009a). Reduction of nitrate in *Shewanella oneidensis* depends on atypical NAP and NRF systems with NapB as a preferred electron transport protein from CymA to NapA. *ISME Journal*. *3*(8), 966-976.

Gao, H., Yang, Z. K., Barua, S., Reed, S. B., Romine, M. F., Nealson, K. H., et al. (2009b). Reduction of nitrate in *Shewanella oneidensis* depends on atypical NAP and NRF systems with NapB as a preferred electron transport protein from CymA to NapA. *ISME J.* *3*(8), 966-976.

Ghorbani, A., Cosenza, P., Revil, A., Zamora, M., Schmutz, M., Florsch, N., and Jougnot, D. (2009). Non-invasive monitoring of water content and textural changes in clay-rocks using spectral induced polarization: A laboratory investigation. *Applied Clay Science*. *43*(3-4), 493-502.

Glasauer, S., Langley, S., Boyanov, M., Lai, B., Kemner, K., and Beveridge, T. (2007). Mixed-valence cytoplasmic iron granules are linked to anaerobic respiration. *Applied and Environmental Microbiology*. *73*(3), 993-996.

Gong, Y., Liu, Y., Xiong, Z., and Zhao, D. (2014). Immobilization of mercury by carboxymethyl cellulose stabilized iron sulfide nanoparticles: reaction mechanisms and effects of stabilizer and water chemistry. *Environmental Science & Technology*. *48*(7), 3986-3994.

Gouy, M. (1910). Sur la constitution de la charge électrique à la surface d'un électrolyte. *Journal de Physique Théorique et Appliquée*. *9*(1), 457-468.

Griebler, C., Mindl, B., Slezak, D., and Geiger-Kaiser, M. (2002). Distribution patterns of attached and suspended bacteria in pristine and contaminated shallow aquifers studied with an in situ sediment exposure microcosm. *Aquatic Microbial Ecology*. *28*(2), 117-129.

Grösbacher, M., Eckert, D., Cirpka, O. A., and Griebler, C. (2018). Contaminant concentration versus flow velocity: drivers of biodegradation and microbial growth in groundwater model systems. *Biodegradation*. *29*(3), 211-232.

Haberer, C. M., Rolle, M., Cirpka, O. A., and Grathwohl, P. (2012). Oxygen transfer in a fluctuating capillary fringe. *Vadose Zone Journal*. *11*(3).

Haberer, C. M., Rolle, M., Liu, S., Cirpka, O. A., and Grathwohl, P. (2011). A high-resolution non-invasive approach to quantify oxygen transport across the capillary fringe and within the underlying groundwater. *Journal of Contaminant Hydrology*. *122*(1-4), 26-39.

Hammes, F., Goldschmidt, F., Vital, M., Wang, Y., and Egli, T. (2010). Measurement and interpretation of microbial adenosine tri-phosphate (ATP) in aquatic environments. *Water Research*. *44*(13), 3915-3923.

Hao, N., Moysey, S. M., Powell, B. A., and Ntarlagiannis, D. (2015). Evaluation of Surface Sorption Processes Using Spectral Induced Polarization and a ^{22}Na Tracer. *Environmental Science & Technology*. *49*(16), 9866-9873.

He, F., and Zhao, D. (2007). Manipulating the size and dispersibility of zerovalent iron nanoparticles by use of carboxymethyl cellulose stabilizers. *Environmental Science & Technology*. *41*(17), 6216-6221.

Heenan, J. W., Ntarlagiannis, D., Slater, L. D., Beaver, C. L., Rossbach, S., Revil, A., et al. (2017). Field-scale observations of a transient geobattery resulting from natural attenuation of a crude oil spill. *Journal of Geophysical Research: Biogeosciences*. *122*(4), 918-929.

Heidelberg, J. F., Paulsen, I. T., Nelson, K. E., Gaidos, E. J., Nelson, W. C., Read, T. D., et al. (2002). Genome sequence of the dissimilatory metal ion–reducing bacterium *Shewanella oneidensis*. *Nature Biotechnology*. *20*(11), 1118-1123.

Heijnen, J., and Van Dijken, J. (1992). In search of a thermodynamic description of biomass yields for the chemotrophic growth of microorganisms. *Biotechnology and Bioengineering*. *39*(8), 833-858.

Hibbing, M. E., Fuqua, C., Parsek, M. R., and Peterson, S. B. (2010). Bacterial competition: surviving and thriving in the microbial jungle. *Nature Reviews Microbiology*. *8*(1), 15.

Hobbie, J. E., Daley, R. J., and Jasper, S. (1977). Use of nuclepore filters for counting bacteria by fluorescence microscopy. *Applied and Environmental Microbiology*. *33*(5), 1225-1228.

Hotchkiss, R. D. (1944). Gramicidin, tyrocidine, and tyrothricin. *Advances in Enzymology - and Related Areas of Molecular Biology*. *4*, 153-199.

Hotze, E. M., Phenrat, T., and Lowry, G. V. (2010). Nanoparticle aggregation: challenges to understanding transport and reactivity in the environment. *Journal of Environmental Quality*. *39*(6), 1909-1924.

Houle, D., Carignan, R., and Ouimet, R. (2001). Soil organic sulfur dynamics in a coniferous forest. *Biogeochemistry*. *53*(1), 105-124.

Houle, D., Marty, C., Duchesne, L., and Gagnon, C. (2014). Humus layer is the main locus of secondary SO4 production in boreal forests. *Geochimica et Cosmochimica Acta*. *126*, 18-29.

Imer, D., Merbold, L., Eugster, W., and Buchmann, N. (2013). Temporal and spatial variations of soil CO 2, CH 4 and N 2 O fluxes at three differently managed grasslands. *Biogeosciences*. *10*(9), 5931-5945.

Jenkinson, D., and Oades, J. (1979). A method for measuring adenosine triphosphate in soil. *Soil Biology and Biochemistry*. *11*(2), 193-199.

Joergensen, R. G., and Mueller, T. (1996). The fumigation-extraction method to estimate soil microbial biomass: calibration of the k_{EC} value. *Soil Biology and Biochemistry*. *28*(1), 33-37.

Johnson, K., Jiang, Y., Kleerebezem, R., Muyzer, G., and van Loosdrecht, M. C. (2009). Enrichment of a mixed bacterial culture with a high polyhydroxyalkanoate storage capacity. *Biomacromolecules*. *10*(4), 670-676.

Joo, S. H., and Zhao, D. (2017). Environmental dynamics of metal oxide nanoparticles in heterogeneous systems: a review. *Journal of Hazardous Materials*. *322*, 29-47.

Jost, D., Winter, J., and Gallert, C. (2011). Water and oxygen dependence of growing in silica sand capillary fringes. *Vadose Zone Journal*. *10*(2), 532-540.

Jougnot, D., Ghorbani, A., Revil, A., Leroy, P., and Cosenza, P. (2010). Spectral induced polarization of partially saturated clay-rocks: A mechanistic approach. *Geophysical Journal International*. *180*(1), 210-224.

Jougnot, D., and Linde, N. (2013). Self-potentials in partially saturated media: the importance of explicit modeling of electrode effects. *Vadose Zone Journal*. *12*(2).

Joyce, R. A., Glaser II, D. R., Werkema Jr, D. D., and Atekwana, E. A. (2012). Spectral induced polarization response to nanoparticles in a saturated sand matrix. *Journal of Applied Geophysics*. *77*, 63-71.

Kappler, A., Emerson, D., Edwards, K., Amend, J., Gralnick, J., Grathwohl, P., et al. (2005). Microbial activity in biogeochemical gradients–new aspects of research. *Geobiology*. *3*(3), 229-233.

Kelso, B., Smith, R. V., Laughlin, R. J., and Lennox, S. D. (1997). Dissimilatory nitrate reduction in anaerobic sediments leading to river nitrite accumulation. *Applied and Environmental Microbiology*. *63*(12), 4679-4685.

Kemna, A., Binley, A., Cassiani, G., Niederleithinger, E., Revil, A., Slater, L., et al. (2012). An overview of the spectral induced polarization method for near-surface applications. *Near Surface Geophysics*. *10*(6), 453-468.

Kinniburgh, D. G., Milne, C. J., Benedetti, M. F., Pinheiro, J. P., Filius, J., Koopal, L. K., and Van Riemsdijk, W. H. (1996). Metal ion binding by humic acid: application of the NICA-Donnan model. *Environmental Science & Technology*. *30*(5), 1687-1698.

Klebanoff, S. J. (1993). Reactive nitrogen intermediates and antimicrobial activity: role of nitrite. *Free Radical Biology and Medicine*. *14*(4), 351-360.

Kleerebezem, R., and Van Loosdrecht, M. C. (2010). A generalized method for thermodynamic state analysis of environmental systems. *Critical Reviews in Environmental Science and Technology*. *40*(1), 1-54.

Knight, R. (1991). Hysteresis in the electrical resistivity of partially saturated sandstones. *Geophysics*. *56*(12), 2139-2147.

Knight, R., Pyrak-Nolte, L., Slater, L., Atekwana, E., Endres, A., Geller, J., et al. (2010). Geophysics at the interface: Response of geophysical properties to solid-fluid, fluid-fluid, and solid-solid interfaces. *Reviews of Geophysics*. *48*(4).

Koopal, L., Van Riemsdijk, W., De Wit, J., and Benedetti, M. (1994). Analytical isotherm equations for multicomponent adsorption to heterogeneous surfaces. *Journal of Colloid and Interface Science*. *166*(1), 51-60.

Korte, H. L., Saini, A., Trotter, V. V., Butland, G. P., Arkin, A. P., and Wall, J. D. (2015). Independence of nitrate and nitrite inhibition of Desulfovibrio vulgaris Hildenborough and use of nitrite as a substrate for growth. *Environmental Science & Technology*. *49*(2), 924-931.

Kruschwitz, S., Binley, A., Lesmes, D., and Elshenawy, A. (2010). Textural controls on low-frequency electrical spectra of porous media. *Geophysics*. *75*(4), WA113-WA123.

Kulakovskaya, T., Pavlov, E., and Dedkova, E. N. (2016), *Inorganic Polyphosphates in Eukaryotic Cells*, Springer.

Lamelas, C., Benedetti, M., Wilkinson, K. J., and Slaveykova, V. I. (2006). Characterization of H+ and Cd2+ binding properties of the bacterial exopolysaccharides. *Chemosphere*. *65*(8), 1362-1370.

Larsen, M., Borisov, S. M., Grunwald, B., Klimant, I., and Glud, R. N. (2011). A simple and inexpensive high resolution color ratiometric planar optode imaging approach: application to oxygen and pH sensing. *Limnology and Oceanography: Methods*. *9*(9), 348-360.

Lee, C. K., Kim, A. J., Santos, G. S., Lai, P. Y., Lee, S. Y., Qiao, D. F., et al. (2016). Evolution of cell size homeostasis and growth rate diversity during initial surface colonization of *Shewanella oneidensis*. *ACS Nano*. *10*, 9183−9192.

Legg, B. A., Zhu, M., Comolli, L. R., Gilbert, B., and Banfield, J. F. (2014). Impacts of ionic strength on three-dimensional nanoparticle aggregate structure and consequences for environmental transport and deposition. *Environmental Science & Technology*. *48*(23), 13703-13710.

Lennon, J. T., and Jones, S. E. (2011). Microbial seed banks: the ecological and evolutionary implications of dormancy. *Nature Reviews Microbiology*. *9*(2), 119-130.

Leroy, P., and Revil, A. (2009). A mechanistic model for the spectral induced polarization of clay materials. *Journal of Geophysical Research: Solid Earth*. *114*, B10202.

Leroy, P., Revil, A., Kemna, A., Cosenza, P., and Ghorbani, A. (2008). Complex conductivity of water-saturated packs of glass beads. *Journal of Colloid and Interface Science*. *321*(1), 103-117.

Lesmes, D. P., and Frye, K. M. (2001). Influence of pore fluid chemistry on the complex conductivity and induced polarization responses of Berea sandstone. *Journal of Geophysical Research: Solid Earth*. *106*(B3), 4079-4090.

Lesmes, D. P., and Morgan, F. D. (2001). Dielectric spectroscopy of sedimentary rocks. *Journal of Geophysical Research: Solid Earth*. *106*(B7), 13329-13346.

Lever, M. A., Rogers, K. L., Lloyd, K. G., Overmann, J., Schink, B., Thauer, R. K., et al. (2015). Life under extreme energy limitation: a synthesis of laboratory-and field-based investigations. *FEMS Microbiology Reviews*. *39*(5), 688-728.

Li, L., Maher, K., Navarre-Sitchler, A., Druhan, J., Meile, C., Lawrence, C., et al. (2017). Expanding the role of reactive transport models in critical zone processes. *Earth-Science Reviews*. *165*, 280-301.

Liang, Q., Zhao, D., Qian, T., Freeland, K., and Feng, Y. (2012). Effects of stabilizers and water chemistry on arsenate sorption by polysaccharide-stabilized magnetite nanoparticles. *Industrial & Engineering Chemistry Research*. *51*(5), 2407-2418.

Lin, K.-S., Mdlovu, N. V., Chen, C.-Y., Chiang, C.-L., and Dehvari, K. (2018). Degradation of TCE, PCE, and 1, 2–DCE DNAPLs in contaminated groundwater using polyethylenimine-modified zero-valent iron nanoparticles. *Journal of Cleaner Production*. *175*, 456-466.

Linley, S., Holmes, A., Leshuk, T., Nafo, W., Thomson, N. R., Al-Mayah, A., et al. (2019). Targeted nanoparticle binding & detection in petroleum hydrocarbon impacted porous media. *Chemosphere*. *215*, 353-361.

Liu, C., Kota, S., Zachara, J. M., Fredrickson, J. K., and Brinkman, C. K. (2001). Kinetic analysis of the bacterial reduction of goethite. *Environmental Science & Technology*. *35*(12), 2482-2490.

Liu, Y. (1998). Energy uncoupling in microbial growth under substrate-sufficient conditions. *Applied Microbiology and Biotechnology*. *49*(5), 500-505.

Lobete, M. M., Fernandez, E. N., and Van Impe, J. F. (2015). Recent trends in non-invasive in situ techniques to monitor bacterial colonies in solid (model) food. *Frontiers in Microbiology*. *6*, 148.

Louie, S. M., Phenrat, T., Small, M. J., Tilton, R. D., and Lowry, G. V. (2012). Parameter identifiability in application of soft particle electrokinetic theory to determine polymer and polyelectrolyte coating thicknesses on colloids. *Langmuir*. *28*(28), 10334-10347.

Low, E. W., and Chase, H. A. (1999). Reducing production of excess biomass during wastewater treatment. *Water Research*. *33*(5), 1119-1132.

Lund, A. L., Slater, L. D., Atekwana, E. A., Ntarlagiannis, D., Cozzarelli, I., and Bekins, B. A. (2017). Evidence of Coupled Carbon and Iron Cycling at a Hydrocarbon-Contaminated Site from Time Lapse Magnetic Susceptibility. *Environmental Science & Technology*. *51*(19), 11244-11249.

Lyon-Marion, B. A., Becker, M. D., Kmetz, A. A., Foster, E., Johnston, K. P., Abriola, L. M., and Pennell, K. D. (2017). Simulation of magnetite nanoparticle mobility in a heterogeneous flow cell. *Environmental Science: Nano*. *4*(7), 1512-1524.

MacFarlane, D., Cherry, J., Gillham, R., and Sudicky, E. (1983). Migration of contaminants in groundwater at a landfill: a case study: 1. Groundwater flow and plume delineation. *Journal of Hydrology*. *63*(1-2), 1-29.

Mackay, D. M., Freyberg, D., Roberts, P., and Cherry, J. (1986). A natural gradient experiment on solute transport in a sand aquifer: 1. Approach and overview of plume movement. *Water Resources Research*. *22*(13), 2017-2029.

Maier, U., Rügner, H., and Grathwohl, P. (2007). Gradients controlling natural attenuation of ammonium. *Applied Geochemistry*. *22*(12), 2606-2617.

Marinsky, J. A., Lin, F. G., and Chung, K. S. (1983). A simple method for classification of the physical state of colloidal and particulate suspensions encountered in practice. *The Journal of Physical Chemistry*. *87*(16), 3139-3145.

Marshall, D. J., and Madden, T. R. (1959). Induced polarization, a study of its causes. *Geophysics*. *24*(4), 790-816.

McClain, M. E., Boyer, E. W., Dent, C. L., Gergel, S. E., Grimm, N. B., Groffman, P. M., et al. (2003). Biogeochemical hot spots and hot moments at the interface of terrestrial and aquatic ecosystems. *Ecosystems*. *6*(4), 301-312.

Mellage, A., Eckert, D., Grösbacher, M., Inan, A. Z., Cirpka, O. A., and Griebler, C. (2015). Dynamics of suspended and attached aerobic toluene degraders in small-scale fow-through sediment systems under growth and starvation conditions. *Environmental Science & Technology*. *49*(12), 7161-7169.

Mellage, A., Smeaton, C. M., Furman, A., Atekwana, E. A., Rezanezhad, F., and Van Cappellen, P. (2018). Linking spectral induced polarization (SIP) and subsurface microbial processes: Results from sand column incubation experiments. *Environmental Science & Technology*. *52*(4), 2081–2090.

Merbold, L., Steinlin, C., and Hagedorn, F. (2013). Winter greenhouse gas fluxes (CO2, CH4 and N2O) from a subalpine grassland. *Biogeosciences*. *10*(5), 3185.

Mihalcescu, I., Gateau, M. V.-M., Chelli, B., Pinel, C., and Ravanat, J.-L. (2015). Green autofluorescence, a double edged monitoring tool for bacterial growth and activity in micro-plates. *Physical Biology*. *12*(6), 066016.

Mitchell, M. J., and Fuller, R. D. (1988). Models of sulfur dynamics in forest and grassland ecosystems with emphasis on soil processes. *Biogeochemistry*. *5*(1), 133-163.

Müller, B., Stierli, R., and Gächter, R. (2008). A low-tech, low-cost passive sampler for the long-term monitoring of phosphate loads in rivers and streams. *Journal of Environmental Monitoring*. *10*(7), 817-820.

Myers, C. R., and Nealson, K. H. (1988). Bacterial manganese reduction and growth with manganese oxide as the sole electron acceptor. *Science*. *240*(4857), 1319-1321.

Nancharaiah, Y. V., and Lens, P. (2015). Ecology and biotechnology of selenium-respiring bacteria. *Microbiology and Molecular Biology Reviews*. *79*(1), 61-80.

Naudet, V., Revil, A., Bottero, J. Y., and Bégassat, P. (2003). Relationship between self-potential (SP) signals and redox conditions in contaminated groundwater. *Geophysical Research Letters*. *30*(21).

Naudet, V., Revil, A., Rizzo, E., Bottero, J.-Y., and Bégassat, P. (2004). Groundwater redox conditions and conductivity in a contaminant plume from geoelectrical investigations. *Hydrology and Earth System Sciences Discussions*. *8*(1), 8-22.

Neal, A. L., Rosso, K. M., Geesey, G. G., Gorby, Y. A., and Little, B. J. (2003). Surface structure effects on direct reduction of iron oxides by Shewanella oneidensis. *Geochimica et Cosmochimica Acta*. *67*(23), 4489-4503.

Nikolausz, M., Kappelmeyer, U., Székely, A., Rusznyák, A., Márialigeti, K., and Kästner, M. (2008). Diurnal redox fluctuation and microbial activity in the rhizosphere of wetland plants. *European Journal of Soil Biology*. *44*(3), 324-333.

Nilsen, V., Wyller, J., and Heistad, A. (2012). Efficient incorporation of microbial metabolic lag in subsurface transport modeling. *Water Resources Research*. *48*(9).

Nordsiek, S., and Weller, A. (2008). A new approach to fitting induced-polarization spectra. *Geophysics*. *73*(6), F235-F245.

Ntarlagiannis, D., Atekwana, E. A., Hill, E. A., and Gorby, Y. (2007). Microbial nanowires: Is the subsurface "hardwired"? *Geophysical Research Letters*. *34*(17).

Ntarlagiannis, D., Williams, K. H., Slater, L., and Hubbard, S. (2005a). Low-frequency electrical response to microbial induced sulfide precipitation. *Journal of Geophysical Research: Biogeosciences*. *110*, G02009.

Ntarlagiannis, D., Yee, N., and Slater, L. (2005b). On the low-frequency electrical polarization of bacterial cells in sands. *Geophysical Research Letters*. *32*, L24402.

Numata, K., Morisaki, K., Tomizawa, S., Ohtani, M., Demura, T., Miyazaki, M., et al. (2013). Synthesis of poly-and oligo (hydroxyalkanoate) s by deep-sea bacteria, Colwellia spp., Moritella spp., and Shewanella spp. *Polymer Journal*. *45*(10), 1094.

Ohshima, H. (1995). Electrophoresis of soft particles. *Advances in Colloid and Interface Science*. *62*(2-3), 189-235.

Okay, G., Leroy, P., Ghorbani, A., Cosenza, P., Camerlynck, C., Cabrera, J., et al. (2014). Spectral induced polarization of clay-sand mixtures: Experiments and modeling. *Geophysics*. *79*(6), E353-E375.

Olhoeft, G. (1985). Low-frequency electrical properties. *Geophysics*. *50*(12), 2492-2503.

Øyaas, J., Storrø, I., Svendsen, H., and Levine, D. W. (1995). The effective diffusion coefficient and the distribution constant for small molecules in calcium-alginate gel beads. *Biotechnology and Bioengineering*. *47*(4), 492-500.

Pan, Y., Ye, L., Ni, B.-J., and Yuan, Z. (2012). Effect of pH on N2O reduction and accumulation during denitrification by methanol utilizing denitrifiers. *Water Research*. *46*(15), 4832-4840.

Parsons, L. R., and Bandaranayake, W. M. (2009). Performance of a new capacitance soil moisture probe in a sandy soil. *Soil Science Society of America Journal*. *73*(4), 1378-1385.

Pelton, W., Ward, S., Hallof, P., Sill, W., and Nelson, P. H. (1978). Mineral discrimination and removal of inductive coupling with multifrequency IP. *Geophysics*. *43*(3), 588-609.

Peralta, A. L., Ludmer, S., and Kent, A. D. (2013). Hydrologic history influences microbial community composition and nitrogen cycling under experimental drying/wetting treatments. *Soil Biology and Biochemistry*. *66*, 29-37.

Personna, Y. R., Ntarlagiannis, D., Slater, L., Yee, N., O'Brien, M., and Hubbard, S. (2008). Spectral induced polarization and electrodic potential monitoring of microbially mediated iron sulfide transformations. *Journal of Geophysical Research: Biogeosciences*. *113*, G02020.

Peruzzo, L., Schmutz, M., Franceschi, M., Wu, Y., and Hubbard, S. S. (2018). The relative importance of saturated silica sand interfacial and pore fluid geochemistry on the spectral induced polarization response. *Journal of Geophysical Research: Biogeosciences*.

Pett-Ridge, J., and Firestone, M. (2005). Redox fluctuation structures microbial communities in a wet tropical soil. *Applied and Environmental Microbiology*. *71*(11), 6998-7007.

Pett-Ridge, J., Silver, W. L., and Firestone, M. K. (2006). Redox fluctuations frame microbial community impacts on N-cycling rates in a humid tropical forest soil. *Biogeochemistry*. *81*(1), 95-110.

Phenrat, T., Cihan, A., Kim, H.-J., Mital, M., Illangasekare, T., and Lowry, G. V. (2010). Transport and deposition of polymer-modified Fe0 nanoparticles in 2-D heterogeneous porous media: Effects of particle concentration, Fe0 content, and coatings. *Environmental Science & Technology*. *44*(23), 9086-9093.

Philippot, L., and Hojberg, O. (1999). Dissimilatory nitrate reductases in bacteria. *Biochimica et Biophysica Acta 1446*(1-2), 1-23.

Placencia-Gómez, E., Parviainen, A., Slater, L., and Leveinen, J. (2015). Spectral induced polarization (SIP) response of mine tailings. *Journal of Contaminant Hydrology*. *173*, 8-24.

Placencia-Gómez, E., Slater, L., Ntarlagiannis, D., and Binley, A. (2013). Laboratory SIP signatures associated with oxidation of disseminated metal sulfides. *Journal of Contaminant Hydrology*. *148*, 25-38.

Placencia-Gómez, E., and Slater, L. D. (2014). Electrochemical spectral induced polarization modeling of artificial sulfide-sand mixtures. *Geophysics*. *79*(6), EN91-EN106.

Plette, A. C., Benedetti, M. F., and van Riemsdijk, W. H. (1996). Competitive binding of protons, calcium, cadmium, and zinc to isolated cell walls of a gram-positive soil bacterium. *Environmental Science & Technology*. *30*(6), 1902-1910.

Plette, A. C., van Riemsdijk, W. H., Benedetti, M. F., and van der Wal, A. (1995). pH dependent charging behavior of isolated cell walls of a gram-positive soil bacterium. *Journal of Colloid and Interface Science*. *173*(2), 354-363.

Podella, C. W., and Hauptmann, N. S. (2009), Altering metabolism in biological processes, edited, Google Patents.

Prodan, C., Mayo, F., Claycomb, J., Miller Jr, J., and Benedik, M. (2004). Low-frequency, low-field dielectric spectroscopy of living cell suspensions. *Journal of Applied Physics*. *95*(7), 3754-3756.

Pronk, G. J., Heister, K., Vogel, C., Babin, D., Bachmann, J., Ding, G.-C., et al. (2017). Interaction of minerals, organic matter, and microorganisms during biogeochemical interface formation as shown by a series of artificial soil experiments. *Biology and Fertility of Soils*, 1-14.

Qambrani, N. A., Hwang, J.-H., and Oh, S.-E. (2016). Comparison of chromium III and VI toxicities in water using sulfur-oxidizing bacterial bioassays. *Chemosphere*. *160*, 342-348.

Rasband, W. S. (2015), ImageJ, edited by U. S. N. I. o. Health, pp. 1997-2016, Bethesda, Maryland, USA.

Rath, K. M., Maheshwari, A., and Rousk, J. (2017). The impact of salinity on the microbial response to drying and rewetting in soil. *Soil Biology and Biochemistry*. *108*, 17-26.

Raz-Yaseef, N., Torn, M. S., Wu, Y., Billesbach, D. P., Liljedahl, A. K., Kneafsey, T. J., et al. (2017). Large CO2 and CH4 emissions from polygonal tundra during spring thaw in northern Alaska. *Geophysical Research Letters*. *44*(1), 504-513.

Redmile-Gordon, M., White, R., and Brookes, P. (2011). Evaluation of substitutes for paraquat in soil microbial ATP determinations using the trichloroacetic acid based reagent of. *Soil Biology and Biochemistry*. *43*(5), 1098-1100.

Rees, H. C., Oswald, S. E., Banwart, S. A., Pickup, R. W., and Lerner, D. N. (2007). Biodegradation processes in a laboratory-scale groundwater contaminant plume assessed by fluorescence imaging and microbial analysis. *Applied and Environmental Microbiology*. *73*(12), 3865-3876.

Revil, A. (2013). Effective conductivity and permittivity of unsaturated porous materials in the frequency range 1 mHz–1GHz. *Water Resources Research*. *49*(1), 306-327.

Revil, A., Atekwana, E., Zhang, C., Jardani, A., and Smith, S. (2012). A new model for the spectral induced polarization signature of bacterial growth in porous media. *Water Resources Research*. *48*(9), W09545.

Revil, A., Coperey, A., Shao, Z., Florsch, N., Fabricius, I. L., Deng, Y., et al. (2017). Complex conductivity of soils. *Water Resources Research*. *53*(8), 7121-7147.

Revil, A., and Florsch, N. (2010). Determination of permeability from spectral induced polarization in granular media. *Geophysical Journal International*. *181*(3), 1480-1498.

Revil, A., and Glover, P. (1998). Nature of surface electrical conductivity in natural sands, sandstones, and clays. *Geophysical Research Letters*. *25*(5), 691-694.

Revil, A., and Linde, N. (2006). Chemico-electromechanical coupling in microporous media. *Journal of Colloid and Interface Science*. *302*(2), 682-694.

Revil, A., Mendonça, C., Atekwana, E., Kulessa, B., Hubbard, S., and Bohlen, K. (2010). Understanding biogeobatteries: Where geophysics meets microbiology. *Journal of Geophysical Research: Biogeosciences*. *115*(G1).

Rezanezhad, F., Couture, R.-M., Kovac, R., O'Connell, D., and Van Cappellen, P. (2014). Water table fluctuations and soil biogeochemistry: An experimental approach using an automated soil column system. *Journal of Hydrology*. *509*, 245-256.

Riedel, T. E., Berelson, W. M., Nealson, K. H., and Finkel, S. E. (2013). Oxygen consumption rates of bacteria under nutrient-limited conditions. *Applied and Environmental Microbiology*. *79*(16), 4921-4931.

Riepe, L., Rink, M., and Schopper, J. (1979), Relations between specific surface dependent rock properties, paper presented at Transactions of the 6th European Logging Symposium, Paper D.

Ringuet, S., Sassano, L., and Johnson, Z. I. (2011a). A suite of microplate reader-based colorimetric methods to quantify ammonium, nitrate, orthophosphate and silicate concentrations for aquatic nutrient monitoring. *J. Environ. Monit.* *13*(2), 370-376.

Ringuet, S., Sassano, L., and Johnson, Z. I. (2011b). A suite of microplate reader-based colorimetric methods to quantify ammonium, nitrate, orthophosphate and silicate concentrations for aquatic nutrient monitoring. *Journal of Environmental Monitoring*. *13*(2), 370-376.

Roden, E. E. (2008), Microbiological controls on geochemical kinetics 1: fundamentals and case study on microbial Fe(III) oxide reduction, in *Kinetics of Water-Rock Interaction*, edited, pp. 335-415, Springer.

Rottenberg, H. (1990). Decoupling of oxidative phosphorylation and photophosphorylation. *Biochimica et Biophysica Acta (BBA)-Bioenergetics*. *1018*(1), 1-17.

Rühle, F. A., von Netzer, F., Lueders, T., and Stumpp, C. (2015). Response of transport parameters and sediment microbiota to water table fluctuations in laboratory columns. *Vadose Zone Journal*. *14*(5).

Russell, J. B. (2007). The energy spilling reactions of bacteria and other organisms. *Journal of Molecular Microbiology and Biotechnology*. *13*(1-3), 1-11.

Russell, J. B., and Cook, G. M. (1995). Energetics of bacterial growth: balance of anabolic and catabolic reactions. *Microbiological Reviews*. *59*(1), 48-62.

Rütting, T., Boeckx, P., Müller, C., and Klemedtsson, L. (2011). Assessment of the importance of dissimilatory nitrate reduction to ammonium for the terrestrial nitrogen cycle. *Biogeosciences*. *8*(7), 1779-1791.

Rütting, T., Huygens, D., Müller, C., Van Cleemput, O., Godoy, R., and Boeckx, P. (2008). Functional role of DNRA and nitrite reduction in a pristine south Chilean Nothofagus forest. *Biogeochemistry*. *90*(3), 243-258.

Saini, G. (2014). Metabolic uncoupling: biomass control strategy in microbial processes. *Journal of Microbial and Biochemical Technology*. *6*, e117.

Saini, G., and Wood, B. D. (2008). Metabolic uncoupling of Shewanella oneidensis MR-1, under the influence of excess substrate and 3, 3′, 4′, 5-tetrachlorosalicylanilide (TCS). *Biotechnology and Bioengineering*. *99*(6), 1352-1360.

Saiyouri, N., Hicher, P. Y., and Tessier, D. (2000). Microstructural approach and transfer water modelling in highly compacted unsaturated swelling clays. *Mechanics of Cohesive-Frictional Materials*. *5*(1), 41-60.

Saleh, N., Phenrat, T., Sirk, K., Dufour, B., Ok, J., Sarbu, T., et al. (2005). Adsorbed triblock copolymers deliver reactive iron nanoparticles to the oil/water interface. *Nano Letters*. *5*(12), 2489-2494.

Saleh, N., Sirk, K., Liu, Y., Phenrat, T., Dufour, B., Matyjaszewski, K., et al. (2007). Surface modifications enhance nanoiron transport and NAPL targeting in saturated porous media. *Environmental Engineering Science*. *24*(1), 45-57.

Saltikov, C. W., Cifuentes, A., Venkateswaran, K., and Newman, D. K. (2003). The ars detoxification system is advantageous but not required for As (V) respiration by the genetically tractable *Shewanella* species strain ANA-3. *Applied and Environmental Microbiology*. *69*(5), 2800-2809.

Sasaki, A., Hagimori, Y., Nakatsubo, T., and Hoshika, A. (2009). Tidal effects on the organic carbon mineralization rate under aerobic conditions in sediments of an intertidal estuary. *Ecological Research*. *24*(4), 723-729.

Sato, M., and Mooney, H. M. (1960). The electrochemical mechanism of sulfide self-potentials. *Geophysics*. *25*(1), 226-249.

Schmidt, C. S., Richardson, D. J., and Baggs, E. M. (2011). Constraining the conditions conducive to dissimilatory nitrate reduction to ammonium in temperate arable soils. *Soil Biology and Biochemistry*. *43*(7), 1607-1611.

Schön, J. H. (1996), *Handbook of Geophysical Exploration: Seismic Exploration. Physical Properties of Rocks: Fundamentals and Principles of Petrophysics*, Pergamon.

Schwartz, N., and Furman, A. (2014). On the spectral induced polarization signature of soil organic matter. *Geophysical Journal International*. *200*(1), 589-595.

Schwartz, N., Huisman, J., and Furman, A. (2012). The effect of NAPL on the electrical properties of unsaturated porous media. *Geophysical Journal International*. *188*(3), 1007-1011.

Schwarz, G. (1962). A theory of the low-frequency dielectric dispersion of colloidal particles in electrolyte solution1, 2. *The Journal of Physical Chemistry*. *66*(12), 2636-2642.

Schwertmann, U. (1991), Solubility and dissolution of iron oxides, in *Iron nutrition and interactions in plants*, edited, pp. 3-27, Springer.

Schwertmann, U., and Fechter, H. (1982). The point of zero charge of natural and synthetic ferrihydrites and its relation to adsorbed silicate. *Clay Minerals*. *17*(4), 471-476.

Seeliger, S., Janssen, P. H., and Schink, B. (2002). Energetics and kinetics of lactate fermentation to acetate and propionate via methylmalonyl-CoA or acrylyl-CoA. *FEMS Microbiology Letters*. *211*(1), 65-70.

Shefer, I., Schwartz, N., and Furman, A. (2013). The effect of free-phase NAPL on the spectral induced polarization signature of variably saturated soil. *Water Resources Research*. *49*(10), 6229-6237.

Shi, Z., Fan, D., Johnson, R. L., Tratnyek, P. G., Nurmi, J. T., Wu, Y., and Williams, K. H. (2015). Methods for characterizing the fate and effects of nano zerovalent iron during groundwater remediation. *Journal of Contaminant Hydrology*. *181*, 17-35.

Sijbesma, W. F., Almeida, J. S., Reis, M. A., and Santos, H. (1996). Uncoupling effect of nitrite during denitrification by Pseudomonas fluorescens: An in vivo 31P-NMR study. *Biotechnology and Bioengineering*. *52*(1), 176-182.

Simunek, J., Van Genuchten, M. T., and Sejna, M. (2005). The HYDRUS-1D software package for simulating the one-dimensional movement of water, heat, and multiple solutes in variably-saturated media. *University of California-Riverside Research Reports*. *3*, 1-240.

Skold, M., Revil, A., and Vaudelet, P. (2011). The pH dependence of spectral induced polarization of silica sands: Experiment and modeling. *Geophysical Research Letters*. *38*(12).

Slater, L. (2007). Near surface electrical characterization of hydraulic conductivity: From petrophysical properties to aquifer geometries—A review. *Surveys in Geophysics*. *28*(2-3), 169-197.

Slater, L., Day-Lewis, F., Ntarlagiannis, D., O'Brien, M., and Yee, N. (2009). Geoelectrical measurement and modeling of biogeochemical breakthrough behavior during microbial activity. *Geophysical Research Letters*. *36*(LI4402).

Slater, L., and Glaser, D. (2003). Controls on induced polarization in sandy unconsolidated sediments and application to aquifer characterization. *Geophysics*. *68*(5), 1547-1558.

Slater, L., and Lesmes, D. (2002). Electrical-hydraulic relationships observed for unconsolidated sediments. *Water Resources Research*. *38*(10).

Slater, L., Ntarlagiannis, D., Personna, Y. R., and Hubbard, S. (2007). Pore-scale spectral induced polarization signatures associated with FeS biomineral transformations. *Geophysical Research Letters*. *34*, L21404.

Slater, L., Ntarlagiannis, D., and Wishart, D. (2006). On the relationship between induced polarization and surface area in metal-sand and clay-sand mixtures. *Geophysics*. *71*(2), A1-A5.

Slater, L., Ntarlagiannis, D., Yee, N., O'Brien, M., Zhang, C., and Williams, K. H. (2008). Electrodic voltages in the presence of dissolved sulfide: Implications for monitoring natural microbial activity. *Geophysics*. *73*(2), F65-F70.

Smeaton, C. M., Fryer, B. J., and Weisener, C. G. (2009). Intracellular precipitation of Pb by Shewanella putrefaciens CN32 during the reductive dissolution of Pb-jarosite. *Environmental Science & Technology*. *43*(21), 8086-8091.

Sokolov, I., Smith, D., Henderson, G., Gorby, Y., and Ferris, F. (2001). Cell surface electrochemical heterogeneity of the Fe (III)-reducing bacteria Shewanella putrefaciens. *Environmental Science & Technology*. *35*(2), 341-347.

Song, B., Lisa, J. A., and Tobias, C. R. (2014). Linking DNRA community structure and activity in a shallow lagoonal estuarine system. *Frontiers in Microbiology*. *5*, 460.

Soni, K. A., Balasubramanian, A. K., Beskok, A., and Pillai, S. D. (2008). Zeta potential of selected bacteria in drinking water when dead, starved, or exposed to minimal and rich culture media. *Current Microbiology*. *56*(1), 93-97.

Stegen, J. C., Fredrickson, J. K., Wilkins, M. J., Konopka, A. E., Nelson, W. C., Arntzen, E. V., et al. (2016). Groundwater–surface water mixing shifts ecological assembly processes and stimulates organic carbon turnover. *Nature Communications*. *7*, 11237.

Stern, O. (1924). Zur theorie der elektrolytischen doppelschicht. *Zeitschrift für Elektrochemie und angewandte physikalische Chemie*. *30*(21-22), 508-516.

Stolz, J. F., and Oremland, R. S. (1999). Bacterial respiration of arsenic and selenium. *FEMS Microbiology Reviews*. *23*(5), 615-627.

Stumm, W. (1992), *Chemistry of the solid-water interface: processes at the mineral-water and particle-water interface in natural systems*, John Wiley & Son Inc.

Su, H., Fang, Z., Tsang, P. E., Zheng, L., Cheng, W., Fang, J., and Zhao, D. (2016). Remediation of hexavalent chromium contaminated soil by biochar-supported zero-valent iron nanoparticles. *Journal of Hazardous Materials*. *318*, 533-540.

Sumner, J. (1976). Principles of induced polarization for geophysical exploration." Elsevier Publishing Co.

Sverjensky, D. A. (1994). Zero-point-of-charge prediction from crystal chemistry and solvation theory. *Geochimica et Cosmochimica Acta*. *58*(14), 3123-3129.

Tarasov, A., and Titov, K. (2007). Relaxation time distribution from time domain induced polarization measurements. *Geophysical Journal International*. *170*(1), 31-43.

Thorgersen, M. P., Lancaster, W. A., Ge, X., Zane, G. M., Wetmore, K. M., Vaccaro, B. J., et al. (2017). Mechanisms of Chromium and Uranium Toxicity in Pseudomonas stutzeri RCH2 Grown under Anaerobic Nitrate-Reducing Conditions. *Frontiers in Microbiology*. *8*, 1529.

Tiedje, J. M., Sexstone, A. J., Myrold, D. D., and Robinson, J. A. (1983). Denitrification: ecological niches, competition and survival. *Antonie van Leeuwenhoek*. *48*(6), 569-583.

Titov, K., Komarov, V., Tarasov, V., and Levitski, A. (2002). Theoretical and experimental study of time domain-induced polarization in water-saturated sands. *Journal of Applied Geophysics*. *50*(4), 417-433.

Tocheva, E. I., Dekas, A. E., McGlynn, S. E., Morris, D., Orphan, V. J., and Jensen, G. J. (2013). Polyphosphate storage during sporulation in the gram-negative bacterium Acetonema longum. *Journal of Bacteriology*. *195*(17), 3940-3946.

Totsche, K. U., Rennert, T., Gerzabek, M. H., Kögel-Knabner, I., Smalla, K., Spiteller, M., and Vogel, H. J. (2010). Biogeochemical interfaces in soil: the interdisciplinary challenge for soil science. *Journal of Plant Nutrition and Soil Science*. *173*(1), 88-99.

Troyanskaya, O. G., Dolinski, K., Owen, A. B., Altman, R. B., and Botstein, D. (2003). A Bayesian framework for combining heterogeneous data sources for gene function prediction (in Saccharomyces cerevisiae). *Proceedings of the National Academy of Sciences*. *100*(14), 8348-8353.

Tuček, J. í., Prucek, R., Kolařík, J., Zoppellaro, G., Petr, M., Filip, J., et al. (2017). Zero-valent iron nanoparticles reduce arsenites and arsenates to As (0) firmly embedded in core–shell superstructure: challenging strategy of arsenic treatment under anoxic conditions. *ACS Sustainable Chemistry & Engineering*. *5*(4), 3027-3038.

Tveit, A. T., Urich, T., Frenzel, P., and Svenning, M. M. (2015). Metabolic and trophic interactions modulate methane production by Arctic peat microbiota in response to warming. *Proceedings of the National Academy of Sciences*, 201420797.

Ulrich, C., and Slater, L. (2004). Induced polarization measurements on unsaturated, unconsolidated sands. *Geophysics*. *69*(3), 762-771.

Ustra, A., Slater, L., Ntarlagiannis, D., and Elis, V. (2012). Spectral induced polarization (SIP) signatures of clayey soils containing toluene. *Near Surface Geophysics*. *10*(6), 503-515.

Vance, E. D., Brookes, P. C., and Jenkinson, D. S. (1987). An extraction method for measuring soil microbial biomass C. *Soil Biology and Biochemistry*. *19*(6), 703-707.

Vaudelet, P., Revil, A., Schmutz, M., Franceschi, M., and Bégassat, P. (2011a). Changes in induced polarization associated with the sorption of sodium, lead, and zinc on silica sands. *Journal of Colloid and Interface Science*. *360*(2), 739-752.

Vaudelet, P., Revil, A., Schmutz, M., Franceschi, M., and Bégassat, P. (2011b). Induced polarization signatures of cations exhibiting differential sorption behaviors in saturated sands. *Water Resources Research*. *47*(2).

Vavilin, V., Fernandez, B., Palatsi, J., and Flotats, X. (2008). Hydrolysis kinetics in anaerobic degradation of particulate organic material: an overview. *Waste Management*. *28*(6), 939-951.

Vinegar, H., and Waxman, M. (1984). Induced polarization of shaly sands. *Geophysics*. *49*(8), 1267-1287.

Viollier, E., Inglett, P., Hunter, K., Roychoudhury, A., and Van Cappellen, P. (2000). The ferrozine method revisited: Fe (II)/Fe (III) determination in natural waters. *Applied Geochemistry*. *15*(6), 785-790.

Vives-Rego, J., Lebaron, P., and Nebe-von Caron, G. (2000). Current and future applications of flow cytometry in aquatic microbiology. *FEMS Microbiology Reviews*. *24*(4), 429-448.

Von Canstein, H., Ogawa, J., Shimizu, S., and Lloyd, J. R. (2008). Secretion of flavins by Shewanella species and their role in extracellular electron transfer. *Applied and Environmental Microbiology*. *74*(3), 615-623.

Wagner-Riddle, C., Congreves, K. A., Abalos, D., Berg, A. A., Brown, S. E., Ambadan, J. T., et al. (2017). Globally important nitrous oxide emissions from croplands induced by freeze–thaw cycles. *Nature Geoscience*. *10*(4), 279.

Wagner-Riddle, C., Hu, Q., Van Bochove, E., and Jayasundara, S. (2008). Linking nitrous oxide flux during spring thaw to nitrate denitrification in the soil profile. *Soil Science Society of America Journal*. *72*(4), 908-916.

Wang, B., Mezlini, A. M., Demir, F., Fiume, M., Tu, Z., Brudno, M., et al. (2014). Similarity network fusion for aggregating data types on a genomic scale. *Nature Methods*. *11*(3), 333.

Wang, Y.-P., Yu, S.-S., Zhang, H.-L., Li, W.-W., Cheng, Y.-Y., and Yu, H.-Q. (2015). Roles of 3, 3′, 4′, 5-tetrachlorosalicylanilide in regulating extracellular electron transfer of Shewanella oneidensis MR-1. *Scientific Reports*. *5*, 7991.

Wang, Z., and Acosta, E. (2013). Formulation design for target delivery of iron nanoparticles to TCE zones. *Journal of Contaminant Hydrology*. *155*, 9-19.

Wardman, C., Nevin, K. P., and Lovley, D. R. (2014). Real-time monitoring of subsurface microbial metabolism with graphite electrodes. *Frontiers in Microbiology*. *5*, 621.

Watson, I. A., Oswald, S. E., Mayer, K. U., Wu, Y., and Banwart, S. A. (2003). Modeling kinetic processes controlling hydrogen and acetate concentrations in an aquifer-derived microcosm. *Environmental Science & Technology*. *37*(17), 3910-3919.

Weigand, M., and Kemna, A. (2016a). Debye decomposition of time-lapse spectral induced polarisation data. *Computers & Geosciences*. *86*, 34-45.

Weigand, M., and Kemna, A. (2016b). Relationship between Cole–Cole model parameters and spectral decomposition parameters derived from SIP data. *Geophys. J. Int. 205*(3), 1414-1419.

Weigand, M., and Kemna, A. (2016c). Relationship between Cole–Cole model parameters and spectral decomposition parameters derived from SIP data. *Geophysical Journal International*. *205*(3), 1414-1419.

Weller, A., Slater, L., Nordsiek, S., and Ntarlagiannis, D. (2010). On the estimation of specific surface per unit pore volume from induced polarization: A robust empirical relation fits multiple data sets. *Geophysics*. *75*(4), WA105-WA112.

Weller, A., Zhang, Z., Slater, L., Kruschwitz, S., and Halisch, M. (2016). Induced polarization and pore radius—A discussion. *Geophysics*. *81*(5), D519-D526.

Werkema, D. D., Glaser, D., Joyce, R., Hawkins, D., and Atekwana, E. (2010), *A Feasibility Study on the Geophysical Response to Nanoparticles in the Subsurface*, US Environmental Protection Agency, Office of Research and Development.

Williams, K. H., Hubbard, S. S., and Banfield, J. F. (2007). Galvanic interpretation of self-potential signals associated with microbial sulfate-reduction. *Journal of Geophysical Research: Biogeosciences*. *112*, G03019.

Williams, K. H., Kemna, A., Wilkins, M. J., Druhan, J., Arntzen, E., N'Guessan, A. L., et al. (2009a). Geophysical monitoring of coupled microbial and geochemical processes during stimulated subsurface bioremediation. *Environmental Science & Technology*. *43*(17), 6717-6723.

Williams, K. H., Nevin, K. P., Franks, A., Englert, A., Long, P. E., and Lovley, D. R. (2009b). Electrode-based approach for monitoring in situ microbial activity during subsurface bioremediation. *Environmental Science & Technology*. *44*(1), 47-54.

Williams, K. H., Ntarlagiannis, D., Slater, L. D., Dohnalkova, A., Hubbard, S. S., and Banfield, J. F. (2005). Geophysical imaging of stimulated microbial biomineralization. *Environmental Science & Technology*. *39*(19), 7592-7600.

Wong, J. (1979). An electrochemical model of the induced-polarization phenomenon in disseminated sulfide ores. *Geophysics*. *44*(7), 1245-1265.

Wood, B. D., Ginn, T. R., and Dawson, C. N. (1995). Effects of microbial metabolic lag in contaminant transport and biodegradation modeling. *Water Resources Research*. *31*(3), 553-563.

Wu, Y., Slater, L., Versteeg, R., and LaBrecque, D. (2008). A comparison of the low frequency electrical signatures of iron oxide versus calcite precipitation in granular zero valent iron columns. *Journal of Contaminant Hydrology*. *95*(3-4), 154-167.

Wu, Y., Versteeg, R., Slater, L., and LaBrecque, D. (2009). Calcite precipitation dominates the electrical signatures of zero valent iron columns under simulated field conditions. *Journal of Contaminant Hydrology*. *106*(3), 131-143.

Xie, M., Agus, S., Schanz, T., and Kolditz, O. (2004). An upscaling method and a numerical analysis of swelling/shrinking processes in a compacted bentonite/sand mixture. *International Journal for Numerical and Analytical Methods in Geomechanics*. *28*(15), 1479-1502.

Xiong, Z., He, F., Zhao, D., and Barnett, M. O. (2009). Immobilization of mercury in sediment using stabilized iron sulfide nanoparticles. *Water Research*. *43*(20), 5171-5179.

Xiu, Z.-M., Ma, J., and Alvarez, P. J. (2011). Differential effect of common ligands and molecular oxygen on antimicrobial activity of silver nanoparticles versus silver ions. *Environmental Science & Technology*. *45*(20), 9003-9008.

Yan, S., Liu, Y., Liu, C., Shi, L., Shang, J., Shan, H., et al. (2016). Nitrate bioreduction in redox-variable low permeability sediments. *Science of the Total Environment*. *539*, 185-195.

Yang, L., Zhou, Y., Zhu, S., Huang, T., Wu, L., and Yan, X. (2012). Detection and quantification of bacterial autofluorescence at the single-cell level by a laboratory-built high-sensitivity flow cytometer. *Analytical Chemistry*. *84*(3), 1526-1532.

Yin, S., Chen, D., Chen, L., and Edis, R. (2002). Dissimilatory nitrate reduction to ammonium and responsible microorganisms in two Chinese and Australian paddy soils. *Soil Biology and Biochemistry*. *34*(8), 1131-1137.

Yoon, S., Sanford, R. A., and Löffler, F. E. (2013). *Shewanella* spp. use acetate as an electron donor for denitrification but not ferric iron or fumarate reduction. *Applied and Evironmental Microbiology*. *79*(8), 2818-2822.

Yuan-Hui, L., and Gregory, S. (1974). Diffusion of ions in sea water and in deep-sea sediments. *Geochimica et Cosmochimica Acta*. *38*(5), 703-714.

Zhang, C., Ntarlagiannis, D., Slater, L., and Doherty, R. (2010). Monitoring microbial sulfate reduction in porous media using multipurpose electrodes. *Journal of Geophysical Research: Biogeosciences*. *115*, G00G09.

Zhang, C., Revil, A., Fujita, Y., Munakata-Marr, J., and Redden, G. (2014). Quadrature conductivity: A quantitative indicator of bacterial abundance in porous media. *Geophysics*. *79*(6), D363-D375.

Zhang, C., Slater, L., Redden, G., Fujita, Y., Johnson, T., and Fox, D. (2012). Spectral induced polarization signatures of hydroxide adsorption and mineral precipitation in porous media. *Environmental Science & Technology*. *46*(8), 4357-4364.

Zhang, H., Fu, H., Wang, J., Sun, L., Jiang, Y., Zhang, L., and Gao, H. (2013). Impacts of nitrate and nitrite on physiology of *Shewanella oneidensis*. *PLoS ONE*. *8*(4), e62629.

Zhang, T., Murphy, M. J., Yu, H., Bagaria, H. G., Yoon, K. Y., Nielson, B. M., et al. (2015). Investigation of nanoparticle adsorption during transport in porous media. *SPE Journal*. *20*(04), 667-677.

Zhou, A.-x., Zhang, Y.-l., Dong, T.-z., Lin, X.-y., and Su, X.-s. (2015). Response of the microbial community to seasonal groundwater level fluctuations in petroleum hydrocarbon-contaminated groundwater. *Environmental Science and Pollution Research*. *22*(13), 10094-10106.

Zisser, N., Kemna, A., and Nover, G. (2010a). Dependence of spectral-induced polarization response of sandstone on temperature and its relevance to permeability estimation. *Journal of Geophysical Research: Solid Earth*. *115*(B9).

Zisser, N., Kemna, A., and Nover, G. (2010b). Relationship between low-frequency electrical properties and hydraulic permeability of low-permeability sandstones. *Geophysics*. *75*(3), E131-E141.

- Appendices -

Appendix A: Supplementary Information for Chapter 2

Modified from the supporting information in:

Mellage, A., Pronk, G.J., Milojevic, T., Endres, A.L., Furman, A., Atekwana, E.A., Rezanezhad, F. and Van Cappellen, P. (in preparation). Non-invasive monitoring of a reactive soil transition zone during water table fluctuations using spectral induced polarization (SIP) and electrodic potential (EP).

ATP profiles at 99 days

Columns F1 and C1 of the fluctuating and static treatments, respectively, were sacrificially sampled at 99 days. The ATP concentration depth-profiles are presented in Figure AA 1, alongside the ATP profiles from the remaining 4 replicates, sampled at the end of incubation, which are also presented in the main text. Figure AA 1 illustrates the decreasing trend in ATP content with depth, with highest values close to the surface and lowest values in the zone below the water table.

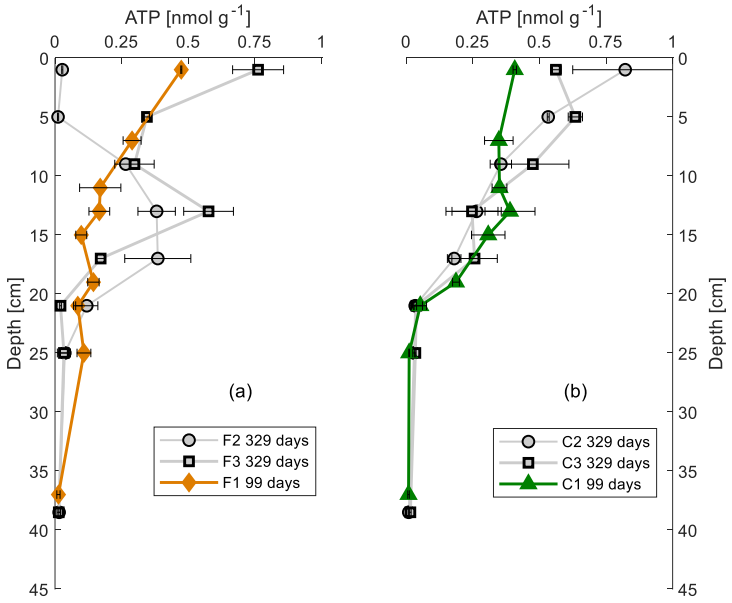

Figure AA 1. Adenosine tri-phosphate (ATP) concentration depth profiles at 99 and 329 days measured from the sacrificial sampling of different replicates in the (a) fluctuating and (b) static treatments.

Electrode-electrolyte chemical interactions: electrodic potential (EP)

Following a 400 mV anomaly recorded in the fluctuating column, F3, between measurement and reference non-polarizing gel-filled Ag-AgCl electrodes, during DRN_2 (see main text), the electrodes where the anomaly was measured (located at depths 15, 18, 21 and 24 cm) were removed (during period IMB_4, at 223 days) from the artificial soil filled column and inspected for possible contamination. The electrodes were placed in a de-ionized water-filled sample holder, shown in Figure AA 2, also fitted with current Ag-AgCl coil electrodes at either end, enabling SIP measurements. The agar gel filling of the electrodes at 18 and 21 cm were visibly blackened, with 18 cm being the most pronounced (Figure AA 2). The blackening of the gel suggests significant contamination of the agar gel stemming from the pore water itself. The blackening is characteristic of elevated levels of sulfide, which in the presence of Fe^{2+} precipitates as iron-sulfide minerals (Personna et al., 2008; Slater et al., 2008).

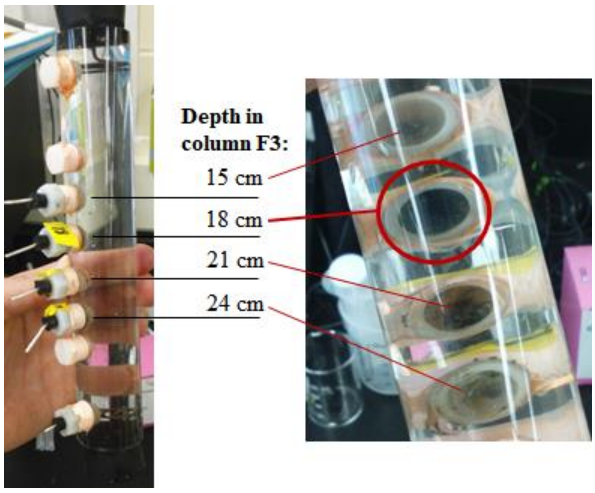

Figure AA 2. Visual inspection of potential electrodes removed from fluctuating WT column F3, following a 400 mV anomaly measured along the 18 to 24 cm depth interval. The electrodes were placed in a de-ionized water-filled sample holder. Blackening of the electrode gel filling, especially at 18 and 21 cm, provides evidence for significant contamination of the gel and possible interactions between the electrode ionic species, stemming from the pore water, present in the gel.

The coating of the electrodes in F3 was examined using energy dispersive X-ray spectrometry (EDS) (TM300 Table Top Scanning Electron Microscopre, Hitachi Technologies, Canada). Results from EDS analysis of both a fresh Ag-AgCl electrode and the 18 cm potential electrode in F3 are summarized in Figure AA 3. The relative elemental compositions of the fresh electrode (Figure AA 3a) shows that it is predominantly composed of Ag and Cl, whereas the electrode coating at 18 cm (Figure AA 3b) was predominantly composed of Ag and S. The relative elemental compositions determined by EDS suggest that the blackened electrodes underwent non-negligible chemical interactions with ionic species that migrated into the agar gel coating. The coating most likely changed composition from AgCl to Ag_2S. Therefore, the measure voltage anomalies are, at least in large part, electrodic potentials (controlled by the anodic and cathodic half-cell reactions outlined in the main text (equations 2.4 and 2.5), and not self-potential signals.

In order to assess whether the outlined electrodic reactions had compromised our SIP data acquisition, we compared the spectral phase shift ($-\varphi$) response of the electrodes in DI water, to that of freshly prepared Ag-AgCl electrodes. The results, outlined in Figure AA 4, show almost identical responses from both the fresh and blackened electrodes. The destructive nature of the electrode coating sample for EPS analysis required that the electrodes that were removed, be replaced. SIP signals measured prior to removal and after replacement for SIP measurement depths 19.5 and 25.5 cm are compared in Figure AA 5. Both measurements at 223 and 230 days were during an imbibition period (IMB_4). The results in Figure AA 5 show very little variation between the electrodes (fresh vs. blackened), suggesting that the coating chemistry modification, which generated the EP anomaly had a negligible effect on SIP measurements.

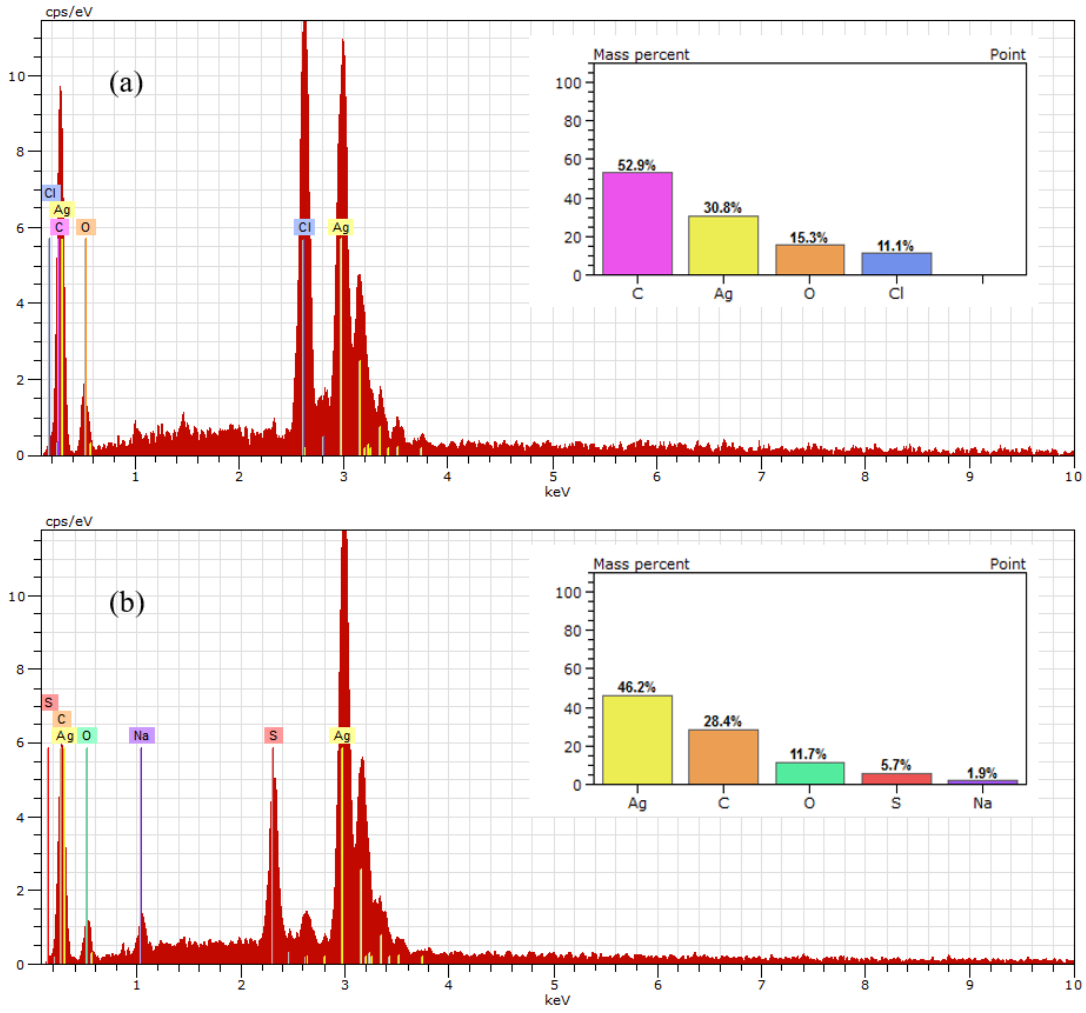

Figure AA 3. Energy dispersive X-ray spectrometry (EDS) (TM300 Table Top Scanning Electron Microscopre, Hitachi Technologies, Canada) results for relative elemental composition of the electrode coating from (a) a fresh Ag-AgCl electrode and (b) the potential electrode at 18 cm in column F3, effectively coated with Ag_2S.

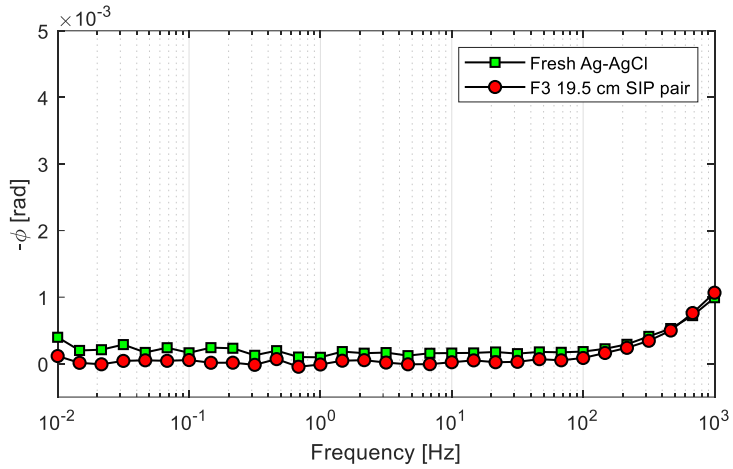

Figure AA 4. Phase shift (-φ) response (over 31 log frequency steps) of freshly prepared Ag-AgCl potential electrodes and the blackened potential electrodes removed from 18 and 21 cm (the 19.5 cm SIP measurement pair) in column F3.

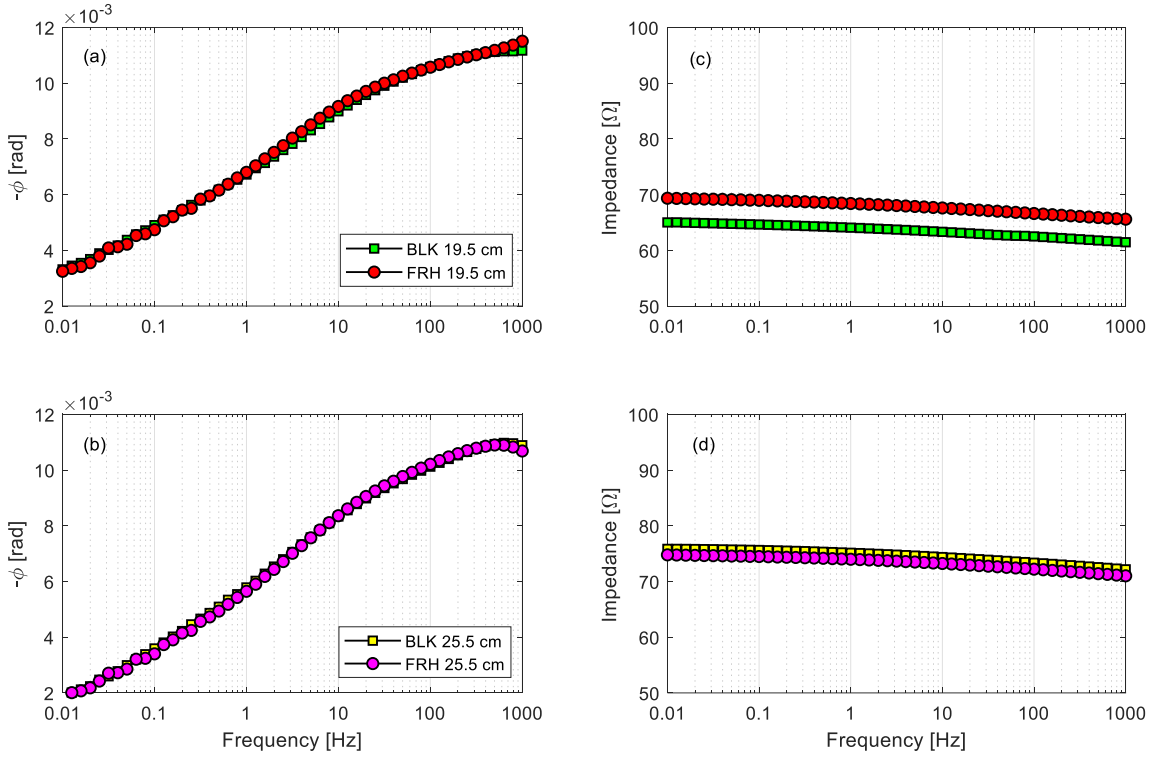

Figure AA 5. Spectral induced polarization (SIP) phase shift (-φ) and impedance signals measured at 19.5 (a and c) and 25.5 cm (b and d) in column F3 prior to blackened (BLK) electrode removal at 223 days and with fresh (FRH) Ag-AgCl electrodes at 230 days.

Surface area to pore-volume ratio (S_{por})

Specific surface area (SSA) was measured using the N_2-BET method (Gemini VII 2930, Micrometrics, USA) for each of the soil components separately, and the artificial soil mixture, prior to packing of the columns. The surface area measured for the mixture, and that calculated based on the mass fractions of each material in the mixture, were 9.34 and 9.61 $m^2 g^{-1}$, respectively. The measured SSAs for each of the soil materials are presented in Table AA 1. The matrix density of the artificial soil (ρ_s = 2.51 g cm^{-3}) was determined based on the mass fraction of the individual components and their density (a matrix density of 1.60 g cm^{-3} was assumed for the soil humus, the cut-off density that separates humus from mineral matter (Christensen, 1992).

Table AA 1. Matrix density (ρ_s) and N_2-BET measured specific surface area (SSA) for each of the individual artificial soil constituents.

Material	**Matrix Density (ρ_s) [g cm^{-3}]**	**N_2-BET SSA [$m^2 g^{-2}$]**
Quartz sand	2.65	Below detection
Montmorillonite	2.01	63.97
Organic matter (humus)	1.6	1.15
Goethite	4.3	123.56

Real conductivity (σ') at 13.5 cm normalized to pore water conductivity

Pore water electrical conductivity (EC) measured between 183 and 293 days, at 15 cm, was gap-filled by linearly interpolating between measurement points. Real conductivity (σ'), measured at 13.5 cm, was divided by the interpolated EC values in order to isolate the contribution of saturation on the temporal dynamics in σ'. The normalized σ' (i.e., σ'/EC) is plotted in Figure AA 6, along with σ' and EC. Figure AA 6 highlights variations in the EC normalized real conductivity, in response to drainage and imbibition. The apparent variations provide evidence to the strong control of saturation on σ'.

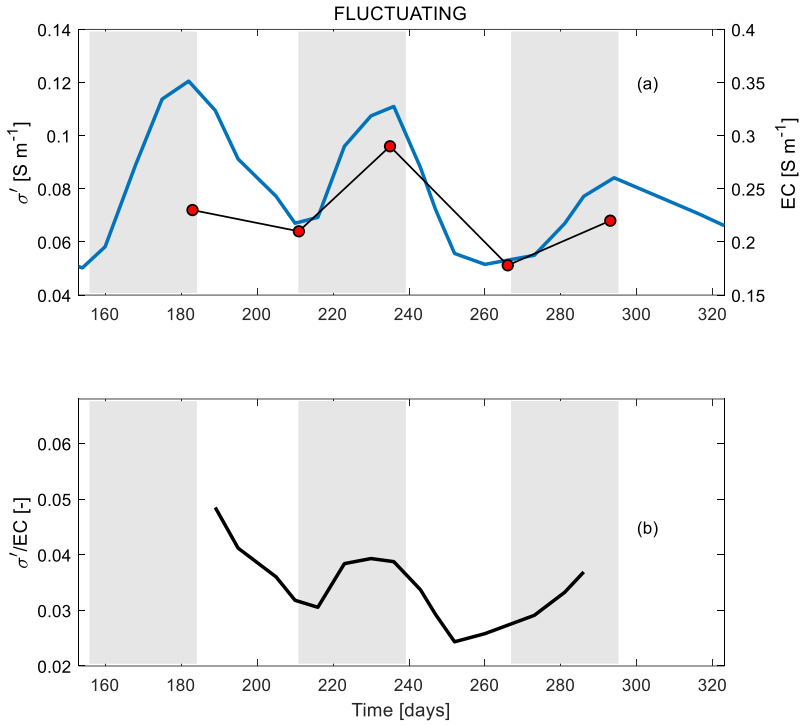

Figure AA 6. Time series σ' data (at 13.5 cm) during the period were not EC measurements are missing from pore water samples at 15 cm (a), and σ' normalized to interpolated EC measurements to highlight the saturation dependence in the temporal σ' signals. Grey shaded areas correspond to imbibition periods, and white areas in the plot correspond to drainage periods.

Appendix B: Supplementary Information for Chapter 3

Modified from the supporting information in:

Mellage, A., C. M. Smeaton, A. Furman, E. A. Atekwana, F. Rezanezhad, and P. Van Cappellen (2018). Linking Spectral Induced Polarization (SIP) and Subsurface Microbial Processes: Results from Sand Column Incubation Experiments. *Environmental Science & Technology*. 52(4), 2081-2090.

Microbial growth medium

The saturating pore-water within the column batch reactors was a microbial growth medium (M1) prepared after Myers and Nealson(Myers and Nealson, 1988) and modified for the specific conditions in this study. The media was buffered to a pH of 7.5 with filter sterilized HEPES buffer, to a concentration of 20 mM and consisted of: 9 mM $(NH_4)SO_4$, 1.5 µM Na_2SeO_4, 0.1 mM KH_2PO_4, 0.1 mM NaCl, 0.05 mM $NiCl_2.H_2O$, 0.05 mM $CoSO_4.7H_2O$, 1 mM $MgSO_4$, 5.4 µM $FeSO_4.7H_2O$, 0.5 mM $CaCl_2.2H_2O$. Most notably sodium succinate $Na_2C_4H_4O_4$, Na_2EDTA and amino acids were omitted from the original media recipe. The above composition was used for washing the cells and then inoculating them into an electron donor / electron acceptor and carbon source containing growth media of the same composition, amended with filter sterilized 20 mM Na-Lactate and 1 mM $NaNO_3$. This was the final composition of the saturating pore water (growth media) for packing the column batch reactors. Where not explicitly stated, solutions were autoclaved at 121°C.

Shewanella oneidensis MR-1 were harvested from LB-agar plates and inoculated into 20 [g L^{-1}] Luria Bertani (LB) media and grown overnight at 32°C at 60 rpm to late log phase (for 14-16 h). The LB-cell suspension was centrifuged (at 3500 rpm), decanted, and washed with the M1 media three times and diluted to a final OD_{600} of 0.033 (3.5×10^7 cells/mL).

Transport parameters

The effective diffusion coefficient, D_e [$m^2\ s^{-1}$], was determined from the molecular diffusion, D_m [$m^2\ s^{-1}$], coefficient of each of the aqueous species (i), in the model, assuming a homogenous porosity, ϕ [-], according to the following relationship:

$$D_e^i = \frac{D_m^i}{1 - \ln(\phi^2)} \qquad \text{AB.1}$$

Table AB 1. Molecular diffusion coefficients.

Species		D_m [$m^2\ s^{-1}$]	**Reference**
Lactate	$C_3H_5O_3^-$	1.10×10^{-9}	(Øyaas et al., 1995)
Acetate	$C_2H_3O_2^-$	9.89×10^{-10}	(Fischer and Weiss, 1986)
Nitrate	NO_3^-	1.90×10^{-9}	(Yuan-Hui and Gregory, 1974)
Nitrite	NO_2^-	1.98×10^{-9}	(Yuan-Hui and Gregory, 1974)
Ammonium	NH_4^+	1.91×10^{-9}	(Yuan-Hui and Gregory, 1974)
Bicarbonate	HCO_3^-	1.18×10^{-9}	(Yuan-Hui and Gregory, 1974)
Ferrous iron	Fe^{2+}	2.00×10^{-9}	(Cook, 1984)

ATP concentrations

ATP concentrations are commonly used as a proxy for microbial cell viability/activity in pure cultures, industrial and environmental samples (see Hammes et al. (2010) and references therein). Figure AB 1 illustrates the relationship between cell counts and ATP concentrations for *S. oneidensis* measured after overnight growth in Luria Bertrani (LB) broth and inoculated/diluted into PBS. Consequently, this relationship was used in the main text to calculate an estimated range of expected cell densities based on measured ATP values (Table AB 2), as a comparison to model results. This was meant as a qualitative comparison, as it is expected that intracellular ATP concentrations may change as a function of growth stage (i.e., decrease after exponential phase) and size (Eydal and Pedersen, 2007).

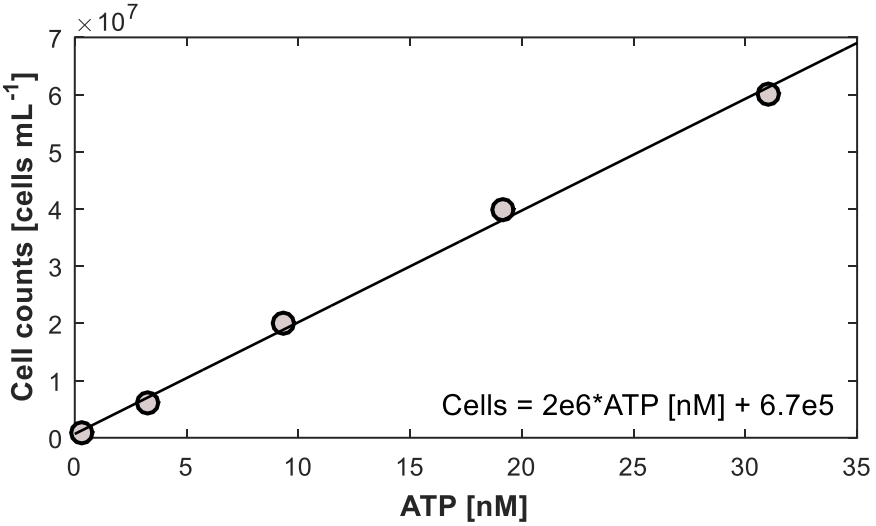

Figure AB 1. Empirical relationship between measured ATP concentrations and cell densities.

Measured ATP concentrations increased in both the QS and FS layers for the initial 70 h of the experiment which coincided with increasing rates of DNRA (see Chapter 3, Figure 3-10). ATP concentrations between top and bottom FS layers differed and the magnitude of the ATP concentration in the QS layer was higher than that in the top layer. ATP is not a direct quantitative measure of cell abundance and was used as a qualitative metric for microbial metabolic activity and as rough validation for microbial abundances. Differences between the layers could be a reflection of the time at which each sample was taken (i.e., slightly "missing" peak concentrations, due to intra-replicate heterogeneity) as well as Fe^{2+} interference with the measurement itself.

Table AB 2. Measured ATP concentrations (± standard deviation) for the iron coated (FS) top and bottom inclusions and the quartz sand (QS) inclusion; n = 3.

Time [h]	**ATP [nmol L_{PM}^{-1}]**								
	FS (TOP)			*QS (MID)*			*FS (BOTT)*		
11	7.09	±	0.22	10.04	±	0.06	6.01	±	0.28
24	6.17	±	0.06	6.09	±	0.17	10.47	±	0.12
68	15.34	±	0.04	31.58	±	0.13	35.17	±	0.14
118	4.35	±	0.44	10.57	±	0.37	35.04	±	0.14
165	7.93	±	0.07	1.09	±	0.81	6.63	±	0.09
237	2.95	±	0.06	11.38	±	0.18	31.99	±	0.29

SIP phenomenological models

Example of Cole-Cole goodness of fit (Weigand and Kemna, 2016c) for measured impedance magnitude $|Z|$ [Ω] and phase shift $|\varphi|$ [mrad] in the ferrihydrite coated quartz sand layer. The Cole-Cole model fit measured SIP data and was used to extract time dependent relaxation time and chargeability values.

We speculate that the decrease in the measured impedance below 0.1 Hz is a measurement artefact. Nevertheless, due to its occurrence below 0.1 Hz and low magnitude it does not represent a significant source of error. The spectral σ'' peaks associated with microbial processes presented in the main text lie between 1 and 100 Hz, well above the spectral range of the measured inaccuracy.

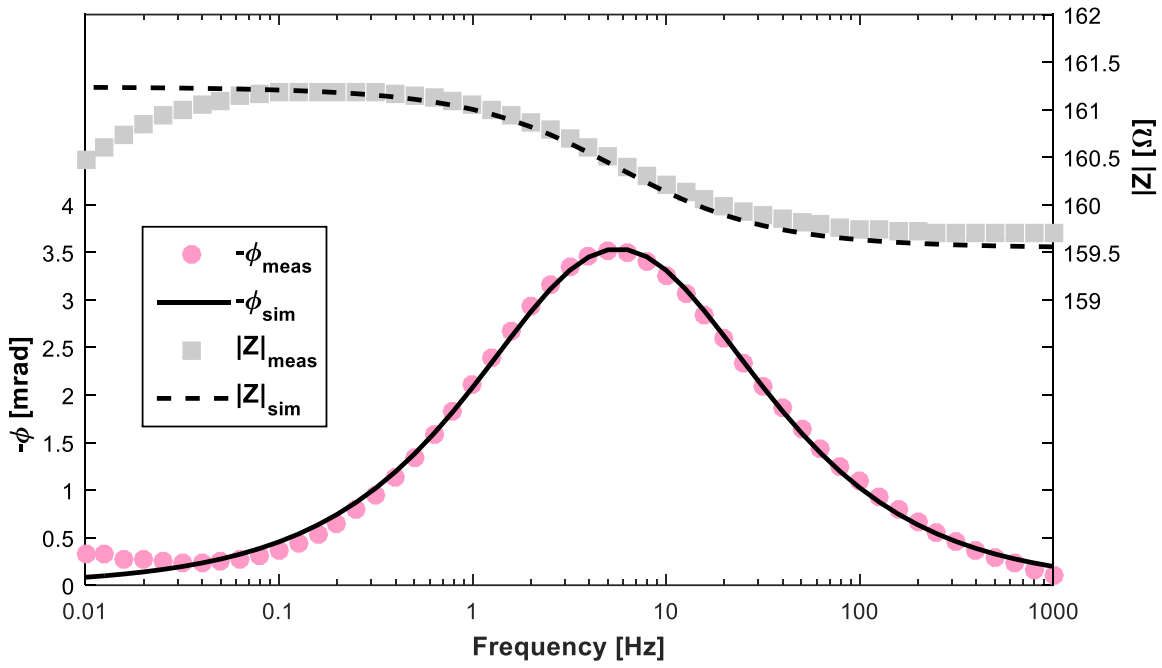

Figure AB 2. Fit of single Cole-Cole equation to SIP impedance and phase shift data.

Cell density estimation from normalized chargeability

The normalized chargeability values extracted from the Cole-Cole relaxation were used to estimate cell abundance within the iron coated (top) layer. The model used was developed by Revil et al. (2012):

$$m_n = \frac{2}{3}\left(\frac{\phi}{1-\phi}\right) m_B\left(\beta_{(+)} V_B \rho_B CEC_B\right) C_B \qquad \text{AB.2}$$

where m_n is the normalized chargeability [S m^{-1}], m_B[-] is the Archie cementation exponent (Archie, 1942), $\beta_{(+)}$ is the counter-ion mobility within the Stern layer [m^2 s^{-1} V^{-1}], V_B is the volume of one bacteria [m^3], ρ_B is the mass density of active bacteria [kg m^3], CEC_B is the cation exchange capacity of an active cell [C kg^{-1}] and C_B is the number of cells per unit bulk volume.

The normalized chargeability data used to determine the cell density based on the model are presented in Figure AB 3. Figure AB 3b shows the predicted cell concentrations generated using equation SE4. The abundance of cells is overestimated by almost two orders of magnitude in reference to the simulated cell density curves as well as the initial measured cell density within the microbial growth media (see main text). This discrepancy could be due to the fact that parameters like the CEC_B and $\beta_{(+)}$ are influenced by microbial metabolic activity and do not remain constant.

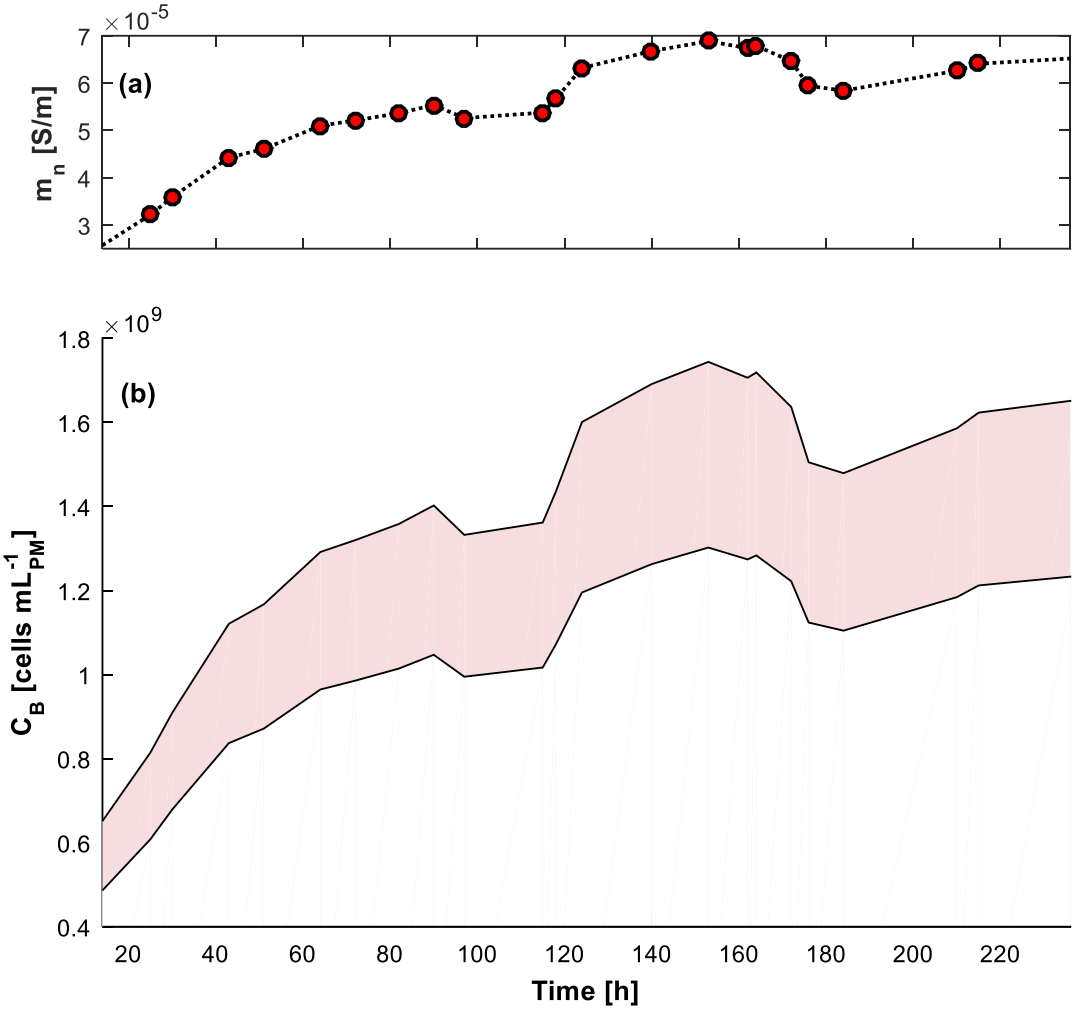

Figure AB 3. Estimated microbial growth curve (b) from normalized chargeability (a) data, using either a constant cell volume. A range (shaded pink area) of predicted growth curves is presented according to the range in the cementation exponent for different cell types in Revil et al. (2012), m_B 1.12 – 1.5 [-]. The parameters used for the calculation were extracted from Revil et al. (2012): $\beta_{(+)}$ = 4.7·10^{-10} [m^2 s^{-1} V^{-1}], CEC_B = 2·10^5 [C kg^{-1}] and ρ_B = 1020 [kg m^3].

Varying cell size

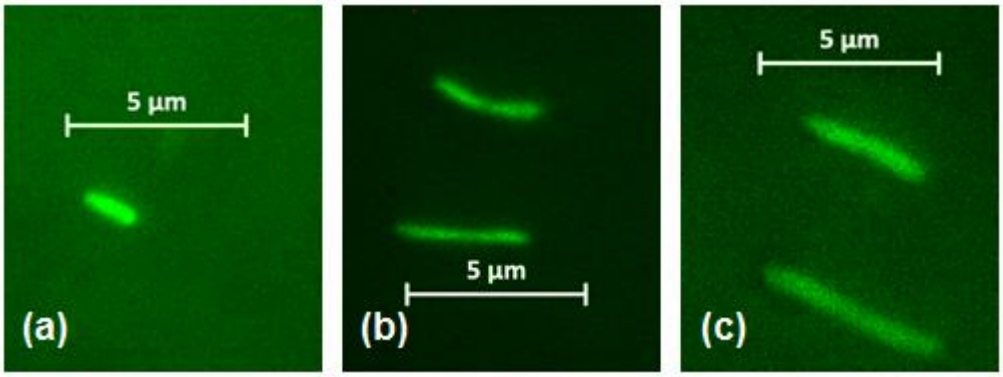

Figure AB 4. Images of individual, stained cells of *S. oneidensis* under 100x magnification, showing varying cell size dependent on environmental conditions: (a) devoid of electron donor/acceptor and carbon source, (b) lactate and fumarate present for growth and (c) cells recently inoculated into growth media containing lactate and nitrate after having been cultured in LB media. Images (a) and (b) are from a preliminary experiment with higher cell densities in quartz sand.

Appendix C: Supplementary Information for Chapter 4

Modified from the supporting information for:

Mellage, A., Smeaton, C.M., Furman, A., Atekwana, E.A., Rezanezhad, F. and Van Cappellen, P. (submitted). Bacterial Stern-layer diffusion: Experimental determination with spectral induced polarization (SIP) and sensitivity to nitrite toxicity. *Geophysical Journal International.* GJI-S-18-1031L.

Flow-through column tracer injection

A continuous tracer injection (Cl^-) was performed in one of the flow-through columns packed with quartz sand in order to determine the time for 1 pore volume (t_{PV}). A sodium chloride solution, with an average Cl^- concentration of 2.2 ($\pm$0.03) mM, was injected for 14.5 hours at an average flow rate of 9.84 ($\pm$0.52) mL h^{-1}. Periodic outflow (roughly every 20 minutes) samples were taken, by collecting effluent over 20 minute intervals. Cl^- concentrations were measured in the outflow samples using a chloride ion selective electrode (Thermo Fisher Scientific, Beverly, MA, USA) connected to a conductivity probe (Orion 290A, Thermo Fisher Scientific). Hydrus 1D (H1D) (Simunek et al., 2005) was used to numerically solve the advection-dispersion equation for conservative transport and simulate Cl^- breakthrough in the experimental columns. The fit (D = 0.21 cm^2 h^{-1}; v = 1.84 cm h^{-1}) of equation 1 to outflow breakthrough is illustrated in Figure AC 1. The analysis from Figure AC 1, allowed for the estimation of t_{PV} = 8.575 hours. From Figure AC 1 it is evident that at 12 hours (1.4 PV), the outflow concentration is equal to that at the inflow.

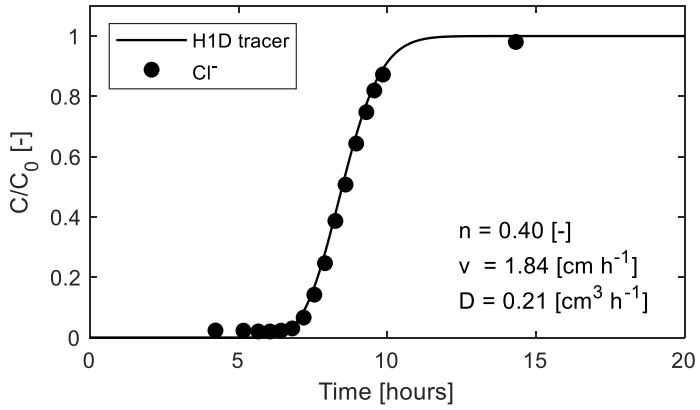

Figure AC 1. Normalized concentration (C/C_0) breakthrough curve for a continuous Cl^- tracer injection.

Flow cytometry size calibration

Cell size was determined at every sampling time point using non-fluorescent microbeads (Flow cytometry size calibration kit, F-13838, Thermofisher). The relationship derived from the median forward scatter intensity (FSC-A) and the size of the different non-fluorescent microbeads (Figure AC 2) was used to calculate the size of *S. oneidensis* cells using the median FSC-A of each cell density sample.

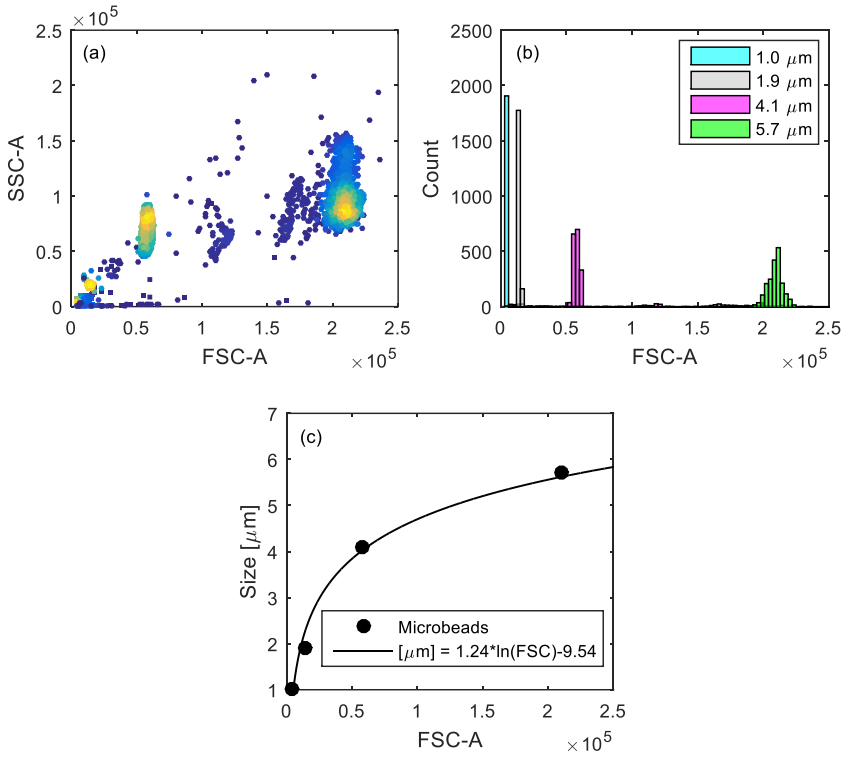

Figure AC 2. Flow cytometry non-fluorescent microbead size calibration (F-13838 size calibration kit, Thermofisher) used to estimate the size of unstained, unfixed *S. oneidensis* cells. Side scatter (SSC-A) and forward scatter (FSC-A) intensities of the four microbeads are plotted against each other in (a), total counts and FSC-A are plotted in (b) and the relationship between mirobead size and median FSC-A intensity is shown in (c).

SIP-columns

Normalized peak imaginary conductivity (σ''), for the two columns fitted with electrodes for SIP measurements, is presented in Figure AC 3. Normalized σ'' was calculated as the difference between measured σ'' and σ'' immediately following the first injection (*i.e.*, minimum), divided by the difference between the maximum and minimum. A comparison of spectral σ'' signals for both columns, 10 hours prior to the first injection (during the establishment phase), and shortly after the first injection, is presented in Figure AC 4. After the first injection of NO_3^- and lactate, at 0 hours, the increasing trend in σ'' was similar in both columns, G1 and G2. The trend in σ'' diverged between the two columns after the second injection. The drop in σ'' after 191 hours was less abrupt in column G1 than in column G2, but the recovery was short-lived in G1, and σ'' steadily decreased until the end of the final incubation period under no-flow conditions. The increases in σ'' following an abrupt dip in the response in G2, matched the measured trends in cell density (see main text). Due to the discrepancy between the columns after the second injection, these were sacrificially sampled in duplicate, at the end of incubation, t = 315 hours. The measured cell density in each column was different by a factor of 2.44 (3.23×10^6 and 1.36×10^6 cells mL_{PM}^{-1}, for columns G2 and G1, respectively), and each corresponded to the observed trends in σ'' measured in the separate columns.

Each sampling point constituted a separate, sacrificially sampled flow-through reactor. The trend in the geochemical data presented in the main text provides confidence of similar biogeochemistry between reactors. Nevertheless, the difference in trends in σ'' in the SIP columns, specifically after 215 hours, suggest that the microbial community underwent higher decay after recovering from a dip in σ'', likely associated with NO_2^- inhibitory effects (Zhang et al., 2013; Sijbesma et al., 1996). The temporal dynamics in σ'' measured in G2, follow the unified trend measured across all biogeochemical markers more closely and was therefore relied on for discussion of the overall dataset and postulation of a quantitative relationship between SIP and biomass concentrations.

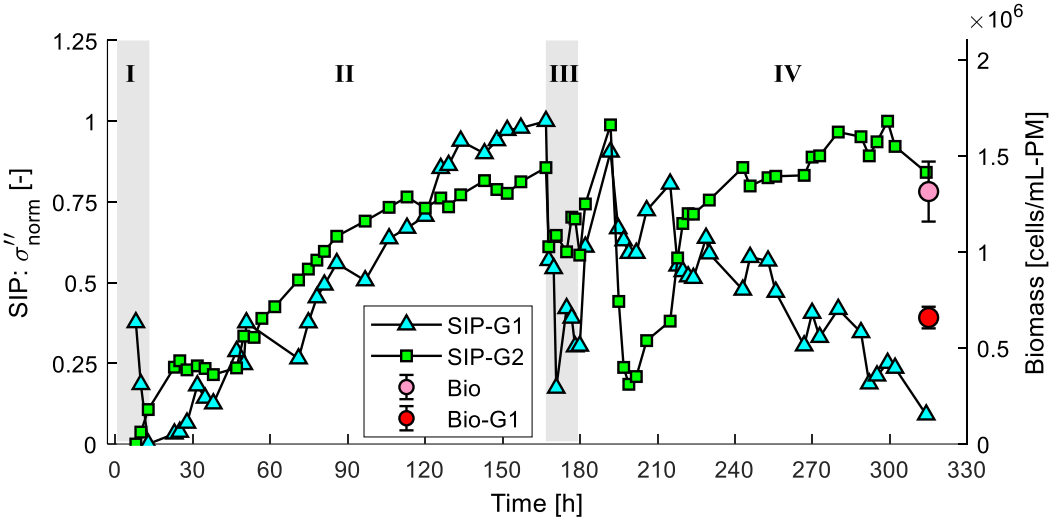

Figure AC 3. Imaginary conductivity, normalized for the maximum measured in each column (σ''_{norm}) for both SIP measurement columns, G1 and G2. Injection periods of lactate and NO_3^- are illustrated by grey rectangles. Final cell density measurements in both SIP columns sampled in duplicate at 315 hours, are plotted alongside the σ''_{norm} data.

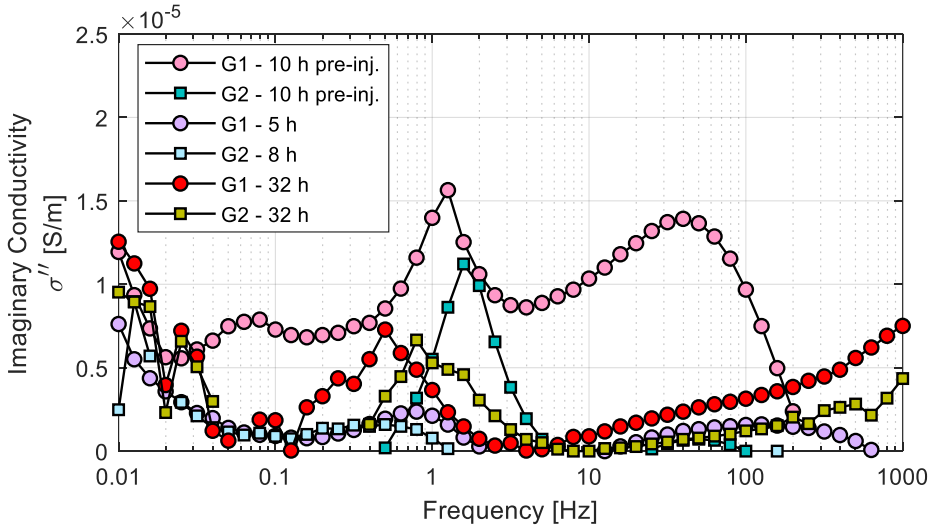

Figure AC 4. Spectral imaginary conductivity comparison between columns G1 and G2 10 hours prior and shortly after the first injection.

Lactate and acetate data

Lactate, at 10 mM, was present in the growth medium used as both the packing solution and inflow solution, to stimulate growth in the columns. Acetate is a product of lactate oxidation (for details see: Mellage et al. (2018)) during dissimilatory nitrate reduction to ammonium (DNRA). Both carbon source (lactate) and degradation product (acetate) were measured using ion chromatography (Dionex ICS-5000 equipped with a capillary IonPac® AS18 column).

Lactate concentration increased during the first injection, from the concentration measured following the pre-equilibration phase (Figure AC 5). It was then consumed resulting in the increased production of acetate. The column sampled immediately prior to injection of inflow solution at 167 hours, had no detectable lactate, and higher than expected acetate concentrations (both expected to remain constant after 35 hours). Propionate, was detected at high concentrations in this column, suggesting that lactate was fermented (Seeliger et al., 2002). There were no other samples in which significant concentrations of propionate were detected, and no propionate was detected in any of the outflow samples taken during the second injection (outflow concentration data is not presented), suggesting that the fermentation pathway in the column, sacrificially sampled at 167 hours, did not occur in any other replicate. This serves as justification for omitting the cell density measurement taken from that column, in the discussion of the results in the main text.

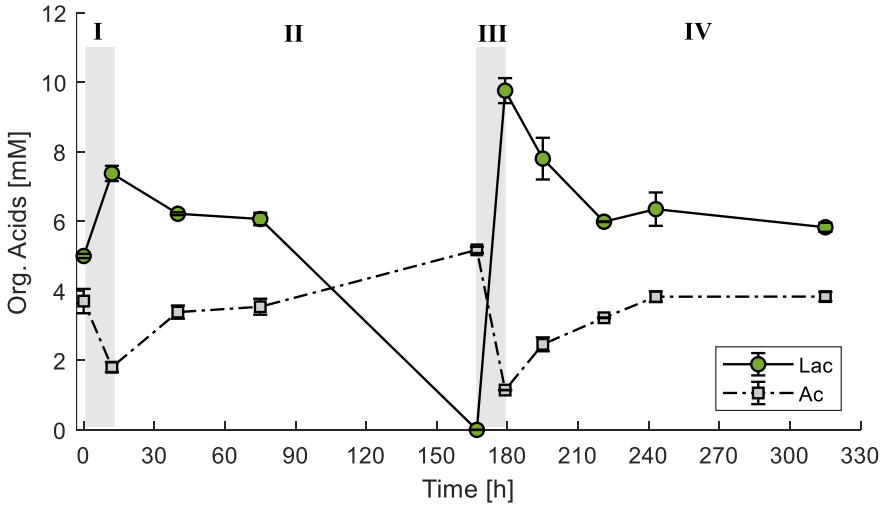

Figure AC 5. Lactate and acetate concentration time-series.

ATP time series

The supernatant of the bulk sand samples treated for cell enumeration with flow-cytometry (see main text) were subsampled for adenosine triphosphate (ATP) content. ATP concentrations were determined through triplicate luminescence measurements (FlexStation 3 Multi-Mode Microplate Reader, Molecular Devices, LLC) in multiwell-plate format using a cell viability assay kit (BacTiter-GloTM Microbial Cell Viability Assay) (Mellage et al., 2018). Measured ATP concentrations during the experiment are presented in Figure AC 6. In accordance to the discussion in the main text, the ATP content for the sample immediately before phase II, the second injection, is omitted from Figure AC 6 because that column did not behave as a replicate (see main text for details).

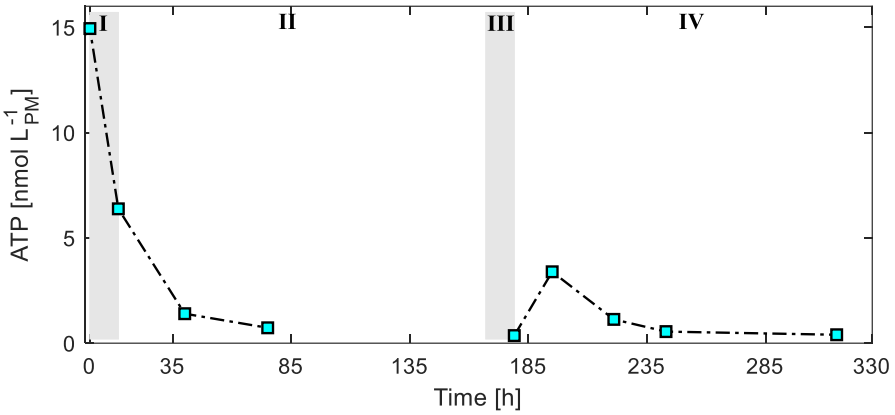

Figure AC 6. Adenosine triphosphate (ATP) concentrations measured in the sacrificially sampled reactors. The sample immediately prior to phase II, the second injection is omitted due to the detection of lactate fermentation products (see Chapter 4 for further details).

Non-growth (NG) control

A non-growth (NG) column, meant to serve as a control, was packed with media devoid of lactate and NO_3. A comparison of time series SIP data for peak real and imaginary conductivity and peak $-\varphi$, between columns G2 and NG, is presented in Figure AC 7. The NG column was incubated for the same period as all growth columns (480 hours). Data in Figure AC 7 are following the first injection (at 165 hours). The NG was never subjected to flow conditions, and therefore, σ' did not drop (Figure AC 7a). Both the σ'' and $-\varphi$ in the NG column, remained below magnitudes measured in column G2, and relatively constant during the time-period shown in Figure AC 7b and c.

The constant trends in SIP response, in the NG column are in agreement with the expected effect of the lactate and NO_3^- free conditions, on *Shewanella oneidensis.* The lack of growth-stimulating injection periods resulted in no significant changes in the temporal response of SIP signals in the control column.

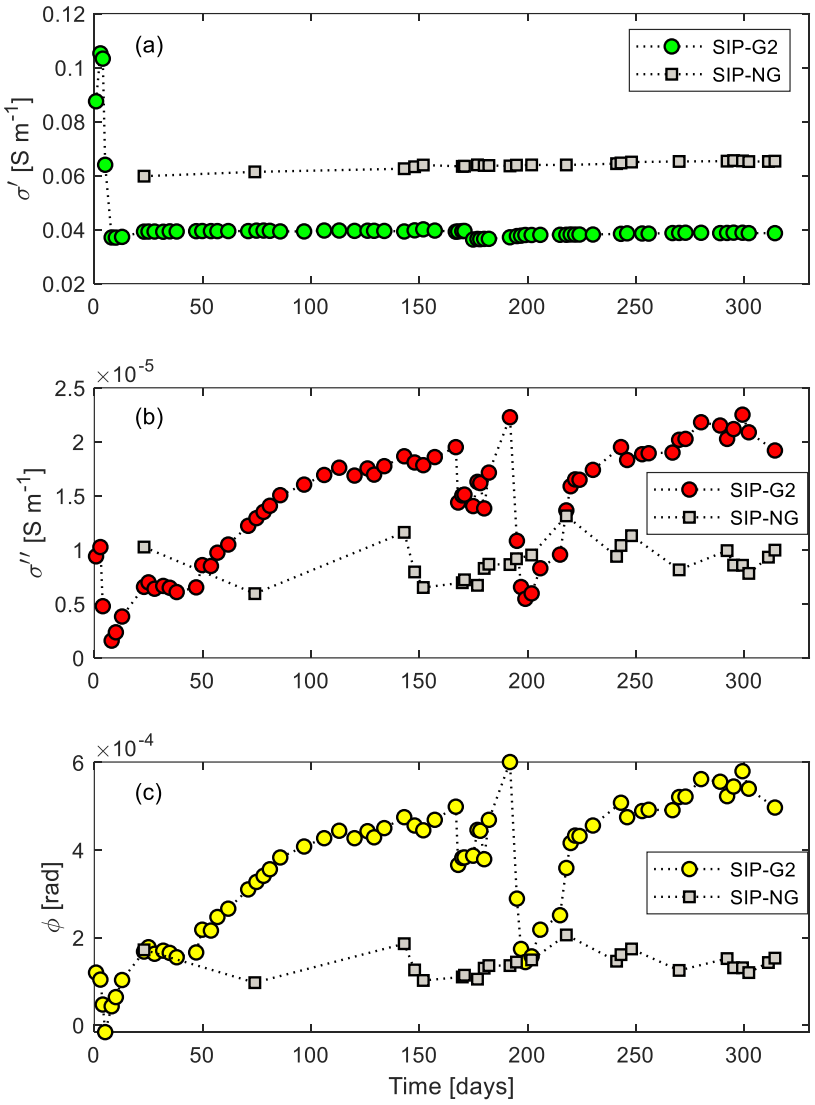

Figure AC 7. Complex conductivity response of sip column G2 of the growth incubation experiments undergoing two injections of nitrate and lactate compared to the response of a non-growth (NG) control column devoid of electron acceptor and electron donor.

Real conductivity (σ') and relaxation time

In the main text we hypothesize that in response to NO_2^- accumulation, bacterial membranes undergo changes, which alter ionic mobility and surface diffusion properties in the cell electrical double layer (EDL). Here, we compare real conductivity (σ') trends with τ dynamics as an added line of evidence, to highlight that τ anomalies arise from changes in the surface charge density of the cells. These changes alter aqueous and sorbed concentrations of cations, resulting in the measured increase in σ' at the times of the anomalies, plotted in Figure AC 8.

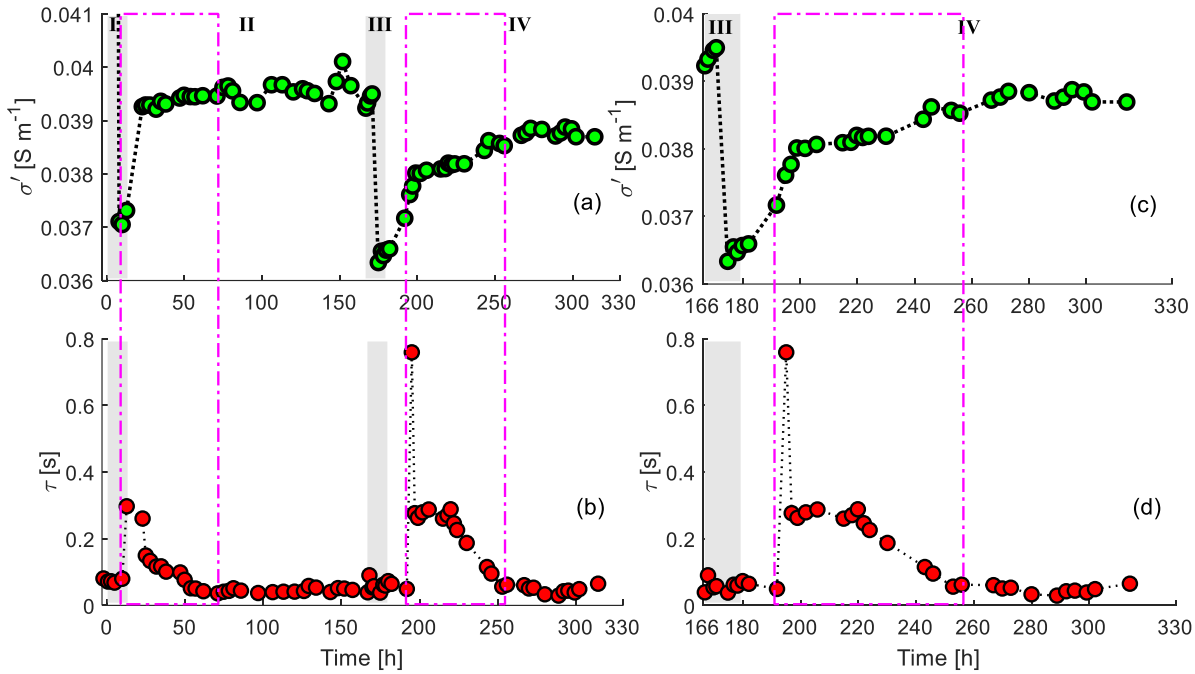

Figure AC 8. Comparison between real conductivity (σ') and relaxation time (τ), during all experimental phases (a and b), and during phases III and IV (c and d), highlighting the more pronounced τ anomaly.

Appendix D: Supplementary Information for Chapter 5

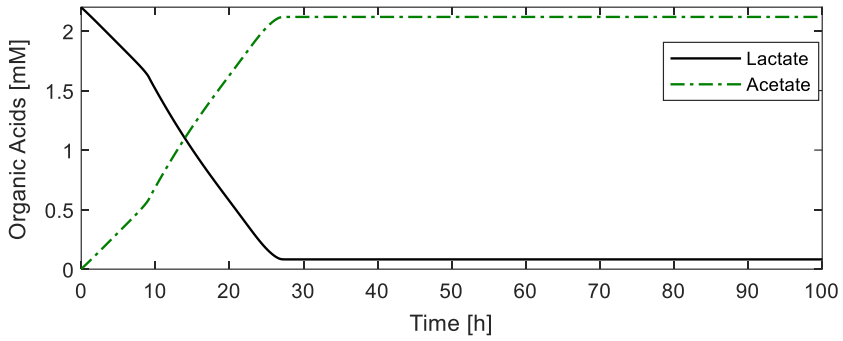

Figure AD 1. Simulated lactate and acetate concentrations during the well-mixed cell slurry experiment (Smeaton, unpublished).

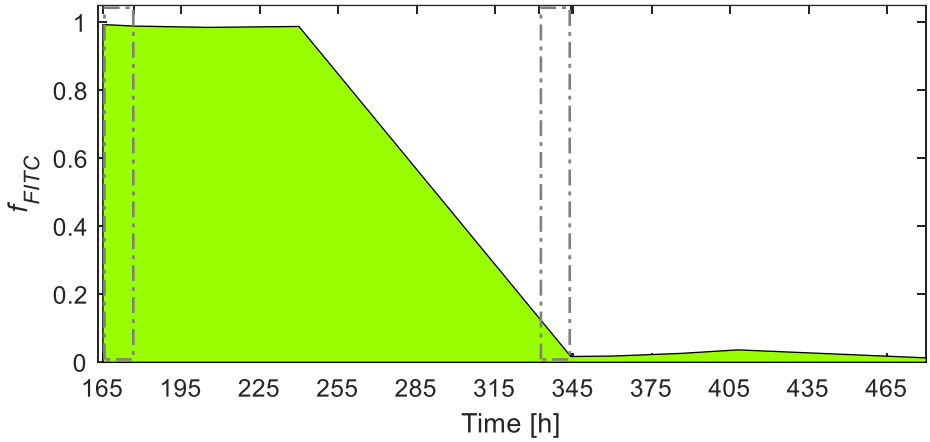

Figure AD 2. Proportion of green autofluorescence, f_{FITC}, measured during each sacrificial sampling event.

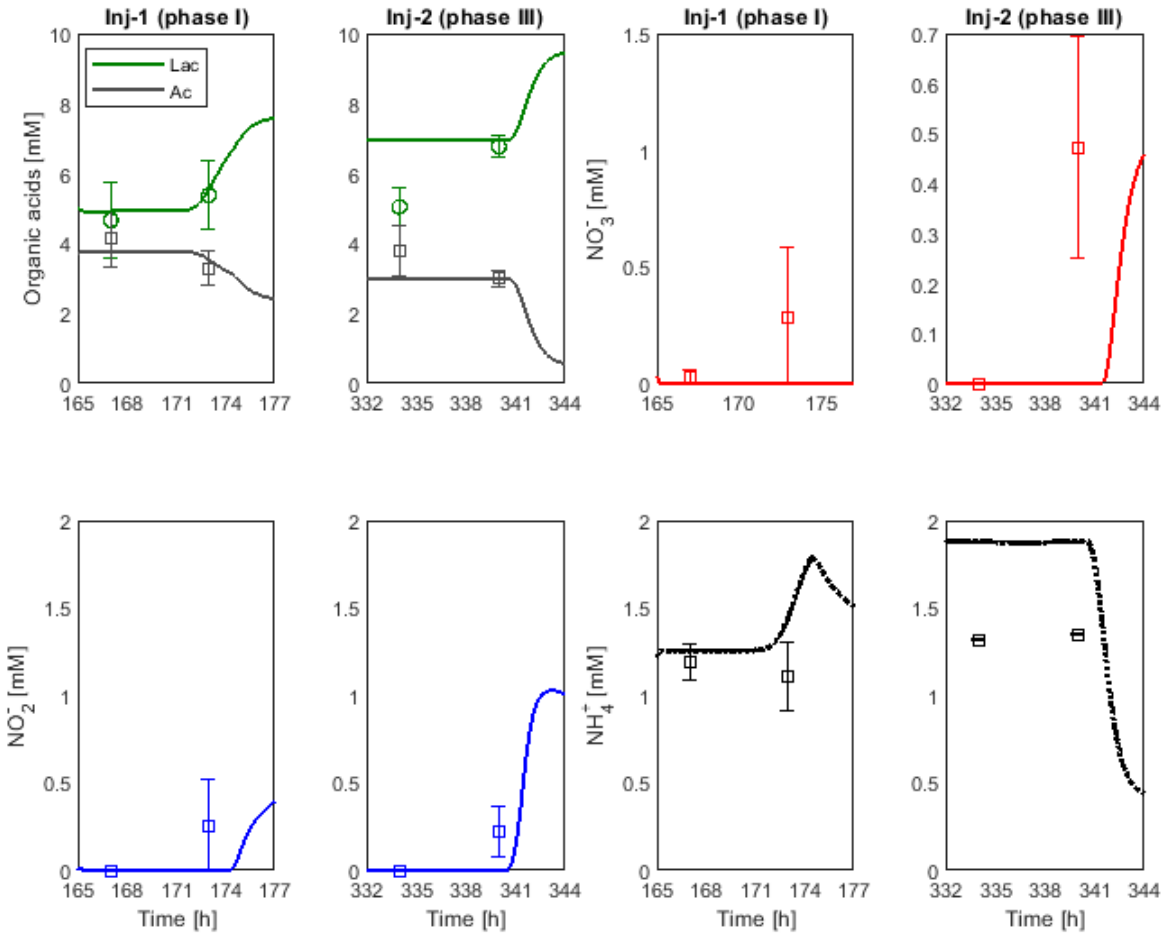

Figure AD 3. Flow-injection simulated breakthrough curves compared to average outflow sample measurements at 2 and 8 hours after the onset of each injection (n = 9 for phase I and n = 5 for phase III).

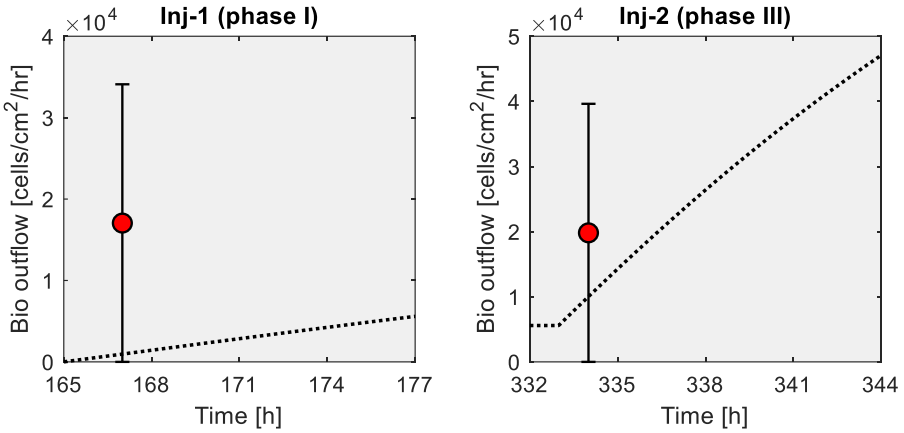

Figure AD 4. Average measured outflow flux of cells 2 hours into injection during phases I and III, compared to the simulated rate of flow-induced decay in the columns.

Appendix E: Supplementary Information for Chapter 6

Modified from the supporting information for:

Mellage, A., Holmes, A.B., Linley, S., Vallée, L., Rezanezhad, F., Thomson, N., Gu, F. and Van Cappellen, P. (2018). Sensing coated iron-oxide nanoparticles with spectral induced polarization (SIP): Experiments in natural sand packed flow-through columns. *Environmental Science & Technology*. DOI: 10.1021/acs.est.8b03686.

Iron-oxide nanoparticle synthesis

Synthesis was adapted from methods previously reported (Chan and Gu, 2013). $FeSO_4 \cdot 7H_2O$ (>99%, Sigma Aldrich) and $FeCl_3 \cdot 6H_2O$ (>99%, Sigma Aldrich) were added to deoxygenated water at a molar ratio of 2:3 ($FeSO_4$:$FeCl_3$), then purged with N_2 gas for 30 minutes while stirred, after which NH_4OH (28-30%, Sigma Aldrich) and oleic acid (>90%, Sigma Aldrich) were added to final concentrations of 4 and 0.22 mol/L, respectively. This solution was sealed and stirred at 70 °C for 1 h, then stirred at 90 °C under flowing N_2 for 1 h to purge evolved NH_3 gas. After cooling to room temperature, the black, magnetic precipitate was recovered by magnetic decantation and washed 3x by deoxygenated Millipore DI water (Millipore Elix 5), and then 3x by ethanol (99%, Fisher Scientific) before being dried under flowing N_2. Pluronic nanoparticle coating was applied through a phase-transfer process in which the dried nanoparticles and additional oleic acid were added to hexane at a concentration of 90 g/L and 1% v/v, respectively. The resulting suspension was added to a 10 g/L solution of Pluronic P104 (BASF Canada) at a concentration of 10 % v/v and probe sonicated for 30 min to emulsify the water and hexane phases (Fisher Scientific FB505 Sonic Dismembrator, 200 W). The emulsified nanoparticle sample was transferred to a separatory funnel and separated over 48 h. The resulting aqueous nanoparticle suspension was drained, sealed, and refrigerated until use.

Nanoparticle characterization

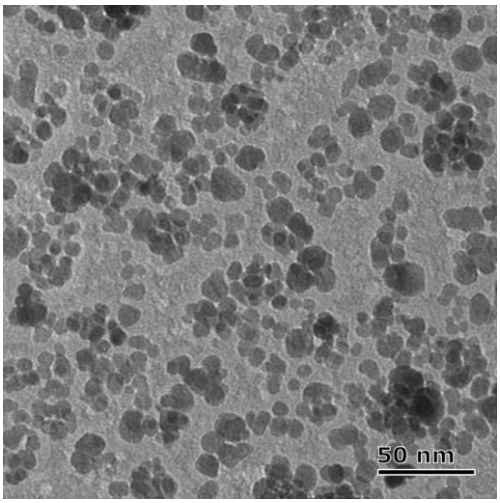

Figure AE 1. Transmission electron microscope of Pluronic P104 coated iron oxide nanoparticles showing an internal iron oxide diameter of 9.70 ± 2.70 nm.

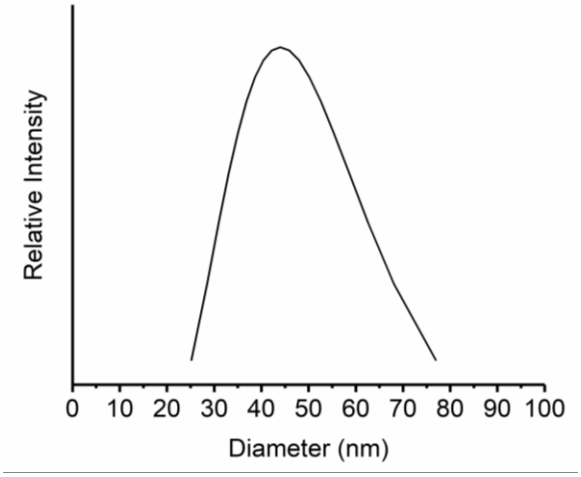

Figure AE 2. Diffracted light scattering (DLS) size distribution measuring the hydrodynamic radius of the Pluronic P104 coated iron oxide nanoparticles.

Borden sand grain size distribution

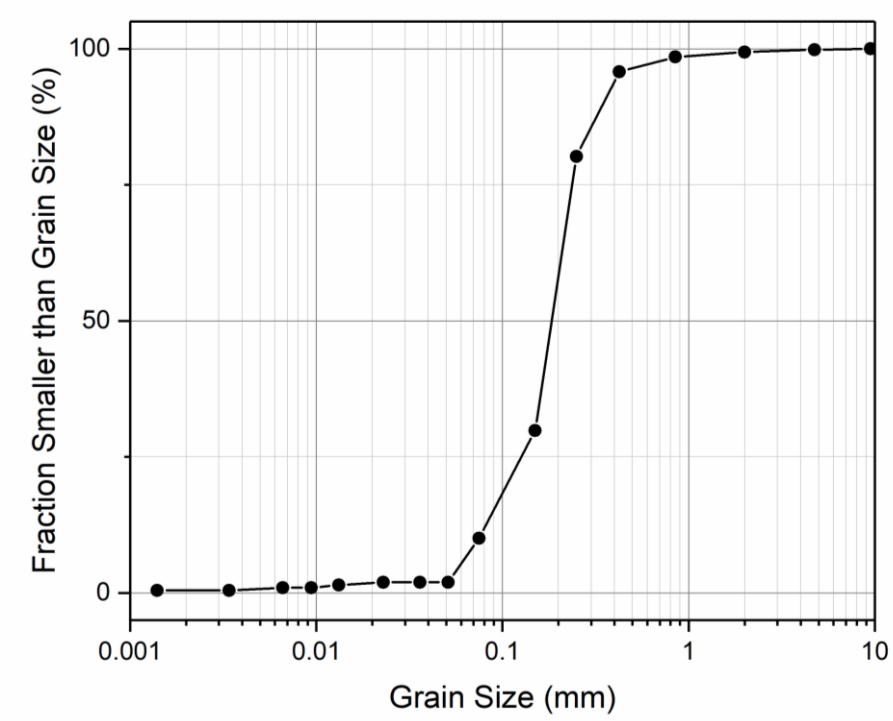

Figure AE 3. Grain size analysis of Borden sand.

Peak impedance and phase shift data

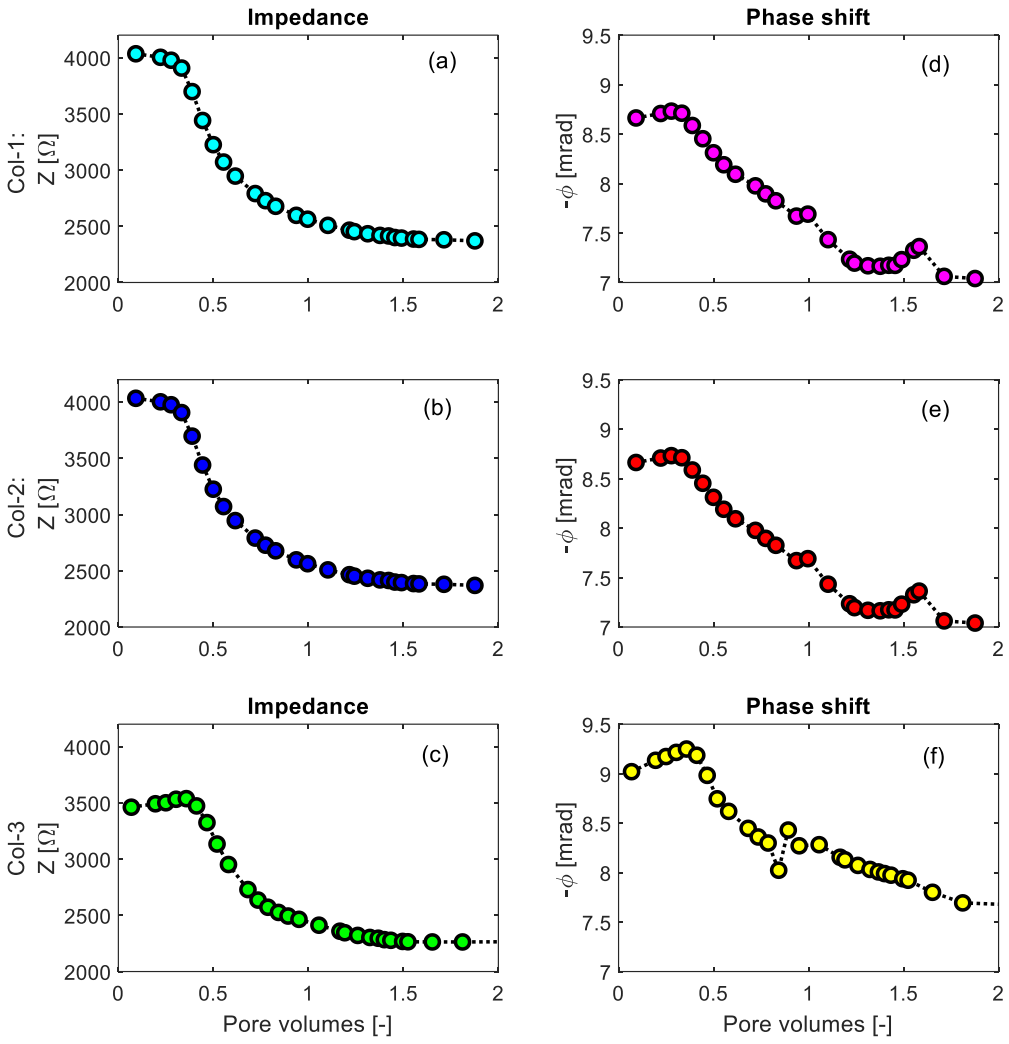

Figure AE 4. Measured peak impedance (Z) and phase shift (-φ) (below 1000 Hz) in all three columns during SPION injection.

SIP response in Column 2

The spectral imaginary conductivity (σ'') response measured in column 2 was omitted from the main text to avoid redundancy and is presented here. Similar to columns 1 and 3, column 2 exhibits an increase in σ'' above 80 Hz with increasing time since SPION injection. Electromagnetic coupling (EMC) effects are more pronounced in this column and appear at 2000 Hz. In order to compare all three collected datasets peak σ'' below 1000 Hz were compared to one another to minimize any bias stemming from EMC effects.

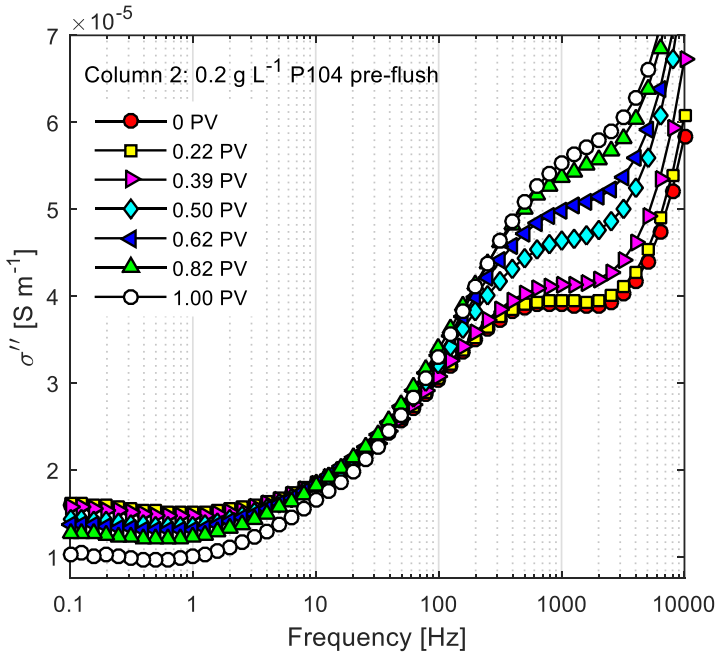

Figure AE 5. Imaginary conductivity (σ'') spectral response measured in column 2 during SPION injection. Each spectra represents an increasing pore volume (PV) with respect to injection time (PV = 0). The spectral response show evidence of electromagnetic coupling effects at frequencies above 2,000 Hz.

SIP baseline changes during pre-flush

The peak σ'' for all columns during all three injection phases (1 mM NaCl equilibration, P104 pre-flush and SPION injection) are presented in Figure AE 6. All columns were flushed with monionic 1 mM NaCl solution to allow the recently packed Borden sand to settle under upward flowing conditions to equilibrate the column to a steady SIP baseline. Flushing of monoionic solution was done for a minimum of 38 hours (2 pore volumes) for all columns Figure AE 6a-c. Columns 1 and 2 were both flushed with P104 Pluronic surfactant Figure AE 6d and e, prior to SPION injection. Figure AE 6d and e illustrate a measured decrease in peak σ'' during P104 injection, likely stemming from sorption related interactions between the surfactant and the Borden sand (Vaudelet et al., 2011b).

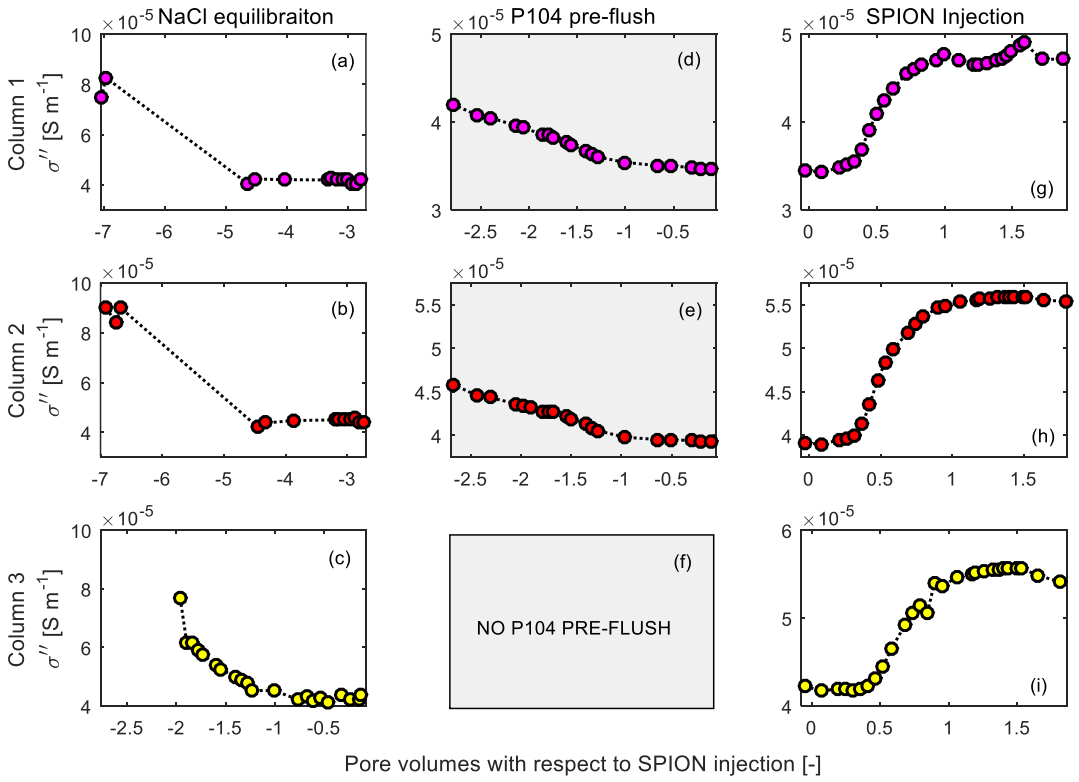

Figure AE 6. Peak imaginary conductivity (σ'') below 1000 Hz measured in all flow-through columns. Panel columns represent the different equilibration, pre-flush and injection phases. All columns were equilibrated with a 1 mM NaCl flush (a-c), columns 1 and 2 were then pre-flushed with a solution containing 0.2 g L^{-1} P104 Pluronic surfactant (d-f) and 1 mM NaCl and all columns were injected with a SPION suspension (g-i).